Spectroscopic Investigations of Nanoscale Aggregates and Their Electron Transfer Properties in Solution

by

Mingyan Wu

BS, Shandong University, China, 2000

MS, Shandong University, China, 2003

Submitted to the Graduate Faculty of

Art and Science in partial fulfillment

of the requirements for the degree of

Doctor of Philosophy

University of Pittsburgh

2011

UNIVERSITY OF PITTSBURGH

Art and Science

This dissertation was presented

by

Mingyan Wu

It was defended on

June 3rd, 2011

and approved by

Prof. Tara Meyer, Department of Chemistry

Prof. Sunil Saxena, Department of Chemistry

Prof. Jung-Kun Lee, Department of Mechanical Engineering

and Materials Science

Dissertation Advisor: Prof. David H. Waldeck, Department of Chemistry

Spectroscopic Investigations of Nanoscale Aggregates and Their Electron Transfer Properties in Solution

Mingyan Wu, PhD

University of Pittsburgh, 2011

In part I, the changes in the absorption and fluorescence properties of poly-(*p*-phenylene-ethynylene) (PPE)-based conjugated polyelectrolytes were investigated as a function of the solution conditions such as concentration, temperature, solvent, surfactant, and the ionic strength. The equilibrium between unaggregated and aggregated forms of the polymer was described and quantified. The fluorescence quenching of polymers by positively charged and neutral macromolecules were also investigated and showed that the quenching depends on electrostatic, hydrophobic, and energy transfer interactions with the quencher. A detailed study using fluorescence correlation spectroscopy was performed and allowed us to probe the templating of a surfactant OTAB on the polyelectrolytes well below its critical micelle concentration. Furthermore, it was found that the optical and aggregation properties of these conjugated polyeletrolytes can be manipulated by changing the charge density along the polymer backbone.

In part II, assemblies of CdSe and CdTe NPs were controlled by the electrostatic attraction of the charged functionalities placed on the NP surface coating. Electron transfer (ET) in assemblies of these NPs was studied in aqueous solution by fluorescence quenching. Three factors were found to determine how the ET depends on the nature of the NP assemblies by both

steady-state and time-resolved fluorescence measurements: the interparticle distance, the energetic alignment of the NP bands (hence the size of the NPs), and the direction of the electric field between the NPs, created by their surface charges. In addition, the assemblies of CdSe NPs on a dithiol coated Au electrode were created and their electronic energetics were quantified. The energy level alignment of the filled and unfilled electronic states of CdSe NPs with respect to the Au Fermi level was investigated by both cyclic voltammetry and photoemission spectroscopy separately. These two measurements showed that the CdSe filled states become 'pinned' to the Fermi level of the Au electrode. Furthermore, the preliminary electrochemical studies at the interface were carried out in order to investigate the organization and reactivity of nanoparticles/dyads at ITIES.

TABLE OF CONTENTS

LIST OF TABLES

LIST OF FIGURES

LIST OF SCHEMES

Dedicated to my father

(1946-2008)

ACKNOWLEDGMENTS

It is a pleasure to thank the many people who made this thesis possible.

I would like to give my first and the most important appreciations to my advisor, Prof. David. H. Waldeck. His enthusiasm for science encourages me to keep on studying; his helpful advice and suggestions make my projects go more smoothly; and his kind help and patience make the life here in a totally different country a lot easier. Without him I could not have overcome all kinds of obstacles and could not have gone so far. He is a person I would truly respect and I deeply appreciate all the support, valuable guidance, and understanding he has provided during these years.

My sincere thanks also goes to Dr. Palwinder Kaur, Dr. Hongjun Yue, and Dr. Lei Wang, the former group members graduated in 2007 and 2010. I worked with Dr. Kaur on the polymer project since I joined the group in 2006, Dr. Yue trained me on the FCS and Dr. Wang cooperated with me on the solar cell project. I learned a lot from all of them and really appreciate all the help they have provided. Without them the projects would have been incomplete.

I wish to extend my warmest thanks to all the others who have helped me with nanocrystal solar cell project, especially Prof. Petoud and Dr. Andrenne Yingling for providing the lab space and helpful discussions for nanoparticle synthesis at the beginning of that project. I also owe many thanks to Prof. Amemiya and his postdoc, Dr. Ryoichi Ishimatsu, who kindly offered lots of valuable information on liquid-liquid interface studies.

I offer my regards and blessings to all of those who supported me in any respect during the completion of the projects, especially the other group members: Dr. Emil Wierzbinski, Dr. Prasun Mukherjee, Dr. Kathryn Davis, Dr. Amit Paul, Dr. Subhasis Chakrabarti, Xing, Daniel, Matt, Robin, Brian and Yang, who are always nice to talk to whenever I had questions.

I would also extend my appreciation to the main office staff, machine shop, electronics shop and glass shop staff, who helped me from time to time at various occasions.

I wish to thank my entire family, my parents, sisters, and brothers for their constant support and encouragement throughout these trying years. In particular, I am deeply indebted to my father for his care and love. He worked industriously to support the big family and spared no effort to provide the best possible environment for me to grow up and attend school. Although he is no longer with us, he is forever remembered. I am sure he shares our joy and happiness in heaven. Finally, I wish to express my deepest gratitude to my husband Dr. Ziqin Feng for his unconditional love and support in these years: he took over most of the responsibilities of housework whenever I got tired, drove me to lab and pick me up when needed, even accompanied me at late night in lab if I am afraid to be alone in basement. Without him, this thesis would not be possible.

PART I

1.0 INTRODUCTION TO CONJUGATED POLYELECTROLYTES

1.1 RETROSPECTIVE OF CONJUGATED POLYMERS AND CONJUGATED POLYLELECTROLYTES

1.1.1 Conjugated Polymers (CPs)

π-conjugated polymers (CPs) are polyunsaturated compounds in which the backbone carbon atoms are sp^1- or sp^2-hybridized. Because of their interesting properties, namely, strong light absorption, strong fluorescence, electroactivity, good transport properties for charge carriers and excitons,[1-6] and their use in applications, ranging from light-emitting diodes (LEDs),[7-10], plastic lasers[11]to light-emitting electrochemical cells (LECs),[12,13] biochemical sensors [14-20], conjugated polymers (CPs) have been a subject of great interest in the past two decades. Figure 1.1 shows structures of some commonly seen CPs, including poly(*para*-phenylene vinylene) (PPV), poly(*para*-phenylene) (PPP), polyacetylene (PA), poly(*para*-phenylene ethynylene) (PPE), poly(alkylthiophene) (PAT), and polyfluorene (PF).

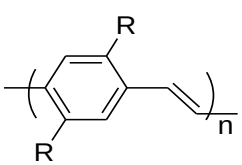

poly(*para*-phenylene vinylene)

(PPV)

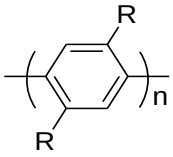

poly(*para*-phenylene)

(PPP)

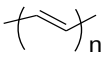

polyacetylene

(PA)

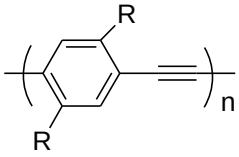

poly(*para*-phenylene ethynylene)

(PPE)

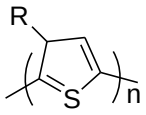

poly(alkylthiophene)

(PAT)

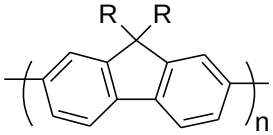

poly fluorene

(PF)

Figure 1.1 Structures of some commonly seen CPs are shown.

Without solubilizing side chains on the conjugated backbones, these CPs are difficult to dissolve in many solvents. The addition of solubilizing side chains has proved very effective in improving the solubility and processibility of CPs,[21-23] and this has triggered a massive research effort focused on the synthesis, photophysical properties and application of structurally diverse CPs.[24,25]Although poly(*para*-phenylene vinylene) (PPV) has found the most attention since Friend's 1990 report of organic polymeric LEDs,[7] poly(*para*-phenylene ethynylene) (PPE) based CPs, the structurally closest relative to PPV, have attracted significant attention in the past decade. [26-29]

Aggregation and solid state behavior are fascinating topics in the science of conjugated polymers, in which morphology and supramolecular ordering have an immediate effect on their optical properties.[30]The Bunz group examined the optical properties of dialkyl-PPEs (PPE-$C_{12}H_{25}$*)* in solution and the solid state.[29,31] In chloroform a broad absorption band centered at

385 nm is observed, while the thin films of these materials are distinctly yellow with a sharp absorption at λ_{max} of 435 nm (figure 1.2a). In order to understand the change in the spectra from solution to the solid state the solvatochromic behavior was examined. Addition of a nonsolvent (methanol) to a chloroform solution causes a new and sharp absorption band to appear at 435 nm, which corresponds to the absorption observed in the solid state. This red-shifted optical feature has been attributed to aggregate formation in the solid state and in the poor solvent.

The optical spectra of thin solid films of dialkyl-PPEs show thermochromicity as well.[32] While the absorption band of PPE-C_8H_{17} at 439 nm is prominent at room temperature, it disappears at temperatures above 463 K. Rather, the spectrum obtained at T > 463 K resembles that of the polymer in the good solvent chloroform at ambient temperature (see figure 1.2 b). The 439 nm

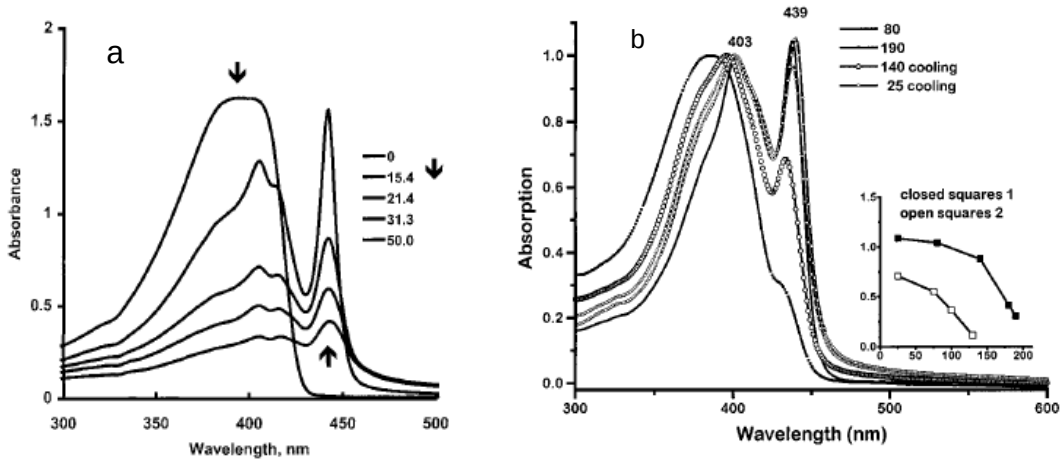

Figure 1.2. Panel a) shows absorption spectra of dialkyl-PPE (PPE-C12H25) based conjugated polymer in chloroform/methanol mixtures. Inset: % methanol; arrows indicate the growth or decline of bands with increasing methanol concentration; and panel b) shows tempera ture-dependent UV/vis spectra of a thin film of dialkyl-PPE based conjugated polymer (PPE-C_8H_{17}) on a quartz substrate. The inset shows the ratio of the band observed at 439 nm to that at 403 or

387 nm in dependence of the temperature. The upper graph displays the values obtained for PPE-C_8H_{17}, while the lower line is obtained from a similar study for PPE-$C_{12}H_{25}$. Reproduced from ref 30,31.

band is assigned to an aggregation-induced band and the pronounced thermochromic behavior is attributed to the order-disorder transition when melting from the liquid crystal into an isotropic state. Chu et al. observed that a new red-shifted peak near 460nm appears when the solution of a small model compound PPE-OC_4H_9, which has a conjugation length similar to that of the analogous polymer, was cooled to below 263 K in the mixed solvent methanol: THF (20:1).[33] The emission spectrum also displays a red shift and new vibronic bands. Upon further decreasing the temperature, the intensity of the peak at the red edge becomes more pronounced (figure 1.3a and b). These changes have been attributed to aggregation induced planarization of the backbone, facilitating π- π stacking at low temperature.

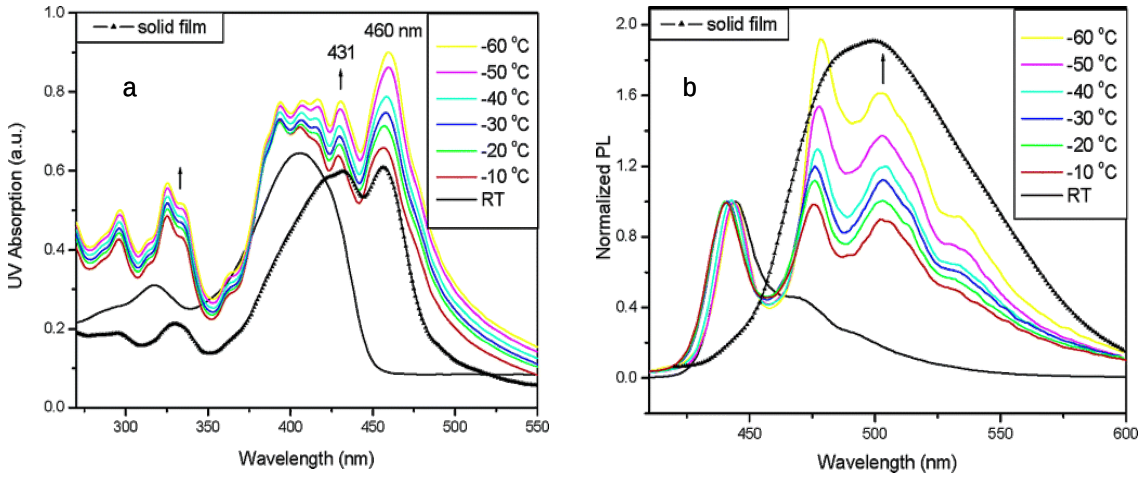

Figure 1.3 shows the absorption a) and emission spectra b) of PPE polymer in a mixture solvent (2.16 × 10^{-5} M) of methanol and THF (methanol/THF = 20:1 by volume) at various temperatures. The spectrum of the film (▲) is also shown for direct comparison. Reproduced from ref [33].

1.1.2 Conjugated Polyelectrolytes (CPEs)

Studies of PPE based conjugated polyelectrolytes (CPEs) have become increasingly popular.[34] Conjugated polyeletrolytes (CPEs) are a class of conjugated polymers that feature charged solubilizing side groups, such as sulfonate (SO_3^-), carboxylate (CO_2^-), phosphonate (PO_4^{2-}), and ammonium (NR_3^+). They combine the optoelectronic advantages of conjugated polymers with the unique properties of polyelectrolytes. Because of the charged and polar nature of the ionic side groups, CPEs can be soluble in water and polar organic solvents, and consequently they can be processed into thin films and supramolecular assemblies.[5,6,35-37] In addition, CPEs interact strongly with other ionic species, such as metal ions,[14] molecular ions,[3,35,38,39] polyelectrolytes,[40] proteins,[40-44] and DNA,[45-47]and this property has been exploited to fabricate rapid-response and high-sensitivity biochemical sensors.

Because of the favorable interaction between the polarizable π-electron clouds of their large planar backbones, CPEs also possess an intrinsic tendency to organize into π-stacked aggregates or supramolecular structures in solution and in the solid state.[48]Consequently, the optical properties of the aggregates differ from that of the individual strands, usually in an undesired way, e.g., a red shift in emission and decrease in the photoluminescence quantum yields.[49,50] A variety of optical experiments done by Schwarz et al.[51] suggest that the electronic properties of conjugated ionomer films mirror those of the solutions from which they are cast. They claim that morphological control of the film can be achieved by spin-casting from solutions with the appropriate conditions. In addition, it is possible to control the thickness and morphology of LBL (layer-by layer) films by varying the deposition solution conditions, such as ionic strength and pH.[35,52-54] Moreover, it is well appreciated that the photophysical properties and quenching behaviour of CPEs vary dramatically with a change of solvent conditions, such as

solvent polarity, temperature, ionic strength, charge on quencher, concentration of surfactant or polyelectrolytes with counterions, solution pHs.[4,27,35,55-61] Exploring and understanding the aggregation of CPEs, and its effect on their photophysical properties in different environments, are valuable for the development of these materials.

In the past few years, much attention has focused on understanding the structure-property relationship and solvation/aggregation of CPs/CPEs under different conditions. Based on previous studies, various strategies were applied to improve the solvation of polymers. Swager et al.[62] observed that pentiptycene-derived PPEs show exceptionally high solubility in organic solvents and little or no shift of the 0-0 absorption and emission bands in thin films, whereas nonpentiptycene-derived PPEs display substantial red shifts relative to solution values. In addition, all pentiptycene-derived PPEs have higher fluorescence quantum yields in solution and solid thin films than those of nonpentiptycene-derived PPEs. These features are attributed to the ability of the pentiptycene moieties to prevent π-stacking of conjugated polymer backbones thereby weakening the interpolymer interactions.

When CPEs are dissolved in polar organic or aqueous solutions (good solvents), i.e. when CPEs exist in solution in a non-aggregated state, the photophysical properties of the material are remarkably similar to those of a neutral analog dissolved in a non-polar organic solvent. Schanze and co-workers[4] reported the solvent-dependence of the absorption and fluorescence of PPE-SO_3^- which provides very clear evidence for the strong effect that aggregation has upon the

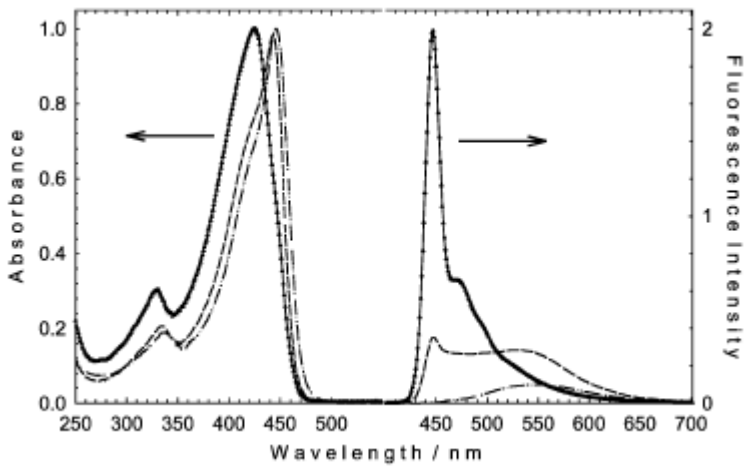

Figure 1.4 shows absorption (left) and fluorescence (right) spectra of PPE-SO_3^- in MeOH (Δ), (1:1) H_2O/MeOH (---), and H_2O (— - —). Fluorescence spectra are area normalized to reflect relative quantum yields. This figure is reproduced from ref 4.

photophysics of CPEs (figure 1.4). It is apparent from the data that as the volume fraction of water in the solvent increases, the absorption red-shifts and the fluorescence red-shifts and broadens significantly. In addition, the fluorescence quantum yield decreases with increasing water content. All these features are consistent with a model that in the good solvent-methanol, the CPE exists in a relatively unaggregated state so that the photophysical properties resemble those of the neutral analog in non-polar organic solvent, but in the poor solvent, water, the polymer aggregates and displays the broad, less efficient emission peak. The red-shift of the absorption in a water rich solvent is attributed to the increase of structural ordering of the phenylene rings in the PPE backbone which increases the conjugation length, and the broad photoluminescence band has been attributed to an excimer-like state that dominates the photophysical properties of aggregated polymers, presumably caused by π-stacking of adjacent polymer chains.[4,35]

In the case of weak polyelectrolytes, in which the side groups partially dissociate at intermediate pH, the solvent/aggregation behaviour can be controlled by modifying the solution pH. [35,57,61,63] Bazan and co-workers[60] investigated how solution pH changes control the degree of aggregation of P1-BT_0 and P1-BT_{15}(figure 1.5).

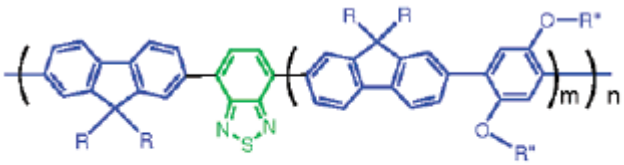

R* = $(CH_2CH_2O)_3CH_2CH_2COONa$

P1-BT_x

X=%BT

Figure 1.5 The structure of P1-BT_X is shown. Reproduced from ref 60.

Figure 1.6 shows the spectra of P1-BT_0 in water as a function of pH. With decrease of the solution pH, the absorption red shifts and broadens; the fluorescence red shifts and quenches 64% in intensity as the pH decreases from 7 to 4.

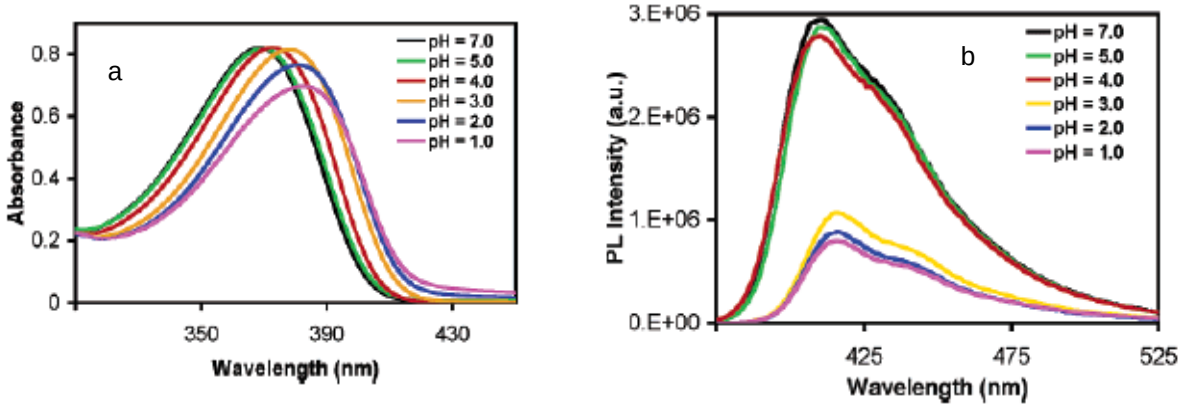

Figure 1.6 shows panel a) absorption spectra panel b) emission spectra of P1-BT_0 ([RU]) 3.8 $\times 10^{-5}$ M) in water as the pH is incrementally decreased from 7 to 1. Reproduced from ref 60.

Figure 1.7 shows the absorption spectra for P1-BT_{15} as a function of pH. Although some change in absorbance occurs, the data show that the spectra do not shift as the solution pH decreases, and the fluorescence intensity of the BT emission increases as the pH decreases from 4 to 3. Dynamic light scattering results show that the effective diameter of the two polymers are in the range of 300-400 nm at pH>5. As the pH decreases, both polymers show a sudden increase in particle size at a pH≈3.5, to about 2700-3000 nm. These data are in agreement with aggregation of chains occurring upon protonation of pendant groups. The lack of a red shift in absorption spectra of P1-BT_{15} suggests

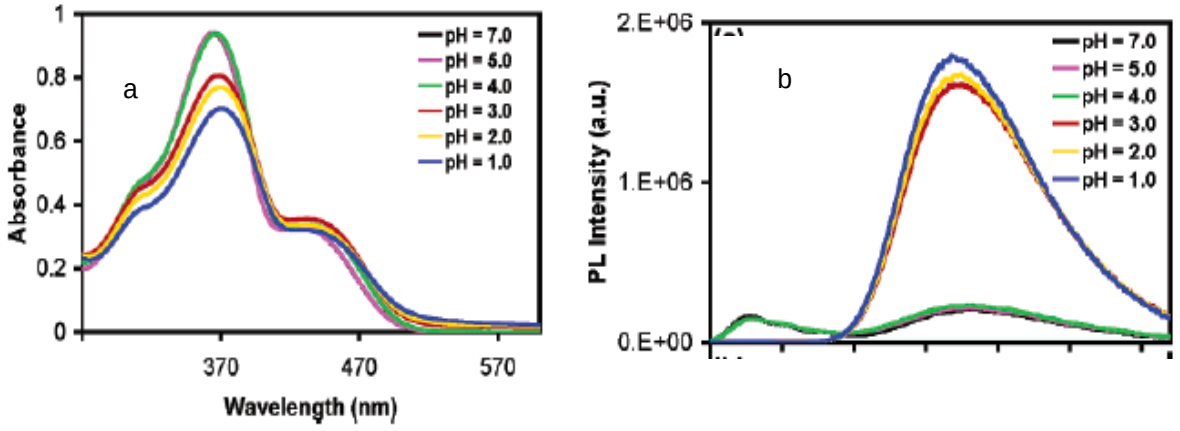

Figure 1.7 shows panel a) absorption spectra panel b) emission spectra of P1-BT_{15} ([RU]) 4.3 ×10^{-5} M) in water as the pH is incrementally decreased from 7 to 1. Reproduced from ref 60.

that the degree of electronic delocalization in single chains does not change; the emission enhancement of BT can be attributed to the improved FRET from fluorene-phenylene to BT units as the degree of polymers aggregation grows.

Pinto et al.[35] observed that at high pH the absorption and fluorescence spectra of PPE-PO_3^- closely resemble the spectra of neutral PPEs in good solvents such as THF or $CHCl_3$. With decrease of the pH, the absorption red shifts by 35nm; new peak appears at the red edge and the

fluorescence red shifts and broandens (figure 1.8). Fan et al.[57]showed that the cationic PPE(PPE-NR_3^+) which has quaternized amine group in all side chains exhibits an intrinsic

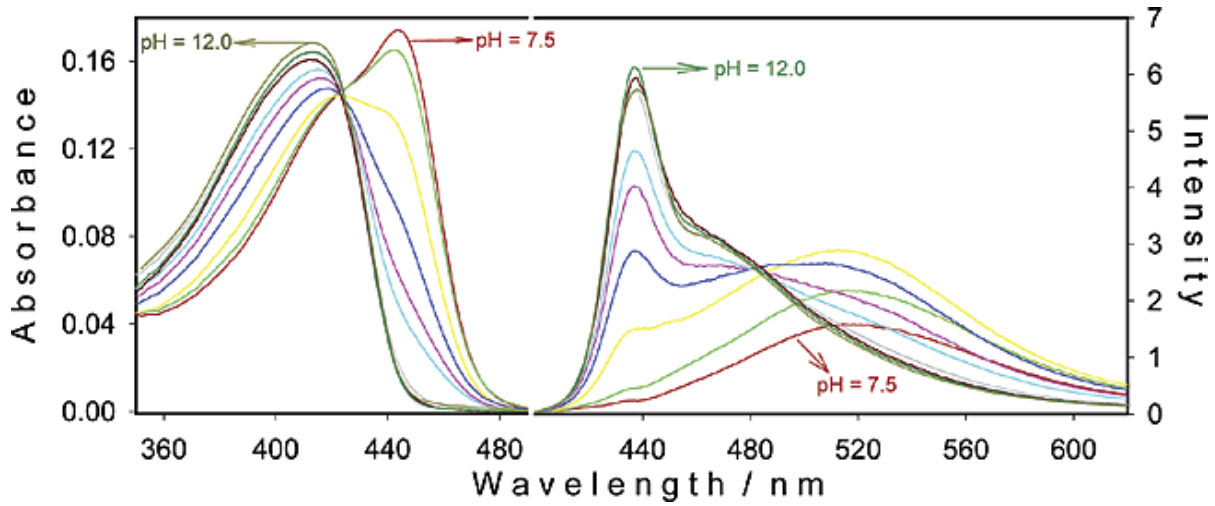

Figure 1.8 shows absorption spectra of PPE-PO_3^- in aqueous solution as a function of pH. (right) Fluorescence spectra of PPE-PO_3^- in aqueous solution as a function of pH. [PPE-PO_3^-] = 1 μM in phosphate buffer at 1 mM, pH range from 7.5 to 12.0 in 0.5 pH unit interval. This figure is taken from ref 35.

water solubility compared with other cationic PPEs containing side chains with different hydrophilicity. They explored the effect of pH and ionic strength on PPE-$N(C_2H_5)_3^+$ and showed that addition of salt in a neutral environment causes planarization of the PPE-$N(C_2H_5)_3^+$ backbone but no aggregation, whereas addition of salt in an alkaline environment significantly promotes interchain aggregation and planarization of the backbone. Altogether these pH effects on the photophysical properties of CPEs imply that controlling the electrostatic repulsion interactions between polymer chains by protonation or deprotonation of the side chains provides some control over the level of aggregation.

Previous studies also showed that the properties of CPEs undergo dramatic changes upon addition surfactants[36,58,64,65] or heavy metal ions thereby ionic strength. [66-68] Despite these effects, it appears that no systematic study of the charge density effects on the photophysical properties of polyphenylethynylene (PPE) based anionic CPEs has been reported. Recently Kaur et al.[55] reported the solvation and aggregation behaviour of PPE-SO_3Na-L in diluted solution. In addition to that polymer, this thesis reports on three other anionic CPEs, which differ from PPE-SO_3Na-L by the side group from sulfonate to carboxylate and the charge density along the backbone, and compares the photophysical properties exhibited by these four conjugated PPE-based polyelectrolytes under different solution conditions: solvent, concentration, temperature, ionic strength, pH and surfactant. Fluorescence correlation spectroscopy (FCS) was applied to measure the hydrodynamic radius of the polymers under the different solution conditions.

1.2 FLUORESCENCE CORRELATED SPECTROSCOPY (FCS)

1.2.1 Introduction

Fluorescence Correlation Spectroscopy (FCS) is an established experimental technique for measuring fluorescence intensity fluctuations in a small open volume element defined by a laser beam and a confocal geometry in solution. [69-72] The major sources of the fluctuations within the confocal volume are molecular diffusion by Brownian motion, convection, conformational changes, photophysical processes, and chemical reactions that change the fluorescence yield (figure 1.9). The parameters of molecular dynamics and kinetic process can be extracted by an analysis of the time correlation function of the fluorescence fluctuations. To date, FCS has been

broadly used to determine the concentrations and diffusion coefficients of molecules being investigated in biology and chemistry fields.

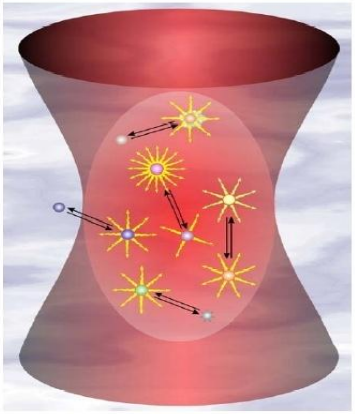

Figure 1.9 Molecular mechanisms that might give rise to fluorescence fluctuations comprise particle movements, conformational changes, and chemical or photophysical reactions.

At its first introduction by Madge, Elson and Webb in 1972, FCS was applied to measure diffusion and chemical dynamics of DNA-drug intercalation.[73]Following this pioneering work, a number of publications concerning the chemical rates of binding-unbinding reactions as well as coefficients of translational and rotational diffusion have emerged.[74] Nevertheless, these early studies suffered from poor signal-to-noise ratios, mainly because of low detection efficiency, large ensemble numbers, and insufficient background suppression. With recent developments in photonics and electronics, major improvements has been made, including the use of strong and stable excitation light source like lasers, and ultrasensitive detectors, e.g. avalanche photodiodes with single-photon sensitivity.[75] The final breakthrough was achieved by Rigler and his coworkers by combining the FCS technique with confocal detection.[76] In a confocal set up

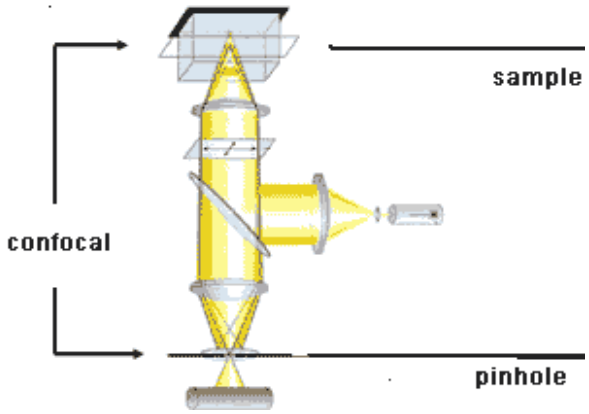

Figure 1.10 illustrates the confocal setup of FCS

(Figure 1.10), the incoming laser light is strongly focused by a high numerical aperture objective (ideally NA>0.9) to a diffraction limited spot. Only the few fluorophores within the illuminated region are excited. In addition, a pinhole is introduced in the image plane, which blocks all light not coming from the focal region. This work generated a flurry of technical improvements and improved the sensitivity of the technique to the single-molecule level, thereby creating a renewed interest in FCS. Currently, FCS has entered a new age with the introduction of Zeiss and Evotech's confocor commercial instrument, and its common use in drug-screening assays.[72]

1.2.2 FCS Instrumentation

A home made FCS instrument was constructed by modifying a Zeiss IM 35 inverted microscope (see Scheme 1).[77] The excitation source is a single wavelength (438 ± 3 nm) solid state diode laser (iBeam 440). The laser beam is coupled to the microscope by a single-mode optical fiber (A) which acts as a spatial filter and a beam expander. The dichroic mirror (C) reflects the laser beam and allows fluorescence to pass through. The laser beam is then focused

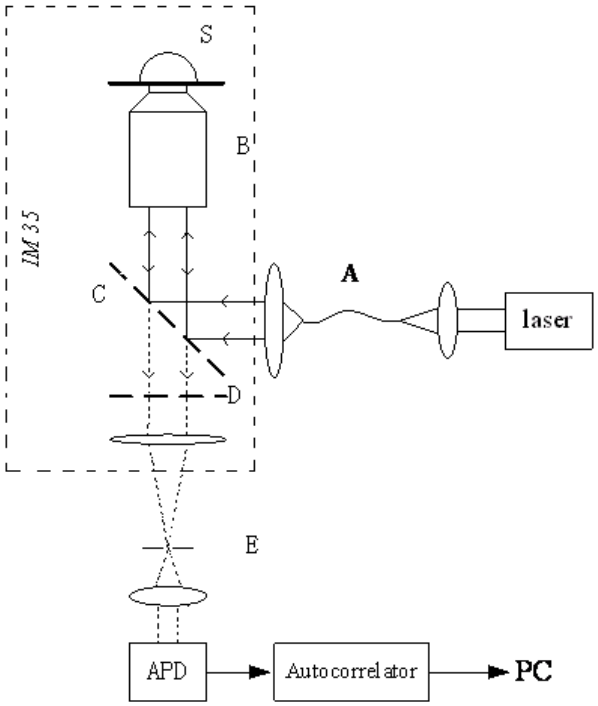

Scheme 1.1 Schematic representation of the FCS instrument, reproduced from reference 77.

by an objective lens (B) (Olympus UPlanfluor 40X/1.30 oil) into a volume of femtoliter size in the sample (S). By the same objective, the fluorescence is collected. The scattered laser light is blocked by an emission filter (D). At the other port of the microscope, the fluorescence is focused and coupled to a photon counting avalanche photodiode (APD) through a pinhole of 50 μm in diameter (E). In this confocal setup only the fluorescence from the objective's focal point is detected by the APD. The signal from the APD provides a fluorescence versus time trajectory and is processed by an autocorrelator (BI-9000, Brookhaven Instrument Co.) to generate an autocorrelation function. The autocorrelation function is fit by a model to provide a correlation time for the dynamics.

1.2.3 FCS Theory and Measurement

In a confocal illumination/detection optical set up, the intensity of the excitation light at the focal point can be expressed by a Gaussian illumination intensity profile:

$$I = I_0 \exp\left(-\frac{2\left(x^2+y^2\right)}{\omega_{xy}^2}\right)\exp\left(-\frac{2z^2}{\omega_z^2}\right) \tag{1.1}$$

where I_0 is the intensity at the geometric center of the illumination spot; x and y are displacements perpendicular to the optical axis, z is the displacement along the optical axis; ω_{xy} is the lateral radius, and ω_z is the axial radius (where intensity declines by $1/e^2$ from peak value) of the observation volume.[78]

The normalized autocorrelation function $G(\tau)$ is defined as :

$$G(\tau) = \frac{\langle \delta I(t)\delta I(t+\tau)\rangle}{\langle I(t)\rangle^2} \tag{1.2}$$

where t is the experimental time coordinate, and τ is a delay time. In the limit that diffusion is the only cause of fluorescence fluctuations and only one component exists, the correlation function may be written as:

$$G(\tau) = \frac{1}{\overline{N}}\left(1+\frac{\tau}{\tau_D}\right)^{-1}\left(1+\frac{\tau}{\omega^2\tau_D}\right)^{-1/2} \tag{1.3}$$

where $\overline{N}$ is the average number of fluorescent molecules in the observation volume, τ_D is the correlation time, and ω is defined as $\omega = \omega_z / \omega_{xy}$ .The correlation time τ_D is defined as

$$\tau_D = \frac{\omega_{xy}^2}{4D} \tag{1.4}$$

where D is the diffusion coefficient. The diffusion coefficient of a spherical particle can be estimated by the Stokes-Einstein equation, so that

$$D = \frac{k_B T}{6\pi\eta R_H} \tag{1.5}$$

where k_B is the Boltzmann constant, T is the temperature, η is the viscosity of solution, and R_H is the radius of the spherical particles.

In order to calculate the diffusion coefficient D, the lateral radius of the confocal volume ω_{xy} needs to be characterized first. The instrument was calibrated using 10 nM Rhodamine 6G solutions with known diffusion coefficients ($D = 4.14\times10^{-6}$ cm^2 s^{-1}).[68] The ω_{xy} was measured to be 0.39 μm and ω was around 9. The concentrations of the polymer solutions were controlled to be 10^{-7} M and the laser power was kept as low as 30 μW to avoid photobleaching and optical trapping. The time trajectory of fluorescence was collected for 3 to 10 min and the autocorrelation function was calculated and then fit by Equation 3 using a Levenberg-Marquardt algorithm.

1.3 REFERENCES

(1) Patil, A. O.; Ikenoue, Y.; Wudl, F.; Heeger, A. J. *J. Am. Chem. Soc.* **1987**, *109*, 1858-1859.

(2) Shi, S.; Wudl, F. *J. Am. Chem. Soc.* **1990**, *23*, 2119-2124.

(3) Chen, L.; McBranch, D. W.; Wang, H.-L.; Helgeson, R.; Wudl, F.; Whitten, D. G. *Proc. Natl. Acad. Sci. USA* **1999**, *96*, 12287-12292.

(4) Tan, C.; Pinto, M. R.; Schanze, K. S. *Chem. Commun.* **2002**, 446-447.

(5) Lukkari, J.; Salomaki, M.; Viinikanoja, A.; Aaritalo, T.; Paukkunene, J.; Kocharova, N.; Kankare, J. *J. Am. Chem. Soc.* **2001**, *123*, 6083-6091.

(6) Cutler, C. A.; Bouguettaya, M.; Reynolds, J. R. *Adv. Mater.* **2002**, *14*, 684-688.

(7) Kraft, A.; Grimsdale, A. C.; Holmes, A. B. *Angew. Chem.* **1998**, *37*, 403.

(8) Ho, P. K. H.; Kim, J. S.; Burroughes, J. H.; Becker, H. L.; Li, S. F. Y.; Brown, T. M.; Cacialli, F.; Friend, R. H. *Nature* **2000**, *404*, 481-484.

(9) Sirringhaus, H.; Tessler, N.; Friend, R. H. *Science* **1998**, *280*, 1741-1744.

(10) Zhang, C.; Broun, D.; Heeger, A. J. *J. Appl. Phys.* **1993**, *73*, 5177.

(11) Hide, F.; Diaz-Garcia, M. A.; Schwartz, B. J.; Heeger, A. J. *Acc. Chem. Res.* **1997**, *30*, 430.

(12) Pei, Q. B.; Yu, G.; Zhang, C.; Yang, Y.; Heeger, A. J. *Science* **1995**, *269*, 1086.

(13) Blom, P. W. M.; de Jong, M. J. M. *Appl. Phys. Lett.* **1996**, *68*, 3308.

(14) Harrison, B. S.; Ramey, M. B.; Reynolds, J. R.; Schanze, K. S. *J. Am. Chem. Soc.* **2000**, *122*, 8561.

(15) Rininsland, F.; Xia, W.; Wittenburg, S.; Shi, X.; Stankewicz, C.; Achyuthan, K.; McBranch, D.; Whitten, D. *Proc. Natl. Acad. Sci. USA* **2004**, *101*, 15295-15300.

(16) Liu, M.; Kaur, P.; Waldeck, D. H.; Xue, C.; Liu, H. *Langmuir* **2005**, *21*, 1687-1690.

(17) McQuade, D. T.; Pullen, A. E.; Swager, T. M. *Chem. Rev.* **2000**, *100*, 2537-74.

(18) Schanze, K. S.; Pinto, M. R. *Proc. Natl. Acad. Sci. USA* **2004**, *101*, 7505-7510.

(19) Heeger, A. J.; Diaz-Garcia., M. A. *Curr. Opin. Solid State Mater.* **1983**, *3*, 16.

(20) Thomas II, S. W.; Joly, G. D.; Swager, T. M. *Chem. Rev.* **2007**, *107*, 1339-1386.

(21) McDonald, R. N.; Campbell, T. W. *J. Am. Chem. Soc.* **1960**, *82*, 4669.

(22) Rehahn, M.; Schluter, A. D.; Wegner, G.; Feast, W. J. *Polymer* **1989**, *30*, 1054.

(23) Rehahn, M.; Schluter, A. D.; Wegner, G.; Feast, W. J. *polymer* **1989**, *30*, 1060.

(24) Feast, W. J.; Tsiboulis, J.; Powe, K. L.; Groenendaal, B. L.; Meijer, E. W. *Polymer* **1996**, *37*, 5017.

(25) Reddinger, J. L.; Reynolds, J. R. *Adv. Polym. Sci.* **1999**, *145*, 57.

(26) Bunz, U. H. F. *Chem. Rev.* **2000**, *100*, 1605-1644.

(27) Haskins-Glusac, K.; Pinto, M. R.; Tan, C.; Schanze, K. S. *J. Am. Chem. Soc.* **2004**, *126*, 14964-14971.

(28) Breitenkamp, R. B.; Tew, G. N. *Macromolecules* **2004**, *37*, 1163-1165.

(29) Halkyard, C. E.; Rampey, M. E.; Kloppenburg, L.; Studer-Martinez, S. L.; Bunz, U. H. F. *Macromolecules* **1998**, *31*, 8655-8659.

(30) Hunter, C. A. *Angew. Chem.* **1993**, *32*, 1584.

(31) Fiesel, R.; Halkyard, C. E.; Rampey, M. E.; Kloppenburg, L.; Studer-Martinez, S. L.; Scherf, U.; Bunz, U. H. F. *Macromol. Rapid Commun.* **1999**, *20*, 107-111.

(32) Miteva, T.; Palmer, L.; Kloppenburg, L.; Neher, D.; Bunz, U., H. F. *Macromolecules* **2000**, *33*, 652-654.

(33) Chu, Q.; Pang, Y. *Macromolecules* **2005**, *38*, 517-520.

(34) Pinto, M. R.; Schanze, K. S. *Synthesis* **2002**, 1293-1309.

(35) Pinto, M. R.; Kristal, B. M.; Schanze, K. S. *Langmuir* **2003**, *19*, 6523-6533.

(36) Thunemann, A. F.; Ruppelt, D. *Langmuir* **2001**, *17*, 5098-5102.

(37) Jones, R. M.; Bergstedt, T. S.; McBranch, D. W.; Whitten, D. G. *J. Am. Chem. Soc.* **2001**, *123*, 6726-7.

(38) Chen, L.; McBranch, D. W.; Whitten, D. G. *Chem. Phys. Lett.* **2000**, *330*, 27-33.

(39) Tan, C.; Atas, E.; Muller, J. G.; Pinto;, M. R.; Kleiman, V. D.; Schanze, K. S. *J. Am. Chem. Soc.* **2004**, *126*, 13685-13694.

(40) Wang, D.; Gong, X.; Heeger, P. S.; Rinisland, F.; Bazan, G. C.; Heeger, A. J. *Proc. Natl. Acad. Sci. USA* **2001**, *99*, 49-53.

(41) Kumaraswamy, S.; Bergstedt, T.; Shi, X.; Rininsland, F.; Kushon, S.; Xia, W. *Proc. Natl. Acad. Sci. USA* **2004**, *101*, 7511.

(42) Wilson, J. N.; Wang, Y.; Lavigne, J. J.; Bunz, U. *Chem. Commun.* **2003**, 1626.

(43) Pinto;, M. R.; Schanze, K. S. *Proc. Natl. Acad. Sci. U. S. A.* **2004**, *101*, 7505.

(44) Ambade, A. V.; Sandanaraj, B. S.; Klaikherd, A.; Thayumanavan, S. *Polymer International* **2007**, *56*, 474-481.

(45) Liu, B.; Bazan, G. C. *Chem. Mater.* **2004**, *16*, 4467-4476.

(46) Kushon, S. A.; Ley, K. D.; Bradford, K.; Jones, R. M.; McBranch, D.; Whitten, D. *Langmuir* **2002**, *18*, 7245-7249.

(47) Gaylord, B. S.; Heeger, A. J.; Bazan, G. C. *Proc. Natl. Acad. Sci. USA* **2002**, *99*, 10954-10957.

(48) Hoeben, F. J. M.; Jonkheijm, P.; Meijer, E. W.; Schenning, A. P. H. J. *Chem. Rev.* **2005**, *105*, 1491.

(49) Thunemann, A. F.; Ruppelt, D. *Langmuir* **2000**, *16*, 3221.

(50) Schnablegger, H.; Antonietti, M.; Goltner, C.; Hartmann, J.; Colfen, H.; Samori, P.; Rabe, J. P.; Hager, H.; Heitz, W. J. *Colloid. Interface Sci* **1999**, *212*, 24.

(51) Nguyen, T.-Q.; Schwartz, B. J. *J. Chem. Phys.* **2002**, *116*, 8198-8208.

(52) Dubas, S. T.; Schlenoff, J. B. *Macromolecules* **2001**, *34*, 3736.

(53) Dubas, S. T.; Schlenoff, J. B. *Macromolecules* **1999**, *32*, 8153.

(54) Shiratori, S. S.; Rubner, M. F. *Macromolecules* **2000**, *33*, 4213.

(55) Kaur, P.; Yue, H.; Wu, M.; Liu, M.; Treece, J.; Waldeck, D. H.; Liu, H.; Xue, C. *J. Phys. Chem. B* **2007**, *111*, 8589-8596.

(56) Chu, Q.; Pang, Y. *Macromolecules,* **2003**, *36*, 4614-4618.

(57) Fan, Q.; Zhou, Y.; Lu, X. M.; Hou, H. M.; Huang, W. *Macromolecules,* **2005**, *38*, 2927-2936.

(58) Chen, L.; Xu, S.; McBranch, D. W.; Whitten, D. G. *J. Am. Chem. Soc.* **2000**, *122*, 9302-9303.

(59) Huang, Y.-Q.; Fan, Q.-L.; Xiao-Mei;, L.; Fang, C.; Liu, S.-J.; Wei, H. *J. Polymer Sci.* **2006**, *44*, 5778-5794.

(60) Wang, F.; Bazan, G. C. *J. Am. Chem. Soc.* **2006**, *128*, 15786-15792.

(61) Gao, Y.; Wang, C.-C.; Wang, L.; Wang, H.-L. *Langmuir* **2007**, *23*, 7760-7767.

(62) Yang, J. S.; Swager, T. M. *J. Am. Chem. Soc.* **1998**, *120*, 11864.

(63) Wang, F.; Bazan, G. C. *J. Am. Chem. Soc* **2006**, *128*, 15786-15792.

(64) Gaylord, B. S.; Wang, S.; Heeger, A. J.; Bazan, G. C. *J. Am. Chem. Soc.* **2001** *123*, 6417-6418.

(65) Wang, C.; Tam, K. C. *J. Phys. Chem. B* **2004**, *108*, 8976-8982.

(66) Jiang, H.; Zhao, X.; Schanze, K. S. *Langmuir* **2006**, *22*, 5541-5543.

(67) Kim, I. B.; Dunkhorst, A.; Gilbert, J.; Bunz, U. H. F. *Macromolecules* **2005**, *38*, 4560-4562.

(68) Kim, I.-B.; Bunz, U. H. F. *J. Am. Chem. Soc.* **2006**, *128*, 2818-2819.

(69) Koppel, D. E. *Phys. Rev. A* **1974**, *10*, 1938-1945.

(70) Pristinski, D. K., V.; Sukhishvili, S. A *J. Chem. Phys.* **2004**, *122*, 14907-14907.

(71) Van Rompaey, E.; Sanders, N.; Van Craenenbroeck, E.; Engelborghs, Y.; De Smedt, S. C.; Demeester, J. *Macromolecules* **2000**, *33*, 8280-8288.

(72) Krichevsky, O.; Bonnet, G. *Rep. Prog. Phys.* **2002**, *65*, 251-297.

(73) Magde D, E.; Webb, W. W. *Phys. Rev. Lett.* **1972**, *29*, 705.

(74) Thompson, N. L. *Topics in Fluorescence Spectroscopy Techniques* **1991**, *1*, 337.

(75) Rigler, R.; Elson, E. S. *Fluorescence correlation spectroscopy: theory and applications* **2001**, *Springer-verlag, Berlin*.

(76) Rigler, R.; Mets, U.; Widengren, J.; Kask, P. *Eur. Biophys. J.* **1993**, *22*, 169.

(77) Yue, H.; Wu, M.; Waldeck, D. H. *Submitted*.

(78) Hess, S. T.; Webb, W. W. *Biophys J.* **2002**, *83*, 2300.

(79) *GPC studies were performed by American Polymer Std., 8680 Tyler Blvd. Mentor, OHIO, 44060*.

(80) Morris, J. V.; Mahaney, M. A.; Huber, J. R.; Fluorescence quantum yield determinations.: 1976; Vol. 80, p 969-974.

2.0 SOLVATION AND AGGREGATION OF POLYPHENYLETHYNYLENE BASED ANIONIC POLYELECTROLYTES IN DILUTE SOLUTIONS

This work has been published as Palwinder Kaur, Hongjun Yue, Mingyan Wu, Min Liu, Jennifer Treece, David H. Waldeck, Cuihua Xue, and Haiying Liu, J. Phys. Chem. B.; (2007); 111, 8589-8596. Thesis author worked with the first author in spectroscopic experiments.

2.1 ABSTRACT

The absorption and fluorescence properties of a polyphenylethynylene based conjugated polyelectrolyte with sulfonate solubilizing groups (**PP2**) are shown to change dramatically with solution conditions because of the equilibrium between unaggregated and aggregated forms of the polymer. The fluorescence of **PP2** is strongly quenched on addition of counterions such as Na^+, K^+, Li^+ and TBA^+, an effect which arises from the creation of salt stabilized aggregates. The formation of aggregates has been further corroborated by concentration and temperature studies in water and comparisons to DMSO solvent, in which the polymer does not aggregate. In aqueous solutions, the addition of the cationic surfactant, octadecyltrimethyl ammonium, causes the polymer aggregrates to dissociate and creates polymer/surfactant aggregrates that have spectral properties like that of the unaggregated polymer.

2.2 INTRODUCTION

Conjugated polymers are of great interest because of their tunable photophysical properties[1-8] and their promise in application[9], such as bio-chemical sensors,[10-18] lasers[19], LEDs[20-22] etc.

One class of conjugated polymers which is being studied extensively is polyphenylethynylene (PPE) based conjugated polymers. Over the past decade a number of reports concerned with the synthesis and photophysical characterization of PPEs in solution has been published.[23-28] These polymers have shown to change their optical properties with solvent. Bunz et al[24,29] has shown that addition of non-solvent (methanol) to a chloroform solution of for dialkyl PPEs leads to the development of a new red-shifted band in the absorption spectrum which is similar to the absorption observed in the solid state. In addition, the fluorescence emission from these dialkyl PPE solutions is broad and red shifted, similar to that seen for the solid state. Bunz attributed these changes in the optical spectra to aggregate formation in the poor solvent, methanol and proposes that the interaction of the π- systems by π-stacking causes the bathochromic shift. This interpretation is corroborated by concentration studies.[29] The optical spectra at low concentration are similar to those observed in good solvent and at higher concentration; the spectra are similar to that seen in the solid state or in the poor solvent, indicating the PPEs are aggregated at higher concentration.

Besides solvatochromic behavior these PPE based conjugated polymers also show thermochromicity. Pang et al[26,27] observed that on changing the temperature (25^{o} C to – 108^{o} C) for PPE-OC_6H_{13} in good solvent (THF) the emission spectrum shifted red and the vibronic structure became more pronounced. These effects have been attributed to planarization of chromophores and reduced molecular motion at low temperature. Interesting behavior was

observed for PPE-OC_6H_{13} in mixture of solvent and poor solvent (THF and methanol). As PPE-OC_6H_{13} in a mixture of THF and the poor solvent is cooled, the emission spectrum shifts red and a new peak starts to appear at -30^o C and the absorption spectrum also develops a sharp red shifted peak. These changes are attributed to aggregation induced by planarization of the backbone facilitating π- π stacking at low temperature. These concentration and temperature changes for the spectra of PPE based conjugated polymers are consistently explained by 'planarization' and aggregation, hence π- π stacking of the backbone.

More recently interest has shifted to PPE based conjugated polyelectrolytes.[30] These PPEs are water soluble, undergo fluorescence quenching with a series of cationic quenchers and have a potential for biological and chemical sensing.[10-18] A number of research groups have studied the fluorescence quenching of these polyelectrolytes by addition of heavy metal ions,[31-33] surfactants[34,35] and with change in pH,[36,37] however little effort has focused on aggregate formation and subsequent fluorescence quenching induced by simple salts (such as NaCl, KCl etc.). To develop these PPE based polyelectrolytes into practical sensors, it is important to understand their photophysical behavior in different environments such as ionic strength and addition of surfactant.

Anionic PPEs soluble in water but can form aggregates upon change in the environmental conditions. These aggregates are characterized by the appearance of a sharp red shifted peak in absorption and a broad red shifted emission, similar to what is observed for neutral PPE based polymers in bad solvent..[26,27]Schanze et al[38] showed that PPE with sulfonate terminated side chains (PPE-SO_3^-) has its fluorescence quantum yield reduced by changing the solvent from methanol to water. The spectral changes observed were similar to that found for PPE in poor solvent, so Scahnze attributed them to formation of aggregates of PPE-SO_3^-. Recently Bunz et

al[31,32] studied the addition of metal ions such as Pb^{2+}, Hg^{2+}, Ca^{2+}, Mg^{2+} etc. to solutions of carboxy terminated side chains on a PPE backbone (PPE-CO_2^-). Similar quenching behavior was observed by Schanze et al[39] for PPE-CO_2^- with a lower charge density, as compared to the one used by Bunz, on addition of Ca^{2+} ions. It was proposed that since Ca^{2+} is a closed-shell ion and cannot act as an electron or energy acceptor, the fluorescence quenching observed on addition of Ca^{2+} arises from aggregation of the polymer chains. Beside the solvent and metal ion studies, Schanze et al[37] reported the formation of interchain aggregates for PPE-PO_3^- on decreasing the pH. Huang et al [36] later showed the effect of pH and ionic strength on PPE-$N(C_2H_5)_3^+$ and reported that addition of salt in an neutral environment only creates planarization of the PPE-$N(C_2H_5)_3^+$ backbone whereas addition of salt in an alkaline environment significantly promotes interchain aggregation.

These PPE based polyelectrolytes have also been shown to undergo spectral changes in surfactant solutions.[34,35,40] The emission spectrum shifts red on addition of surfactant to PPE-CO_2^- and the shifts has been interpreted using hard soft acid base theory (HSAB theory) showing that spectra shift to higher wavelength when the counterion becomes more polarizable.

It is clear from all these studies that either planarization or interchain aggregation is responsible for fluorescence quenching in PPE based polyelectrolytes on addition of heavy metal ions, changing pH, or solvent changes. This work explores the fluorescence quenching behavior in simple electrolytes in order to disentangle effctes of aggregates from other effects of metal ions. And explain the effect of addition of surfactant (ODTMA) to PPE based polyelectrolyte.

This work reports the effect of addition of simple ionic salts such as NaCl, KCl, surfactants etc. on optical properties of (poly[2,5-bis(3-sulfonatopropoxy)-1,4-phenylethynylene-alt-1,4-polyphenylene ethynylene],identified as **PP2**. These studies show that the **PP2's**

fluorescence is quenched on addition of ionic salts and this quenching is accompanied by the appearance of a sharp red shifted peak in the absorption spectrum due to formation of polymer aggregates. The fluorescence is enhanced on heating the polymer solution and on addition of surfactant due to breaking of **PP2** aggregates. Further to develop a fundamental understanding of the types of aggregates formed FCS studies have been done on **PP2** to get an insight in to the size of these aggregates. These studies show that the solution properties (solvent, temperature, ionic strength and surfactant) control the spectral properties of a conjugated polyelectrolyte by manipulating the equilibria between aggregated and unaggregated forms of the polymer.

2.3 EXPERIMENTAL

Material: Poly[2,5-bis(3-sulfonatopropoxy)-1,4-phenylethynylene-alt-1,4-polyphenylene ethynylene] (identified as **PP2**) is a polyelectrolyte with two negative charges per repeat unit and was prepared in a manner similar to that reported in the literature.[41] ODTMA (octadecyltrimethyl ammonium bromide), PEG (polyethylene glycol), TBAF (tetra butyl ammonium fluoroborate), TEAF (tetraethyl ammonium fluoroborate) and AF (ammonium fluoroborate) were bought from Sigma-Aldrich. Size exclusion chromatography[42] was used to determine the molecular weight and it was found that molecular weight of **PP2** in DMSO (a good solvent) is 38,100 Da with a polydispersity of 3.04.

The experimental polymer solutions were highly diluted; for example, the highest concentration of **PP2** was 3.9×10^{-6} M in polymer repeat units (all concentrations reported in paper are in terms of polymer repeat unit). At these concentrations the effect of the polymer on solution properties, such as viscosity, can be neglected. For studies in electrolyte solutions, the

concentration of background electrolyte was always much higher than the concentration of polyelectrolyte and the ionic strength was determined by the background electrolyte. In the current experiment, the nature of the electrolyte and the ionic strength of electrolyte were varied from $5x10^{-4}$ M to 0.1 M.

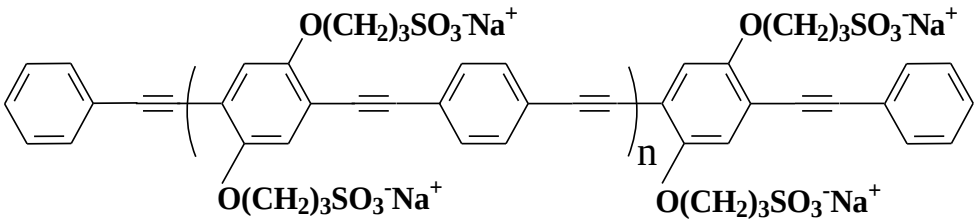

Figure 2.1 Chemical structure of PP2

Steady state spectroscopy: Steady-state absorption spectra were measured on an Agilent 8453 spectrometer and the steady-state emission spectra were measured on a Spex Fluorolog 0.22 m double spectrometer.

Time dependent fluorescence spectroscopy: The time-resolved fluorescence data were collected using the time-correlated single photon counting method.[18] The instrument response function was measured using a sample of colloidal $BaSO_4$. The samples were excited at 438 nm using a diode laser (PIL043, A.L.S. GmbH) and the emission was collected at different wavelengths. The fluorescence decay curves were fit by a convolution and compare method using IBH-DAS6 analysis software. Other details of the TCSPC apparatus can be found in ref [43].

Fluorescence Correlation Spectroscopy (FCS): FCS is a non-invasive single molecule method which obtains dynamic and kinetic information by following the fluctuation trajectory of fluorescence about the equilibrium state.[44-48] FCS was performed on a home made FCS instrument based on a Zeiss IM35 inverted microscope. Details of the instrumentation will be provided elsewhere.[49] The sample was excited at 438 nm through an objective lens (Olympus UPlanfluor 40X/1.30 Oil) and the fluorescence was collected by the same lens. The

concentrations of the polymer solutions were controlled to be 5.2×10^{-8} M and 2.5×10^{-6} M. To avoid photobleaching and optical trapping, the laser power was kept low, 24 μW, as measured at the front of the objective lens. Each measurement lasted 2 to 5 min, during which the time trajectory of fluorescence was monitored and only those having stable fluorescence intensity were kept. The corresponding autocorrelation function G(t) was fit by equation (1)

$$G(t) = \frac{1}{\overline{N}}\left(1+\frac{t}{\tau_D}\right)^{-1}\left(1+\frac{\omega_{xy}^2 t}{\omega_z^{\,2}\tau_D}\right)^{-1/2} \tag{2.1}$$

to extract the correlation time τ_D. $\overline{N}$ is the average number of fluorescent molecules in the focal volume; ω_{xy} is the radius of the focal spot in the transverse direction, and ω_z is the Rayleigh range of the excitation beam (see reference [50] for details relating to equation 1). The correlation time τ_D is related to the translational diffusion coefficient D of the fluorophore by

$$\tau_D = \frac{\omega_{xy}^2}{4D} \tag{2.2}$$

The apparatus was calibrated and tested using a 10 nM Rhodamine 6G aqueous solution, assuming the diffusion coefficient $D = 4.27\times10^{-6}$ cm^2 s^{-1}. The Stokes-Einstein approximation, equation (3) was used to extract the hydrodynamic radius R_H from the measured diffusion coefficient

$$D = \frac{k_B T}{6\pi\eta R_H} \tag{2.3}$$

where η is the shear viscosity, T is the temperature and k_B is Boltzmann's constant.

Zeta Potential measurements: The electrophoretic mobility measurements were performed at 25^0C with an electrical field strength of 15V/cm by using a "Zeta Plus" zeta-potential analyzer from Brookhaven Instrument Co.

2.4 RESULTS AND DISCUSSION

2.4.1 Solvent and Concentration Effects

Figure 2.2 A shows the electronic absorption and the emission spectra of **PP2** in water and DMSO at 2.0×10^{-6} M. In DMSO the fluorescence band is narrow, displays vibronic structure and has a small Stokes shift. These spectra are similar to that reported in the literature for neutral dialkyl and dialkoxy PPE as well as anionic PPE-SO_3^- based conjugated polymers in good solvents [24,26,27,38]. This correspondence suggests that the electronic properties are governed mainly by the backbone, rather than the side chains. In contrast, the aqueous polymer solutions display a broad and red shifted emission band. This broad fluorescence band has been attributed to an excimer like state that dominates the photophysical properties of aggregated polymers and arises from π-stacking of phenylene rings.[37,38] The absorption spectrum also changed on changing the solvent. In water the absorption spectrum has a very well defined red peak at 439 nm whereas in DMSO this red shifted peak disappears and overall the spectrum shifts blue. These findings are similar to that reported by Schanze[38] and suggests that water is a poor solvent, in which the **PP2** aggregates, and DMSO is a good solvent, in which **PP2** does not aggregate.

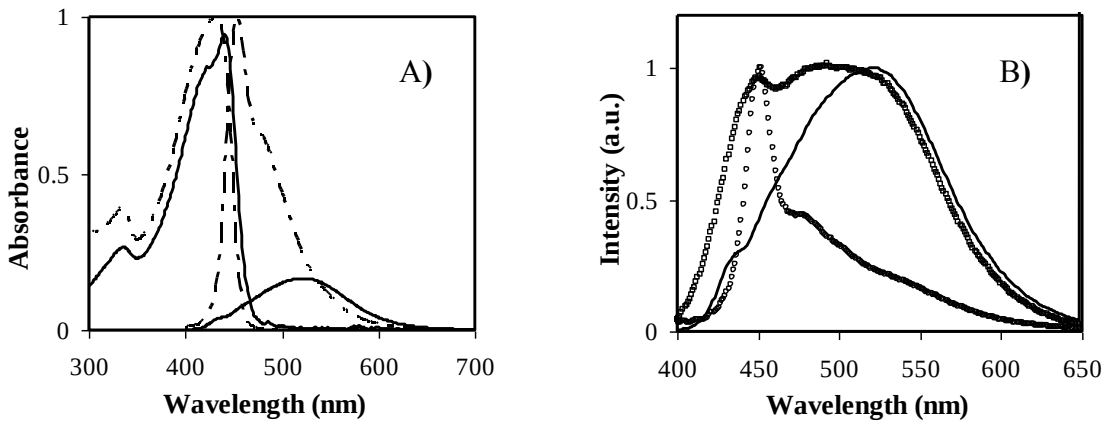

Figure 2.2 ***A)*** *Normalized absorption and emission spectra for PP2 in DMSO (— – —) and water (——)* ***B)*** *Emission spectra for PP2 in water at different concentrations (2.0×10^{-6}(—), 8.8×10^{-8}(□), 1.0×10^{-8} (○) M).*

The concentration dependence of **PP2** in water was studied in detail. Figure 2.2B shows the emission spectra for **PP2** at three different concentrations. The spectrum at the highest concentration ($2.0\text{x}10^{-6}$ M) is the same as that shown in panel A. As the concentration of polymer is lowered an emission band on the blue edge of the spectrum 'grows in'. At the lowest concentration ($8.8\text{x}10^{-8}$ M) the emission spectrum resembles that obtained for **PP2** in DMSO, indicating that the polymer is unaggregated at these low concentrations.[24] At intermediate concentration ($1.1\text{x}10^{-8}$ M) the spectrum displays features of both aggregated and unaggregated forms of polymer.

Figure 2.3 shows the emission and absorption spectra of **PP2** as the temperature is varied. Heating of the aqueous **PP2** solutions to 90^{o} C causes the band on the red edge of the absorption spectrum to disappear; the spectrum becomes more like that observed for **PP2** in DMSO. In addition, the fluorescence spectra show that a band on the blue edge of the emission 'grows in' with increasing temperature. Although a significant amount of the broad red-shifted emission

remains, the band on the blue edge is similar to that observed for **PP2** in DMSO. Upon cooling the **PP2** solution to room temperature (45 minutes cooling time) the emission maxima do not shift, however the amplitude of the broad band emission increases slightly in amplitude. After nine hours at room temperature, the absorption spectrum shows a red shifted shoulder and the amplitude of the broad red shifted band increases. These studies indicate that **PP2** aggregates are dissociated upon heating but that the reaggregation at room temperature occurs slowly.

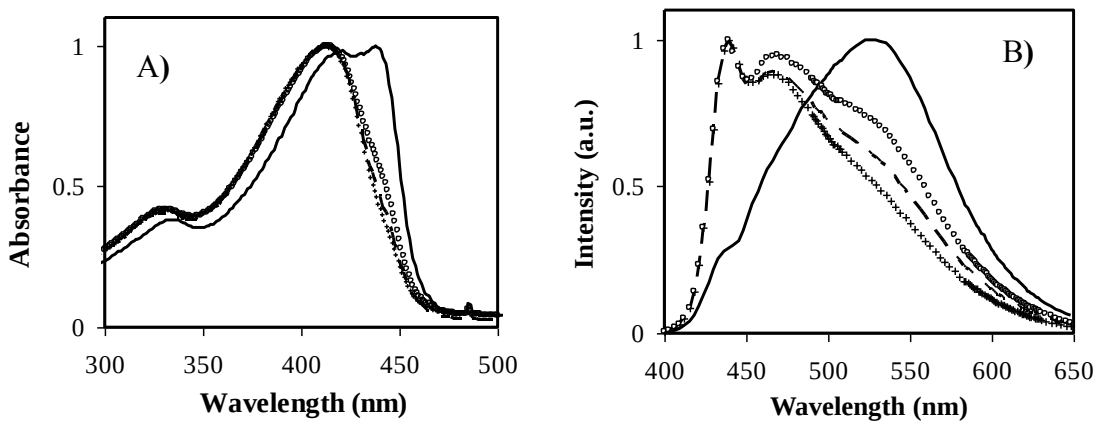

*Figure 2.3 A) Absorption spectra of **PP2** (2.0×10^{-6} M) in water at room temperature (—), 90°C (++), Cooled to room temperature from 90°C (— —) and 9 hrs later (○).3B)Emission spectra of **PP2** in water at room temperature (—), 90°C (++), Cooled to room temperature from 90°C (— —) and 9 hrs later (○).*

Lifetime data for **PP2** was collected in water and DMSO at $2.0\text{x}10^{-6}$ M. As in previous studies[38] the fluorescence decay profile of **PP2** in DMSO was wavelength independent and nearly exponential. The major lifetime component in a biexponential fit to the data was 535 ps and the fluorescence decay has a correlation time, $\langle\tau_F\rangle$[38], of 327 ps. This nonexponentiality contrasts with earlier reports of Schanze that the emission is exponential, however it does not

display a wavelength dependence and may result from polydispersity in the polymer sample. In water the fluorescence decay profile must be fit by a sum of three or more exponentials and it displays a strong wavelength dependence; $<\tau_F>$ ranges from 878 ps to 2.4 ns as the emission wavelength changes from 480 nm to 600 nm. Although both solvents display some inhomogeneity in the fluorescence decay law, the inhomogeneity in aqueous solutions appears to be more pronounced. The wavelength dependence of the fluorescence decay law in water is consistent with the presence of both aggregated and unaggregated forms that possess different emissive states.[37,38]

FCS Studies: FCS studies demonstrate the aggregation of **PP2** in water. Figure 2.4 shows the measured autocorrelation functions for **PP2** at two concentrations (5.2×10^{-8} M to 2.5×10^{-6} M) and fits of the data by equation (1). The decrease in amplitude of the autocorrelation function for the higher concentration data arises because more fluorophores appear in the excitation volume, see equation (1). The correlation time τ_D for the autocorrelation function increases by approximately 400-fold with the concentration increase. At low concentration τ_D=563 μs, D=$5.92\text{x}10^{-7}\text{cm}^2$/s and using a spherical model one gets a hydrodynamic radius of R_H = 4.2 nm (using equation 1 with η= 0.89 cP and ω_{xy}= 0.39 μm). If one uses a rigid rod model instead of spherical model, the hydrodynamic radius of PP2 at low concentration is 26.2 nm.(Please see supplemental information for details of model). At high concentration a much larger hydrodynamic radius, R_H=1.5 μm, was obtained. Corresponding FCS studies were performed on **PP2** in DMSO at low (~10^{-9} M) and high (~10^{-7} M) concentration, and the hydrodynamic radius (5.1 nm) does not change with concentration. To conclude, no aggregation takes place in DMSO even at higher concentration, whereas aggregation occurs in water at higher concentration.

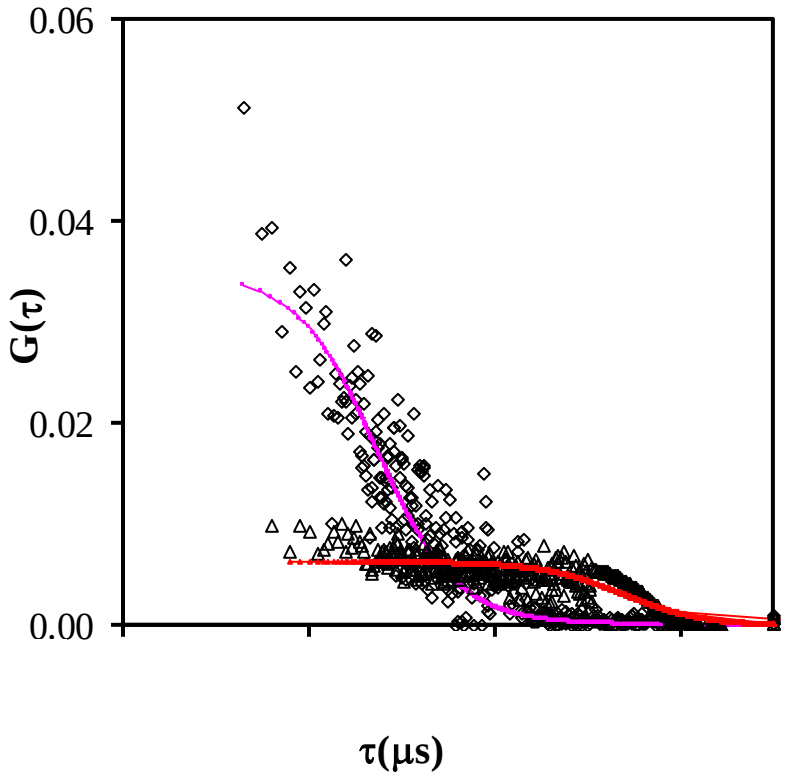

Figure 2.4 Autocorrelation function for ***PP2*** *in water at lower, 5.2×10^{-8} M (◊) and higher, 2.5×10^{-6} M(Δ).*

The much larger hydrodynamic radius for the polymer at high concentration is consistent with aggregates of the polymer. Using a spherical model and the hydrodynamic radius as a measure of the aggregate size, then a comparison to the 4.2 nm radius of a single monomer chain suggests that about 5x10^{7} polymer chains constitute the aggregate. Calculations using the rigid rod model gives a number of about 6x10^{5}. These data indicate the existence of unimolecular species at lower concentration and aggregates at higher concentration. To have a better understanding of how many molecules are in an aggregate, a better model to connect the diffusion coefficient and the particle size may be required.

The hydrodynamic radius R_H of 4.2 nm is consistent with single polymer chains at low concentration. Using a molecular weight of 38100 g/mole, the contour length of the polymer is calculated to be 92 nm. Comparing this value to a Kuhn length of 30 nm, which is typical of polyphenylethynylene,[51] implies that a Gaussian chain model is not appropriate. Instead, we use the Kratky-Porod wormlike chain model,[51] and calculate a radius of gyration R_G for **PP2** of 11.6 nm. Comparing this to our measured R_H gives R_G/R_H is 2.8. Studies for polymers with similar backbone have yielded a ratio of 2.[51]

These results demonstrate that **PP2** aggregates at higher concentration ($2.0x10^{-6}$ M polymer repeat unit) in water, but appear to exist as single strands at lower concentrations in water. The aggregation of the polymer, as demonstrated by the FCS studies, correlates with the changes observed in the absorption and emission spectra of the aqueous polymer solutions. The 'aggregates' fluorescence spectra are broad and red shifted (see Figures 2.2) and the 'aggregates' spectrum is inhomogeneous, as revealed by the wavelength dependence of the fluorescence decay law. The 'aggregates' absorption spectra display a band on the red edge, which disappears under conditions of isolated polymer strands in solution. The temperature studies reveal that the aggregation is reversible, but with a very slow time constant.

2.4.2 Effect of Electrolyte on Aggregation

When **PP2** was dissolved in DMSO, the addition of inorganic salts ($LiNO_3$ and $NaClO_4$ were used) did not induce any significant changes in the absorption or fluorescence spectra and did not cause any fluorescence quenching, ranging from an ionic strength of 1mM to 100mM. In contrast, electrolyte had a profound effect on the spectral properties in aqueous solutions.

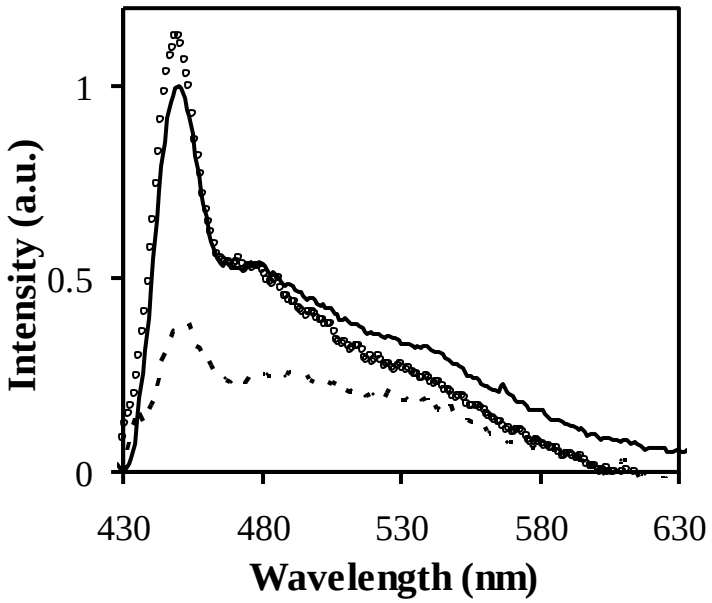

*Figure 2.5 Steady state fluorescence of **PP2** (5.2×10^{-8} M) in water (——), with 50μM NaCl (○) and 100mM NaCl (----).Relative intensities are meaningful.*

Low concentration regime: Figure 2.5 shows the steady-state fluorescence spectrum for aqueous solutions of **PP2** (5.2×10^{-8} M) at different NaCl concentrations. The addition of 50μM NaCl does not change the shape of the steady state emission spectrum; only 7% of the fluorescence was quenched. Similarly, using a spherical model, FCS studies give a hydrodynamic radius of R_H= 3.8 nm in a 50 μM NaCl solution, which is similar to the R_H= 4.2 nm in water at low concentration. In the 100mM NaCl solutions, the steady state fluorescence of **PP2** was quenched by 50% and the relative importance of the broad red shifted emission increased with respect to the sharp band at 451 nm. In addition, the FCS data for the 100mM NaCl solution showed a five fold increase in the hydrodynamic radius, indicating that aggregates of **PP2** form at higher NaCl concentration. Hence, the broad red-shifted emission correlates with increased aggregation, which is induced by the electrolyte. These observations imply that the

PP2 is not shielded effectively at low salt concentration and exists in a mostly unaggregated state, whereas the addition of excess salt better shields the charge on the **PP2** chains, reducing the interchain repulsion and increasing the aggregation.

FCS studies were also performed for **PP2** in DMSO with and without $NaNO_3$. The hydrodynamic radius remained the same for **PP2** in the presence and absence of $NaNO_3$ indicating no significant formation of aggregates upon addition of salt.

High Concentration regime: Although **PP2** is already aggregated in aqueous solutions with **PP2** concentrations of 2.0×10^{-6} M, addition of electrolyte affects the spectral characteristics.

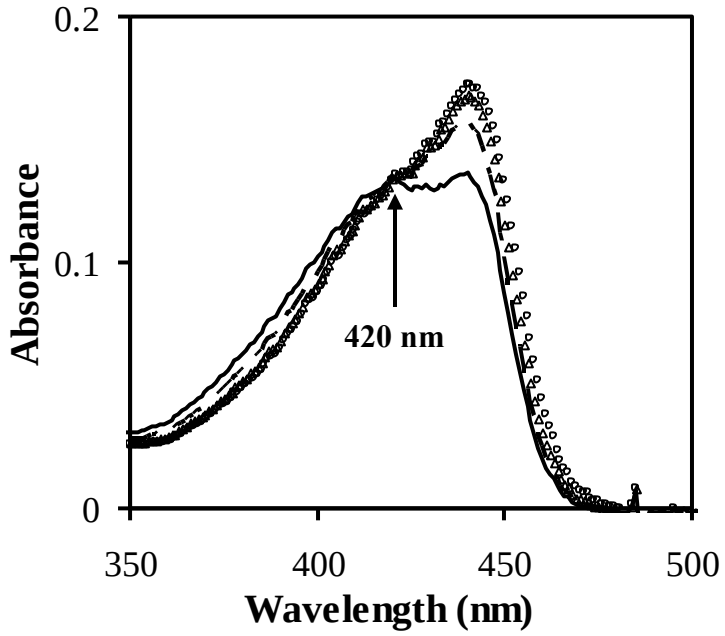

*Figure 2.6 Absorption spectra of **PP2** (2.0×10^{-6} M) in water for NaCl solutions of different ionic strength; 0 mM(—), 2.5 mM(– –), 5 mM(Δ), 20 mM (○). The arrow indicates the isosbestic point.*

Figure 2.6 shows the absorption spectra of **PP2** in NaCl solutions for ionic strengths ranging from 0 mM to 20 mM. The absorption spectrum of **PP2** in water has absorption peaks at λ_{max} at 439 nm and 421 nm. Upon increasing the ionic strength the red shifted peak grows in intensity and its position shifts by 2-3 nm on further addition of salt. An isosbestic point occurs near 420 nm, as if two distinct chromophoric states of the polymer (unaggregated and aggregated) are present.

By assuming a two species equilibrium reaction (**PP2**+$M^+ \leftrightarrow$ **PP2:**M), the absorption spectra were fit to obtain a stability constant, K. An example of the fitting results for **PP2** in NaCl solutions is in the supplemental information. Table 2.1 presents the stability constant K and gives the absorption peaks of the two 'species' for different electrolyte solutions. In this analysis, the percentage of the 'bluer aggregate species' decreased to 24% in 3 mM NaCl solution. These observations indicate the presence of different aggregates in the absence and presence of salt. We hypothesize that when salt is added, "self associated" aggregates of **PP2** are formed which presumably have ions incorporated in them. The formation of these aggregates is corroborated by FCS studies (a larger average size with salt) and also reflected by the growth of the red shifted peak in absorption spectrum

Table 2.1 Spectral characteristics and model parameters for a two species model of PP2 in electrolyte solutions.

Salt	Isosbestic point(nm)	**PP2·M**$^+$ λ_{max} (nm)	Stability Constant(ln K)	Percentage of unaggregated **PP2** in 3 mM salt solution
LiCl	419	445	3.30	32
NaCl	420	445	3.22	24
KCl	425	447	3.23	26
AF	421	444	3.64	16
TEAF	422	444	3.77	12
TBAF	425	454	3.58	18

The emission spectrum also changes with the addition of salt (figure 2.7A). Without NaCl added to the solution, **PP2** has a broad emission with a maximum at 525 nm and a shoulder near 435 nm. The shoulder at 435 nm disappears completely upon the addition of NaCl to the solution. Figure 2.7B shows how the relative fluorescence quantum yield of the **PP2** emission changes with increasing ionic strength, for three excitation wavelengths: 380 nm, 419 nm and 439 nm. The data show that the fluorescence intensity ratio of **PP2** in NaCl solution to that in water increases until 2.0 mM of NaCl (see the insert in 2.7B). The fluorescence decreases by almost 80% on further increase of ionic strength to 50 mM and becomes almost constant at an ionic strength >50 mM. No difference in the fluorescence quenching efficiency was observed for different excitation wavelengths.

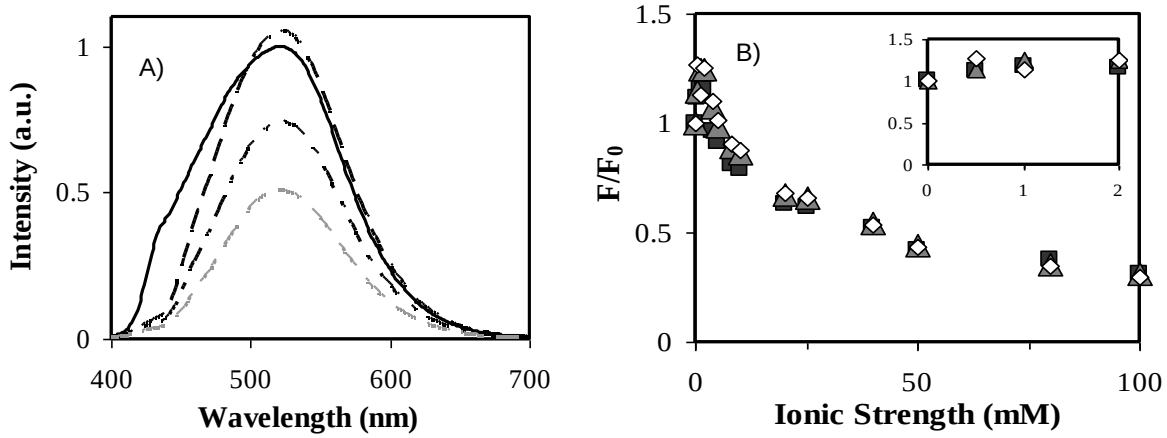

Figure 2.7 ***A)*** *Fluorescence spectra of* ***PP2*** *(2.0×10^{-6} M) in water for NaCl solutions of different ionic strength; 0 mM(—), 2.5 mM(– –), 5 mM(— - —), 20 mM (— —)* ***B)*** *Fluorescence intensity ratio of* ***PP2*** *in ionic NaCl solution (F) to that in water (F_0) versus the ionic strength at three different excitations,380 nm(■), 419 nm(▲) and 439 nm(◊).*

The spectral and photophysical properties in other 1:1 small electrolytes were nearly identical to the behavior observed in NaCl solutions. For the inorganic cations, the isosbestic points and the red peak's spectral shift correlate with the radius of the cation [Li^+ (0.59 Å), Na^+ (1.02 Å) to K^+ (1.33 Å)]. The degree of fluorescence quenching changed somewhat with the nature of the electrolyte, however. The fluorescence quenching in NaCl and KCl solutions were very similar; the LiCl solutions had a slightly lower quenching. The fluorescence quenching in the organic salts TBAF, TEAF and AF was weaker than that observed for the inorganic cations. These data are provided in the supplemental information.

Other observations: In contrast to the significant effect of temperature on the polymer aggregation in water, temperature had little effect for **PP2** with NaCl in water. An aqueous solution of **PP2** with 20mM NaCl was heated to 90^0 C. Although the fluoresence intensity

increased by 10%, the absorption and emission spectra of **PP2** before and after heating were the same. This behavior contrasts sharply with that seen for **PP2** in deionized water. This observation suggests that the aggregates in the salt solution are more tightly bound; i.e. do not dissociate as readily upon heating as they do in water.

From these ionic strength studies, we infer that addition of counter ions shields the charge on the **PP2** backbone, reduces the interchain repulsions, and promotes the formation of tighter aggregates.

2.4.3 Effect of Surfactant on Aggregation

Low Concentration: The emission and absorption spectrum of **PP2** in the low concentration regime ($1.1x10^{-8}$ M) was measured before and after addition of the cationic surfactant, ODTMA. Figure 8 shows the fluorescence spectrum for $1.1x10^{-8}$ M **PP2** in water and with 50 μM ODTMA; it does not change. In contrast, FCS experiments give a correlation time which is approximately three times larger for **PP2** in the ODTMA solution than for **PP2** in water. This correlation time gives a diffusion coefficient of $D=2.09 \times 10^{-7}$ cm^2/s and a hydrodynamic radius of R_H= 11.7 nm using a spherical model (see equation 1). This significant change of hydrodynamic size, caused by ODTMA indicates complexation between the **PP2**, a polyanion, and the ODTMA, a cationic surfactant, to form heteroaggregates (**PP2:** ODTMA).

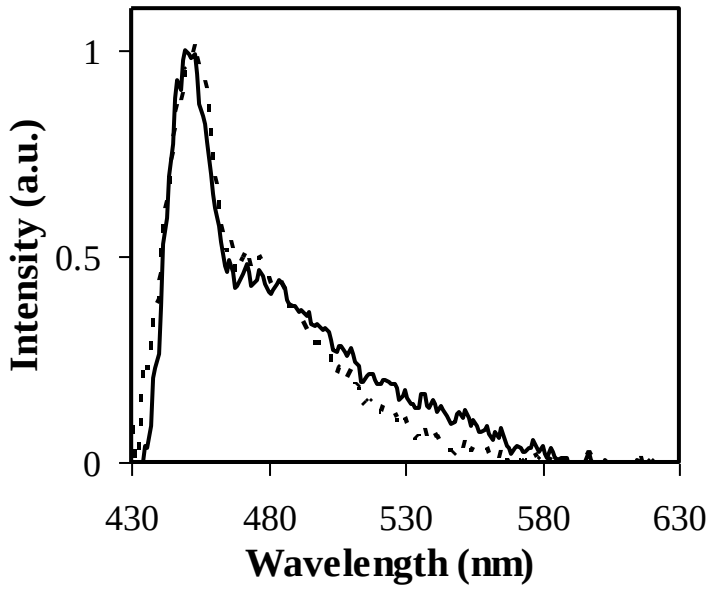

*Figure 2.8 Emission spectrum of **PP2** ($1.1x10^{-8}$ M) in water without (—) and with 50μM ODTMA (---)*

The association of ionic surfactants with polyelectrolytes has been reported previously for PPV and PPE.[34,35,53] These heteroaggregates of **PP2** and ODTMA are different from the homoaggregates (**PP2:PP2**) formed in water at high concentration and the aggregates formed on addition of electrolyte, which were discussed earlier. Presumably, they consist of individual **PP2** molecules associated with a number of different surfactant molecules. The hydrodynamic radius, using a spherical model, of 11.7 nm indicates a volume that is 20-25 times larger than that of a **PP2** molecule and suggests that about 165 ODTMA molecules are bound to the polymer. If all the charged groups on **PPE** are coordinated by ODTMA then for n=73, determined from average molecular weight, each **PPE** molecule should have 146 ODTMA molecules attached to it. Hence, the agreement is good.

High Concentration: Figure 2.9A shows the absorption spectrum for $2.0x10^{-6}$ M (concentration in polymer repeat unit) **PP2** solutions of ODTMA. As the concentration of ODTMA increases, the peak absorption at 439 nm, which is associated with the **PP2** aggregates, decreases in intensity until it disappears. In addition, the spectrum shifts blue by about 26 nm; the color of the **PP2** solution changs from yellow to light yellow. The blue shift is attributed to the decrease in conjugation because of breaking of the aggregates. In aggregates many polymers chains are stacked on each other increasing the effective conjugation length and hence red shift in absorption spectrum. No isosbestic point is observed on addition of ODTMA.

Figure 2.9B shows the dependence of the fluorescence spectrum on the ODTMA concentration. As the ODTMA concentration increases, a sharp peak at 451 nm grows in, similar to that observed at low concentrations and in DMSO. The intensity ratio of the shoulder and the

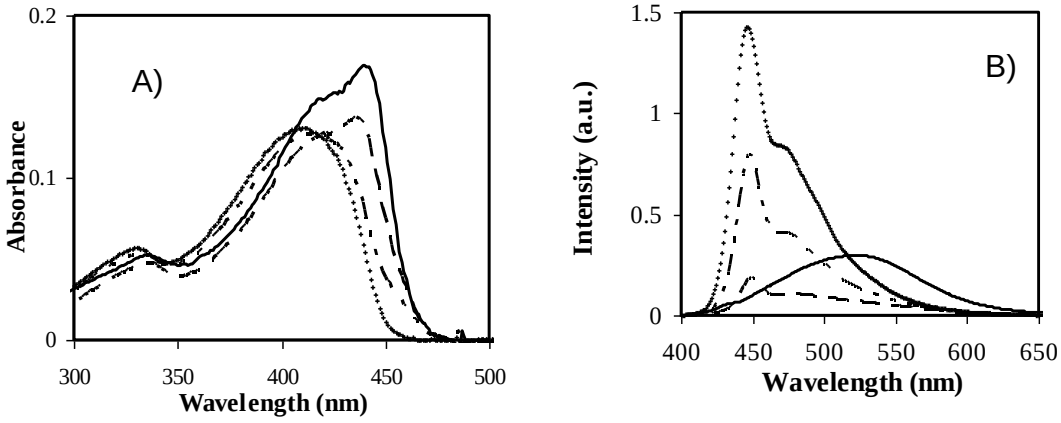

*Figure 2.9**A)** Absorption spectrum of **PP2**(2.0×10^{-6} M) in water at different ionic strength solutions of ODTMA; 0 mM(——), 0.005 mM (— —),0.025 mM(— – – —) and 0.05 mM(+) **9B)** Emission spectrum of **PP2**(2.0×10^{-6} M) in water at different ionic strength solutions of ODTMA. 0 mM(——), 0.005 mM (— —),0.025 mM(— – – —) and 0.05 mM(+)*

sharp peak remain constant for ODTMA >0.01mM. This behavior should be contrasted with that obtained at low concentration. At low concentration, **PP2** is already unaggregated and addition of surfactant does not change the steady state spectrum. At higher concentration the **PP2** is homoaggregated and the addition of surfactant seems to dissociate these homoaggregates (**PP2:PP2**) and form heteroaggregates (**PP2**: ODTMA).

The dissociation of the homoaggregates is further corroborated by lifetime measurements. The fluorescence lifetime,$<\tau_F>$, changes from 878 ps in water to 183 ps in the presence of 0.05mM ODTMA. In addition to the decrease in the $<\tau_F>$, the quantum yield in the presence of 0.05 mM ODTMA solution increases by three times over that in water. The decrease in $<\tau_F>$ and corresponding increase in quantum yield demonstrates that addition of ODTMA to **PP2** changes the nature of the emitting state to one with a higher radiative rate. The radiative rates for **PP2** with 0.05mM ODTMA were approximately 12 times higher than that found in water.

The formation of complexes between ODTMA and **PP2** ($2.0x10^{-6}$ M) was further investigated by measuring the zeta potential of **PP2** as a function of ODTMA concentration. Figure 2.10 shows how the zeta potential varies with the addition of surfactant. On addition of surfactant the zeta potential increases and becomes more and more positive as the concentration of surfactant is increased. The binding between **PP2** and ODTMA molecules causes charge neutralization, and a zeta potential of zero occurs when the **PP2** molecules are neutralized by ODTMA molecules. At zero, the solution has 182 ODTMA molecules for each **PP2** molecule, which is in good agreement with 166 obtained from the FCS measurements at low concentration of **PP2**. At higher concentration of ODTMA the change in the sign of the zeta potential implies that excess surfactant molecules bind on a **PP2:**surfactant complex.[54]

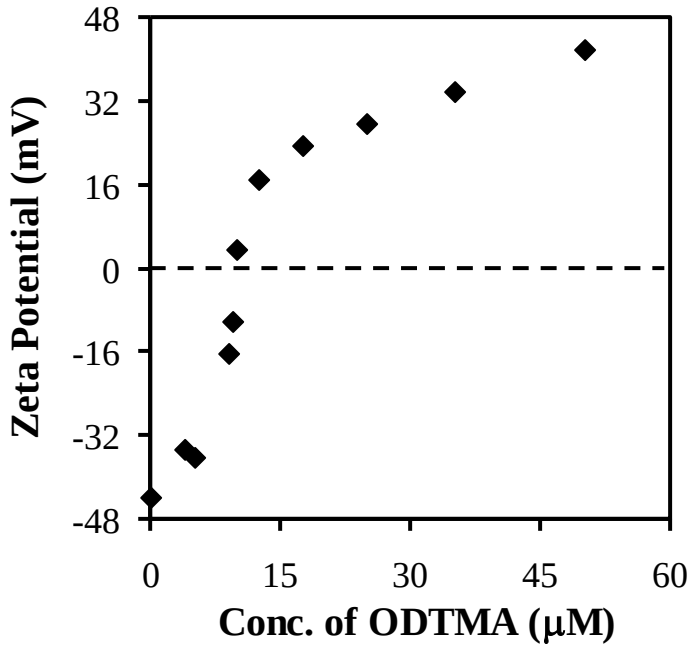

*Figure 2.10 Zeta potential vs concentration of ODTMA for **PP2** in water.*

These studies support the argument that the ODTMA forms heteroaggregates with **PP2** and dissociates the homoaggregates (**PP2:PP2**). Scheme 2.1 illustrates the type of aggregates formed on addition of ODTMA. In water **PP2** is in aggregated form, the **PP2** strands are wrapped on each other but on addition of ODTMA, these aggregates dissociate and each **PP2** molecule is surrounded by ODTMA molecules.

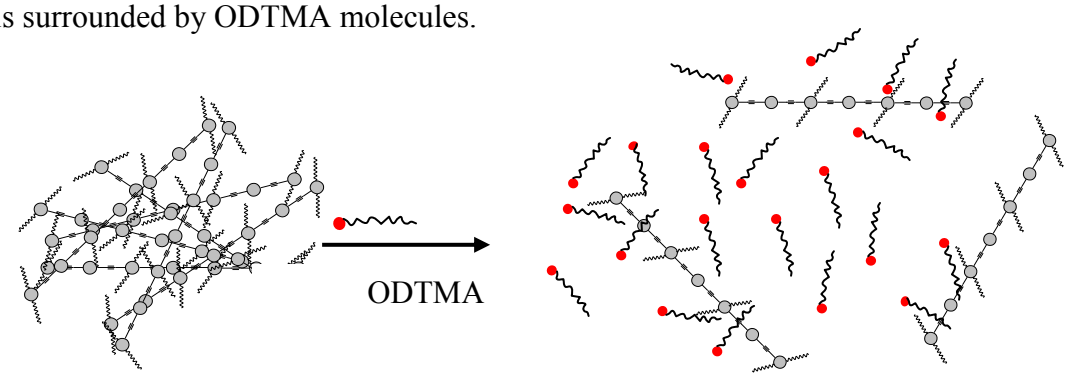

Scheme 2.1 Formation of heteroaggregates on addition of ODTMA

Steady-state spectra and FCS studies show that when **PP2** is at low enough concentration, the addition of surfactant does not change the photophysical properties of **PP2**. At higher

concentration, the addition of surfactant changes the absorption and emission spectra so that they look similar to those observed for the unaggregated form of the **PP2**.

PEG (Nonionic surfactant): The absorption spectrum of **PP2** shifts red on addition of PEG, but no isosbestic point is observed. On addition of PEG the **PP2** fluorescence spectrum develops a sharp peak at 448 nm, however the broad red peak at 530 nm remains, even at large excess of PEG. Time resolved fluorescence studies show that the decay law of the excited state is nonexponential and exhibits a strong dependence on the emission wavelength. Lastly, the average lifetime is slower than that found for **PP2** with 0.05mM ODTMA indicating that PEG does not break the homoaggregates fully. The neutral surfactant does not interact strongly enough with the **PP2** in order to dissociate the homoaggregates.

2.5 SUMMARY AND CONCLUSION

It is evident that the solution properties affect the **PP2** aggregation and hence the optical properties and the excited state lifetime of **PP2**. **PP2** has an emission spectrum with evidence of vibronic structure in DMSO and in water with ODTMA surfactant. At low concentration in water the **PP2** spectrum is indicative of an unaggregated form. As the concentration of **PP2** in water increases the well-defined emission band disappears and a broad, red-shifted emission band appears. The large change in hydrodynamic radius of the fluorophore, as determined by FCS, correlates with these spectral changes and demonstrates the aggregation. In addition, the temperature studies show that aggregated **PP2** can be dissociated at high temperature.

At concentrations of 10^{-6} M **PP2** in water, the absorption spectrum displays a band on the red edge from the aggregate and the emission spectrum is dominated by the aggregated form,

broad and red-shifted. The addition of small electrolyte ions to the solution perturbs these spectral characteristics and appears to stabilize the aggregates. In NaCl solutions the size of the aggregates, as determined by FCS, are larger than that found in water, and heating of the solutions to 90^{o} C does not dissociate the aggregates. The steady-state spectra of **PP2** display similar behavior for the different cations and anions that are studied, indicating that specific interactions such as ion pair formation may not be important.

Addition of ODTMA surfactant to **PP2** in water causes remarkable changes in the fluorescence and absorption spectra. Comparison with the spectra in DMSO, indicates that the ODTMA dissociates the homoaggregates of **PP2.** The zeta potential measurement and FCS studies at low **PP2** concentration demonstrate that ODTMA forms its own complexes with **PP2**. The fluorescence quantum yield of **PP2** in 0.05 mM ODTMA increases by approximately three times as compared to water. The decrease in the excited state lifetime and corresponding increase in quantum yield demonstrates that addition of ODTMA to **PP2** changes the nature of the emitting state to one with a higher radiative rate. The radiative rate for **PP2** with 0.05mM ODTMA is approximately 12 times higher than that found in water. The change in the radiative rate supports the conclusion that the emitting chromophore changes under different solution conditions, and supports the explanation that the aggregate emission is 'excimer-like'.

These studies have important implications for the use of these materials in sensing. The above studies show that the photophysical properties of polyphenylethynylene are very sensitive to electrolyte concentration and surfactants. For example, the fluorescence intensity of **PP2** decreased with increasing ionic strength of inorganic and organic salts, because of the formation of aggregates.[55-58] If the aggregates and the unaggregated form have different sensitivities for the analyte, then the aggregation will need to be controlled for sensing applications. A number of

workers have reported that the Stern-Volmer constant depends on the concentration of the conjugated polyelectrolyte.[37] Studies of the effect of ionic strength on Stern-Volmer constant are under way and will be published elsewhere.

2.6 ACKNOWLEDGEMENT

We acknowledge support from the U.S. National Science Foundation (CHE-0415457).

2.7 REFERENCES

(1) Bunz, U. H. F.; Imhof, J. M.; Bly, R. K.; Bangcuyo, C. G.; Rozanski, L.; Bout, D. A. V. *Macromolecules* **2005**, *38*, 5892-5896.

(2) Jones, R. M.; Bergstedt, T. S.; McBranch, D. W.; Whitten, D. G. *J Am Chem Soc* **2001**, *123*, 6726-7.

(3) Levitsky, I. A.; Kim, J.; Swager, T. M. *J. Am. Chem. Soc* **1999**, 1466-1472.

(4) Perahia, D.; Traiphol, R.; Bunz, U. H. F.; *Macromolecules* **2001**, *34*, 151-155.

(5) Rothberg, L. J.; Yan, M.; Galvin, M. E.; Kwock, E. W.; Miller, T. M.; Papadimitrakopoulos, F. *Synthetic Metals* **1996**, *80*, 41-58.

(6) Wilson, J. N.; Bunz, U. H. F. *J. Am. Chem. Soc* **2005**, *127*, 4124-4125.

(7) Zhou, C. Z.; Liu, T.; Xu, J. M.; Chen, Z. K. *Macromolecules* **2003**, *36*, 1457-1464.

(8) Skotheim, T. E.; Elsenbaumer, R. L.; Reyolds, J. R. *Eds. Handbook of Conducting Polymers* **1998**, *Marcel Decker: New York*.

(9) Moroni, M.; J., L. M.; Luzzati, S. *Macromolecules* **1999**, *32*, 562-571.

(10) Gaylord, B. S.; Heeger, A. J.; Bazan, G. C. *Proc. Nat. Acad. Sci.* **2002**, *99*, 10954-10957.

(11) Harrison, B. S.; M.B.;, R.; Reyolds, J. R.; Scahnze, K. S., , . *J.Am. Chem. Soc.* **2000**, *122*, 8561.

(12) Kushon, S. A.; Ley, K. D.; Bradford, K.; Jones, R. M.; McBranch, D.; Whitten, D. *Langmuir* **2002**, *18*, 7245-7249.

(13) McQuade, D. T.; Pullen, A. E.; Swager, T. M. *Chem Rev* **2000**, *100*, 2537-74.

(14) Rininsland, F.; Xia, W.; Wittenburg, S.; Shi, X.; Stankewicz, C.; Achyuthan, K.; McBranch, D.; Whitten, D. *Proc. Nat. Acad. Sci.* **2004**, *101*, 15295-15300.

(15) Schanze, K. S.; Pinto, M. R. *Proc. Nat. Aca. Sci.* **2004**, *101*, 7505-7510.

(16) Heeger, A. J.; Diaz-Garcia., M. A. *Curr. Opin. Solid State Mater.* **1983**, *3*, 16.

(17) Kim, I. B.; Dunkhorst, A.; Gilbert, J.; Bunz, U. H. F. *Macromolecules* **2005**, *38*, 4560-4562.

(18) Liu, M.; Kaur, P.; Waldeck, D. H.; Xue, C.; Liu, H. *Langmuir* **2005**, *21*, 1687-1690.

(19) Hide, F.; Diaz-Garcia, M. A.; Schwartz, B. J.; Andersson, M. R.; Pei, Q.; Heeger, A. J. *Science* **1996**, *273*, 1833-1836.

(20) Ho, P. K. H.; Kim, J. S.; Burroughes, J. H.; Becker, H. L.; Li, S. F. Y.; Brown, T. M.; Cacialli, F.; Friend, R. H. *Nature* **2000**, *404*, 481-484.

(21) Sirringhaus, H.; Tessler., N.; Friend, R. H. *Science* **1998**, *280*, 1741-1744.

(22) Zhang, C.; Broun, D.; Heeger, A. J. *J. Appl. Phys.* **1993**, *73*, 5177.

(23) Bunz, U. H. F. *Chem. Rev.* **2000**, *100*, 1605-1644.

(24) Halkyard, C. E.; Rampey, M. E.; Kloppenburg, L.; Studer-Martinez, S. L.; Bunz, U. H. F. *Macromolecules* **1998**, *31*, 8655-8659.

(25) Breitenkamp, R. B.; Tew, G. N. *Macromolecules* **2004**, *37*, 1163-1165.

(26) Chu, Q.; Pang, Y. *Macromolecules,* **2003**, *36*, 4614-4618.

(27) Chu, Q.; Pang, Y.; Ding, L.; Karasz, F. E. *Macromolecules* **2002**, *35*, 7569-7574.

(28) Miteva, T.; Palmer, L.; Kloppenburg, L.; Neher, D.; Bunz, U., H. F. *Macromolecules* **2000**, *33*, 652-654.

(29) Fiesel, R.; Halkyard, C. E.; Rampey, M. E.; Kloppenburg, L.; Studer-Martinez, S. L.; Scherf, U.; Bunz, U. H. F. *Macromolecular Rapid Communications* **1999**, *20*, 107-111.

(30) Haskins-Glusac, K.; Pinto, M. R.; Tan, C.; Schanze, K. S. *J. Am. Chem. Soc.* **2004**, *126*, 14964-14971.

(31) Kim, I.-B.; Bunz, U. H. F. *J. Am. Chem. Soc.* **2006**, *128*, 2818-2819.

(32) Kim, I.-B.; Dunkhorst, A.; Gilbert, J.; Bunz, U. H. F. *Macromolecules* **2005**, *38*, 4560-4562.

(33) Kim, I.-B.; Phillips, R.; Bunz, U. H. F. *Macromolecules* **2007**, *40*, 814-817.

(34) Thunemann, A. F.; Ruppelt, D. *Langmuir* **2001**, *17*, 5098-5102.

(35) Thunemann, A. F. *Adv. Mater.* **1999**, *11*, 127-130.

(36) Fan, Q.; Zhou, Y.; Lu, X. M.; Hou, H. M.; Huang, W. *Macromolecules,* **2005**, *38*, 2927-2936.

(37) Pinto, M.; Kristal, B. M.; Schanze, K. S. *Langmuir* **2003**, *19*, 6523-6533.

(38) Tan, C.; Pinto, M. R.; Schanze, K. S. *Chem Comm.* **2002**, 446-447.

(39) Jiang, H.; Zhao, X.; Schanze, K. S. *Langmuir* **2006**, *22*, 5541-5543.

(40) Lavigne, J. J.; Broughton D. L. ; Wilson, J. N.; Erdogan, B.; Bunz, U. H. F. *Macromolecules* **2003**, *36*, 7409-7412.

(41) Kim, S.; Jackiw, J.; Robinson, E.; Schanze, K. S.; Reynolds, J. R.; Baur, J.; Rubner, M. F.; Boils, D. *Macromolecules* **1998**, *31*, 964-974.

(42) *GPC studies were performed by American Polymer Std. OHIO*.

(43) Liu, M.; Waldeck, D. H.; Oliver, A. M.; Head, N. J.; Paddon-Row, M. N. *Journal of the American Chemical Society* **2004**, *126*, 10778-10786.

(44) Koppel, D. E. *Physical Review A* **1974**, *10*, 1938-1945.

(45) Magde, D.; Elson, E.; Webb, W. W. *Physical Review Letters* **1972**, *29*, 705-708.

(46) Pristinski, D.; Kozlovskaya, V.; Sukhishvili, S. A. *Journal of Chemical Physics* **2004**, *122*, 14907-14907.

(47) Van Rompaey, E.; Sanders, N.; Van Craenenbroeck, E.; Engelborghs, Y.; De Smedt, S. C.; Demeester, J. *Macromolecules* **2000**, *33*, 8280-8288.

(48) Leng, X. S., K.; Buffle, J. *J.Coll. Inter. Sci.* **2002**, *251*, 64.

(49) Yue, H.; Waldeck, D. H.; Xue, C.; Liu, H. *Manuscript in preparation*.

(50) Krichenvsky, O.; Bonnet, B. *Rep.Prog.Phys.* **2002**, *65*, 251-297.

(51) Cotts, P. M.; Swager, T. M.; Zhou, Q. *Macromolecules* **1996**, *29*, 7323-7328.

(53) Chen, L.; Xu, S.; McBranch, D.; Whitten, D. *J. Am. Chem. Soc* **2000**, *122*, 9302-9303.

(54) Yuan, L. L.-J., D.; Hiroyuki, N.; and Kenichi. N *J. Coll. Inter. Sci.* **2003**, *264*, 561-564.

(55) Bronich, T. K.; Kabanov, A. V.; Kabanov, V. A.; Yu, K.; Eisenberg, A. *Macromolecules* **1997**, *30*, 3519-3525.

(56) Kuhn, P. S. L., Y.; Barbosa, M.C. **1998**, 299, 51-56. *Chemical Physics Letters,* 1998, *299*, 51.

(57) Macknight, W. J.; Ponomarenko, E. A.; Tirrell, D. A. *Acc. Chem. Res.* **1998**, *31*, 781-788.

(58) Samori, P.; Severin, N.; Muellen, K.; Rabe, J. P. *Adv. Mat.* **2000**, *12*, 579-582.

3.0 DEPENDENCE OF POLYPHENYLETHYNYLENE POLYELECTROLYTE'S FLUORESCENCE QUENCHING ON THE ELECTROSTATIC AND HYDROPHOBIC PROPERTIES OF THE QUENCHER

This work has been published as Palwinder Kaur, Mingyan Wu, Laura Anzaldi, David H. Waldeck, Cuihua Xue, and Haiying Liu, Langmuir.; (2007); 23, 13203-13208.Thesis author did FCS measurements and worked with the first author in other spectroscopic experiments.

This study investigates the changes in sensitivity and optical properties of a polyphenylethynylene (**PP2**) based polyelectrolyte by positively charged and neutral macromolecules. This work shows that the change in the fluorescence yield of **PP2** can arise from a number of factors, including electrostatic, hydrophobic and energy transfer interactions with the quencher and also changes in the solution conditions such as concentration and ionic strength. This fluorescence quenching is attributed to the formation of aggregates that form upon addition of different quenchers to **PP2** solution and/or the solution conditions. The extent of aggregation of **PP2** is shown to depend on the type of interaction between **PP2** and quencher, the concentration of **PP2** and the ionic strength of the solution.

3.1 INTRODUCTION

Conjugated polymers have been extensively studied as materials with a unique combination of properties. As a result of these properties, a variety of novel applications are under development, including light-emitting diodes,[10] lasers,[79] and solar cells.[80] This class of materials has also found potential utility in the biosensor field[17,81-84]. The fluorescence intensity of these polymers can be made to respond to very minute quantities of analytes. The sensitivity of these materials arises from extremely rapid exciton diffusion along the conjugated polyelectrolyte chain to the quencher binding site, which significantly increases the effective "quenching radius" of the quencher. Excitons are created by absorption of a photon and then they migrate along the polymer backbone. Analyte binding produces a trapping site whereby the excitation is effectively deactivated, typically by electron transfer, energy transfer or conformational changes in polymer. Such behavior has been referred to in the literature as the "molecular wire effect".[85-87]

A number of conjugated polymer materials are fluorescent (PPV, PPP, polythiophenes, and others) and have been demonstrated to perform as sensing agents for chemical and biological molecules.[15,16,67,88-94] An important development is the use of anionic functionalities on the polymer backbone to make the materials water soluble and useful for biological sensing. Typically, these anionic functionalities are designed to correspond to a bound, or associated, analyte species that quenches the excitation. The bulk of the research effort on these materials has explored the ability of different polymer backbones and receptor strategies to sense the macromolecules, whereas the fluorescence quenching mechanism and the factors that affect the optical properties are still not very clear. Fan et al[95] showed that the fluorescence quenching of

PPV based polyelectrolyte by the protein cytochrome-*c* arises from a combination of ultrafast photoinduced

Electron transfer and the formation of bound complexes between cationic and anionic polyelectrolytes. Liu et al.[16] showed that the quenching in polyphenylethynylene based polyelectrolyte results from conformational changes that occur upon binding the polyelectrolyte to the protein, dendrimer etc. and further showed that electron and energy transfer mechanism need not be present. From such studies it is clear that complex formation between the polymer and the analyte plays an important role in fluorescence quenching of the polyelectrolytes. Recently Kim et al[96] demonstrated fluorescence quenching of PPE based polyeletrolytes and oligomers by a number of analytes such as histones, lysozymes, myoglobin, hemoglobin etc. They showed that the net negative charge of the PPE plays a significant role but is not the only factor in the interaction of proteins with these polyelectrolytes. A number of factors such as electrostatic, hydrophobic interactions, electron transfer, energy transfer etc. are likely to contribute to the fluorescence quenching of these polyelectrolytes. Sometimes one factor is a dominant contributor to the fluorescence quenching and sometimes a combination of factors is important. Hence, it is important to understand how each of these factors affects the sensitivity of these polyelectrolytes towards the presence of quencher.

This work reports how the fluorescence quenching of a polyphenylethynylene based polyelectrolyte (**PP2**) changes in the presence of different macromolecules (proteins, dendrimers and surfactants) and under different solution conditions (concentration and ionic strength). The change in the optical properties and relative fluorescence quantum yield of **PP2** in the presence of different macromolecules is explained by the different kind of interactions that are present between **PP2** and macromolecules. The fluorescence quenching in the case of protein and

dendrimers quencher is attributed to the formation of polymer aggregates via electrostatic and hydrophobic interactions between multiple polymer strands and the quencher molecules. The affect of solution condition on the sensitivity of **PP2** has been studied by varying the concentration of polymer and ionic strength of solution.

3.2 EXPERIMENTAL

Material: Poly[2,5-bis(3-sulfonatopropoxy)-1,4-phenylethynylene-alt-1,4-polyphenylene ethynylene] (identified as **PP2**) is a polyelectrolyte with two negative charges per repeat unit and was prepared in a manner similar to that reported in the literature.[97] Cytochrome-*c* was bought from Sigma and was used without further purification. PAMAM-3G was bought from Dendritech, Inc. and protonated using trifluoroacetic acid. Six-arm poly(ethylene oxide) hydroxy terminated, dipentaerythritol Core (PEG-OH), M. Wt. 12 KDa was purchased from Polymer Source Inc. DEM-3.5 G was a gift from Professor T. Chapman at University of Pittsburgh. Size exclusion chromatography[98] was used to determine the molecular weight of **PP2** in DMSO (a good solvent), 38,100 Da with a polydispersity of 3.04. The experimental polymer solution was highly diluted (10^{-6}~10^{-8} M in terms of polymer repeat unit). All concentrations in this paper are reported in terms of polymer repeat unit. At these concentrations the effect of the polymer on solution properties, such as viscosity, can be neglected.

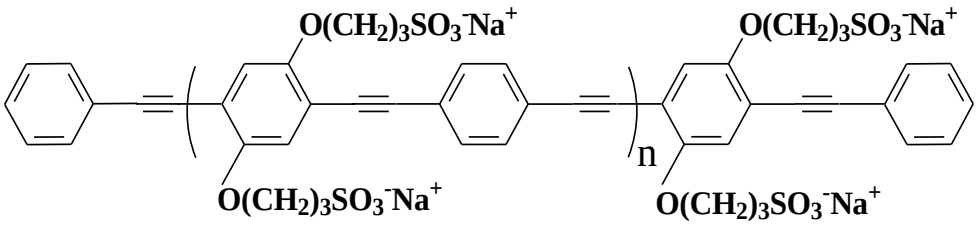

Figure 3.1 Chemical structure of PP2

Steady state spectroscopy: Steady-state absorption spectra were measured on an Agilent 8453 spectrometer and the steady-state emission spectra were measured on a Spex Fluorolog 0.22 m double spectrometer.

Stern-Volmer Constant: The Stern-Volmer constants were obtained using the Stern-Volmer equation[99] described as follows.

$$\frac{F_0}{F} = 1 + K_{sv}[Q] \tag{3.1}$$

with F_0 being the fluorescence intensity of the conjugated polymer by itself and F being the fluorescence intensity of the conjugated polymer after addition of a given concentration of quencher $[Q]$. K_{sv} is the Stern-Volmer constant and can be extracted from the slope of the graph that plots F_0/F versus quencher concentration with intercept 1. The Stern-Volmer constants reported in this paper were obtained by fitting the data at very low quencher concentration ranging from 0- 0.4 μM.

Time dependent fluorescence spectroscopy: The time-resolved fluorescence data were collected using the time-correlated single photon counting method.[16] The instrument response function was measured using a sample of colloidal $BaSO_4$. The samples were excited at 438 nm using a diode laser (PIL043, A.L.S. GmbH) and the emission was collected at different wavelengths. The fluorescence decay curves were fit by a convolution and compare method

using IBH-DAS6 analysis software. Other details of the TCSPC apparatus can be found in reference [100].

Fluorescence Correlation Spectroscopy (FCS): FCS is a non-invasive single molecule method which obtains dynamic and kinetic information by following the fluctuation trajectory of fluorescence about the equilibrium state.[101-105] FCS was performed on a home made FCS instrument based on a Zeiss IM35 inverted microscope. Details of the instrumentation will be provided elsewhere.[106] The sample was excited at 438 nm through an objective lens (Olympus UPlanfluor 40X/1.30 Oil) and the fluorescence was collected by the same lens. The concentrations of the polymer solutions were controlled to be 5.2×10^{-8} M and 2.5×10^{-6} M. To avoid photobleaching and optical trapping, the laser power was kept low, 24 μW, as measured at the front of the objective lens. Each measurement lasted 2 to 5 min, during which the time trajectory of fluorescence was monitored and only those having stable fluorescence intensity were kept. The corresponding autocorrelation function G(t) was fit by equation (2)

$$G(t) = \frac{1}{\overline{N}}\left(1+\frac{t}{\tau_D}\right)^{-1}\left(1+\frac{\omega_{xy}^2 t}{\omega_z^{\,2}\tau_D}\right)^{-1/2} \tag{3.2}$$

to extract the correlation time τ_D. $\overline{N}$ is the average number of fluorescent molecules in the focal volume; ω_{xy} is the radius of the focal spot in the transverse direction, and ω_z is the Rayleigh range of the excitation beam (see reference [107] for details relating to equation 2). The correlation time τ_D is related to the translational diffusion coefficient D of the fluorophore by

$$\tau_D = \frac{\omega_{xy}^2}{4D} \tag{3.3}$$

The apparatus was calibrated and tested using a 10 nM Rhodamine 6G aqueous solution, assuming the diffusion coefficient $D = 4.14\times10^{-6}$ cm^2 s^{-1}.[108] The Stokes-Einstein approximation,

equation (4) was used to extract the hydrodynamic radius R_H from the measured diffusion coefficient

$$D = \frac{k_B T}{6\pi\eta R_H} \tag{3.4}$$

where η is the shear viscosity, T is the temperature and k_B is Boltzmann's constant.

3.3 RESULTS AND DISCUSSION

It has been reported in the literature that the photophysical properties of polyphenyethynylene based conjugated polymers change with the temperature, concentration, ionic strength and solution environment.[109] The recent study by Kaur et al[109] has shown that the PPE based polyelectrolytes exist as independent strands at low concentration in good solvent and they aggregate at high concentrations and in the presence of salts, causing the fluorescence to quench. Figure 3.2 shows the variation of emission spectrum of **PP2** with concentration and ionic strength. **PP2** exists as individual polymer strands at very low concentration (~10^{-8} M) and is aggregated at higher concentration (~10^{-6} M). Similarly **PP2** aggregates at higher ionic strength and the fluorescence is highly quenched (Figure 3.2).

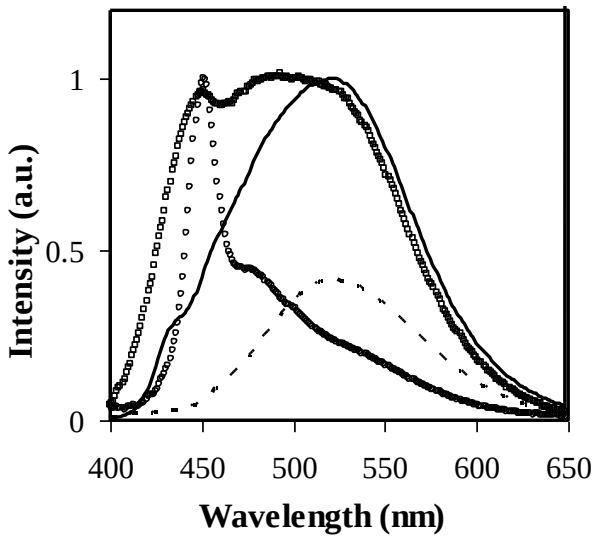

Figure 3.2 Emission spectra for PP2 in water at different concentrations (2.0×10^{-6}(—), 8.8×10^{-8}(□), 1.0×10^{-8} (○) M) and at 50 mM Na_3PO_4 at 2.0×10^{-6} PP2 concentration (----)

3.3.1 Quenching of PP2 by Cytochrome-c

Fluorescence quenching experiments were done at different concentrations of **PP2** with ferric cytochrome-*c*. Figure 3.3A shows the dependence of the Stern-Volmer constant on the concentration of **PP2.** As the concentration of the **PP2** was increased the Stern-Volmer constant decreased by a factor of nearly ten and then became constant. The work of Kaur et al show that **PP2** aggregates at concentrations above 10^{-6} M, hence these data show that **PP2** is more sensitive in its unaggregated form. To corroborate this result further, quenching experiments were done at different ionic strengths for a **PP2** concentration of 10^{-6} M (Figure 3.3B). On increasing the ionic strength of the solutions, the Stern-Volmer constant decreased by a factor of nearly 2.3. Experiments at ionic strength higher than 60mM were not performed because of poor solubility

of **PP2** in these higher ionic strength solutions. These results imply that when **PP2** is in a relatively unaggregated form, it is more readily quenched.

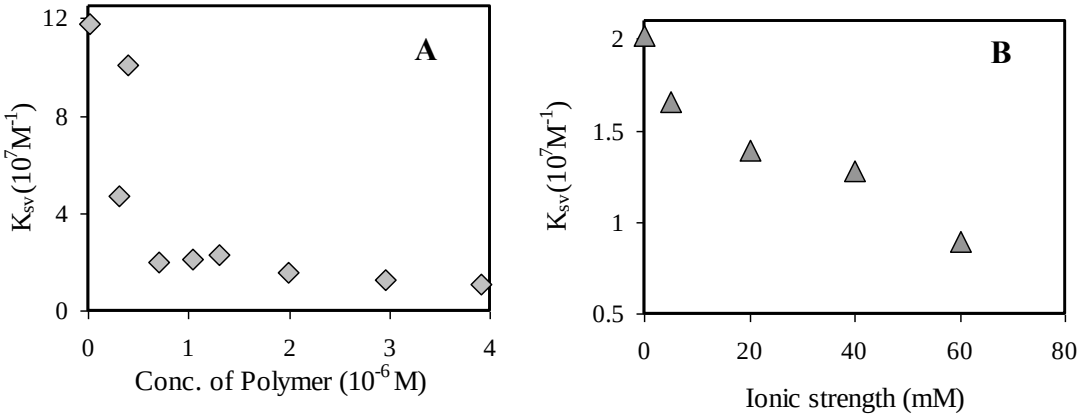

Figure 3.3 Dependence of Stern-Volmer constant on concentration of PP2 at an intrinsic ionic strength of polymer only (A). and on ionic strength at a PP2 concentration of 10^{-6} M in (B).

Since **PP2** is more sensitive in an unaggregated form, quenching experiments were performed for **PP2** (~ 2 x 10^{-7} M) in unaggregated form. To further ensure that the **PP2** exists in an unaggregated form, the **PP2** solutions were first heated to dissociate any aggregates and then cooled to room temperature; see reference [109]. On addition of ferric cytochrome-*c* to the unaggregated **PP2** solution, a new red shifted peak was observed in the absorption spectrum. This red peak has been attributed to aggregate formation in the previous literature.[26,109] Figure 3.4 shows the absorption and emission spectra of the heated **PP2** before and after addition of 0.4 μM cytochrome-*c*. The addition of ferric cytochrome-*c* quenched the fluorescence of **PP2** by 98 %. Hence the protein induces polymer aggregation and it effectively quenches the fluorescence.

The fluorescence quenching mechanism of **PP2** in the presence of ferric cytochrome-*c* was elucidated by performing quenching experiments with different forms of cytochrome-*c*'s namely ferrous, and apo, denatured forms of the protein. It was found that the quenching by

ferric and ferrous forms of the protein is similar; suggesting that the electron transfer quenching is not dominant. Apo cytochrome-*c* also quenched the fluorescence but with an efficiency nearly fourteen times lower than that for the native protein. Further the denatured cytochrome-*c*[1] quenched the polymer fluorescence but with 80% of the efficiency of the native protein. Comparison of these quenching efficiencies suggests that the energy transfer quenching as well as the induced aggregation upon addition of cytochrome-*c* govern the fluorescence quenching of **PP2**.

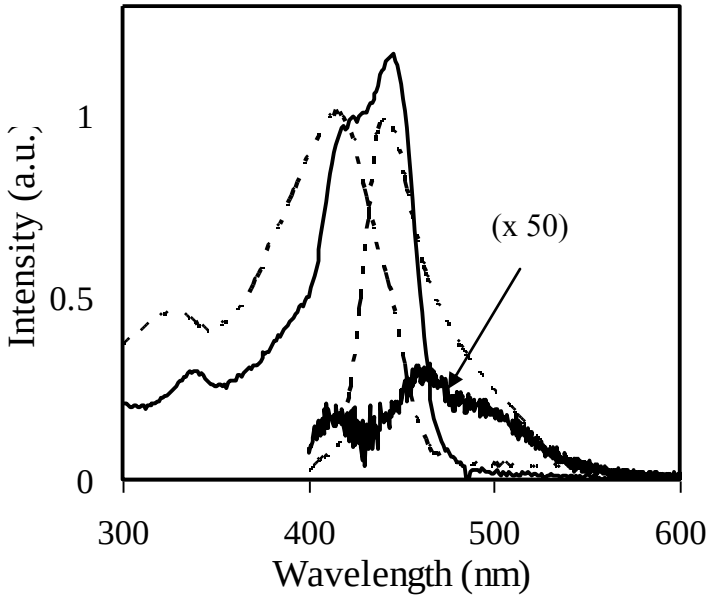

Figure 3.4 Absorption and emission spectra of unaggregated PP2 in water without (— --—) and with 0.4 μM ferric cytochrome-c (—). The emission of PP2 in the presence of 0.4 μM ferric cytochrome-c has been magnified 50 times for clarity.

[1] Ferric cytochrome-*c* was heated to 353 K and then cooled back to room temperature. The denaturation was verified using CD and UV/Vis spectroscopy.

To further investigate the aggregation induced on addition of ferric cytochrome-*c* into **PP2** solution and to explain the appearance of a red shifted peak on addition of ferric cytochrome-*c*, the **PP2**-cytochrome-*c* solution was passed through a 0.25 μm filter and the emission and absorption were recorded again. The absorption was attenuated nearly ten times as compared to **PP2**-cytochrome-*c* solution before filtration. In order to make sure that the attenuation was not coming from **PP2** sticking to the filter, **PP2** in water was passed through 0.25 μm filter. The absorption and emission of **PP2** in water did not change. Hence the **PP2**-cytochrome-*c* solution contains aggregates that are retained by the filter, implying that aggregates > 0.25 μm are formed on addition of micromolar amounts of ferric cytochrome-*c*.

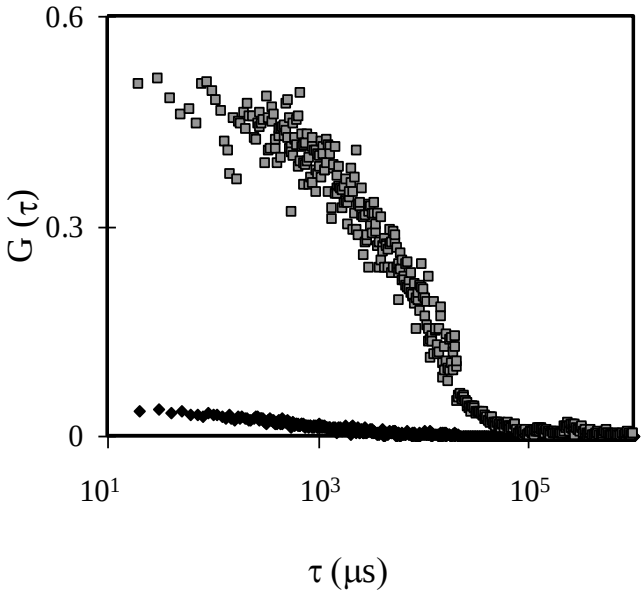

Figure 3.5 Autocorrelation function for PP2 in water (♦) and with 0.4 μM cytochrome-c (■)

To further corroborate the hypothesis of aggregate formation on addition of ferric cytochrome-*c*, FCS studies were performed. Hydrodynamic radius, R_H, was obtained for **PP2** in water using equation 3. In the absence of cytochrome-*c*, **PP2** had a correlation time of 686 μs

and hence R_H of 4.4 nm (η= 0.89 cP and ω_{xy}= 0.39 μm), whereas on addition of 0.4 μM cytochrome-*c* no correlation was observed indicating the presence of very big particles (Figure 3.5). This behavior is similar to the one seen for autocorrelation function of 0.2μm fluorecein beads further corroborating the fact that very large particles are formed.

From the filtration and FCS experiments it is clear that **PP2** forms large aggregates when it interacts with the ferric cytochrome-*c*. Since **PP2** is negatively charged and ferric cytochrome-*c* is positively charged, we conclude that multiple polymer strands interact with the ferric cytochrome-*c* molecules electrostatically which leads to polymer aggregation.

3.3.2 Importance of Electrostatic Binding

The ionic strength dependence implies that electrostatic interactions play an important role in the quenching of the **PP2** fluorescence via aggregation of polymer strands. If this is true, than analyte with higher charge should form even bigger aggregates with **PP2** since it can bring more polymer strands together via electrostatic interaction. To test this hypothesis, quenching experiments with PAMAM 3G and **PP2** were performed. PAMAM 3G is similar in size to ferric cytochrome-*c* (diameter = 3.0 nm), however it has a charge of +32e at neutral pH. On addition of 10 μM PAMAM 3G the absorption spectrum shows a red shifted peak (see figure 3.6A), similar to that seen on addition of ferric cytochrome-*c* indicating aggregates are formed. The fluorescence was also quenched, but by only 30 %, which is smaller than that of ferric cytochrome-*c* (Figure 3.6A). On passing the **PP2**-PAMAM-3G solution through a 0.2 μm filter, the absorbance did not change and the fluorescence also did not change, indicating that any aggregates formed are smaller in size than the 200 nm filter. To further see if there is any

contribution from other factors such as electron transfer since PAMAM-3G has amine groups, quenching experiments were done at pH 2 and pH 4 where even inner amines are charged. The quenching efficiency was found to be the same as that found at pH 7. The quenching experiments were also done at pH 12 where PAMAM-3G is not charged and the surface amine groups might act as electron donors. No quenching was seen at higher pH. These data indicate that the quenching occurs by electrostatic aggregation of **PP2** with PAMAM-3G and it does not involve electron transfer.

FCS experiments were performed to better quantify the size of the aggregates formed on addition PAMAM-3G to **PP2**. Figure 3.6B shows the autocorrelation function for **PP2** in the presence of PAMAM-3G. The correlation time increased by a factor of nearly 1.4 times ($\tau_{PAMAM\text{-}3G}$ = 850 μs, R_H= 6 nm) as compared to **PP2** in water (τ_{H2O} = 640 μs, R_H= 4.4 nm) indicating that

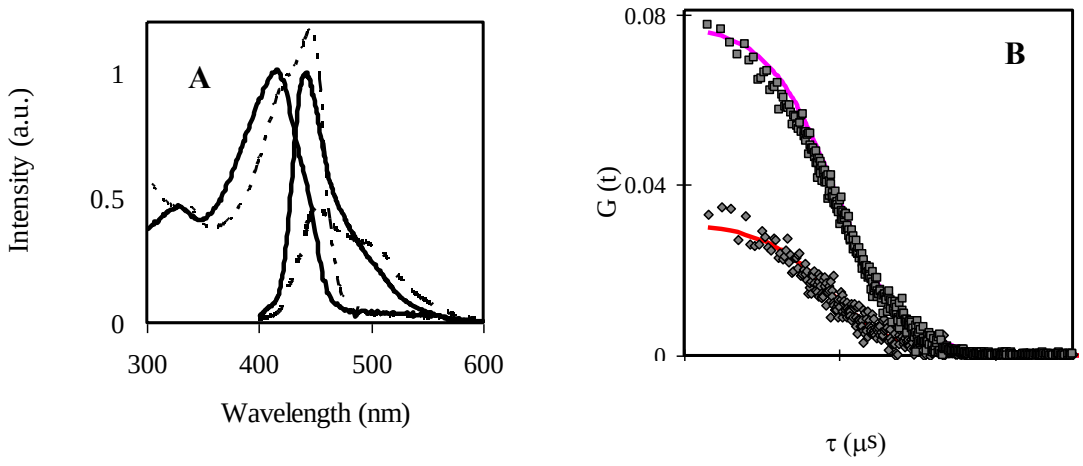

Figure 3.6(A) Absorption and emission spectra of unaggregated PP2 in water (—) and with 10 μM PAMAM-3G (— -- —). (B) Autocorrelation function for PP2 in water (♦) and with 10 μM PAMAM-3G (■)

aggregates are formed on addition of PAMAM-3G, but they are much smaller than those formed by **PP2** in the presence of cytochrome-*c* (> 0.25 μm). Two observations were made for **PP2** in

the presence of 10 μM PAMAM-3G. First that small aggregates are formed and second that fluorescence quenching efficiency is weaker for PAMAM-3G than cytochrome-*c*, presumably because it does not have an energy transfer centre.

3.3.3 Importance of Hydrophobic Interactions

An important difference between PAMAM-3G and ferric cytochrome-*c* is the presence of hydrophobic interactions for ferric cytochrome-*c*. The importance of hydrophobic interactions were explored by performing quenching experiments with PEG-OH which has a hydrophobic core and is neutral (Figure 3.7A). The addition of 50 μM PEG-OH to a ~2 $x10^{-7}$ M solution of **PP2,** which **e**xists as aggregates, appears to create indepedent strands of **PP2** in solution. . On addition of 50 μM PEG-OH, the absorption spectrum red shifts but does not indicate the formation of aggregates species. Also the addition of PEG-OH enhances the fluorescence of **PP2** rather than quenching it (Figure 3.7B). This behavior is similar to what has been observed for **PP2** with octadecyl trimethylammonium bromide (ODTMA) already reported in the literature.[109] Further, FCS studies show that the correlation time increases by a factor of nearly three (τ_{H2O} = 1920 μs, R_H= 13.2 nm), indicating larger particles than are formed in the PAMAM-3G/**PP2** solution. Hence aggregates form but they are not the quenched red emitting homoaggregates of **PP2**. It may be that the addition of PEG-OH forms heteroaggregates between **PP2** and PEG-OH as observed for surfactant ODTMA.

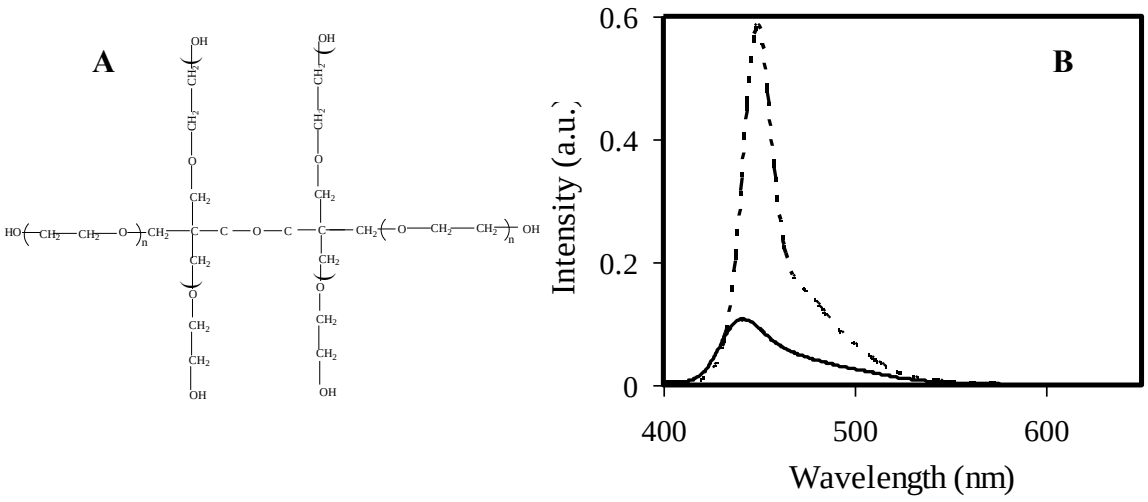

*Figure 3.7 (A)Chemical Strcuture of PEG-OH. (B) Emission spectra of **PP2** without (—) and with 50 μM PEG-OH (— -- —).*

3.3.4 Importance of Hydrophobic and Electrostatic Interactions

In order to probe if hydrophobic and electrostatic interactions play an important role in the interaction between polymer and the analyte, fluorescence quenching experiments were performed in the presence of DEM3.5G. Figure 3.8A shows the chemical structure of DEM-3.5G dendrimer which was used for the quenching experiments. This dendrimer has both a hydrophobic and a charged component.

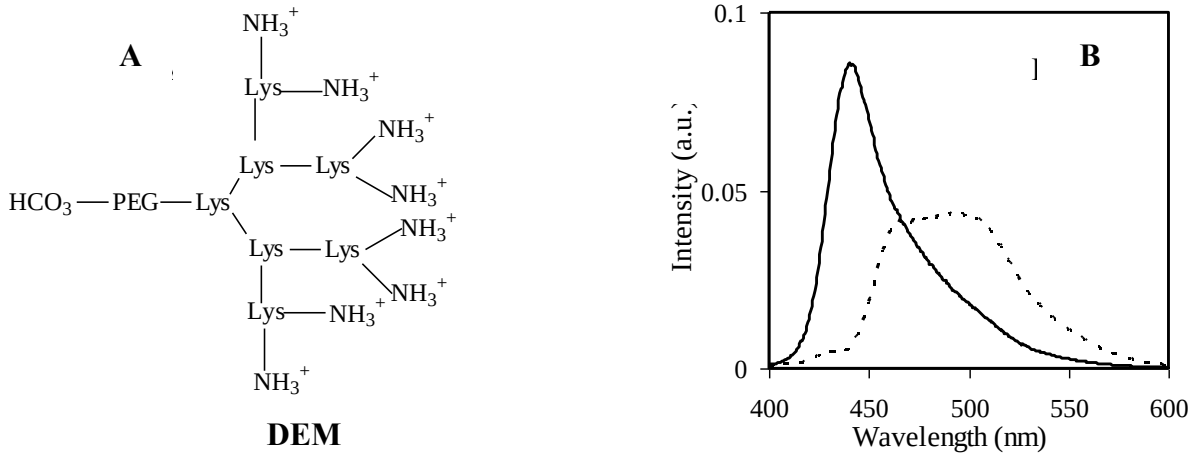

Figure 3.8 ***(A)****Structure of DEM3.5G (****B****) Emission spectra of* ***PP2*** *in water (—) and in the presence of 8.9 mM DEM3.5G (---).*

On addition of 8.9 mM DEM-3.5G to a ~2 x10^{-7} M solution of **PP2**, the emission was quenched by only 20 % but became very broad and displayed a red emission band (Figure 3.8B). A new red-shifted peak was observed in the absorption spectrum, as well. The spectral changes indicate the formation of aggregates. Filtration of the **PP2** solution with 8.9 mM DEM-3.5G caused the fluorescence to decrease by 95 % and the absorbance to attenuate, corroborating the conclusion that large aggregates are formed. As with the ferric cytochrome-*c* system FCS experiments on the aggregates showed large particles but could not be quantified.

3.4 CONCLUSION

These studies show how the interaction between **PP2** and analyte change the optical properties of **PP2**. From the quenching experiments done with the macromolecules ferric cytochrome-*c*, PAMAM-3G and DEM3.5G, it is clear that interaction of these analytes induces

aggregation of **PP2** in aqueous solutions. In the case of the protein ferric cytochrome-*c*, the fluorescence is quenched by 98 % and very big aggregates (>0.25 μm) are formed. The high quenching by ferric cytochrome-*c* results because it induces aggregation and it provides a chromophore that can quench the fluorescence by energy transfer. Contributions from each of these factors were studied by observing the optical properties of **PP2** in the presence of different quenching partners. Experiments with PAMAM-3G and DEM3.5G showed that both electrostactic and hydrophobic interactions are important for inducing aggregation in **PP2**, however these interactions are not sufficient to quench the fluorescence of **PP2** as effectively as ferric cytochrome-*c* where the presence of energy transfer centre makes the fluorescence quenching very efficient. Further it was shown that PEG-OH does not induce aggregatiom of multiple **PP2** strands. It appears that PEG-OH molecules hydrophobically interact with the polymer backbone, dissociating the homoaggregates and enhancing the fluorescence. These studies provide insight into the importance of different kind of interactions that might be responsible for fluorescence quenching of polymer because such multiple interactions will be present for analysis in complex biological systems.

Further these studies show that the sensitivity of **PP2** is also affected by its aggregation state. The polymer is unaggregated at low concentration (~10^{-8} M) and at this concentration the highest Stern-Volmer constant is observed, suggesting that polymer is most sensitive when it is in its unaggregated form. This is further corroborated by the ionic strength dependence studies of Stern-Volmer constant. As the ionic strength increases, the polymer aggregates and the sensitivity decreases indicating polymer is not very sensitive in its aggregated state. This behavior may arise because polymer in unaggregated state can interact more effectively with the quencher i.e. it can wrap around the quencher more easily than when it is in aggregated form.

Similar kinds of behavior was shown by Harrison et al[110] for PPE based conjugated polyelectrolytes but no explanation was provided.

3.5 ACKNOWLEDGEMENT

D.H.W. acknowledges support from the U.S. National Science Foundation (CHE-0415457)

3.6 REFERENCES

(1) Zhang, C.; Broun, D.; Heeger, A. J. *J. Appl. Phys.* **1993**, *73*, 5177.

(2) Hide, F.; Diaz-Garcia, M. A.; Schwartz, B. J.; Andersson, M. R.; Pei, Q.; Heeger, A. J. *Science* **1996**, *273*, 1833-1836.

(3) Yu, G.; Gao, J.; Hummelen, J.; Wudl, F.; Heeger, A. J. *Science* **1995**, *270*, 1789.

(4) Chen, L.; McBranch, D. W.; Wang, R.; Whitten, D. *Chem Phys. Lett.* **2000**, *330*, 27.

(5) DiCesare, N.; Pinto, M. R.; Schanze, K. S.; Lakowicz, J. R. *Langmuir* **2002**, *18*, 7785.

(6) Heeger, P. S.; Heeger, A. J. *Proc. Natl. Acad. Sci. U.S.A.* **1999**, *96*, 12219.

(7) McQuade, D. T.; Pullen, A. E.; Swager, T. M. *Chem Rev* **2000**, *100*, 2537-74.

(8) Tan, C.; Pinto, M. R.; Schanze, K. S. *Chem.Comm.* **2002**, 446.

(9) McQuade, D. T.; Pullen, A. E.; Swager, T. M.; Lacowitz, J. R. *Langmuir* **2002**, *18*, 7785.

(10) Swager, T. M. *Acc. Chem. Res.* **1998**, *31*, 201.

(11) Zhow, Q.; Swager, T. M. *J. Am. Chem. Soc.* **1995**, *117*, 12593.

(12) Pinto, M. R.; Scahnze, K. S. *Proc. Nat. Aca. Sci.* **2004**, *101*, 7505.

(13) Rininsland, F.; Xia, W.; Wittenburg, S.; Shi, X.; Stankewicz, C.; Achyuthan, K.; McBranch, D.; Whitten, D. *Proc. Nat. Acad. Sci.* **2004**, *101*, 15295-15300.

(14) Kim, I. B.; Dunkhorst, A.; Gilbert, J.; Bunz, U. H. F. *Macromolecules* **2005**, *38*, 4560-4562.

(15) Liu, B.; Bazan, G. C. *Chem. Mater.* **2004**, *16*, 4467.

(16) Kumaraswamy, S.; Bergstedt, T. S.; Shi, X.; Rininsland, F.; Kushon, S. A.; Xia, W.; Achyuthan, K.; McBranch, D. W.; Whitten, D. *Proc. Nat. Aca. Sci.* **2004**, *101*, 7511.

(17) Disney, M. D.; Zheng, J.; Swager, T. M.; Seeberger, P. H. *J Am Chem Soc* **2004**, *16*, 13343.

(18) Wosnick, J. H.; Mello, C. M.; Swager, T. M. *J Am Chem Soc* **2005**, *127*, 3400.

(19) Liu, M.; Kaur, P.; Waldeck, D. H.; Xue, C.; Liu, H. *Langmuir* **2005**, *21*, 1687-1690.

(20) Thomas III, S. W.; Joly, G. D.; Swager, T. M. *Chem. Rev.* **2007**, *107*, 1339.

(21) Zhang, T.; Fan, H.; Zhou, J.; Liu, G.; Feng, G.; Jin, Q. *Macromolecules* **2006**, *39*, 7839.

(22) Fan, C.; Plaxco, K. W.; Heeger, A. J. *J Am Chem Soc.* **2002**, *124*, 5642.

(23) Kim, I. B.; Dunkhorst, A.; Bunz, U., H. F. *Langmuir* **2005**, *21*, 7985.

(24) Kim, S.; Jackiw, J.; Robinson, E.; Schanze, K. S.; Reynolds, J. R.; Baur, J.; Rubner, M. F.; Boils, D. *Macromolecules* **1998**, *31*, 964-974.

(25) Kim, I. B.; Dunkhorst, A.; Bunz, U., H. F. *Langmuir* **005**, *21*, 7985-7989.

(26) Lacowitz, J. R. *Principles of Fluorescence Spectroscopy,Plenum Press NY* **1983**.

(27) Liu, M.; Waldeck, D. H.; Oliver, A. M.; Head, N. J.; Paddon-Row, M. N. *Journal of the American Chemical Society* **2004**, *126*, 10778-10786.

(28) Koppel, D. E. *Physical Review A* **1974**, *10*, 1938-1945.

(29) Magde, D.; Elson, E.; Webb, W. W. *Physical Review Letters* **1972**, *29*, 705-708.

(30) Pristinski, D.; Kozlovskaya, V.; Sukhishvili, S. A. *Journal of Chemical Physics* **2004**, *122*, 14907-14907.

(31) Van Rompaey, E.; Sanders, N.; Van Craenenbroeck, E.; Engelborghs, Y.; De Smedt, S. C.; Demeester, J. *Macromolecules* **2000**, *33*, 8280-8288.

(32) Leng, X. S., K.; Buffle, J. *J.Coll. Inter. Sci.* **2002**, *251*, 64.

(33) Yue, H.; Waldeck, D. H.; Xue, C.; Liu, H. *Manuscript in preparation*.

(34) Krichenvsky, O.; Bonnet, B. *Rep.Prog.Phys.* **2002**, *65*, 251-297.

(35) Culbertson, C. T.; Jacobsen, C. S.; Ramsey, J. M. *Talanta* **2002**, *56*, 365-373.

(36) Kaur, P.; Yue, H.; Wu, M.; Liu, M.; Treece, J.; Waldeck, D. H. *J. Phys. Chem. B* **2007**, *DOI: 10.1021/jp071307o*.

(37) Bunz, U. H. F. *Chem. Rev.* **2000**, *100*, 1605-1644.

4.0 EVOLUTION IN THE COMPLEXES BETWEEN POLY (PHENYLETHYNYLENE) BASED POLYELECTROLYTES AND OCTADECYL TRIMETHYLAMMONIUMBROMIDE AS REVEALED BY FLUORESCENCE CORRELATION SPECTROSCOPY

This work has been published as Hongjun Yue, Mingyan Wu, David H. Waldeck, Cuihua Xue, and Haiying Liu, J. Phys. Chem. B.; (2008); 112, 8218-8226. Thesis author synthesized the polymers and did some spectroscopic measurements with the first author.

Abstract

Poly (phenylethynylene) based conjugated polyelectrolytes are a class of polyions having rigid backbones. We present an FCS study on the hydrodynamic properties of complexes formed by two PPE-SO_3^- polymers, having different charge density, with octadecyl trimethylammoniumbromide (OTAB) below the critical micelle concentration. The ratio concentration ration C_{OTAB} /$C_{monomer}$ ranges from 0.2 to 1800 in this work. The hydrodynamic radius of the complexes as a function of OTAB concentration has three regimes. In the low concentration regime, (C_{OTAB} /$C_{monomer}$ < 6), the complex has a comparable size with the polymer in deionized water. In the intermediate concentration regime (6 <C_{OTAB} /$C_{monomer}$ < 400) the complexes have the largest size and substantial heterogeneity. In the high concentration regime (400 <C_{OTAB} /$C_{monomer}$ < 1800), the complexes have a size that is about three time larger than that

in low concentration regime. The results significantly extend the understanding of the interaction between polyelectrolyte and ionic surfactant, and indicate that the rigidity of polymer backbone and C_{OTAB} /$C_{monomer}$ concentration ratio act to determine the composition of polyelectrolyte/surfactant complexes.

4.1 INTRODUCTION

Conjugated polymers have attracted extensive research interest because of their unique optical and electronic properties.[1-8] PPEs respond to other solutes by a change of their fluorescence intensity and have been investigated as fluorescent sensory materials.[9-17] By side chain functionalization, their properties (hydrophobicity, polarity of charge, charge density, and the solubility) can be tailored for particular purpose.[18-22] Poly (phenylethynylene) (PPE) is a linear semiflexible conjugated polymer,[23,24] which has a persistence length of 10 ~ 15 monomer units (consisting of one phenyl ring and one carbon-carbon triple bond),[25] and displays absorption and emission in the visible range.[8,19,20] The photophysical properties of functionalized PPE depends on the side chain configuration and the different solution conditions.[19,20,26,27] With certain hydrophobicity and charge properties of the side chain, the propensity of polymers to stay in single strands or aggregate in a particular solvent can be manipulated.[28]

This work reports on the hydrodynamic properties of two PPE-SO_3^- polymers with different charge densities in the presence of a cationic surfactant octadecyl trimethylammoniumbromide (OTAB). In particular, the high sensitivity of fluorescence correlation spectroscopy (FCS) is used to obtain hydrodynamic information about the complexes over a wide range of charge ratio of surfactant to polymer from 0.1 to 900. The interaction between polyelectrolytes and

surfactants are an essential self-assembly motif and are important to industrial and biomedical applications.[29-36] Depending on the polyelectrolyte and surfactant properties, their concentrations, and solvent type, polyelectrolyte/surfactant complexes take a variety of morphologies, including single molecular substoichiometric complexes in aqueous solution,[37] stoichiometic complexes in nonaqueous solution,[31,37] polymer/micelle complexes,[34,38] vesicles, and liquid crystals.[29,32,34]

The effects of ionic surfactant on the photophysics of conjugated polyelectrolytes based on poly (phenylenevinylene),[39-43] polythiophene,[44] and others[45,46] have been studied. A substoichiometric amount of ionic surfactant with opposite charge to that of the conjugated polyelectrolyte is able to significantly increase its photoluminescence quantum yield and shift the emission spectra by either preventing interchain aggregation or extending the polymer's conjugation length.

PPE based polyelectrolytes have a rigid backbone structure with a long persistence length which spans 10 to 15 repeated units.[25] PPE complexes have been explored for a variety of applications, such as optoelectronic devices,[47,48] structure-directing agents,[49] and biosensors.[50-52] The solid state structure of stoichiometric complexes was studied using wide- and small-angle X-ray scattering.[47,48] A lamellar structure made up of alternative polymer rich layers (1.16 nm) and surfactant alkyl layers (1.86 nm) were found.[48] Literature reports of the effects of surfactant on the fluorescence of PPE [50-52] shows that the interactions between PPE and surfactant is complicated. The structure of complexes with stoichiometric ratio other than 1:1 is not well addressed, and the composition of the complexes as a function of surfactant concentration is not fully understood. PPE polyanions resemble double stranded DNAs in their rigidity of the polymer chain; dsDNA has a persistence length of 60 nm.[53,54] An in-depth understanding of the

interaction between negatively charged PPE polyanions with charged and uncharged amphiphilic molecules has significant biological implications, especially in nonviral gene delivery realized by the complexes of DNA with cationic lipids[55-59]

A variety of techniques, such as fluorescence spectroscopy,[28] wide- and small-angle X-ray scattering,[47,48] small angle neutron scattering,[43,46] light scattering,[60] zeta potential measurements,[28] isothermal calorimetry,[61,62] and FCS[46,63] have been used to study polyelectrolyte/surfactant interactions. FCS is a non-invasive method that provides dynamic and kinetic information by following the fluorescence fluctuation trajectory near the equilibrium state.[64,65] Analysis of the fluctuations yields information about the diffusion and photophysical and photochemical processes. The FCS technique has been widely employed in the life sciences[66] and to study chromophore labeled polymers.[67,68] PPE polymers are intrinsically fluorescent, FCS can be directly applied to it, however such applications are rare in the literature.

This work presents an FCS study on the hydrodynamic properties of complexes formed by OTAB with two PPE-SO_3^- polymers having different charge density and below the critical micelle concentration. The ratio C_{OTAB} /$C_{monomer}$ (C is in unit of M) ranges from 0.2 to 1800. The hydrodynamic radius of the complexes as a function of OTAB concentration shows three regimes. When C_{OTAB} /$C_{monomer}$ < 6, the complexes have comparable size with the polymer in deionized water and are single strand substoichiometric complexes. When 6 <C_{OTAB} /$C_{monomer}$ < 400, a variety of complexes sizes are measured. These large complexes are likely comprised of multiple strands of complexes held together by the hydrophobic interactions of the alkyl chains in OTAB molecules. When 400 <C_{OTAB} /$C_{monomer}$ < 1800, the complexes are high soluble, well defined, and have a size that is about three times larger than that in low concentration regime and much smaller than that in the intermediate regime. These complexes appear to have a single

polymer chain binding with two layers of OTAB. The inner layer of OTAB interacts with PPE-SO_3^- through electrostatic forces and with the second layer of OTAB through the hydrophobic interactions. The outer layer of OTAB contacts the water with the ionic head groups. The complexes formed between PPE-SO_3^- and OTAB below the CMC[69] and the CAC[29] revealed by FCS significantly extends the understanding of the interaction between polyelectrolytes and ionic surfactants. The observation that the complex containing two layers of OTAB exists below the CMC indicates that the ratio C_{OTAB} /$C_{monomer}$ might be a controlling factor in determining the composition of polyelectrolyte/surfactant complexes.

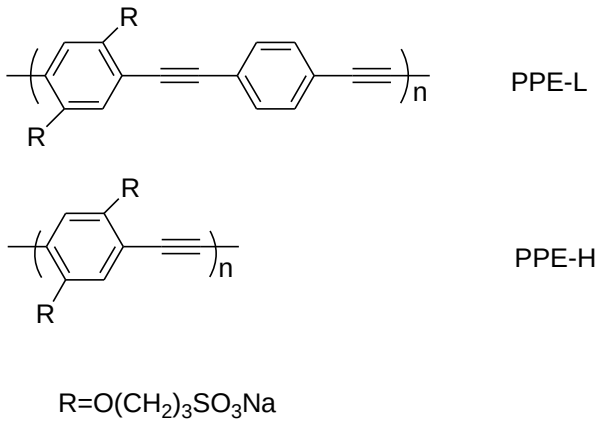

Scheme 4.1 Molecular structure of the functionalized conjugated poly(phenylethylnylene)

4.2 EXPERIMENTAL

Materials. Water used in all experiments was purified by Barnstead-Nanopure system and its resistance was 18.2 MΩ. Two PPEs, labeled as **PPE-L**, **PPE-H**, having structures as shown in Scheme 7.1, were synthesized at Michigan Technological University. The synthesis procedures for these polymers were previously report.[9-12] Octadecyl trimethylammoniumbromide (OTAB),

Octadecyl Sulfate Sodium Salt (ODSS) and all other chemicals were bought from Sigma and were used as received.

Instrumentation. A home made FCS instrument was constructed by modifying a Zeiss IM 35 inverted microscope (See Scheme 7.2). The excitation source is a single wavelength (438 ± 3 nm) solid state diode laser (iBeam 440). The laser beam was coupled to the microscope by a

single-mode optical fiber (A) which acts as a spatial filter and a beam expander. The dichroic mirror(C) reflects the laser beam and allows fluorescence to pass through. The laser beam is then focused by an objective lens (B) (Olympus UPlanfluor 40X/1.30 oil) into a volume of femtoliter size in the sample (S). By the same objective, the fluorescence was collected. The scattered laser light was blocked by an emission filter (D). At the other port of the microscope, the fluorescence was focused and coupled to a photon counting Avalanche Photodiode (APD) through a pinhole (of 100 μm in diameter) (E). In this confocal arrangement only the fluorescence from the objective's focal point is detected by the APD. The signal form the APD provides a fluorescence versus time trajectory and is processed by an autocorrelator (BI-9000, Brookhaven Instrument Co.) to generate an autocorrelation function. The autocorrelation function is fit by a model to provide a correlation time for the dynamic or kinetic process.

FCS Theory. At the objective focal point, the intensity of the excitation light has a Gaussian distribution, and the illumination profile defined by a confocal configuration is approximately expressed as

$$I = I_0 \exp\left(-\frac{2\left(x^2 + y^2\right)}{\omega_{xy}^2}\right)\exp\left(-\frac{2z^2}{\omega_z}\right) \qquad (4.1)$$

where I_0 is the intensity at the geometric center of the illumination spot; x and y are displacements perpendicular to the optical axis, z is the displacement along the optical axis; ω_{xy} and ω_z characterize the illumination volume of the excitation light.

The normalized autocorrelation function $G(\tau)$ is defined as

$$G(\tau) = \frac{1}{\bar{I}^2 T}\int_0^T \delta I(t)\delta I(t+\tau)dt = \frac{\langle \delta I(0)\delta I(\tau)\rangle}{\langle I(0)\rangle^2} \tag{4.2}$$

where I is the fluorescence intensity, δI is fluorescence fluctuation, t is the experimental time coordinate, τ is a delay time, and T is the total experimental time. In the limit that diffusion is the only cause of fluorescence fluctuations, the correlation function may be written as

$$G(\tau) = \frac{1}{\bar{N}}\left(1+\frac{\tau}{\tau_D}\right)^{-1}\left(1+\frac{\tau}{\omega^2\tau_D}\right)^{-1/2} \tag{4.3}$$

where $\bar{N}$ is the average number of fluorescent molecules in the illuminated volume, τ_D is the correlation time, and ω is defined as

$$\omega = \frac{\omega_z}{\omega_{xy}} \tag{4.4}$$

The correlation time τ_D is given by

$$\tau_D = \frac{\omega_{xy}^2}{4D} \tag{4.5}$$

where D is the diffusion coefficient. The diffusion coefficient of a spherical particle can be estimated by Stokes-Einstein equation.

$$D = \frac{k_B T}{6\pi\eta R} \tag{4.6}$$

where k_B is the Boltzmann constant, T is the temperature, η is the viscosity of solution, and R is the hydrodynamic radius of the molecule.

The time average of the fluorescence intensity is determined by

$$\bar{I} = \frac{1}{T}\int dr^3 I(r)\int dt[Q \cdot C(r,t)] \tag{4.7}$$

where *T* is the experiment duration; *I(r)* is the spatial distribution of the illumination intensity, which can be approximated by Equation 7.1; *Q* is the effective fluorescence efficiency determined by the absorbance cross section, the fluorescence quantum yield, instrument setup and the detection efficiency. *C(r,t)*, the instantaneous concentration at the point r, can be written as a constant concentration *C* plus a fluctuation term $C(r,t) = C + \delta C(r,t)$. If the experimental time is long enough, the time average of the fluctuation term dies out.

FCS Experiments. The instrument was calibrated with dyes whose diffusion coefficients are known. 10 nM Rhodamine 6G ($D = 4.27\times10^{-6}$ cm^2 s^{-1})[70] and 10 nM fluorescein ($D = 4.14\times10^{-6}$ cm^2 s^{-1})[70] were used. The ω_{xy} was measured to be 0.39 μm and ω was 15. The concentrations of the polymer solutions were controlled to be 10^{-4} mg/ml or lower depending on the quantum efficiency of the fluorescence. To avoid photobleaching and optical trapping, the laser power was kept as low as 24 μW. The autocorrelation function was collected for 2 to 5 min. The time trajectory of fluorescence was monitored and was fitted by Equation 7.3 using a Levenberg-Marquardt algorithm.

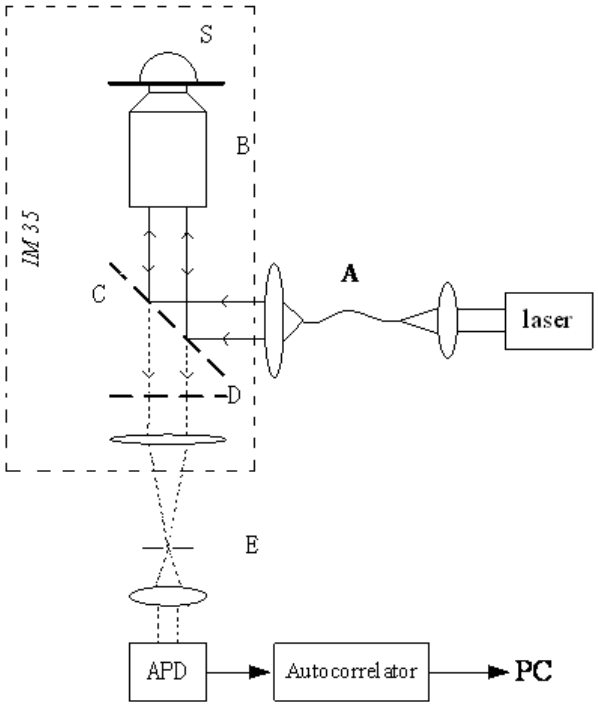

Scheme 4.2 Schematic representation of the FCS instrument (see text for details).

4.3 RESULT

At high concentrations, PPE-SO_3^- aggregates in aqueous solution, hence the concentration of **PPE-L** and **PPE-H** were maintained as low as 2.8×10^{-5} mg/ml and 2.1×10^{-5} mg/ml respectively. The solutions are 1~2 nM in polymers, or 0.050 μM monomer units and 0.10 μM in negative charges, assuming that all of the sulfonate groups on the side chains are ionized. At such low concentrations, the polymers are in a single strand state, i.e. not aggregated.[28] The emission spectra show features belonging to unaggregated polymer in "good" solvent, and the hydrodynamic radius R_H measured with FCS are significantly smaller than that of polymer at a higher concentration.[28] For **PPE-L** the molecular weight M_w is around 20 kDa

and R_H is 2.6 ± 0.3 nm calculated from a correlation time of 498 ± 51 μs and a diffusion coefficient of (7.9 ± 0.8) × 10^{-7} cm^2 s^{-1}. For **PPE-H** the molecular weight M_w is around 10 kDa. and R_H is 1.6 ± 0.2 nm calculated from a correlation time of 299 ± 39 μs and a diffusion coefficient of (1.3 ± 0.2) × 10^{-6} cm^2 s^{-1}.

4.3.1 FCS Measurement

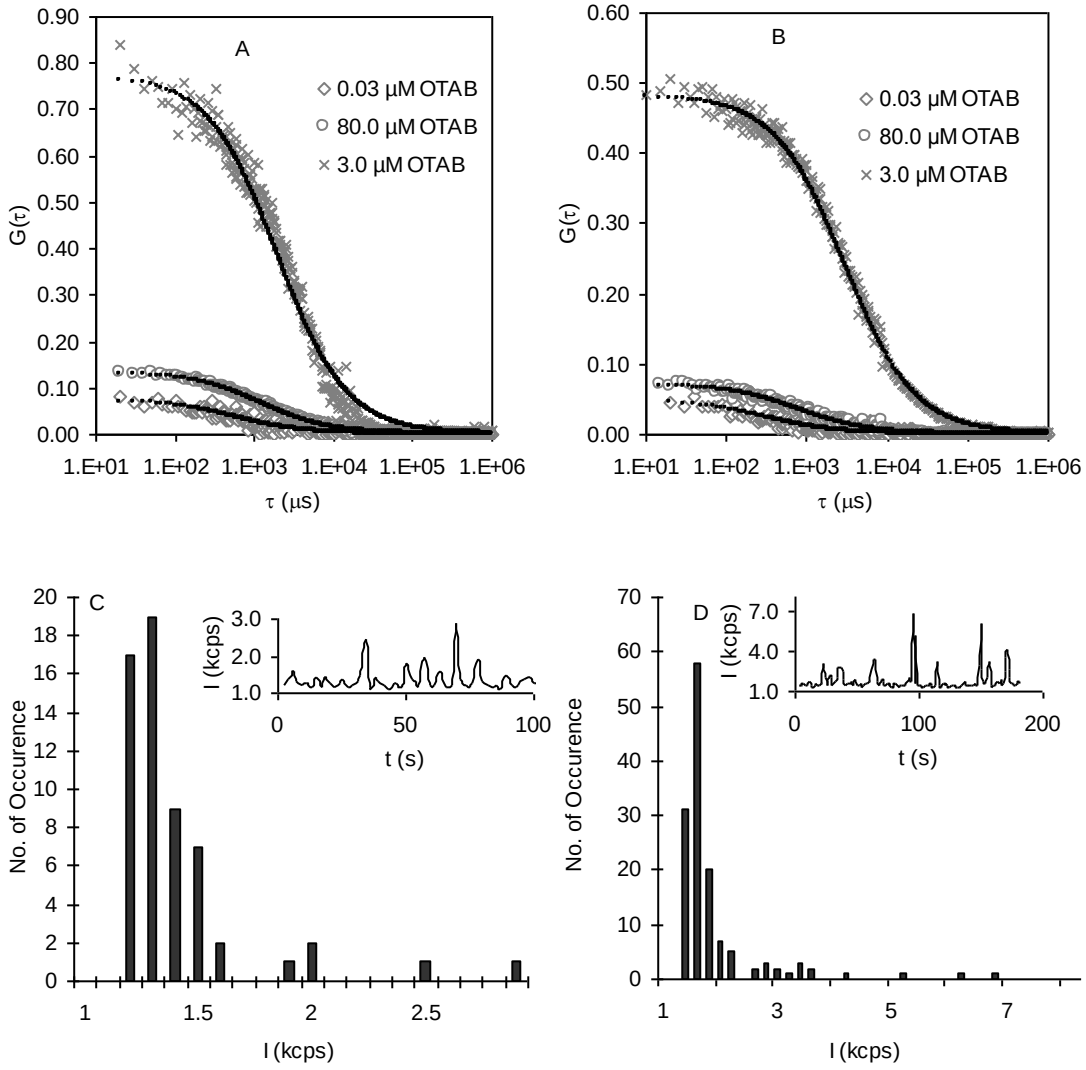

*Figure 4.1 A) Autocorrelation functions of 2.8 ×10^{-5} mg/ml **PPE-L** in three different solution conditions; B) Autocorrelation functions of 2.1 ×10^{-5} mg/ml **PPE-H** in three different solution conditions; C) The photon counting rate histogram of 2.8 ×10^{-5} mg/ml **PPE-L** in 1.0 μM OTAB aqueous solution; D) The photon counting rate histogram of 2.1 ×10^{-5} mg/ml **PPE-H** in 1.0 μM OTAB aqueous solution, insets are the time trajectory of the photon counting rate.*

When photophysical and photochemical processes, such as photobleaching, singlet-triplet transitions and photoinduced isomerization are negligible, the autocorrelation function measured by FCS for a single fluorescent species can be described by Equation 7.3. The fluctuation of the fluorescence intensity is approximately attributed to the polymer's diffusion into and out of the illumination volume. Fitting of the autocorrelation function to a diffusion model yields the correlation time which is determined by the diffusion constant of the fluorescent molecules. **PPE-L** has ca. 80 monomer units and **PPE-H** is ca. 50 monomer units estimated from the molecular weight of these polymer and corresponding monomers. PPE polymers have a persistence length of 10 to 15 monomer units (containing a phenyl ring and a carbon-carbon triple bond).[25] The contour length of **PPE-L** and **PPE-H** are much longer that persistence length, and they have semiflexible structures. In this work, the Stokes-Einstein equation is used to calculate a hydrodynamic radius for **PPE-L** and **PPE-H** in solution, which can then be compared in a relative way for different OTAB concentrations or compared to a more detailed physical model.

In experiments, only the autocorrelation functions from those measurements showing a stable average fluorescence intensity were used to calculate a correlation time. Figure 4.1A shows autocorrelation functions obtained for **PPE-L** in 0.03 μM, 3.0 μM, 80.0 μM OTAB solutions and the fitting of each by Eqn.3. In the presence of 0.03 μM OTAB, which is lower

than the molarity of 0.05 μM **PPE-L**, the experimental autocorrelation function was well described by Eqn 3 with a correlation time of 573 ± 41 μs. The diffusion coefficient calculated using Eqn 5 was (8.6 ± 1.2) × 10^{-7} cm^2 s^{-1} and the hydrodynamic radius calculated using Eqn 6 was 2.5 ± 0.4 nm. These values were not significantly different from those of **PPE-L** in deionized water. In the presence of 3.0 μM OTAB, which is 60 times higher than the molarity of **PPE-L**, the experimental autocorrelation function yielded a correlation time of 2040 ± 43 μs. The corresponding diffusion coefficient was (1.9 ± 0.5) × 10^{-7} cm^2 s^{-1} and the hydrodynamic radius was 12.6 ± 4.5 nm. Under these solution conditions, the fitting quality was poor at the tail of the autocorrelation function and parallel measurements gave a wide distribution of correlation time indicating that a wide range of particle sizes exist. In the presence of 80.0 μM OTAB which was 1600 times higher than the molarity of **PPE-L** 0.05 μM, the experimental autocorrelation function is well fitted by Eqn 3 yielding a correlation time of 1254 ± 12 μs. The corresponding diffusion coefficient is (3.10 ± 0.05) × 10^{-7} cm^2 s^{-1} and the hydrodynamic radius is 6.58 ± 1 nm.

The autocorrelation functions measured for **PPE-H** in 0.03 μM, 3.0 μM, 80.0 μM OTAB solutions and the fitting of each curve are shown in Figure 4.1B. In the presence of 0.03 μM OTAB, the experimental autocorrelation function is well fitted by Eqn 3, yielding a correlation time of 324 ± 25 μs. The diffusion coefficient calculated using Eqn 5 is (1.2 ± 0.2) × 10^{-6} cm^2 s^{-1} and the hydrodynamic radius calculated using Eqn 6 is (1.7 ± 0.2) nm. These values are not significantly different from those of **PPE-H** in deionized water. In the presence of 3.0 μM OTAB which was 60 times higher than the molarity of **PPE-H**, fitting to the experimental autocorrelation function yielded a correlation time of 3066 ± 30 μs. The corresponding diffusion coefficient was (1.23 ± 0.04) × 10^{-7} cm^2 s^{-1} and the hydrodynamic radius was 16.4 ± 0.6 nm. Under these solution conditions, the autocorrelation function was well fitted by Eqn 3. In the

presence of 80.0 μM OTAB which is 1600 times higher than the molarity of **PPE-H** 0.05 μM, the autocorrelation function is well described by Eqn 3 with a correlation time of 798 ± 20 μs. The corresponding diffusion coefficient was (4.9 ± 0.2) × 10^{-7} cm^2 s^{-1} and the hydrodynamic radius was 4.1 ± 0.2 nm.

In the OTAB concentration ranges of 0.01~0.3 μM and 5.0 ~ 80 μM, the experimental autocorrelation functions are described well by a single diffusing species and provide highly reproducible fitting parameters. When the OTAB concentration was in the range of 0.3 ~ 5.0 μM, however, only a few well defined autocorrelation functions were obtained from the FCS trajectories. Often times, the fluorescence time trajectory showed spikes, with a stable baseline, see the insets of the Figure 4.1C and 4.1D for **PPE-L** and **PPE-H** in 1.0 μM OTAB solution. The histograms for these two measurements are shown in Figure 4.1C and 4.1D and suggest that most of the counting history has a narrow distribution of fluorescence events. No autocorrelation function was obtained from these events; they appear as a random background noise. Whenever a spike appeared, an autocorrelation function was obtained. However these autocorrelation functions did not have well a defined shape (such as a magnitude of more than 1, broken or having a sharp peak) and no reliable fitting could be obtained from them. The low probability events in figure 4.1C and 4.1D are attributed either to particles of different size diffusing through the illumination volume or to the particles of comparable size diffusing through the illumination volume by a different trajectory. The spike was indeed fluorescence rather that scattered excitation light because no such spike, or strange autocorrelation function was obtained for a scattering sample (a $BaSO_4$ suspension in DI water). These rare events, fluorescent spikes and ill-shaped autocorrelation function, are attributed to large particles that pass through the

illumination volume in a random trajectory. A diluted suspension of fluorescent beads of 0.1 μm and 2.0 μm in diameter show the same type of behavior.

In summary, for the OTAB concentration ranges of 0.01~0.3 μM and 5.0 ~ 80 μM, the FCS gives rise to reliable measurements and produces information on the diffusion constant and the hydrodynamic radius of the polymer. For the OTAB concentration range of 0.3 ~ 5.0 μM, the FCS measurement could be used to detect the existence of large particles, but could not provide accurate information on the particle size. The radii reported in this concentration regime should not be taken as accurate values, but rather as an indicator that very large particles are present in solution.

4.3.2 Dependence of Polymer Size on the Concentration of Surfactant

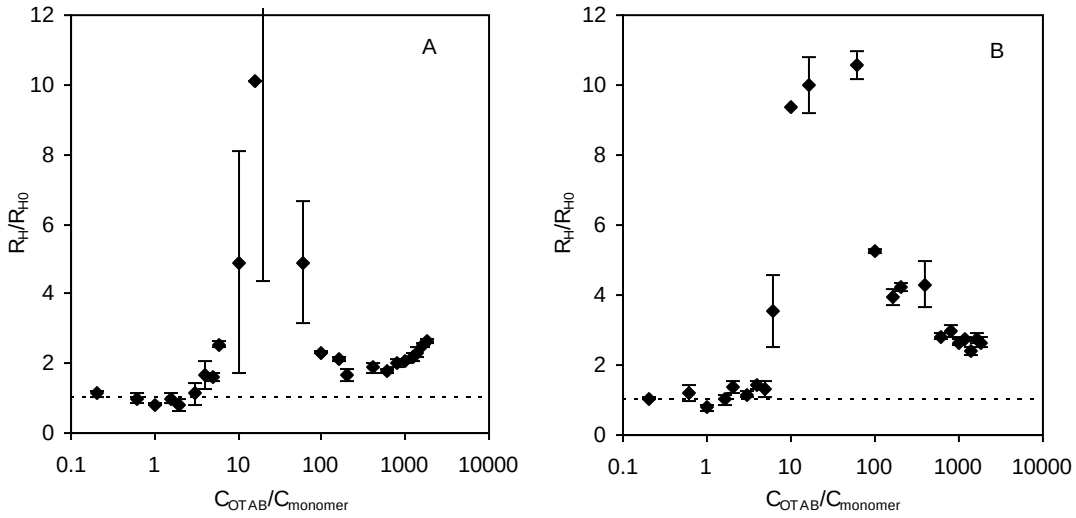

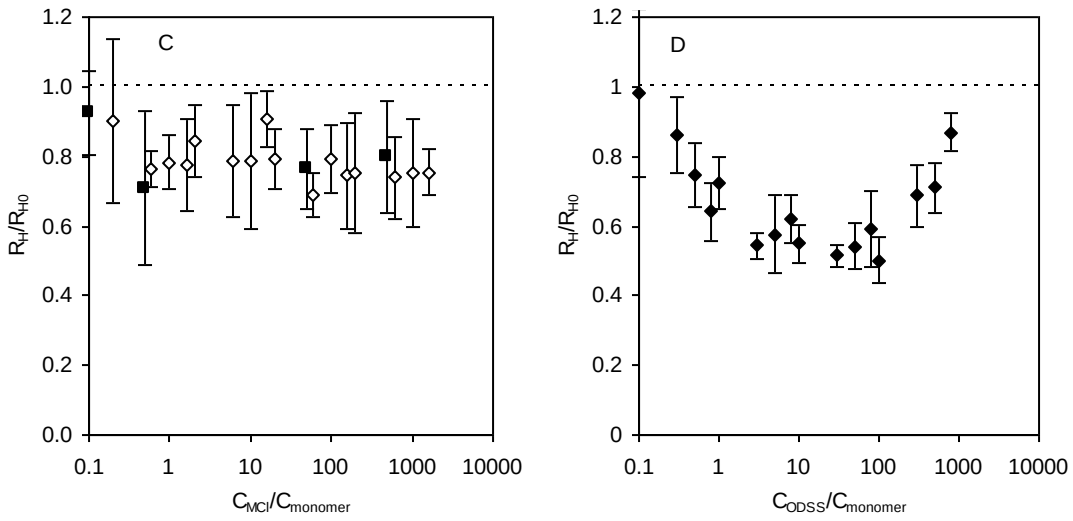

*Figure 4.2 The hydrodynamic radius (R_H) ratio of polymer as a function of solution conditions, R_{H0} represents the hydrodynamic ratio of polymer in deionized water shown in dashed lines in each plot; A)2.8 ×10^{-5} mg/ml **PPE-L** in OTAB aqueous solutions; B) 2.1 ×10^{-5} mg/ml **PPE-H** in OTAB aqueous solutions; C) 2.8 ×10^{-5} mg/ml **PPE-L** in NaCl (solid square)and KCl (blank diamonds) solutions D) 2.8 ×10^{-5} mg/ml **PPE-L** in ODSS solutions.*

It is known that a negatively charge polyelectrolyte and cationic surfactant form electrostatic complexes (Reference 31 and references therein). In this work, the hydrodynamic radius of **PPE-L**/OTAB and **PPE-H**/OTAB complexes were measured as a function of the concentration of OTAB, which was varied from 0.01 μM to 90 μM, about four orders of magnitude. Because the FCS correlation time changes with solution viscosity, the diffusion constant of Coumarin 334 was measured over this OTAB concentration range also. The diffusion coefficient of the dye showed no dependence on the OTAB concentration, indicating that the viscosity change caused by the presence of up to 90 μM OTAB was negligible. Because of the high sensitivity of FCS, the **PPE-L** and **PPE-H** concentration could be controlled as low as 0.05 μM monomer unit or 0.1 μM side chain charges. Such low concentrations of **PPE-L** and **PPE-H** allowed concentration ratios of OTAB to monomer unit ($C_{OTAB}/C_{monomer}$) up to 1800:1 and the

molar ratio of OTAB to the side chain charge of the polymer (C_{OTAB}/C_{charge}) up to 900:1 to be accessed while keeping the OTAB concentration much lower than its critical micelle concentration (CMC) 0.3 mM.[69] Under these conditions both the polymer and the surfactant could be treated as free molecules before mixing, greatly reduced the complexity of the system.

The hydrodynamic radius of **PPE-L**/OTAB and **PPE-H**/OTAB complexes as a function of the molar ratio of OTAB and monomer unit had an "Ω" shape as shown in Figure 4.2A and 7.2B. Three regimes can be identified from these plots.(1) A low concentration regime, where the molarity of OTAB varied from 0.01 μM to 0.3 μM, corresponding to a $C_{OTAB}/C_{monomer}$ range from 0.2 to 6.0 and a C_{OTAB}/C_{charge} range from 0.1 to 3.0. In this regime, the measured R_H shows little dependence on the OTAB concentration and is comparable to the size of the polymer in deionized water. (2) A medium concentration regime, where the molarity of OTAB varies from 0.3 μM to 20 μM, corresponding to a $C_{OTAB}/C_{monomer}$ range from 6 to 400 and a C_{OTAB}/C_{charge} range from 3 to 200. In this regime, the R_H, presumably of PPE/OTAB complexes, first increase and then decrease with increasing OTAB concentration. Near the turning point of the curve where the concentration of OTAB was 1.0 μM, the hydrodynamic radius becomes much larger than 10 times that of PPE in deionized water, too large to be accurately measured by FCS; it is indicated in Figure 4.2A an 7.2B with large error bars. (3) A high concentration regime, where the molarity of OTAB varies from 20 μM to 90 μM, corresponding to a $C_{OTAB}/C_{monomer}$ range from 400 to 1800 and a C_{OTAB}/C_{charge} range from 200 to 900. In this regime, the complexes formed from **PPE-L** and **PPE-H** show a different trend. For **PPE-L**, the polymer of low charge density, the hydrodynamic radius increases with increasing OTAB concentration, whereas for **PPE-H** the polymer of high charge density, the hydrodynamic radius shows little dependence on OTAB concentration.

The large particles detected in PPE/OTAB system can be attributed to the aggregation of water insoluble stoichiometric complexes. However the $C_{OTAB}/C_{monomer}$ at which these particles start to appear is 6.0 not a equimolar ratio as suggested in the literature.[31,37] Ionic strength can have multiple effects on the cooperative binding of surfactants to polyelectrolytes, including a reduction of binding strength because of the screening effects but an enhanced hydrophobic binding.[29] The delayed appearance of the stoichiometric complex might arise from the ionic strength created by the counter ions of the polyelectrolyte.[29]

As comparison, the hydrodynamic radius of **PPE-L** was measured in NaCl, KCl and the anionic surfactant ODSS solutions. The concentration of these solutions was controlled in the same way as in PPE/OTAB experiments. The results are shown in Figure 4.2C for NaCl and KCl. The presence of a monovalent salt slightly decreases the **PPE-L** size, however the polymer hydrodynamic radius shows little dependence on the concentration of the salt. Figure 4.2D shows the result for ODSS, in which the R_H of **PPE-L** first decreases and then increases as the concentration of ODSS increases. Comparing the behavior shown in Figure 4.2A and 4.2B with that shown in Figure 4.2C and 4.2D, it can be conclude that the "Ω" curves were unique for the PPE/OTAB system.

4.3.3 The Average Number of Molecules

Another parameter, which can be obtained from fitting Eqn. 3 to an autocorrelation function is $\bar{N}$, the time average of the number of molecules in the illumination volume determined by $\bar{N} = C \cdot V$, where V is the confocal volume and C is the concentration. $\bar{N}$ is plotted in Figure 4.3A as a function of surfactant concentration. In contrast to the "Ω" shaped hydrodynamic

radius curves in Figure 4.2A and 4.2B, the $\bar{N}$ curves are vertically inverted and have a "v" shape. These curves can also be divided into three regimes according to those found in Figure 4.2A and 4.2B. In the low OTAB concentration regime the average number of particles shows little dependence on the surfacant concentration and was comparable to that of the polymer in deionized water. In the medium OTAB concentration regime, the number of particles sharply decreases with the increase of the surfactant concentration to a value that is almost zero and then increases with the increase of the OTAB concentration. The turning point, where few particles are detected, has a concentration around 1.0 μM; exactly the same value at which very large particles are detected in solution. The lower particle number and larger particle size correlation suggests an aggregation and even precipitation of PPE/OTAB complexes.

In the high OTAB concentration regime, the complex formed from **PPE-L** and **PPE-H** show different trends. For **PPE-L**, the polymer of low charge density, the number of **PPE-L**/OTAB particles reaches a plateau while the size of the complex increases with an increase of

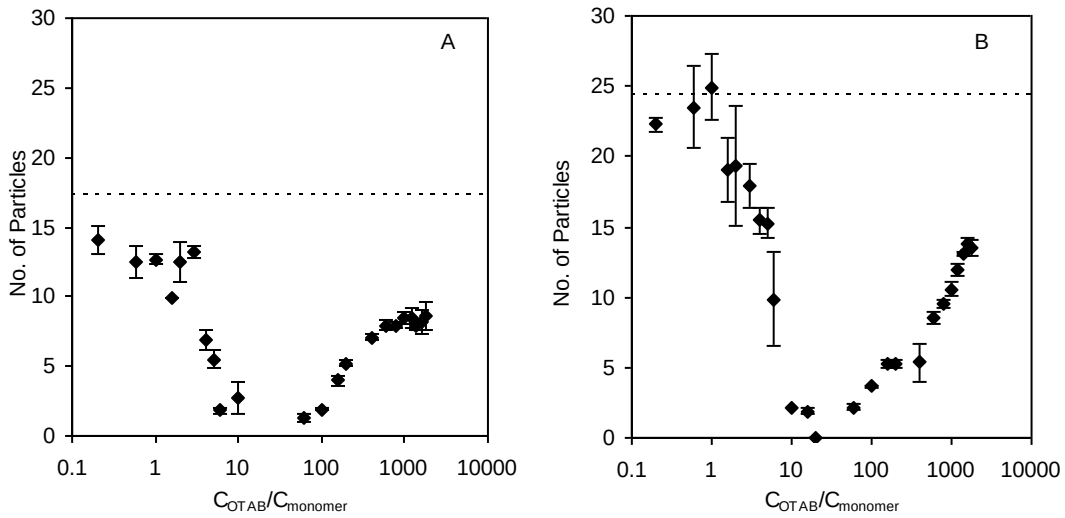

*Figure 4.3 The average number of particles as a function of solution conditions, A)2.8 ×10^{-5} mg/ml **PPE-L** in OTAB aqueous solutions; B) 2.1 ×10^{-5} mg/ml **PPE-H** in OTAB aqueous solutions.*

OTAB concentration (Figure 4.2A and 4.3A). For **PPE-H**, the polymer of high charge density, the number of **PPE-H**/OTAB particles increases with the increase of OTAB concentration while the complex size shows little dependence on OTAB concentration (Figure 4.2B and 4.3B).

4.3.4 The Fluorescence Intensity as a Function of Concentration of Surfactant

In the long time limit, the concentration dependence of the intensity yields information on the effective fluorescence efficiency. In the FCS measurement, the power of the diode laser and other feature of the instrumental configuration were kept the same for all of the measurements. Each experiment lasted for hundreds of seconds. The time scale for a PPE/OTAB complex diffusing in and out of the illumination volume is on the order of microseconds, estimated with $d = \sqrt{4Dt}$, taking a measured value for the diffusion coefficient D and the size of illumination spot ω_{xy} for d. According to Equation 7.7, the average fluorescence intensity is proportional to the product of concentration and the effective fluorescence efficiency. This relationship can be intuitively understood by realizing that even though a slow diffusing species stays in the illumination volume for a longer time and is excited more times, the frequency in which it passes through the excitation volume is less; a fast diffusing species stays in the illumination volume for a shorter time, but it can enter the detection volume more frequently. If the experimental duration is much longer than the diffusion time scale, the magnitude of diffusion coefficient has no effect on the total number of fluorescence photons.

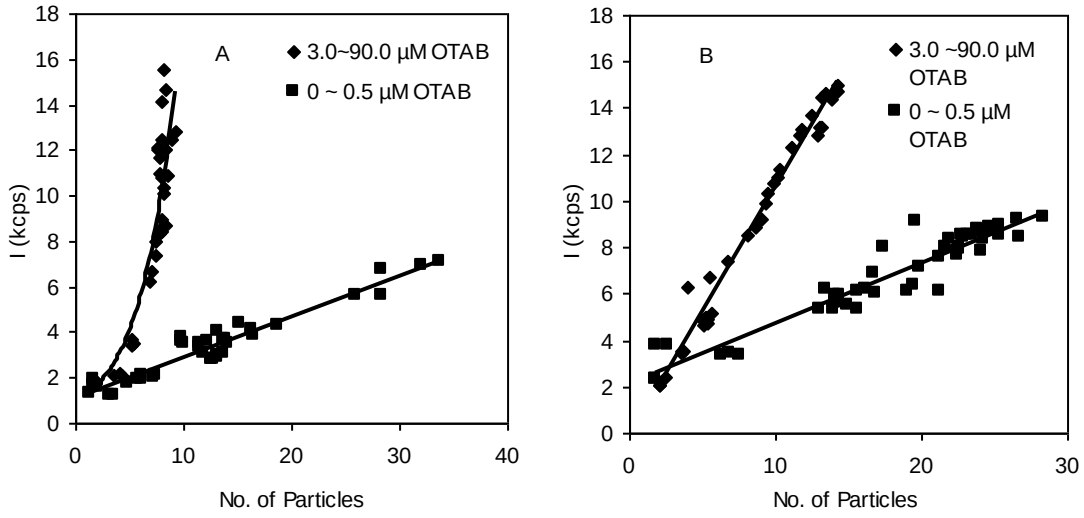

Figure 4.4 The correlation between the average fluorescence intensity and the average number of particles obtained in FCS measurements, A)2.8 ×10^{-5} mg/ml ***PPE-L*** *in OTAB aqueous solutions; B) 2.1 ×10^{-5} mg/ml* ***PPE-H*** *in OTAB aqueous solutions.*

In Figure 4.4, the average fluorescence intensity is plotted versus the average number of particles in the excitation volume for the solutions at low OTAB concentration and at high OTAB concentration; not near 1.0 μM. Panel A is for **PPE-L**/OTAB and panel B is for **PPE-H**/OTAB. For each plot, the intensity and the particle number show two distinct correlations. All of the points corresponding to solutions having OTAB concentration from 0 μM to 0.5 μM fall onto a shallower linear curve, suggesting a comparatively lower fluorescence efficiency. All of the points corresponding to solutions have OTAB concentration from 3.0 μM to 90.0 μM fall onto a sharp rising curve, suggesting higher fluorescence efficiency. Because the instrument conditions were kept the same for all of the experiments, the contrast in the effective fluorescence efficiency indicates a dramatic change in the polymer fluorescence quantum yield. When the OTAB concentration is in the range from 3.0 μM to 90.0 μM, the curve for **PPE-L** is superlinear, suggesting a continuing modification of **PPE-L** fluorescence yield by OTAB

molecules. Under the same conditions, the curve for **PPE-H** is linear and has a slope that is 2.7 times higher than that in deionized water, suggesting an increase of fluorescence efficiency.

4.3.5 The Emission and Excitation Spectra

To understand the behavior shown in Figure 4.4, the steady state emission spectra of **PPE-L** and **PPE-H** were measured for the solution used for the FCS measurements. The spectra of 2.8×10^{-5} mg/ml **PPE-L** in deionized water and in 80 μM OTAB aqueous solution are shown in Figure 4.5A. Those for 2.8×10^{-5} mg/ml **PPE-H** in deionized water and in 90 μM OTAB aqueous solutions are shown in Figure 4.5B. These spectra are normalized to the same height. **PPE-L** in 80 μM OTAB aqueous solution has a peak intensity about 15 times larger than that of **PPE-L** in deionized water, and **PPE-H** in 90 μM OTAB aqueous solution has a peak intensity of 5 times larger than that of **PPE-H** in deionized water. The quantum yield reported for **PPE-L** in deionized water is 0.05 and that for **PPE-L** in 50 μM OTAB solution is 0.15. A shorter life time was reported for **PPE-L** in OTAB solution.[28] The quantum yield of **PPE-H** is 0.026 measured in deionized water and 0.042 measured in 50 μM OTAB solution. For **PPE-H**, the fluorescence lifetime for was found to be similar in deionized water (570 ps) and in OTAB solutions(446 ps). As shown in panel A, the emission spectrum of **PPE-L** in deionized water shows a peak at 436 nm and a shoulder at 508 nm, with a FWHM of 73 nm. These spectra for **PPE-L** in deionized water are consistent mostly with a single strand species, but a small amount of aggregation.[28] The emission spectrum for **PPE-L** 80 μM OTAB aqueous solution shows a peak at 450 nm, with a FWHM of 36 nm. Panel B shows a broad symmetric emission spectrum with a peak at 490 nm with a FWHM of 109 nm for **PPE-H** in deionized water. The emission spectrum for **PPE-H** in 80 μM OTAB aqueous solution shows a peak at 450 nm, with a FWHM of 36 nm.

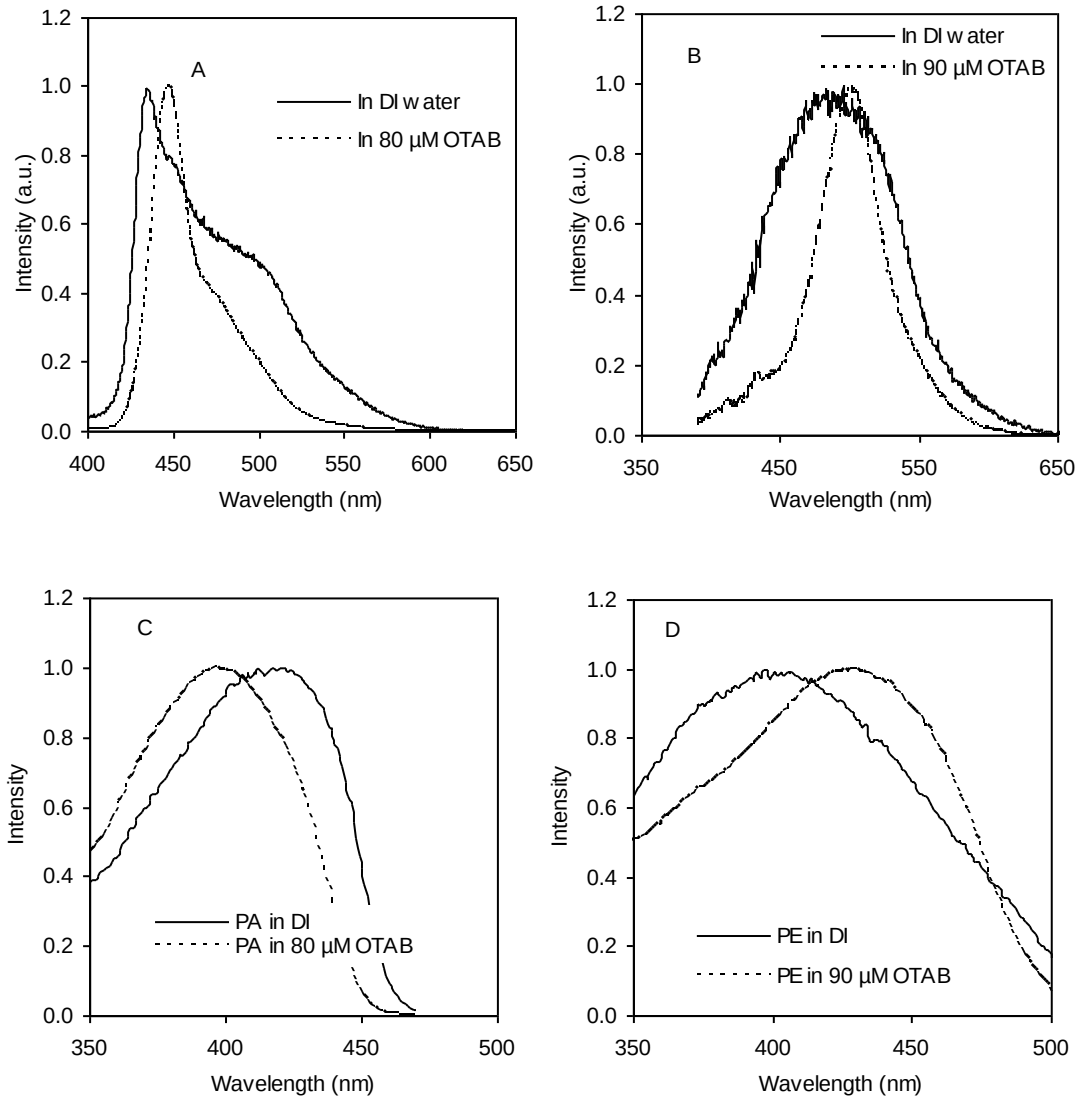

Figure 4.5 The emission spectra of A)2.8 ×10^{-5} mg/ml PPE-L; B) 2.1 ×10^{-5} mg/ml PPE-H. The excitation spectra of C)2.8 ×10^{-5} mg/ml PPE-L; D) 2.1 ×10^{-5} mg/ml PPE-H.

To summarize, at high concentration of OTAB ($C_{OTAB}/C_{monomer}$ up to 1600:1 and 1800:1), the emission spectra of **PPE-L** and **PPE-H** are red shifted (14 nm for **PPE-L** and 16 nm for **PPE-H**) and are narrower (by about two times) than those observed in deionized water. In addition, the fluorescence quantum yields for the two polymers in OTAB solution are increased over that in water.

The excitation spectra of PPE-L and PPE-H were measured and are shown in Figure 4.5C and 4.5D. Consistent with the dominant fluorescence feature of single strand **PPE-L** in dilute aqueous solution, no spectral signature of the aggregation is obvious in the excitation spectrum (Figure 4.5C). In the presence of 80 μM OTAB, the excitation spectrum is blue shifted, but are otherwise similar. For **PPE-H**, the excitation spectrum in 90 μM OTAB solution is red shift with respected to that in deionized water.

Previous ζ-potential studies show that the surface charge of **PPE-L** was inverted in the presence of excess of OTAB.[28] The mobility and ζ-potential for **PPE-H** was measured in deionized water and in 50 μM OTAB solution, a condition that is the same as that previously reported for **PPE-L**. The ζ-potential for **PPE-H** in deionized water is -28 ± 2 mV and the mobility is -1.7 ± 0.7. In OTAB solution the ζ-potential is 53 ± 1 mV and the mobility is 3.95 ± 0.08.

4.4 DISCUSSIONS

The hydrodynamic properties of complexes formed by OTAB with two PPE-SO_3^- polymers, containing different side-chain charge density, below the critical micelle concentration have been directly measured with FCS. The hydrodynamic radius, the number of detected molecules and the effective fluorescence efficiency data consistently suggest that PPE/OTAB complexes fall into three catagories depending on the C_{OTAB} /$C_{monomer}$ ratio. They are single-strand substoichiometric complexes (Figure 4.6a), multiple-strand clusters (Figure 4.6b and 4.6c) and single-strand superstoichiometric complexes (Figure 4.6d and 4.6e).

The formation of the soluble substoichiometric complexes has long been known for flexible polyelectrolytes.[29,31,34] Polymer and surfactant molecules are fastened together by the electrostatic interactions between opposite charges. When C_{OTAB} /$C_{monomer}$ < 6, the complexes have a size comparable with the polymer in deionized water are single strand substoichiometric complexes between PPE-SO_3^- and OTAB. The structures are represented by Figure 4.6a and the charges that are not neutralized make this complex soluble in water. The surfactant chain in these complexes may not be fully extended therefore there is no obvious increase in hydrodynamic radius as expected for the fully extended surfactant chains.

When there is sufficient surfactant, all the charges from the polyelectrolyte will be neutralized and the stoichiometric complex will form by both the electrostatic interactions between opposite charges and the hydrophobic interactions between parallel alkyl chains.[29,31,34] This complex is not soluble in water and tends to aggregate into larger assemblies and precipitate. This accounts for the huge particles and significant heterogeneity found when C_{OTAB} /$C_{monomer}$ > 6. The structure of these kinds of large particles is represented by Figure 4.6b which is extendable in three dimensions. The stoichiometric complexes are usually synthesized by mixing surfactant and polyions in equal molar amount (calculated based on the number of charge).[31,47,48] Accordingly, in our case, large particles should have be observed when the ratio C_{OTAB} /$C_{monomer}$ equals to 2.0 not 6.0. The delay is attributed to screening of the electrostatic interaction by the counter ions from the polymer.[29] The structure represented by Figure 4.6b is in agreement with the structure proposed by Thünemann *et.al* who has used small- and wide-angle X-ray scattering to study the solid state structure of precipitates prepared by mixing the aqueous solutions of PPE-COO^- and cationic surfactants at the stoichiometric ratio.[47,48]

From the structure of the solid state stoichiometric complexes as shown in Figure 4.6b, the large but soluble particles that appear in the higher concentration part of the intermediate regime can be inferred to have a structure like that shown in Figure 4.6c, where the cluster of stoichiometric chains have a boundary layer of OTAB molecules with their charged head groups facing water, rather than the 3-D extendable structure show in Figure 4.6b. Because of the outer layer of OTAB molecules, the clusters are soluble in water and the charge polarity of the particle should be inverted with respected to that of pure PPE-SO_3^- in deionized water. This charge inversion was verified by the zeta potential measurements [28] where the values for PPE-SO_3^- in deionized water and in 50 μM OTAB solutions show opposite signs. Further increase of the OTAB concentration decreases the number of stoichiometric chains in the structure c, reflected by the decreasing trend in the higher concentration part of the intermediate OTAB concentration regime. This trend is conserved until only one stoichiometric chain is left in structure c and leads to structure d.

Depending on the charge density of the polymer, the fate of structure d is different. In the case of **PPE-L** whose charge density is low, the size of the particle increases as C_{OTAB} /$C_{monomer}$ increases from 400 to 1800 while the number of particles is constant, which indicates a continuous modification of the structure d and a final structure like that of e. This causes a supralinear growth of fluorescence intensity versus the number of particles curve (Figure 4.4A). As in the case of **PPE-H** whose charge density is two times larger than that of **PPE-L**, the size of the particle remains constant but the number of particle in the solution increases while C_{OTAB} /$C_{monomer}$ increases from 400 to 1800. The linear fluorescence intensity versus the number of particles curve suggests that the complexes of **PPE-H** in this regime have the same composition.

The change of particle size with the increase of C_{OTAB} /$C_{monomer}$ in the whole tested OTAB

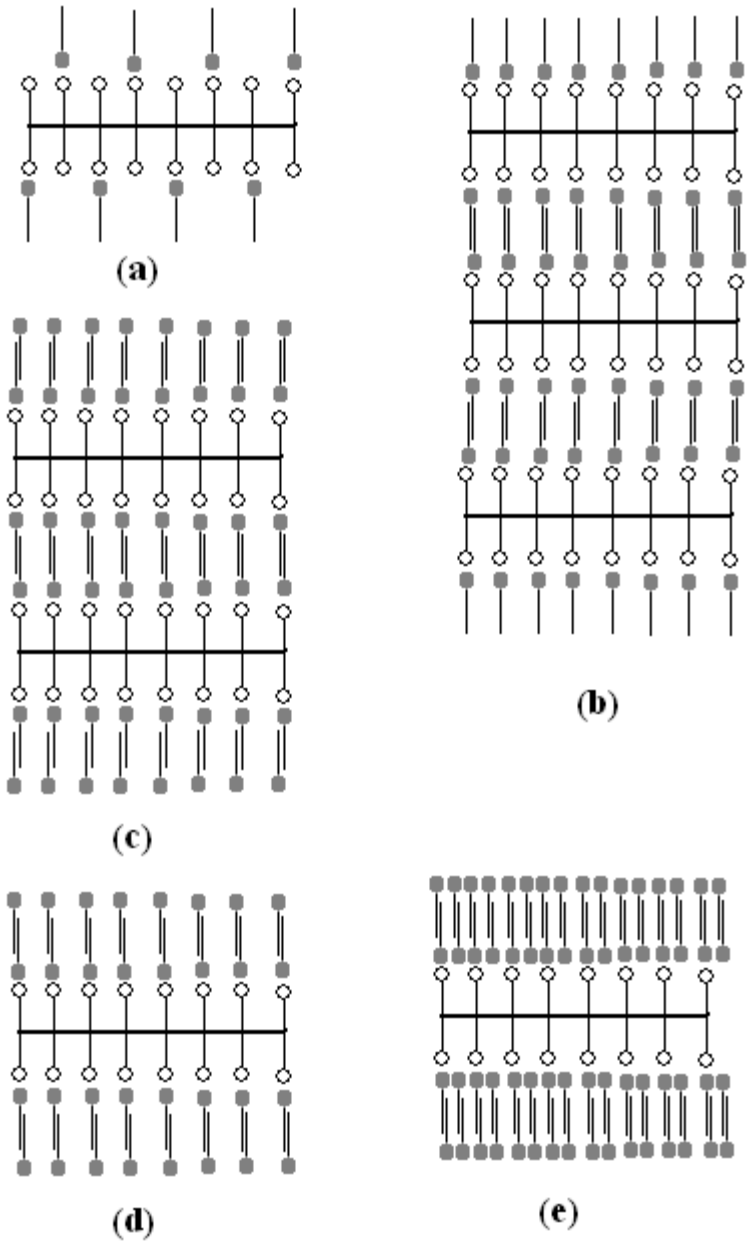

Figure 4.6 The cartoon showing the possible structures of PPE-L/OTAB and PPE-H/OTAB complexes

concentration range can be understood by the continuous change in the stoichiometric ratio in the chemically and physically stable complexes. From structure a to structure e, the stoichiometric

ratio of the complexes, if calculated based on the number of charges from OTAB and PPE-SO_3^-, evolves from < 1 : 1 (a) to 1 : 1 (b) to between 1 : 1 and 2: 1 (c) to 2 : 1 (d) to > 2 : 1.

The charge density of **PPE-H** is two times larger than that of **PPE-L** (see Scheme 7.1). However the hydrodynamic radius of **PPE-L**/OTAB and **PPE-H**/OTAB complexes as a function of OTAB concentration are generally similar, but show some difference in the high concentration regime, see Figure 4.2 and Figure 4.3. In the high concentration regime, the hydrodynamic radius of **PPE-L**/OTAB complexes increases while the average number of complexes detected in the excitation volume is constant asthe OTAB concentration increases. In contrast, the hydrodynamic radius of **PPE-H**/OTAB complexes are constant while the average number of particles in the excitation volume increases as the OTAB concentration increases. The different trends can be understood from the difference in charge density of **PPE-L** and **PPE-H** and the structures shown in Figure 4.6. In the case of **PPE-L**, the charge density is low, so that the hydrophobic interaction holding multiple chains together in structure b and c is smaller. Hence, it is easier to break the complexes into structure d than for the case of **PPE-H**. When the OTAB concentration is increased, more OTAB pairs can insert into the space between side chains of **PPE-L** of structure **d** and form structure e to optimize the hydrophobic interactions between OTAB molecules. Therefore the complex's hydrodynamic radius increases in the high concentration regime. In the case of **PPE-H**, the hydrophobic interaction is stronger, and it is more difficult to break the structure d from large complexes of structure b and c, hence the number of complexes with the same hydrodynamic radius increase more gradually as increase the OTAB concentration increases.

Burrow *et. al.*[71] studied the fluorescence of anionic poly[1,4-phenylene-[9,9-bis(4-phenoxy-butylsulfonate)]fluorene-2,7-diyl]copolymer (PBS-PFP) as a function of cationic surfactant concentration and identified three surfactant concentration regimes.[71] In the low concentration regime, $< 2 \times 10^{-6}$ M, the fluorescence is quenched. In a wide intermediate concentration regime, from 2×10^{-6} to 10^{-3} M, the fluorescence intensity remains constant. In the third regime where the surfactant concentration is above 10^{-3} M, the critical micelle concentration (CMC), the fluorescence is enhanced and spherical aggregates of the complexes were detected. The difference in the fluorescence intensity indicates that polyelectrolyte/surfactant complexes are intrinsically different in these three regimes. The triple-phasic behavior is consistent with the findings on the size of the complexes in this paper.

The conformation of the complexes of flexible conjugated polyions with oppositely charged surfactant or radom coil nonfluorescent polyions have been extensively studied and the three component phase diagram has worked out.[29,72] The general picture is that with increase of the concentration of surfactant, the complexes evolve from substoichiometric complexes to stoichiometric complexes and finally to the encapsulation of polyions by micelles above the CMC.[43,72-75] This picture predicts the detection of structure a and b, but not other structures. Our results contrast with this standard picture in two aspects. First, these results show that a distribution of soluble complex structures evolves with the stoichiometric ratio from 1 : 1 to > 2 : 1. Second the OTAB concentrations in this study are far below the CMC[69] and CAC.[29] The complex structures of c, d and e are not the result of the pre-existing micelle or vesicle structures. It appears that the C_{OTAB} /$C_{monomer}$ ratio is a dominant factor for the composition of the complexes. The contrast between these findings from PPE-SO3- and those from random coil

polyelectrolyte suggests that the rigidity of the polymer backbone plays an important role in determining the conformation between polyions and surfactant.

Different effects of surfactant on the fluorescence of PPE have been reported in the literature.[50-52] With the help of the structures proposed in Figure 4.6, the following prediction can be made. In the low OTAB concentration regime, the fluorescence intensity will first increase because binding of the surfactant breaks or loosens the PPE aggregate. Near the right boundary of this regime the fluorescence quenches because of the precipitation of the PPE polymers. This prediction is consistent with the studies reported by Yu *et. al.*.[50] On the higher OTAB concentration side of the intermediate regime, the fluorescence intensity increases again with increase of the OTAB because of the dissolution of the precipitate and formation of particles having structure c. Experimental results of this kind have been reported by Kaur *et. al.*.[28] It is expected that this enhancement of the fluorescence intensity will stop when all of the PPE chains have the structure of d or e. However this is difficult to observe using steady state fluorescence measurements, because such a method needs a comparatively high concentration and the available highest C_{OTAB} /$C_{monomer}$ is limited by the CMC[69] and CAC[29].

For both **PPE-L** and **PPE-H**, the complex size shows a strong dependence on the charge ratio C_{OTAB}/C_{charge}. The uniform particle size can only be achieved when C_{OTAB}/C_{charge} is in the range of 0.1 to 6.0 where substoichiometric complexes are formed, and when C_{OTAB}/C_{charge} is over 100, multiple chains of PPE exist in the complex with a size decreasing with increasing of C_{OTAB}/C_{charge}. It is interesting to compare these observations to those found for DNA/lipid complexes. In the case of DNA/lipid complexes, the optimized transfection condition has a charge ratio in the range of 0.3-5.0 and DNA particles of 100-700 nm size have been observed by electron microscopy.[59,76] Our data suggests that it is highly possible that insufficient lipid

charge causes the heterogeneity of DNA/lipid complexes which increases the uptake barrier for DNA delivery.

4.5 CONCLUSION

It is shown in this paper that FCS is a powerful tool for studying the interactions between surfactant and fluorescent polyelectrolyte. It yields valueable information that is not accessible by traditional methods. It is found that even in a concentration far lower than the CMC and CAC of OTAB, the PPE-SO_3^-/OTAB complexes exist in a series of structures that have different size, chemical composition, and conformation depending on the comparative concentration of polyelectrolyte and surfactant. This complicated situation indicates that the rigidity of the polymer backbone plays an important role in determining the conformation between polyions and surfactant and the ratio C_{OTAB} /$C_{monomer}$ might be a dominant factor for the composition of the complexes. With the help of the structures inferred from the FCS studies, the contradictory effects of surfactant reported on the PPE fluorescence can be explained by a unified picture. The PPE-SO_3^- represents the type of polyelectrolytes with rigid backbone, including dsDNA. Our results have important implications in the field of gene delivery.

4.6 ACKNOWLEDGEMENTS

I would like to thank Dr Matthew Shtrahman of University of Pittsburgh for his generous help with the FCS instrument. The work is supported by National Science Foundation (CHE-0415457).

4.7 REFERENCE

(1) Zhou, C. Z.; Liu, T.; Xu, J. M.; Chen, Z. K. *Macromolecules* **2003**, *36*, 1457-1464.

(2) Wilson, J. N.; Bunz, U. H. F. *J. Am. Chem. Soc* **2005**, *127*, 4124-4125.

(3) Skotheim, T. E.; Elsenbaumer, R. L.; Reyolds, J. R. *Eds. Handbook of Conducting Polymers* **1998**, *Marcel Decker: New York*.

(4) Rothberg, L. J.; Yan, M.; Galvin, M. E.; Kwock, E. W.; Miller, T. M.; Papadimitrakopoulos, F. *Synthetic Metals* **1996**, *80*, 41-58.

(5) Perahia, D.; Traiphol, R.; Bunz, U. H. F.; *Macromolecules* **2001**, *34*, 151-155.

(6) Levitsky, I. A.; Kim, J.; Swager, T. M. *J. Am. Chem. Soc* **1999**, 1466-1472.

(7) Jones, R. M.; Bergstedt, T. S.; McBranch, D. W.; Whitten, D. G. *J Am Chem Soc* **2001**, *123*, 6726-7.

(8) Bunz, U. H. F.; Imhof, J. M.; Bly, R. K.; Bangcuyo, C. G.; Rozanski, L.; Bout, D. A. V. *Macromolecules* **2005**, *38*, 5892-5896.

(9) Thomas, S. W.; Joly, G. D.; Swager, T. M. *Chem. Rev.* **2007**.

(10) Schanze, K. S.; Pinto, M. R. *Proc. Nat. Aca. Sci.* **2004**, *101*, 7505-7510.

(11) Rininsland, F.; Xia, W.; Wittenburg, S.; Shi, X.; Stankewicz, C.; Achyuthan, K.; McBranch, D.; Whitten, D. *Proc. Nat. Acad. Sci.* **2004**, *101*, 15295-15300.

(12) McQuade, D. T.; Pullen, A. E.; Swager, T. M. *Chem Rev* **2000**, *100*, 2537-74.

(13) Liu, M.; Kaur, P.; Waldeck, D. H.; Xue, C.; Liu, H. *Langmuir* **2005**, *21*, 1687-1690.

(14) Kim, I.-B.; Dunkhorst, A.; Gilbert, J.; Bunz, U. H. F. *Macromolecules* **2005**, *38*, 4560-4562.

(15) Heeger, A. J.; Diaz-Garcia., M. A. *Curr. Opin. Solid State Mater.* **1983**, *3*, 16.

(16) Harrison, B. S.; M.B.;, R.; Reyolds, J. R.; Scahnze, K. S., , . *J.Am. Chem. Soc.* **2000**, *122*, 8561.

(17) Gaylord, B. S.; Heeger, A. J.; Bazan, G. C. *Proc. Nat. Acad. Sci.* **2002**, *99*, 10954-10957.

(18) Haskins-Glusac, K.; Pinto, M. R.; Tan, C.; Schanze, K. S. *J. Am. Chem. Soc.* **2004**, *126*, 14964-14971.

(19) Chu, Q.; Pang, Y.; Ding, L.; Karasz, F. E. *Macromolecules* **2002**, *35*, 7569-7574.

(20) Chu, Q.; Pang, Y. *Macromolecules,* **2003**, *36*, 4614-4618.

(21) Tan, C.; Pinto, M. R.; Schanze, K. S. *Chem Comm.* **2002**, 446-447.

(22) Jiang, H.; Zhao, X.; Schanze, K. S. *Langmuir* **2006**, *22*, 5541-5543.

(23) Jenekhe, S. A.; Osaheni, J. A. *Science* **1994**, *265*, 765-768.

(24) Sariciftci, N. S.; Smilowitz, L.; Heeger, A. J.; Wudl, F. *Science* **1992**, *258*, 1474-1476.

(25) Cotts, P. M.; Swager, T. M.; Zhou, Q. *Macromolecules* **1996**, *29*, 7323-7328.

(26) Halkyard, C. E.; Rampey, M. E.; Kloppenburg, L.; Studer-Martinez, S. L.; Bunz, U. H. F. *Macromolecules* **1998**, *31*, 8655-8659.

(27) Fiesel, R.; Halkyard, C. E.; Rampey, M. E.; Kloppenburg, L.; Studer-Martinez, S. L.; Scherf, U.; Bunz, U. H. F. *Macromolecular Rapid Communications* **1999**, *20*, 107-111.

(28) Kaur, P.; Yue, H.; Wu, M.; Liu, M.; Treece, J.; Waldeck, D. H.; Xue, C.; Liu, H. *J. Phys. Chem. B* **2007,** 111, 8589-8596.

(29) Kogej, K.; Skerjane, J. In *Physical Chemistry of Polyelectrolytes*; Radeva, T., Ed.; Mercel Dekker, Inc.: New York, Basel, 2001, 793-827.

(30) Goddard, E. D. *Journal of Colloid and Interface Science* **2002**, *256*, 228-235.

(31) MacKnight, W. J.; Ponomarenko, E. A.; Tirrell, D. A. *Accounts of Chemical Research* **1998**, *31*, 781-788.

(32) La Mesa, C. *Journal of Colloid and Interface Science* **2005**, *286*, 148-157.

(33) Macdonald, P. M. *Colloids and Surfaces, A: Physicochemical and Engineering Aspects* **1999**, *147*, 115-131.

(34) Tam, K. C.; Wyn-Jones, E. *Chemical Society Reviews* **2006**, *35*, 693-709.

(35) Goddard, E. D. *Colloids and Surfaces* **1986**, *19*, 255-300.

(36) Yeh, F.; Sokolov, E. L.; Walter, T.; Chu, B. *Langmuir* **1998**, *14*, 4350-4358.

(37) Bakeev, K. N.; Shu, Y. M.; Zezin, A. B.; Kabanov, V. A.; Lezov, A. V.; Mel'nikov, A. B.; Kolomiets, I. P.; Rjumtsev, E. I.; MacKnight, W. J. *Macromolecules* **1996**, *29*, 1320-1325.

(38) Morishima, Y.; Mizusaki, M.; Yoshida, K.; Dubin, P. L. *Colloids and Surfaces* **1999**, *147*, 149-159.

(39) Chen, L.; McBranch, D. W.; Wang, H.-L.; Helgeson, R.; Wudl, F.; Whitten, D. G. *PNAS* **1999**, *96*, 12287-12292.

(40) Chen, L.; Xu, S.; McBranch, D.; Whitten, D. *J. Am. Chem. Soc.* **2000**, *122*, 9302-9303.

(41) Fan, C.; Plaxco, K. W.; Heeger, A. J. *J. Am. Chem. Soc.* **2002**, *124*, 5642-5643.

(42) Gaylord, B. S.; Wang, S.; Heeger, A. J.; Bazan, G. C. *J. Am. Chem. Soc.* **2001**, *123*, 6417-6418.

(43) Wang, D.; Moses, D.; Bazan, G. C.; Heeger, A. J.; Lal, J. *Journal of Macromolecular Science, Pure and Applied Chemistry* **2001**, *A38*, 1175-1189.

(44) Ho, H.-A.; Boissinot, M.; Bergeron, M. G.; Corbeil, G.; Dore, K.; Boudreau, D.; Leclerc, M. *Angewandte Chemie International Edition* **2002**, *41*, 1548-1551.

(45) Gaylord, B. S.; Heeger, A. J.; Bazan, G. C. *J. Am. Chem. Soc.* **2003**, *125*, 896-900.

(46) Tapia Maria, J.; Burrows Hugh, D.; Knaapila, M.; Monkman Andrew, P.; Arroyo, A.; Pradhan, S.; Scherf, U.; Pinazo, A.; Perez, L.; Moran, C. *Langmuir* **2006**, *22*, 10170-4.

(47) Thunemann, A. F.; Ruppelt, D. *Langmuir* **2001**, *17*, 5098-5102.

(48) Thunemann, A., F. *Advanced Materials* **1999**, *11*, 127-130.

(49) Clark, A. P. Z.; Shen, K.-F.; Rubin Yves, F.; Tolbert Sarah, H. *Nano letters* **2005**, *5*, 1647-52.

(50) Yu, M. H.; Gan, H. Y.; He, F.; Tang, Y. L.; Zheng, D. G.; Wang, S.; Li, Y. L. *Chinese Chemical Letters* **2006**, *17*, 671-674.

(51) Wosnick, J. H.; Mello, C. M.; Swager, T. M. *Journal of the American Chemical Society* **2005**, *127*, 3400-3405.

(52) Lavigne, J. J.; Broughton, D. L.; Wilson, J. N.; Erdogan, B.; Bunz, U. H. F. *Macromolecules* **2003**, *36*, 7409-7412.

(53) Godfrey, J. E.; Eisenberg, H. *Biophysical Chemistry* **1976**, *5*, 301-8.

(54) Godfrey, J. E. *Biophys Chem FIELD Full Journal Title:Biophysical chemistry* **1976**, *5*, 285-99.

(55) Duzgunes, N.; de Ilarduya, C. T.; Simoes, S.; Zhdanov, R. I.; Konopka, K.; de Lima, M. C. P. *Current Medicinal Chemistry* **2003**, *10*, 1213.

(56) Hirko, A.; Fuxing Tang, A.; Hughes, J. A. *Current Medicinal Chemistry* **2003**, *10*, 1185.

(57) Nakanishi, H.; Tsuchiya, K.; Okubo, T.; Sakai, H.; Abe, M. *Langmuir* **2007**, *23*, 345-347.

(58) Pedroso de Lima, M. C.; Neves, S.; Filipe, A.; Duzgunes, N.; Simoes, S. *Current Medicinal Chemistry* **2003**, *10*, 1221-1231.

(59) Zabner, J.; Fasbender, A. J.; Moninger, T.; Poellinger, K. A.; Welsh, M. J. *J. Biol. Chem.* **1995**, *270*, 18997-19007.

(60) Bastardo, L. A.; Garamus, V. M.; Bergstroem, M.; Claesson, P. M. *Journal of Physical Chemistry B* **2005**, *109*, 167-174.

(61) Lapitsky, Y.; Parikh, M.; Kaler, E. W. *Journal of Physical Chemistry B* **2007**, *ASAP Article, DOI: 10,102/jp0678958*.

(62) Zhao-chang Fan; Shan, L.; Goldsteen, B. Z.; Guddat, L. W.; Thakur, A.; Landolfi, N. F.; Edmundson, M. S. C. M. V. C. Q. P. A. R. A. B. *Journal of Molecular Recognition* **1999**, *12*, 19-32.

(63) Adjimatera, N.; Kral, T.; Hof, M.; Blagbrough, I. S. *Pharmaceutical Research* **2006**, *23*, 1564-1573.

(64) Koppel, D. E. *physical Review A* **1974**, *10*, 1938-1945.

(65) Magde, D.; Elson, E.; Webb, W. W. *Physical Review Letters* **1972**, *29*, 705-708.

(66) *Fluorescence Correlation Spectroscopy, Theory and Applications*; Rigler, R.; Elson, E. S., Eds.; Springer, 2001.

(67) Pristinski, D.; Kozlovskaya, V.; Sukhishvili, S. A. *Journal Of Chemical Physics* **2005**, *122*.

(68) Van Rompaey, E.; Sanders, N.; De Smedt, S. C.; Demeester, J.; Van Craenenbroeck, E.; Engelborghs, Y. *Macromolecules* **2000**, *33*, 8280-8288.

(69) Lu, J. R.; Simister, E. A.; Thomas, R. K.; Penfold, J. *J. Phys. Chem. B* **1993**, *97*, 6024-6033.

(70) Culbertson, C. T.; Jacobson, S. C.; Ramsey, J. M. *Talanta* **2002**, *56*, 365-373.

(71) Burrows, H. D.; Tapia, M. J.; Silva, C. L.; Pais, A. A. C. C.; Fonseca, S. M.; Pina, J.; Seixas de Melo, J.; Wang, Y.; Marques, E. F.; Knaapila, M.; Monkman, A. P.; Garamus, V. M.; Pradhan, S.; Scherf, U. *Journal of Physical Chemistry B* **2007**, *111*, 4401-4410.

(72) Galant, C.; Amiel, C.; Wintgens, V.; Sebille, B.; Auvray, L. *Langmuir* **2002**, *18*, 9687-9695.

(73) Li, Y.; Xu, R.; Couderc, S.; Bloor, D. M.; Warr, J.; Penfold, J.; Holzwarth, J. F.; Wyn-Jones, E. *Langmuir* **2001**, *17*, 5657-5665.

(74) Claesson, P. M.; Bergstroem, M.; Dedinaite, A.; Kjellin, M.; Legrand, J.-F.; Grillo, I. *Journal of Physical Chemistry B* **2000**, *104*, 11689-11694.

(75) Tapia, M., J.; Burrows , H., D.; Knaapila, M.; Monkman Andrew, P.; Arroyo, A.; Pradhan, S.; Scherf, U.; Pinazo, A.; Perez, L.; Moran, C. *Langmuir* **2006**, *22*, 10170-4.

(76) Gershon, H.; Ghirlando, R.; Guttman, S. B.; Minsky, A. *Biochemistry* **1993**, *32*, 7143-7151.

5.0 CHARGE DENSITY EFFECTS ON THE AGGREGATION PROPERTIES OF POLY(P-PHENYLENE-ETHYNYLENE) BASED ANIONIC POLYELECTROLYTES

This work has been published as Mingyan Wu, Palwinder Kaur, Hongjun Yue, David H. Waldeck, Cuihua Xue, and Haiying Liu, J. Phys. Chem. B.; (2008); 112, 3300-3310. Thesis author synthesized the polymers and performed FCS and other spectroscopic experiments.

Abstract

This work shows that low charge density poly(p-phenylene-ethynylene)s (PPE-SO_3Na-L and PPE-CO_2Na-L), which feature sulfonate and carboxylate groups on every other phenyl ring, form aggregates in water, whereas high charge density poly(p-phenylene-ethynylene)s (PPE-SO_3Na-H and PPE-CO_2Na-H), which possess sulfonate or carboxylate groups on every phenyl ring, do not aggregate in water. The formation of aggregates of PPE-SO_3Na-L and PPE-CO_2Na-L is demonstrated by comparing the concentration and temperature dependence of their steady-state spectra in water to that in DMSO, in which the two polymers do not aggregate. For the weak polyelectrolytes PPE-CO_2Na-H and PPE-CO_2Na-L, the solution pH was changed to vary the charge density. In addition, the cationic surfactant, octadecyltrimethyl ammonium (OTAB) is shown to dissociate the low charge density polymer aggregates and to form supramolecular complexes with each of the different polyelectrolytes. Fluorescence correlation spectroscopy was applied to provide insight into the sizes of aggregates under different solution conditions.

5.1 INTRODUCTION

Because of their interesting optical and electronic properties[1-6] and their use in applications, ranging from optical sources [7-13] to biochemical sensors [14-20], conjugated polymers (CPs) have been a subject of great interest over the past two decades. Poly(p-phenylene-ethynylene) (PPE) based conjugated polyelectrolytes (CPEs) are a class of conjugated polymers that feature charged side groups[21] and combine the optoelectronic advantages of conjugated polymers with the unique properties of polyelectrolytes. Because of the charged and polar nature of the ionic side groups, CPEs are soluble in polar solvents, including water, and can be processed into thin films and supramolecular assemblies.[5,6,22-31] In addition, CPEs interact strongly with other ionic species, such as metal ions,[14] molecular ions,[3,22,32,33] polyelectrolytes,[34] proteins[34-38] and DNA,[39-41]and this property has been exploited to fabricate rapid-response and high-sensitivity biochemical sensors. Controlling the behaviour and properties of CPEs in solution remains an important challenge, however.

Because of the favourable interaction between the polarizable π-electron clouds of their large planar backbones, CPEs possess an intrinsic tendency to organize into π-stacked aggregates or supramolecular structures in solution and in films.[42] The optical properties of such aggregates differ from that of the individual strands, e.g., the photoluminescence quantum yield decreases and the emission red shifts.[43,44] Experiments by Schwartz et al.[45] suggest that the electronic properties of conjugated ionomer films reflect those of the solutions from which they are cast, and that morphological control of the film can be achieved by spin-casting from the appropriate

solutions. In addition, it is possible to control the thickness and morphology of LBL (layer by layer) films by varying the deposition solution conditions, such as ionic strength and pH.[22,46-48] Moreover, it is well appreciated that the photophysical properties and quenching behaviour of CPEs vary dramatically with the change of solvent conditions, such as solvent polarity, temperature, ionic strength, charge on quencher, surfactant concentration or solution pH.[4,22,49-56] Exploring and understanding the aggregation of CPEs, and its effect on their photophysical properties in different environments, are valuable for the development of these materials.

In the past few years, much attention has focused on understanding the structure-property relationship and solvation/aggregation of CPs/CPEs under different conditions. Strategies to improve the solvation of polymers include the incorporation of bulky substituents,[57,58] increasing the content of hydrophilic side groups,[53] adding surfactants into the solution,[23,52,59,60] using solvent with proper polarity,[4,49] and adjusting the pH[22,51,55,61]and ionic strength[49,51]of solutions. Schanze et al[4] reported that the spectroscopic properties of poly(p-phenylene-ethynylene) based polyelectrolytes vary strongly with solvent composition, and the spectral data suggest that in H_2O ('poor' solvent) the polymer displays the broad, less efficient, red shifted fluorescence peak which is characteristic of conjugated polymer aggregates.[59,62-64] This broad photoluminescence band has been attributed to an excimer-like state that dominates the photophysical properties of aggregated polymers, presumably caused by π-stacking of adjacent polymer chains.[4,22] In methanol solution ('good' solvent) the fluorescence properties are very similar to those exhibited by organic-soluble PPEs in good solvents.[62] Despite such efforts, it appears that no systematic study of how the density of charged side groups effect the photophysical properties of poly(p-phenylene-ethynylene) (PPE) based anionic CPEs has been reported.

This study reports on four anionic CPEs (see Figure 5.1) that differ in charge density of their side groups. Three of these polymers have been studied by different research groups, however no systematic comparisons of their aggregation properties have been drawn. Recently Kaur et. al.[49] reported the solvation and aggregation behaviour of PPE-SO_3Na-L in dilute solution. In addition

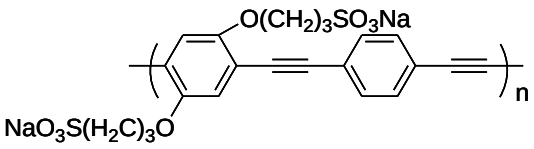

PPE-SO_3Na-L

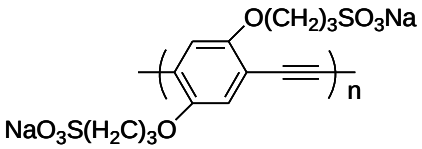

PPE-SO_3Na-H

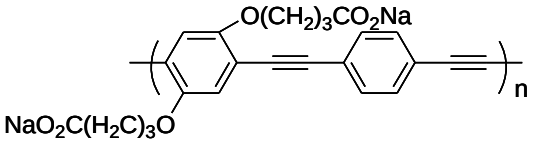

PPE-CO_2Na-L

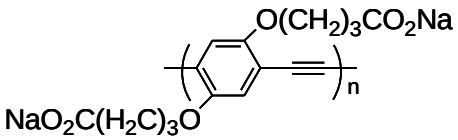

PPE-CO_2Na-H

Figure 5.1 Chemical structures of the conjugated polyelectrolytes are shown.

to that polymer, this study reports on three other anionic CPEs, which differ from PPE-SO_3Na-L by the nature of the charged group (sulfonate versus carboxylate) and the charge density along the backbone (every phenyl unit versus every other phenyl unit). Evaluation and comparison of the photophysical and hydrodynamic properties of these four CPEs demonstrate how these changes in polymer composition impact their aggregation properties.

5.2 EXPERIMENTAL

Materials: Synthesis of the four polymers PPE-SO_3Na-L, PPE-SO_3Na-H, PPE-CO_2Na-L, and PPE-CO_2Na-H (Figure 5.1) was performed in a manner similar to that reported in the literature.[4,65] All the polymer solutions were freshly prepared and sonicated for 1 to 2 min before use. The concentration of the polymer was kept low with an optical density of 0.1, unless noted otherwise. At these concentrations, the self-absorption effect and the effect of the polymer on solution properties, such as viscosity, can be neglected. All concentrations reported here are provided versus polymer repeat unit [PRU].

Table 5.1 Characterization of polymers

Polymer	Molecular weight $< M_w >$	PDI[a]
PPE-CO_2Na-L[b]	29,685	2.47
PPE-CO_2Na-H[b]	42,968	2.87
PPE-SO_3Na-L[c]	38,100	3.04
PPE-SO_3Na-H[c]	9,840	1.11

[a]PDI is the polydispersity index of polymer sample and is defined as $< M_w > / < M_n >$

[b]The $<M_w>$ and PDI of the polymers were determined by gel permeation chromatography using polystyrene in THF as a standard based on the polymer precursor. [C]$<M_w>$ and PDI of the polymers were determined by gel permeation chromatography using Dextran in DMF as a standard.[66]

OTAB (octadecyltrimethyl ammonium bromide) and DPA[67] (9,10-diphenylanthracene) were bought from Sigma-Aldrich and used as received. Water used in all experiments was purified by a Barnstead-Nanopure system and its resistance was 18.2 MΩ.

Steady state spectroscopy: Steady-state absorption spectra were measured on an Agilent 8453 spectrometer and the steady-state emission spectra were measured on an SLM 8000 (Olis upgrade) fluorimeter.

Time dependent fluorescence spectroscopy: The time-resolved fluorescence data were collected using the time-correlated single photon counting (TCSPC) method.[16] The instrument response function was measured using a sample of colloidal $BaSO_4$. The samples were excited at 438 nm using a diode laser (PIL043, A.L.S. GmbH) and the emission was collected at different wavelengths. The fluorescence decay curves were fit by a convolution and compare method using IBH-DAS6 analysis software.[68]

Fluorescence Correlation Spectroscopy (FCS): FCS is an established and sensitive method which obtains dynamic and kinetic information about molecules in a small open volume by following the fluctuation trajectory of fluorescence about the equilibrium state.[69-72] Details of the instrumentation are provided elsewhere.[49,73] The sample was excited at 438 nm using a solid state diode laser and the laser power was kept low to avoid photobleaching and optical trapping. Each measurement lasted 3 to 10 min, during which the time trajectory of fluorescence was monitored and only those having a stable fluorescence intensity were kept. The correlation time τ_D, where $\tau_D = \omega_{xy}^2 / 4D$, is extracted by fitting the autocorrelation function $G(\tau)$ to the equation

$$G(\tau) = \frac{1}{\overline{N}}\left(1+\frac{\tau}{\tau_D}\right)^{-1}\left(1+\frac{\omega_{xy}^2\,\tau}{\omega_z{}^2\,\tau_D}\right)^{-1/2} \qquad (5.1)$$

in which $\overline{N}$ is the average number of fluorophores in the observation volume; ω_{xy} is the lateral radius and ω_z is the axial radius (where the intensity declines by $1/e^2$ from the peak value) of the observation volume,[74] and D is the translational diffusion coefficient. The apparatus was calibrated and tested using a 10 nM Rhodamine 6G aqueous solution, assuming the diffusion

coefficient D = 4.14×10^{-6} cm^{2}s^{-1}.[75] The Stokes-Einstein approximation, $D = \mathrm{k}_B T / 6\pi\eta R_H$ was used to extract the hydrodynamic radius R_H from the measured diffusion coefficient; η is the shear viscosity, T is the temperature in K and k_B is the Boltzmann's constant.

5.3 RESULTS AND DISCUSSION

5.3.1 Solvent Dependence

Figure 5. 2 shows steady-state spectra for the four polymer materials in DMSO and water at micromolar concentrations. The spectra for PPE-SO_3Na-H, PPE-CO_2Na-L, and PPE-CO_2Na-H is new and the data for PPE-SO_3Na-L is reproduced here from earlier work[49] in order to facilitate comparisons. The spectra for the low charge density polymers are shown in Figures 5.2a and 5.2c. Figure 5.2a shows that the absorbance and fluorescence spectra of PPE-SO_3Na-L in DMSO is shifted blue of that recorded in aqueous solution. The fluorescence spectrum of PPE-CO_2Na-L exhibits a behavior nearly identical to PPE-SO_3Na-L, namely a broad, featureless peak in aqueous solution and a narrower blue shifted peak in DMSO (Figure 5.2c). These spectral changes are consistent with earlier work, which has been interpreted in terms of polymer aggregation in water; *i.e.,* water is a 'poor' solvent and DMSO is a 'good' solvent.[4,49]

Fluorescence lifetime and quantum yield measurements show that the excited state properties of the low charge density polymers change dramatically between DMSO and water (see supplemental information). The fluorescence decay of PPE-CO_2Na-L and PPE-SO_3Na-L in water require at least a triple exponential decay law with long average decay times around 2 ns

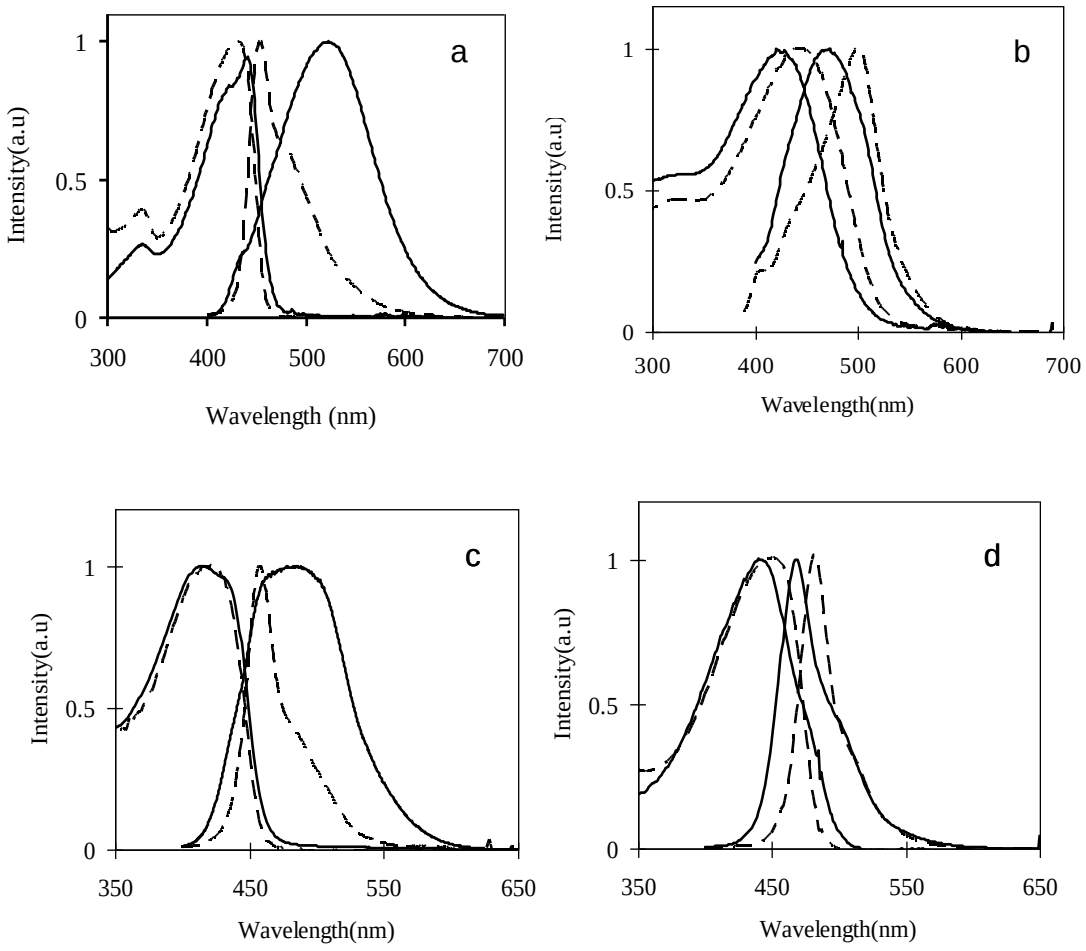

Figure 5.2 Normalized absorption and emission spectra (excited at 380 nm) are shown for ***a)*** *PPE-SO_3Na-L (2.0×10^{-6}M);* ***b)*** *PPE-SO_3Na-H (9.5×10^{-6}M);* ***c)*** *PPE-CO_2Na- L (5.6×10^{-6}M);* ***d)*** *PPE-CO_2Na- H (5.8×10^{-6}M) in DMSO (— —) and water (–)*

at 510 nm. In addition, the decay law is a strong function of the emission wavelength, which is characteristic of emission from an excimer-like aggregate.[59,62-64] Dissolving PPE-CO_2Na-L and PPE-SO_3Na-L into DMSO rather than water causes the average decay times to decrease significantly, from around 2 ns to 590 ps for PPE-CO_2Na-L and 368 ps for PPE-SO_3Na-L, and the decay law becomes independent of the emission wavelength. In addition, the quantum yields

increase from 0.02 to 0.16 for PPE-CO_2Na-L and from 0.05 to 0.22 for PPE-SO_3Na-L when the solvent is DMSO rather than water. Hence, the radiative rates are significantly enhanced, which indicates a change in the nature of the fluorophore's emissive state. These data are consistent with a model in which the fluorescent species in DMSO are individual polymer strands and those in water are aggregated strands, with an excimer-like emission.

In contrast to the low charge density polymers, the absorbance and fluorescence spectra of PPE-SO_3Na-H (Figure5. 2b) and PPE-CO_2Na-H (Figure 5.2d) have similar shapes in DMSO and water. The emission bands in DMSO are shifted to the red of that recorded in aqueous solution, however. The sharp, well-defined emission bands resemble the spectra exhibited by PPE-CO_2Na-L and PPE-SO_3Na-L in the 'good' solvent DMSO, by neutral PPEs in good organic solvents,[62] and a similarly structured polymer in water reported earlier.[56,76] The narrow emission band and small Stokes shift for the high charge density polymers suggests that the spectra do not result from aggregates, but from independent polymer strands. This interpretation is consistent with a stronger mutual electrostatic repulsion between the polymer chains that inhibits the hydrophobic forces and $\pi-\pi$ stacking between the polymer chains.[22,76]

Excited state lifetime and quantum yield measurements corroborate this interpretation (see supplemental information). The fluorescence decay of PPE-CO_2Na-H and PPE-SO_3Na-H in water can be fit by a double exponential decay law with an average decay time of around 260 ps, and the decay law does not change with emission wavelength. In addition, the quantum yields do not change significantly between DMSO and water, indicating that the radiative rates do not change dramatically; in contrast to what was found for the low charge density polymers.

The red shift for the high charge density polymer in DMSO, as compared to water, may reflect an increase in the effective conjugation length of the polymer in DMSO. Assuming that

the placement of charged groups on every phenylene ring inhibits aggregation in water, then the solvent dependence of the emission band must result from properties of the individual strands. It is well known that the persistence length of a polyelectrolyte has a contribution from both the intrinsic stiffness of the chain and the electrostatic repulsions along the chain.[77,78] Given that water (ε~78) is a more polar solvent than DMSO (ε~48) the electrostatic repulsion between adjacent side chains should be shielded more in water, than in DMSO. A longer persistence length implies a stiffer and probably more planar backbone, hence a larger conjugation length and a spectral red shift. [51,79]

5.3.2 Concentration Dependence

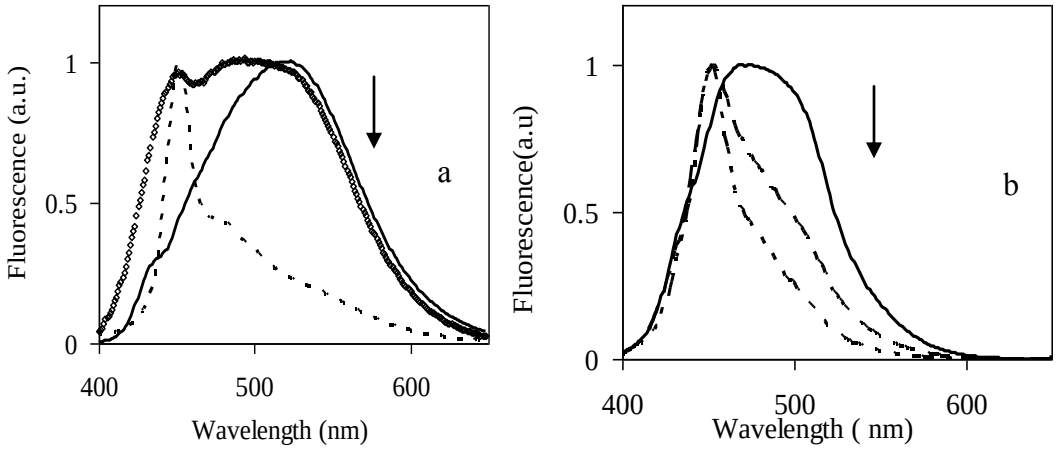

Figure 5.3. Normalized emission spectra (excited at 380 nm) are shown for PPE-SO_3Na-L in water at different concentrations (2.0×10^{-6} (—), 8.8×10^{-8} (◊), 1.0×10^{-8} (----) M) in panel a); and for PPE-CO_2Na-L in water at different concentrations (1.7×10^{-5}(—), 4.2×10^{-7}(---), 1.6×10^{-8} (–••–) M) in panel b). The data in panel a) was reported earlier[55], but it is included here for comparison.

If PPE-CO_2Na-L and PPE-SO_3Na-L form aggregates in aqueous solution, dilution should decrease the population and/or size of the aggregates.[57] Figure 5.3 shows the emission spectra of PPE-SO_3Na-L and PPE-CO_2Na-L at three different concentrations.[49] As the concentration decreases, the emission band at the blue edge becomes more pronounced and the broad, aggregate emission in the red edge decreases in amplitude. At the lowest concentration the spectra are qualitatively similar to those recorded in DMSO, indicating that the polymers are in an unaggregated state at low enough concentration.

In contrast to the dramatic concentration dependence for PPE-CO_2Na-L and PPE-SO_3Na-L, the high charge density materials, PPE-CO_2Na-H and PPE-SO_3Na-H, do not show a concentration dependence (see supplemental information).

5.3.3 Temperature Dependence

Heating experiments were carried out on the four polymer solutions in water. PPE-CO_2Na-L shows a behavior similar to that reported for PPE-SO_3Na-L.[49] Figure 5.4 shows the effect of a heating cycle (room temperature, 363 K, cooled to room temperature) on the absorption and emission spectra. Heating of a PPE-CO_2Na-L solution to 363 K causes the band at the red edge in the absorption spectrum to attenuate significantly. In addition, the fluorescence spectra show that the band at the blue edge, taken to arise from unaggregated polymers, grows in intensity with increasing temperature. Both absorbance and fluorescence spectra at 363K qualitatively resemble those recorded in the 'good' solvent DMSO and at low concentration. Upon cooling the polymers to room temperature, the band features for the aggregates appear to 'grow in' again, indicating that aggregates reform at room temperature.

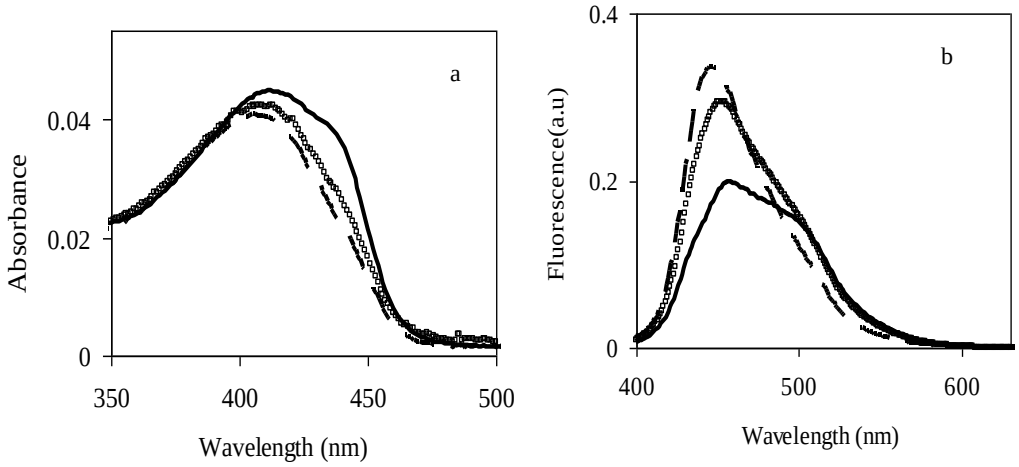

*Figure 5.4. Panel **a)** shows absorption spectra and panel **b)** shows emission spectra (excited at 380 nm)of PPE-CO_2Na-L (2.8×10^{-6} M) in water at room temperature (—), 363 K (- - -), Cooled to room temperature from 363 K (□). Note: The concentration is half that typically used because it is easier to break aggregates at this concentration.*

No significant spectral changes were observed when heating the high charge density polymers PPE-SO_3Na-H and PPE-CO_2Na-H in water and this observation is consistent with these materials already being in an unaggregated state in aqueous solution.

This study shows that aggregate formation is thermodynamically preferred for the low charge density polymer at low temperature, but the aggregates dissociate at high temperature.[80]

5.3.4 pH Effect

Both PPE-SO_3Na-H and PPE-SO_3Na-L are strong polyelectrolytes which dissociate completely in solution for most reasonable pH values. Wang et al. studied the pH effect on PPV-

SO_3Na and found that the photophysical properties did not change dramatically over a wide pH range, from pH = 5 to pH = 14.[81] By contrast, PPE-CO_2Na-H and PPE-CO_2Na-L are weak polyelectrolytes which partially dissociate at intermediate pH. Thus the charge density along the polymer chains can be modified by changing the solution pH. Earlier studies on PPE-CO_2^-,[56] PPE-PO_3^{2-},[22] PPE-$N(C_2H_5)_3^+$ [51]have shown that varying the solution pH changes the

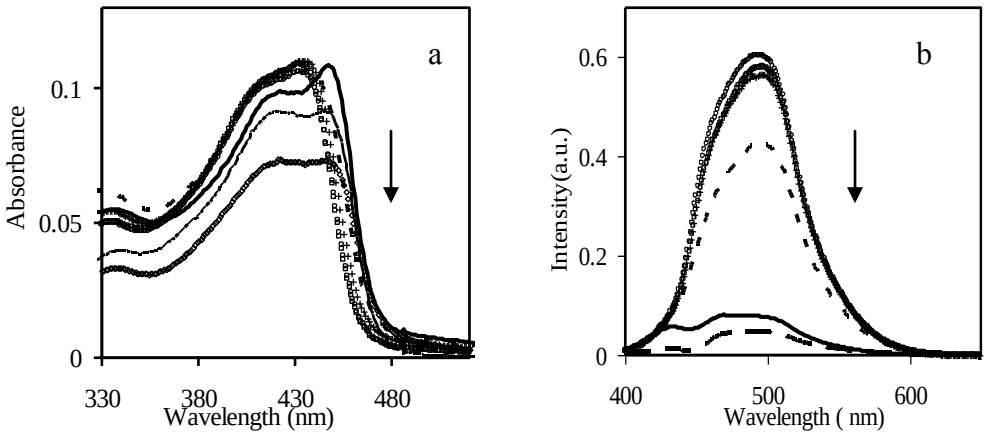

*Figure 5.5. Panel a**)** shows absorption spectra and panel **b)** shows emission spectra (excited at 380 nm) of PPE-CO_2Na-L (5.6×10^{-6} M) in 20 mM aqueous buffer solution: pH = 4 (◊), pH = 5 (— —), pH = 6.2 (—), pH = 7.2 (– –), pH = 8 (++), pH = 10 (○), pH = 12 (□). Note: pH = 9 and pH = 11 spectra are nearly identical to those at pH = 8, pH = 10, and pH = 12, which are not shown here for clarity. The emission spectrum of pH = 4 is nearly identical to pH = 5 and not shown for the same reason. The peaks near 430 nm in the emission spectra at pH = 6 and 5 arise from the water Raman scattering.*

photophysical properties of conjugated polymers dramatically. In the present investigation, the effect of pH on the spectra of the weak polyelectrolytes, PPE-CO_2Na-L and PPE-CO_2Na-H, was studied in 20 mM aqueous buffer solution. In addition, fluorescence correlation spectroscopy (FCS) was used to determine how the aggregate size changes with the solution's pH.

Figure 5.5 a and 5.5 b illustrate the changes in the absorption and fluorescence spectra of PPE-CO_2Na-L as the pH changes over the range of 12.0 - 4.0. When the pH is at 8 or higher, the absorption spectra resemble each other; at pH = 7.2 a small red shift is observed; and at pH = 6.2 the spectrum red shifts at least 6 nm. Upon further decreasing the pH, the absorbance decreases. The fluorescence spectra have an analogous pH dependence. Above pH = 8, the spectra are the same; at pH = 7.2, the fluorescence is quenched by about 30%; and at pH = 6.2 the spectrum broadens and the intensity quenches more than 83%. At pH = 5 or 4 the solutions become dark, and a visible suspension appears after 3-4 hours. The steady state spectra suggest that at pH > 8, PPE-CO_2Na-L exhibits relatively few aggregates, presumably because of the increased interchain electrostatic repulsion at high pH. As the pH decreases, protonation of the carboxylate groups decreases the charge density on the strand, the reduced electrostatic repulsion may lead to the reduced internal torsional angles along the backbone so that the planarized polymer chains can more easily aggregate.[21,51,56] At low enough pH, the polymers start to precipitate. This interpretation is corroborated by the FCS study (*vide infra*).

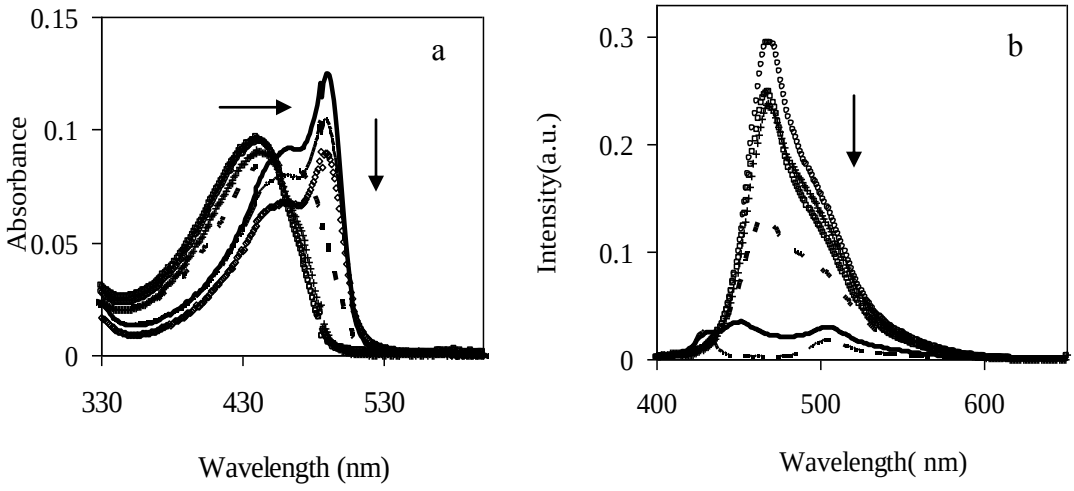

*Figure 5.6. Panel **a)** shows absorption spectra and panel **b)** shows emission spectra of PPE-CO_2Na-H (5.8×10^{-6} M) in 20 mM aqueous buffer solution: pH = 4 (◊), pH = 5 (— —), pH =*

6.2(—), pH = 7.2 (– –), pH = 8 (++), pH = 10 (○), pH = 12 (□). Note: pH = 9 and pH 11 spectra are nearly identical to those at pH = 8, pH = 10, and pH = 12, which are not shown here for clarity. Emission spectrum of pH = 4 is nearly identical to that of pH = 5 and not shown here for clarity. The bump near 430 nm in the emission spectra at pH = 6.2 and 5 arise from the water Raman scattering.

Figures 5.6 a and 5.6 b show how the absorption and emission spectra of PPE-CO_2Na-H change as the pH is varied over the range of 12.0-4.0. When the pH > 8, the absorbance and fluorescence spectra display peaks at 440 nm and 469 nm, respectively, and have an approximate mirror image relationship. When the pH = 7.2, the absorption spectrum red shifts, a shoulder at 474 nm appears, and the fluorescence quenches more than 40%. At pH = 6.2, the fluorescence quenches more than 90%, and a very pronounced sharp peak appears at 490 nm in the absorption spectrum, which suggests aggregate formation.[57] With further decrease of the pH to 5 or 4, the absorbance spectrum's shape remains similar but the transmission decreases and the solutions become dark.

FCS measurements demonstrate that the polymers aggregate and provide information on aggregate size. The concentration of the polymer solutions for the FCS measurements are ten

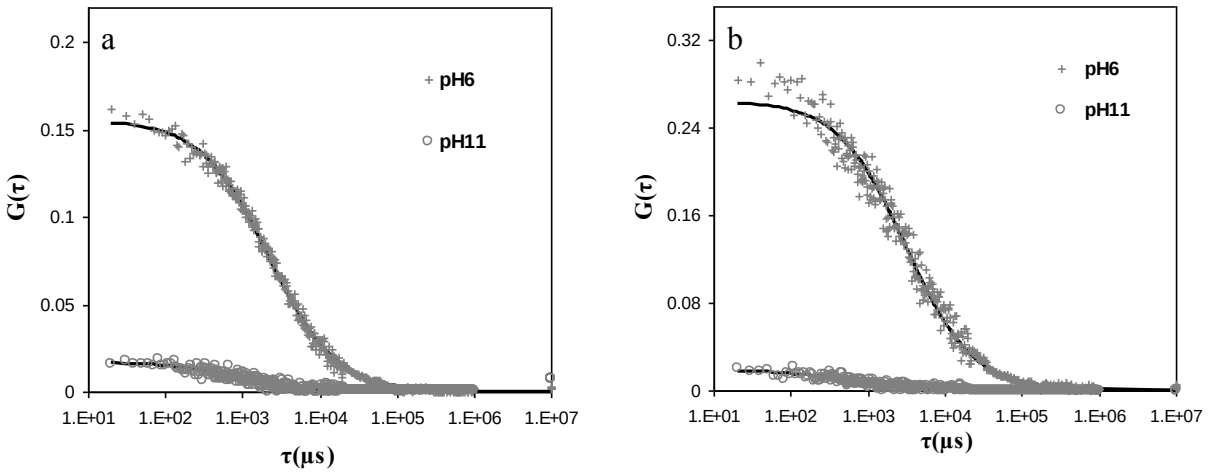

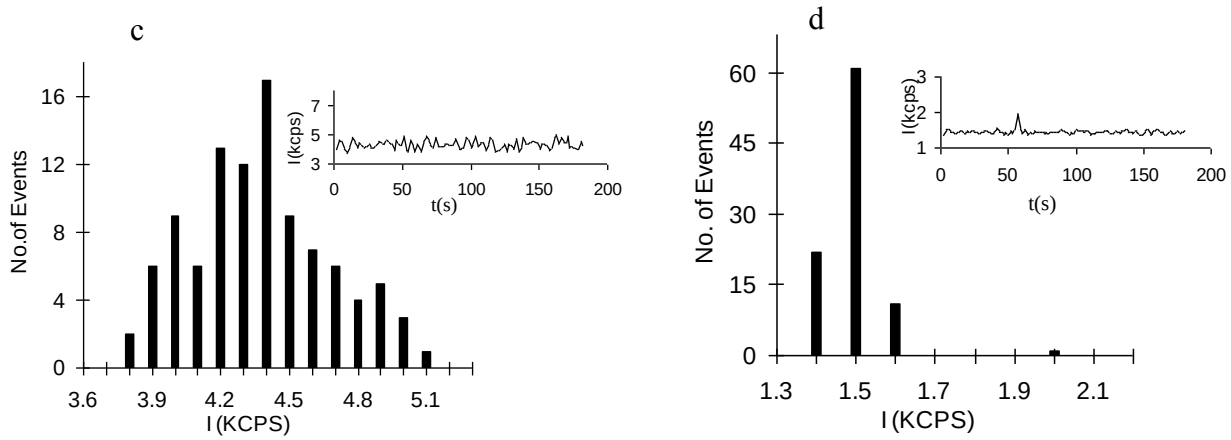

*Figure 5.7 Panel **a)** shows autocorrelation functions of PPE-CO_2Na-L (5.6×10^{-7} M) in pH = 6 and pH = 11 buffer solutions; panel **b)** shows autocorrelation functions of PPE-CO_2Na-H (5.8×10^{-7} M) in pH = 6 and pH = 11 buffer solutions; panel **c)** shows the photon counting rate histogram of PPE-CO_2Na-L (5.6×10^{-7} M) in pH = 6 aqueous solution; and panel **d)** shows the photon counting rate histogram of PPE-CO_2Na-L (5.6×10^{-7} M) in pH = 5 aqueous solution; insets are the time trajectory of the photon counting rate.*

times lower than those used in steady-state spectroscopy experiments (OD=0.01) in order to optimize the appropriate autocorrelation function amplitude and signal-to noise ratio.[82] Figures 5.7a and 5.7b show the autocorrelation functions obtained for PPE-CO_2Na-L and PPE-CO_2Na-H in two pH buffer solutions: pH = 6.2 and pH = 11. The much larger amplitudes of $G(\tau)$ for pH = 6.2 than those of pH = 11 indicate that the average number of fluorophores in the observation volume is smaller at the lower pH. Aggregation is also evident from the experimental correlation times. For PPE-CO_2Na-H, the diffusion times τ_D are 550±100 μs (R_H, a hydrodynamic radius of 2.8-4.0 nm) at pH > 8, and 750±50 μs (R_H of 4.4-5.0 nm) at a pH of 7.2. At a pH of 6.2, where a large red-shift in the absorption spectrum and significant quenching of fluorescence is observed, τ_D increases to 2400 ±150 μs (R_H of 14.2 -16.1 nm). In addition, the average number of

fluorophores observed in the illumination volume at pH=6.2 is significantly reduced. These data clearly suggest that large aggregates exist in solution at this pH. Similar behavior was observed for PPE-CO_2Na-L. At pH values$\geq$ 7.2, τ_D is 650±120 μs (R_H of 3.5-5.0 nm), and at a pH of 6.2, τ_D increases to 2360 ±150 μs (R_H of 13.8-15.7 nm). These data are consistent with the steady-state spectra, which indicate that the polymer is only weakly aggregated at high pH (for this concentration) but aggregate more as the solution pH decreases.

When the solution pH is decreased below 6, ill-shaped autocorrelation functions are observed, and no reliable fitting of Equation 1 to the data could be obtained. Figure 5.7c and 5.7d show histograms of the counting rate history of PPE-CO_2Na-L in pH = 6.2 and pH = 5 solutions, respectively. At pH = 6.2 (Figure 5.7c), the events of the counting rate has a normal distribution around the average value of 4.4 kcps (i.e. kHz). Although the intensity is low compared to that found with the higher pH, no spike or big jump is observed and a well defined autocorrelation function can be obtained. However, at pH = 5 (Figure 5.7d) spikes in the counting rate history are observed, and the histogram reveals a narrow distribution at 1.5 kcps, which corresponds to the background noise. No reasonable autocorrelation functions could be obtained when the spikes appeared. These spikes are attributed to large aggregate particles diffusing in and out of the observation volume in a random trajectory, rather than scattered excitation light. No such spikes were observed on a scattering sample (a $BaSO_4$ suspension in deionized water), but could be found with a diluted suspension of fluorescent beads of 0.1 μm and 2.0 μm in diameter.

Filtration experiments (through 450 nm PTFE filters) were performed on PPE-CO_2Na-H solutions at pH = 5, pH = 6, and pH = 11 and demonstrate the existence of large aggregates. For pH = 6 and pH = 11 (Figure 5.8a), the absorbance was attenuated somewhat by filtration,

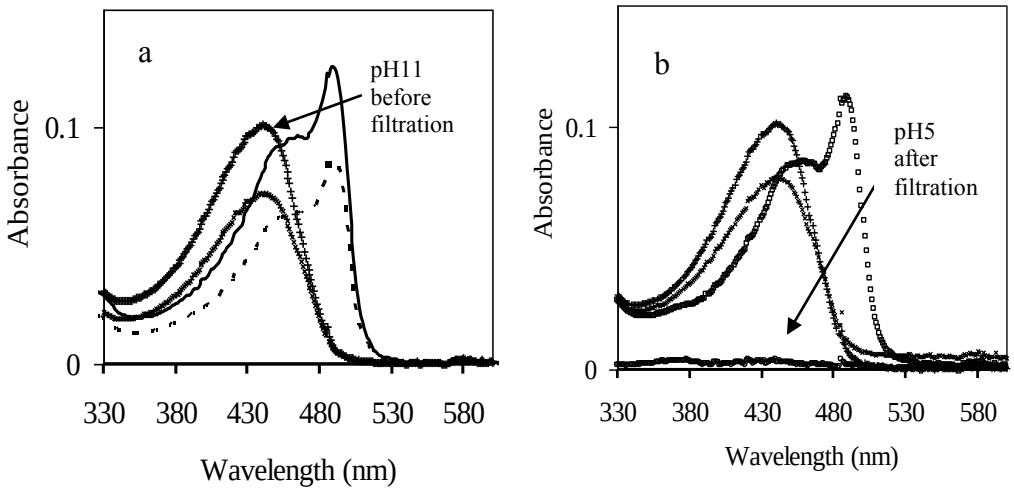

*Figure 5.8. Panel **a)** shows absorption spectra of PPE-CO_2Na-H (5.8×10^{-6} M) in 20 mM aqueous buffer solution: pH = 6.2 before filtration (—), pH = 6 after filtration (– –), pH = 11 before filtration (++), pH = 11 after filtration (×); and panel **b)** shows absorption spectra of PPE-CO_2Na-H (5.8×10^{-6} M) in 20 mM aqueous buffer solution: pH = 5 before filtration (□), pH = 5 after filtration (○), pH = 11 before filtration (++), pH = 5 recovered using same pH = 11 buffer solution (×).*

however most of the polymer chains could pass through the 450 nm size filter. For pH = 5 (Figure 5.8b), the solution's absorbance was strongly attenuated by filtration, indicating that the polymer aggregates are large enough to be blocked by the filter's 450 nm diameter pores. If the filtration residue from the pH = 5 solution is redissolved in a pH = 11 buffer, the original absorption spectrum is recovered. Hence the aggregation is reversible and arises from protonation of the charged side groups.[54]

All pH studies were performed at a constant, 20mM ionic strength; a previous study showed that the solution ionic strength also effects the aggregation properties of conjugated polyelectrolytes.[49]

5.3.5 Ionic Strength Effect

To further explore whether aggregation can be driven by simple metal cations and its dependence on the charge density, the four conjugated polyelectrolytes were studied as a

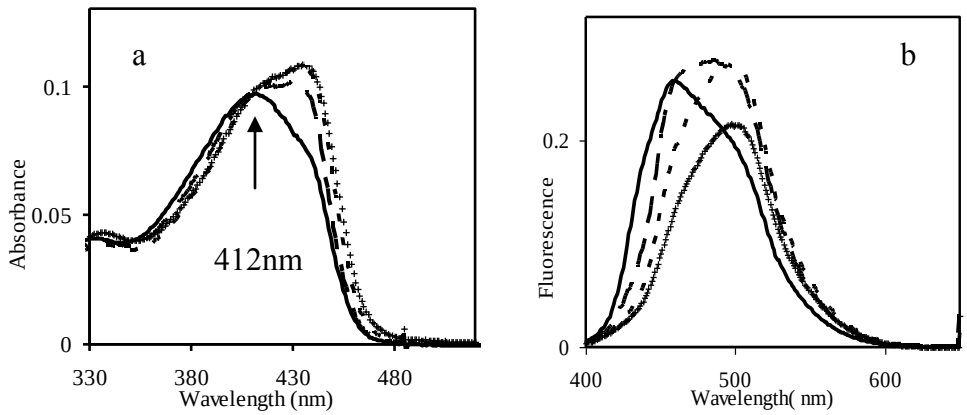

*Figure 5.9. Panel **a)** shows absorption spectra and panel **b)** shows emission spectra of (excited at 380 nm) PPE-CO_2Na-L (5.6×10^{-6} M) in water for NaCl solutions of different ionic strength; 0 mM (—), 3 mM (— ——), 50 mM (– –), 100 mM (++).*

function of ionic strength using the simple salt NaCl. Similar to the previously reported PPE-SO_3Na-L,[49] the absorption spectrum of PPE-CO_2Na-L in water, no NaCl added, displays a peak at 412 nm and a shoulder at 439 nm. Upon addition of NaCl, the shoulder at the red edge grows in intensity and becomes the dominant peak at high enough ionic strength. An isosbestic point occurs near 412 nm, indicating that two distinct chromophoric states exist (Figure 5.9a). Figure 5.9b shows how the fluorescence spectrum red shifts with increasing ionic strength of NaCl; it is also quenched. Both the absorption and fluorescence spectra indicate that the addition of salt enhances the aggregation of the low charge density polymers PPE-CO_2Na-L and PPE-SO_3Na-L.

Adding NaCl to solutions of the high charge density polymer PPE-CO_2Na-H causes more pronounced changes in the absorption spectrum (Figure 5.10a). The absorption spectrum of PPE-

CO_2Na-H in water has a peak at 440 nm, and increasing the ionic strength of NaCl causes a

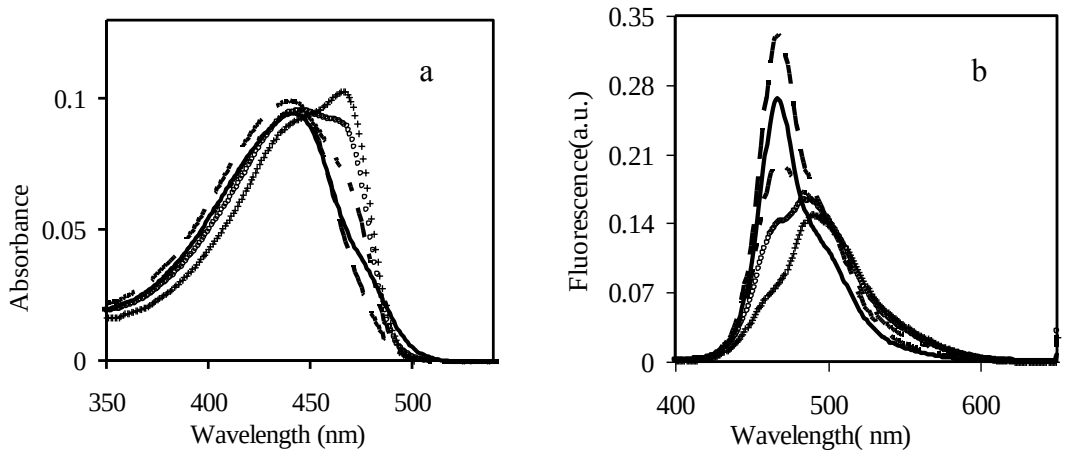

*Figure 5.10. Panel **a)** shows absorption spectra and panel **b)** shows emission spectra of (excited at 380 nm)PPE-CO_2Na-H (5.8×10^{-6} M) in water for NaCl solutions of different ionic strength; 0 mM (—), 5 mM (— —), 50mM (– –), 80 mM (○), 160 mM (++).*

shoulder near 468 nm to appear. This shoulder grows in intensity upon further increasing ionic strength and becomes the main peak at high ionic strength. The fluorescence spectrum of PPE-CO_2Na-H (Figure 5.10b) shows that the sharp peak at 469 nm, which exists in aqueous solution, attenuates and finally disappears as the NaCl concentration increases. Furthermore, a new broad peak near 492 nm appears and grows in intensity; reminiscent of the emission spectrum for PPE-CO_2Na-L in NaCl solution. Adding NaCl into aqueous solutions of PPE-SO_3Na-H causes a red-shifted absorption and quenched fluorescence, similar to that found for PPE-SO_3Na-L.

The interpretation of the ionic strength dependence in terms of aggregation is corroborated by FCS studies. Table 5.2 presents the diffusion times τ_D of PPE-CO_2Na-L and PPE-CO_2Na-H as a function of ionic strength. The correlation time τ_D increases as the ionic strength increases, which indicates that the size of the diffusing fluorophore increases. When the

ionic strength is 144 mM or higher for PPE-CO_2Na-L, big particles appear, indicating that the polymer is "salting out" at high ionic strength.[83]

Table 5.2 Diffusion times dependence of PPE-CO_2Na-L and PPE-CO_2Na-H on increasing the ionic strength of NaCl

Ionic Strength (NaCl mM)	PPE-CO2Na-L τ_D (μS)	PPE-CO2Na-H τ_D (μS)
0	358	509
5	388	749
45	557	1036
90	882	1426
144	Start to see big particles	1148
180	See big particles	1406
288	See big particles	1380

5.3.6 Surfactant Effect

A previous study of the surfactant effect (OTAB) on PPE-SO_3Na-L illustrated that the surfactant could dissociate the polymer aggregates.[49] Addition of OTAB causes a blue shifted absorption spectrum and an enhanced, sharp vibronic structure at the blue edge in the emission spectrum, which strongly suggests that homoaggregates between polymer chains are broken

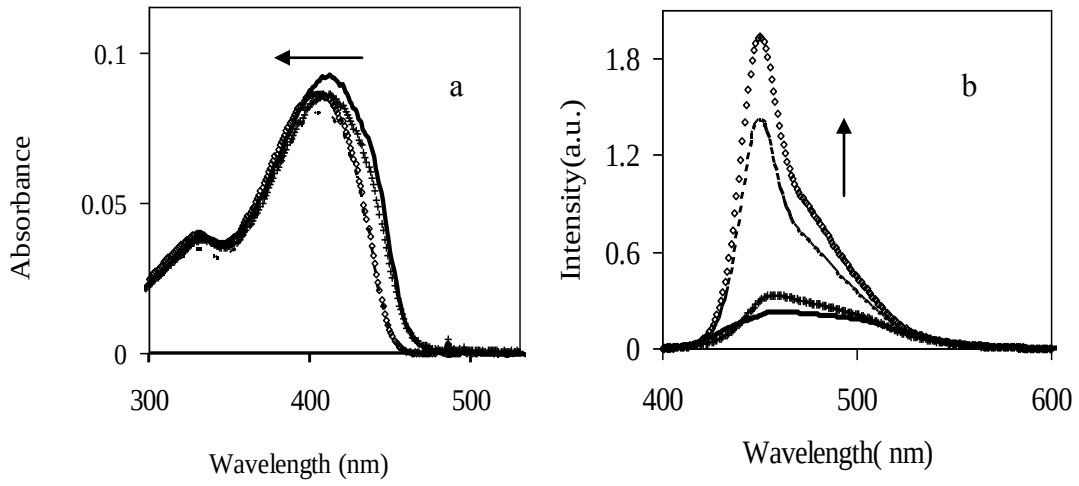

*Figure 5.11 Panel **a)** shows absorption spectra and panel **b)** shows emission spectra (excited at 380 nm) of PPE-CO_2Na-L (5.6×10^{-6} M) in water with different concentration of OTAB: 0 mM (—), 0.008 mM (++), 0.020 mM (– –), 0.050 mM (◊). Arrows indicate the direction of increasing concentration of OTAB.*

and heteroaggregates between polymer and OTAB are formed. This conclusion was further supported by FCS, lifetime and Zeta potential measurements.[49] Figure 5.11 shows the dependence of the steady state spectra of PPE-CO_2Na-L on the OTAB concentration. The behaviour is virtually identical to that reported earlier for PPE-SO_3Na-L.

The low charge density polymer's blue shift can be understood by the mechanism proposed in reference.[49] In that mechanism the blue-shift in absorption and the enhanced fluorescence is attributed to a decrease in the conjugation length of the polymer strands upon dissociation of the aggregates. Previous work suggests that the polymer-polymer aggregation causes the conjugation length of the polymer backbone

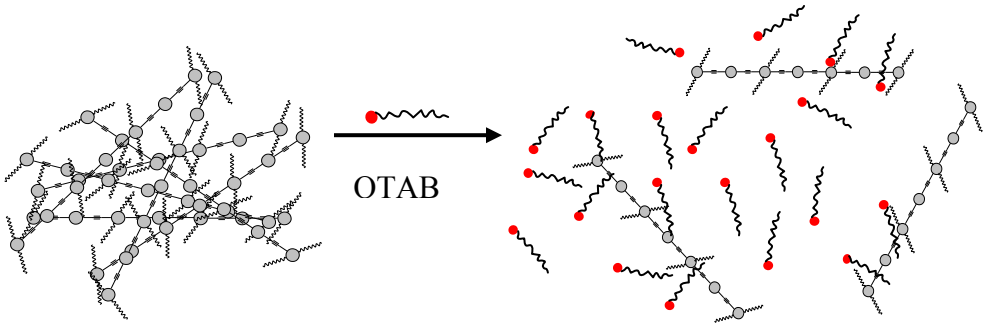

Scheme 5.1. Breaking the homoaggregates of low charge density of polymers on addition of OTAB and forming heterocomplexes.

to increase because of the favorable π-π stacking interactions making the backbone more planar.[63,84] Addition of the OTAB breaks the polymer aggregates and forms a heterocomplex between the polymer and OTAB (see Scheme 5.1). The heterocomplex's conjugated backbone is hypothesized to be less planar than that of the homoaggregates. This model is supported by excited state lifetime and quantum yield measurements. In water, the average lifetime of PPE-CO_2Na-L is about 2 ns and has wavelength dependence. In the presence of 0.050 mM OTAB, the lifetime decreases to 300 ps and does not show wavelength dependence. Also, the quantum yield increases about four times in 0.050 mM OTAB; the radiative rate of the emitting state increases by 24 times over that found in water. This result is consistent with the homoaggregates being broken by forming heterocomplexes between the polymer and OTAB, similar to that previously reported for PPE-SO_3Na-L.[49]

Addition of OTAB to the high charge density polyelectrolytes, PPE-SO_3Na-H (9.5×10^{-6} M) and PPE-CO_2Na-H (5.8×10^{-6} M) in aqueous solution, causes the spectrum to red shift, in contrast to the blue shift observed for the low charge density polymers. The behavior for the high charge density polymers is more complicated than a simple red shift, however. Figure 5.12 shows the dependence of the emission spectra of PPE-SO_3Na-H (Figure 5.12a) and PPE-CO_2Na-H (Figure 5.12b) on the OTAB concentration. At low concentration of OTAB, the spectra red

shift and the emission intensity is enhanced, but at intermediate OTAB concentration (between 0.015 mM and 0.020 mM for PPE-SO_3Na-H, and between 0.010 mM and 0.020 mM

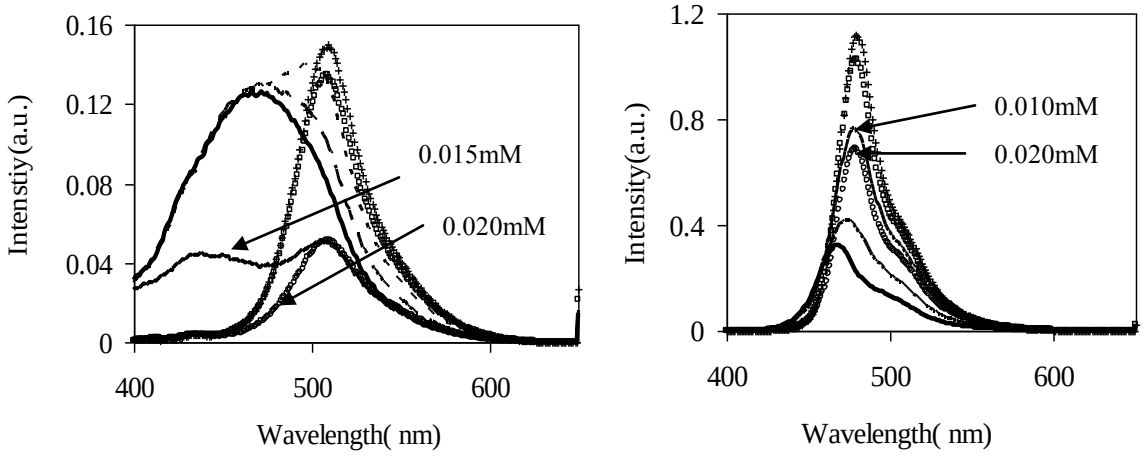

Figure 5.12. Panel ***a)*** *shows emission spectra (excited at 380 nm) of PPE-SO_3Na-H (9.5×10^{-6} M) in water with different concentration of OTAB: 0 mM (—), 0.003 mM (— —), 0.008 mM (– –), 0.015 mM (◊), 0.020 mM (○), 0.040 mM (□),0.050 mM (++), and panel* ***b)*** *shows emission spectra (excited at 380 nm) of PPE-CO_2Na-H (5.8×10^{-6} M) in water with different concentration of OTAB: 0 mM (—), 0.005 mM (– –), 0.010 mM (— —), 0.020 mM (○), 0.040 mM (□), 0.050 mM (++).*

for PPE- CO_2Na-H), the emission intensities attenuate. Upon further increase of the OTAB concentration, the emission intensities increase again.

The mechanism shown in Scheme 2 can explain the red shift and unusual intensity changes of the high charge density polymers with increasing OTAB concentration. Assuming that the high charge density polymers PPE-SO_3Na-H and PPE-CO_2Na-H are unaggregated in water (*vide supra*), the charged side groups are available for binding oppositely charged

surfactant OTAB from the beginning. For example, consider PPE-SO_3Na-H. When the concentration of OTAB is below 0.015 mM, and the polymer concentration is 9.5×10^{-6} M in repeat units, the OTAB concentration is not high enough to neutralize all the charged side chains on the polymer, thus substoichiometric complexes form, driven by the electrostatic attraction between the polymer side groups and OTAB. This complex has a net negative charge and is soluble in water. In this case, the red shift and enhanced emission might arise from an increase in the effective conjugation length upon binding to the surfactant with its long steric alkyl chains.[52] When the concentration of OTAB is increased to 0.015 mM and 0.020 mM, which is nearly equal to the concentration of polymer repeat unit charges, most of the polymer's charged side groups are neutralized by the electrostatic attraction between opposite charges, so that stoichiometric complexes form. The hydrophobic interactions between parallel alkyl chains and π-π stacking between polymer chains cause the aggregation of these stoichiometric complexes into larger aggregates[85-87] that are not very soluble in water and tend to precipitate. With further increase of the OTAB concentration, the excess OTAB can bind with the neutral complex via hydrophobic interactions between alkyl chains, forming superstoichiometric complexes that have net positive charges and are soluble in water.

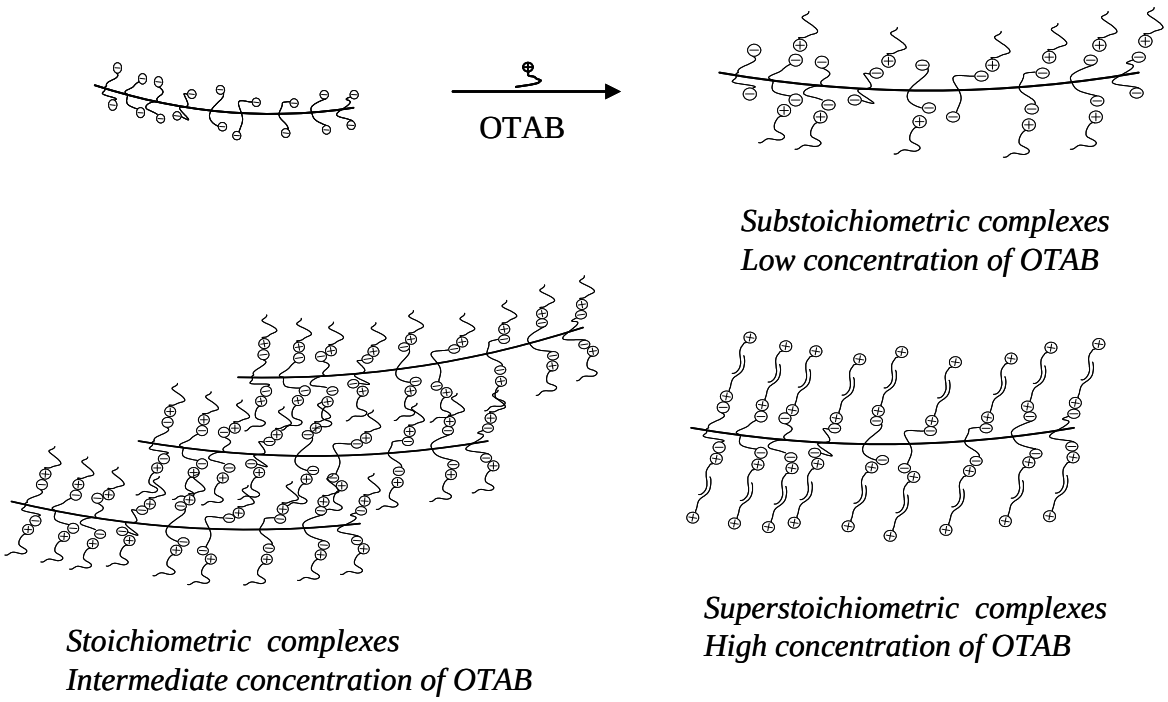

Scheme 5.2. Possible structures of heterocomplexes formed between high charge density polymers and different concentration OTAB. Sodium and bromide ions are not shown in the interest of clarity.

More information regarding the effect of surfactant OTAB comes from FCS data. Figure 5.13a) shows autocorrelation functions measured for PPE- SO_3Na-H (5×10^{-8} M) in 0.03 μM, 3.0 μM, 80.0 μM OTAB solutions and the fitting of each curve. Note that the concentration of PPE-SO_3Na-H in these experiments is lower than the concentration in the steady state experiment (in order to get the best signal to noise ratio as mentioned earlier). As shown in Figure 5.13a, the amplitude of $G(\tau)$ at the intermediate concentration of 3.0 μM of OTAB is much higher than that found at either low or high concentrations of OTAB, indicating that the average fluorophore number is greatly reduced at this concentration. Spikes in the counting rate history and a narrow distribution at low count rates are observed also (Figure 5.13b and its inset). As discussed earlier, this behaviour is attributed to large aggregates that are formed by the stoichiometric complex

between the polymer and the OTAB. This observation agrees very well with the quenched fluorescence intensity observed at intermediate concentration of OTAB in the steady state experiments. More detailed FCS studies of this interactions will be reported elsewhere.[73]

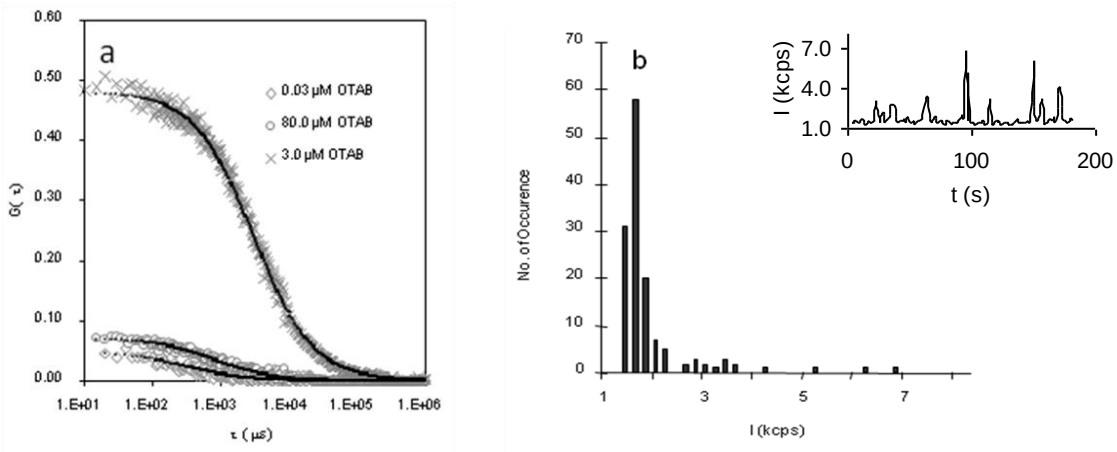

*Figure 5.13 Panel **a)** shows autocorrelation functions of 5.0×10^{-8} M PPE-SO_3Na-H in three different solution conditions; and panel **b)** shows the photon counting rate histogram of 5.0×10^{-8} M PPE-SO_3Na-H in 1.0 μM OTAB aqueous solution*

5.4 SUMMARY AND CONCLUSION

The photophysical properties of four anionic PPE-based conjugated polyelectrolytes under different solution conditions were studied in order to show how the charge density of the polymer chain effects their aggregation. The emission spectra of low charge density polymers in water are dominated by a broad and featureless peak which is characteristic of an excimer-like state, and it is attributed to aggregate formation. Dilution and heating experiments performed on the low charge density polymers identified conditions under which these polymers display

spectra similar to those exhibited in the good solvent–DMSO, in which the polymer is not strongly aggregated. By increasing the charge density on the polymers, to every phenylene ring rather than every other phenylene ring, their solubility in water was increased and their mutual repulsion was enhanced enough to inhibit aggregation. The pH study on the weak conjugated polyelectrolytes suggests that the charge density can be further modified by controlling the solution pH, decreasing the solution pH lowers the charge density and causes aggregates to form. Increasing the solution ionic strength using the simple salt NaCl quenches the emission for all of the polymers. Addition of the surfactant OTAB into the polymer solutions causes the dissociation of the low charge density polymer homoaggregates and causes the formation of heteroaggregates between OTAB molecules and the polyelectrolyte. The large changes in hydrodynamic radius of the fluorophores under various conditions, as determined by FCS, correlate with the spectral changes and demonstrate the aggregation.

This study demonstrates that aggregation and the formation of supramolecular structures in solution depends sensitively on the polyelectrolyte's charge density and the solution conditions. Understanding and predicting the interrelationship of the intermolecular forces in these complex systems and how it determines their self-assembly remains a significant challenge.

5.5 ACKNOWLEDGEMENT

We acknowledge support from the U.S. National Science Foundation (CHE-0415457).

5.6 REFERENCES

(1) Patil, A. O.; Ikenoue, Y.; Wudl, F.; Heeger, A. J. *J. Am. Chem. Soc.* **1987**, *109*, 1858.

(2) Shi, S.; Wudl, F. *J. Am. Chem. Soc.* **1990**, *23*, 2119.

(3) Chen, L.; McBranch, D. W.; Wang, H.-L.; Helgeson, R.; Wudl, F.; Whitten, D. G. *Proc. Natl. Acad. Sci. USA* **1999**, *96*, 12287.

(4) Tan, C.; Pinto, M. R.; Schanze, K. S. *Chem. Commun.* **2002**, 446.

(5) Lukkari, J.; Salomaki, M.; Viinikanoja, A.; Aaritalo, T.; Paukkunene, J.; Kocharova, N.; Kankare, J. *J. Am. Chem. Soc.* **2001**, *123*, 6083.

(6) Cutler, C. A.; Bouguettaya, M.; Reynolds, J. R. *Adv. Mater.* **2002**, *14*, 684.

(7) Kraft, A.; Grimsdale, A. C.; Holmes, A. B. *Angew. Chem.* **1998**, *37*, 403.

(8) Ho, P. K. H.; Kim, J. S.; Burroughes, J. H.; Becker, H. L.; Li, S. F. Y.; Brown, T. M.; Cacialli, F.; Friend, R. H. *Nature* **2000**, *404*, 481.

(9) Sirringhaus, H.; Tessler, N.; Friend, R. H. *Science* **1998**, *280*, 1741.

(10) Zhang, C.; Broun, D.; Heeger, A. J. *J. Appl. Phys.* **1993**, *73*, 5177.

(11) Pei, Q. B.; Yu, G.; Zhang, C.; Yang, Y.; Heeger, A. J. *Science* **1995**, *269*, 1086.

(12) Blom, P. W. M.; de Jong, M. J. M. *Appl. Phys. Lett.* **1996**, *68*, 3308.

(13) Hide, F.; Diaz-Garcia, M. A.; Schwartz, B. J.; Heeger, A. J. *Acc. Chem. Res.* **1997**, *30*, 430.

(14) Harrison, B. S.; Ramey, M. B.; Reynolds, J. R.; Schanze, K. S. *J. Am. Chem. Soc.* **2000**, *122*, 8561.

(15) Rininsland, F.; Xia, W.; Wittenburg, S.; Shi, X.; Stankewicz, C.; Achyuthan, K.; McBranch, D.; Whitten, D. *Proc. Natl. Acad. Sci. USA* **2004**, *101*, 15295.

(16) Liu, M.; Kaur, P.; Waldeck, D. H.; Xue, C.; Liu, H. *Langmuir* **2005**, *21*, 1687.

(17) McQuade, D. T.; Pullen, A. E.; Swager, T. M. *Chem. Rev.* **2000**, *100*, 2537.

(18) Schanze, K. S.; Pinto, M. R. *Proc. Natl. Acad. Sci. USA* **2004**, *101*, 7505.

(19) Heeger, A. J.; Diaz-Garcia., M. A. *Curr. Opin. Solid State Mater.* **1983**, *3*, 16.

(20) Thomas II, S. W.; Joly, G. D.; Swager, T. M. *Chem. Rev.* **2007**, *107*, 1339.

(21) Pinto, M. R.; Schanze, K. S. *Synthesis* **2002**, 1293.

(22) Pinto, M. R.; Kristal, B. M.; Schanze, K. S. *Langmuir* **2003**, *19*, 6523.

(23) Thunemann, A. F.; Ruppelt, D. *Langmuir* **2001**, *17*, 5098.

(24) Jones, R. M.; Bergstedt, T. S.; McBranch, D. W.; Whitten, D. G. *J. Am. Chem. Soc.* **2001**, *123*, 6726.

(25) Yang, R. G., A.; Korystov, D.; Mikhailovsky, A.; Bazan, G. C.; Nguyen, T.-Q. *J. AM. Chem. Soc.* **2006**, *128*, 16532.

(26) Garcia, A.; Yang, R.; Jin, Y.; Walker, B.; Nguyena, T.-Q. *Appl. Phys. Lett.* **2007**, *91*, 153502.

(27) Hoven, C. Y., R.; Garcia, A.; Heeger, A. J.; Nguyen, T.-Q.; Bazan, G. C. *J. AM. Chem. Soc.* **2007**, *129*, 10976.

(28) H. Wu; F. Huang; Y. Mo; W. Yang; D. Wang; J. Peng, Y. C. *Adv. Mater.* **2004**, *16*, 1826.

(29) Chang, C.-H.; Chen, S.-A. *Appl. Phys. Lett.* **2007**, *90*, 103514.

(30) Qiao, Q.; James T. McLeskey, J. *Appl. Phys. Lett.* **2005**, *86*, 153501.

(31) Mwaura, J. K.; Pinto, M. R.; Witker, D.; Ananthakrishnan, N.; Schanze, K. S.; Reynolds, J. R. *Langmuir* **2005**, *21*, 10119.

(32) Chen, L.; McBranch, D. W.; Whitten, D. G. *Chem. Phys. Lett.* **2000**, *330*, 27.

(33) Tan, C.; Atas, E.; Muller, J. G.; Pinto;, M. R.; Kleiman, V. D.; Schanze, K. S. *J. Am. Chem. Soc.* **2004**, *126*, 13685.

(34) Wang, D.; Gong, X.; Heeger, P. S.; Rinisland, F.; Bazan, G. C.; Heeger, A. J. *Proc. Natl. Acad. Sci. USA* **2001**, *99*, 49.

(35) Kumaraswamy, S.; Bergstedt, T.; Shi, X.; Rininsland, F.; Kushon, S.; Xia, W. *Proc. Natl. Acad. Sci. USA* **2004**, *101*, 7511.

(36) Wilson, J. N.; Wang, Y.; Lavigne, J. J.; Bunz, U. *Chem. Commun.* **2003**, 1626.

(37) Pinto;, M. R.; Schanze, K. S. *Proc. Natl. Acad. Sci. U. S. A.* **2004**, *101*, 7505.

(38) Ambade, A. V.; Sandanaraj, B. S.; Klaikherd, A.; Thayumanavan, S. *Polymer International* **2007**, *56*, 474.

(39) Liu, B.; Bazan, G. C. *Chem. Mater.* **2004**, *16*, 4467.

(40) Kushon, S. A.; Ley, K. D.; Bradford, K.; Jones, R. M.; McBranch, D.; Whitten, D. *Langmuir* **2002**, *18*, 7245.

(41) Gaylord, B. S.; Heeger, A. J.; Bazan, G. C. *Proc. Natl. Acad. Sci. USA* **2002**, *99*, 10954.

(42) Hoeben, F. J. M.; Jonkheijm, P.; Meijer, E. W.; Schenning, A. P. H. J. *Chem. Rev.* **2005**, *105*, 1491.

(43) Thunemann, A. F.; Ruppelt, D. *Langmuir* **2000**, *16*, 3221.

(44) Schnablegger, H.; Antonietti, M.; Goltner, C.; Hartmann, J.; Colfen, H.; Samori, P.; Rabe, J. P.; Hager, H.; Heitz, W. J. *Colloid. Interface Sci* **1999**, *212*, 24.

(45) Nguyen, T.-Q.; Schwartz, B. J. *J. Chem. Phys.* **2002**, *116*, 8198.

(46) Dubas, S. T.; Schlenoff, J. B. *Macromolecules* **2001**, *34*, 3736.

(47) Dubas, S. T.; Schlenoff, J. B. *Macromolecules* **1999**, *32*, 8153.

(48) Shiratori, S. S.; Rubner, M. F. *Macromolecules* **2000**, *33*, 4213.

(49) Kaur, P.; Yue, H.; Wu, M.; Liu, M.; Treece, J.; Waldeck, D. H.; Liu, H.; Xue, C. *J. Phys. Chem. B* **2007**, *111*, 8589.

(50) Chu, Q.; Pang, Y. *Macromolecules,* **2003**, *36*, 4614.

(51) Fan, Q.; Zhou, Y.; Lu, X. M.; Hou, H. M.; Huang, W. *Macromolecules,* **2005**, *38*, 2927.

(52) Chen, L.; Xu, S.; McBranch, D. W.; Whitten, D. G. *J. Am. Chem. Soc.* **2000**, *122*, 9302.

(53) Huang, Y.-Q.; Fan, Q.-L.; Xiao-Mei;, L.; Fang, C.; Liu, S.-J.; Wei, H. *J. Polymer Sci.* **2006**, *44*, 5778.

(54) Wang, F.; Bazan, G. C. *J. Am. Chem. Soc.* **2006**, *128*, 15786.

(55) Gao, Y.; Wang, C.-C.; Wang, L.; Wang, H.-L. *Langmuir* **2007**, *23*, 7760.

(56) Haskins-Glusac, K.; Pinto, M. R.; Tan, C.; Schanze, K. S. *J. Am. Chem. Soc.* **2004**, *126*, 14964.

(57) Halkyard, C. E.; Rampey, M. E.; Kloppenburg, L.; Studer-Martinez, S. L.; Bunz, U. H. F. *Macromolecules* **1998**, *31*, 8655.

(58) Yang, J. S.; Swager, T. M. *J. Am. Chem. Soc.* **1998**, *120*, 11864.

(59) Gaylord, B. S.; Wang, S.; Heeger, A. J.; Bazan, G. C. *J. Am. Chem. Soc.* **2001** *123*, 6417.

(60) Wang, C.; Tam, K. C. *J. Phys. Chem. B* **2004**, *108*, 8976.

(61) Wang, F.; Bazan, G. C. *J. Am. Chem. Soc* **2006**, *128*, 15786.

(62) Bunz, U. H. F. *Chem. Rev.* **2000**, *100*, 1605.

(63) Kim, J.; Swager, T. M. *Nature* **2001**, *411*, 1030.

(64) Walters, K. A.; Ley, K. D.; Schanze, K. S. *Langmuir* **1999**, *15*, 5676.

(65) Kim, I.-B.; Dunkhorst, A.; Gilbert, J.; Bunz, U. H. F. *Macromolecules* **2005**, *38*, 4560.

(66) GPC studies were performed by American Polymer Std., 8680 Tyler Blvd. Mentor, OHIO, 44060.

(67) Morris, J. V.; Mahaney, M. A.; Huber, J. R. 9,10-Diphenylanthracene as a reference standard in different solvents; Fluorescence quantum yield determinations., 1976; Vol. 80; pp 969.

(68) Liu, M.; Waldeck, D. H.; Oliver, A. M.; Head, N. J.; Paddon-Row, M. N. *J. Am. Chem. Soc.* **2004**, *126*, 10778.

(69) Koppel, D. E. *Phys. Rev. A* **1974**, *10*, 1938.

(70) Pristinski, D. K., V.; Sukhishvili, S. A. *J. Chem. Phys.* **2004**, *122*, 14907.

(71) Van Rompaey, E.; Sanders, N.; Van Craenenbroeck, E.; Engelborghs, Y.; De Smedt, S. C.; Demeester, J. *Macromolecules* **2000**, *33*, 8280.

(72) Krichevsky, O.; Bonnet, G. *Rep. Prog. Phys.* **2002**, *65*, 251.

(73) Yue, H.; Wu, M.; Waldeck, D. H. *Submitted*.

(74) Hess, S. T.; Webb, W. W. *Biophys J.* **2002**, *83*, 2300.

(75) Culbertson, C. T.; Jacobson, S. C.; Ramsey, J. M. *Talanta* **2002**, *56*, 365.

(76) Kim, I. B.; Dunkhorst, A.; Gilbert, J.; Bunz, U. H. F. *Macromolecules* **2005**, *38*, 4560.

(77) Odijk, T. *J. Polym. Sci. Polym. Phys. Ed.* **1977**, *15*, 477.

(78) Skolnick, J.; Fixman, M. *Macromolecules* **1977**, *10*, 944.

(79) Balanda, P. B.; Ramey, M. B.; Reynolds, J. R. *Macromolecules* **1999**, *32*, 3970.

(80) Deans, R.; Kim, J.; Machacek, M. R.; Swager, T. M. *J. Am. Chem. Soc.* **2000**, *122*, 8565.

(81) Wang, D. *Ph.D. Dissertation, University of California, Santa Barbara, 2001*

(82) Rigler, R.; Elson, E. S. *Fluorescence correlation spectroscopy: theory and applications* **2001**, *Springer-verlag, Berlin*.

(83) Smith, A. D.; Shen, C. K.-f.; Helgeson, R.; Schwartz, B. J. *Res. Chem. Intermed.* **2007**, *33*, 125.

(84) Miteva, T.; Palmer, L.; Kloppenburg, L.; Neher, D.; Bunz, U., H. F. *Macromolecules* **2000**, *33*, 652.

(85) Kogej, K.; Skerjane, J. *Physical Chemistry of Polyelectrolytes*, *Radeva, T., Ed.; Mercel Dekker, Inc.: New York, Basel, 2001, p 793*.

(86) Tam, K. C.; Wyn-Jones, E. *Chem. Soc. Rev.* **2006**, *35*, 693.

(87) MacKnight, W. J.; Ponomarenko, E. A.; Tirrell, D. A. *Acc. Chem. Res.* **1998**, *31*, 781.

PART II

6.0 INTRODUCTION TO NANOCRYTAL-BASED SOLAR CELLS

The growing world energy demands, running out fossil fuels resources, as well as the considerations on green house gas emissions have motivated the tremendous interest in scientific and industrial areas research in developing renewable alternative energy sources. Among the possibilities, solar energy is the most promising renewable energy source and would solve the disastrous energy deficit crisis in the future. Previous studies of solar cells have been dominated by solid-state junction devices, usually made of crystalline or amorphous silicon. Because of expensive and energy-intensive, high-temperature and high-vacuum, fabrication processes, however, the manufacturing cost of these devices make them not competitive compared to fossil fuels.

6.1 SEMICONDUCTOR NANOCRYSTAL BASED SOLAR CELLS

Colloidal semiconductor nanocrystals (NCs), also known as quantum dots (QDs), represent probably the most interesting and important class of inorganic solution processed electronic materials. Because of their novel size-dependent electronic and optical properties,[11,12] they have shown great promise for many applications such as photovoltaic cells,[1-3] bioimaging,[4-6] sensing/detection,[7] light-emitting diodes (LEDs),[8] lasers.[9,10] The worldwide scientific research in this area has grown exponentially over the past two decades and has provided relatively simple and

inexpensive chemical synthesis methods for the creation of nanometer-sized crystals with controlled sizes and shapes, , which are amendable to further synthetic modification. In addition, multiple exciton generation (MEG) in some NCs, e.g., PbSe, by one absorbed photon, is one exciting new phenomenon that is unique to these nanomaterials and offers a mechanism for dramatically improving the efficiency of NC-based solar cells.[13,14]

6.1.1 Synthesis of NCs/QDs

Typically, colloidal nanomaterials are synthesized by reacting appropriate molecular precursors, that is, inorganic salts or organometallic compounds. Production of monodisperse colloids requires a temporally discrete nucleation event followed by slower controlled growth of the existing nuclei (see Figure 6.1).[15] Ostwald ripening is commonly observed in many systems in which the average NCs sizes increase over time and is compensated for by a decrease in the average number of NCs.[16]

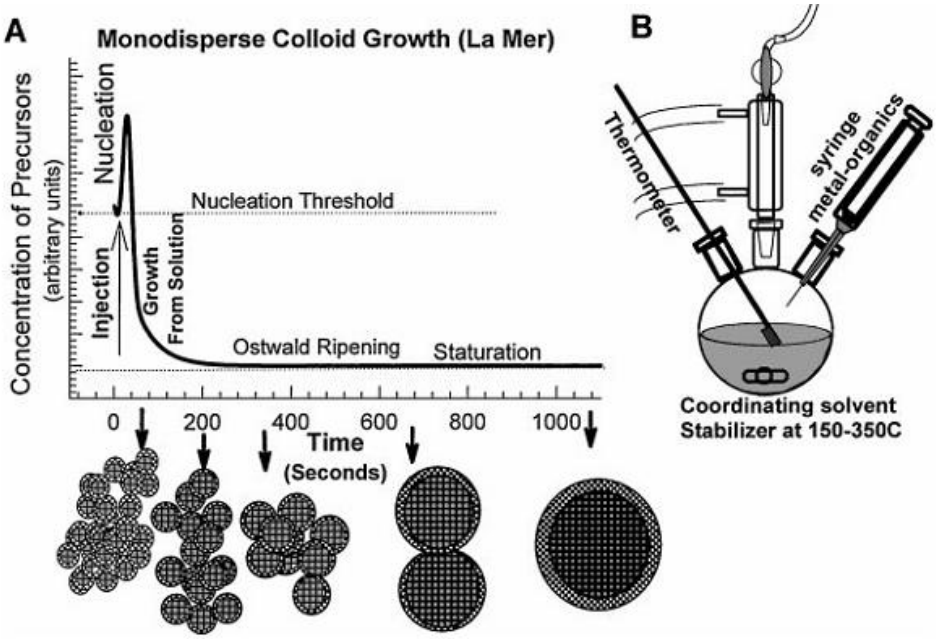

Figure 6.1 ***(A)*** *Cartoon depicting the stages of nucleation and growth for the preparation of monodisperse NCs in the framework of the La Mer model. As NCs grow with time, a size series of NCs may be isolated by periodically removing aliquots from the reaction vessel.* ***(B)*** *Representation of the simple synthetic apparatus employed in the preparation of monodisperse NC samples. Reproduced from ref 15.*

Surfactant molecules play an important role in tuning the kinetics of nucleation and growth of NCs. Typical surfactants include long-chain carboxylic and phosphonic acids, alkanethiols, alkyl phophines (e.g. trioctylphosphine, TOP), alkylphophine oxides (e.g., trioctylphosphine oxide, TOPO) and alkylamines (e.g., hexadecylamine, HDA). Synthesis of monodispersed semiconductor QDs have achieved significant success. Typical reactions used for the synthesis of II-VI (CdSe, CdTe, CdS),[17] III-V (InP, InAs)[18] and IV-VI (PbS, PbSe, PbTe)[1] QDs are outlined by following three reactions.

$$CdO + (C_8H_{17})_3PSe \xrightarrow{300\ ^\circ C,\ HDA\text{-}TOPO\text{-}TOP} CdSe\ nanocrystals$$

$$InCl_3 + [(CH_3)_3Si]_3P \xrightarrow{260^\circ C,\ TOP} InP\ nanocrystals$$

$$Pb(CH_3COO)_2 + (C_8C_{17})_3PSe \xrightarrow{180\ ^\circ C.\ oleic\ acid} PbSe\ nanocrystals$$

Some transmission electron micrographs (TEM) examples of colloidal semiconductor QDs are shown in Figure 6.2

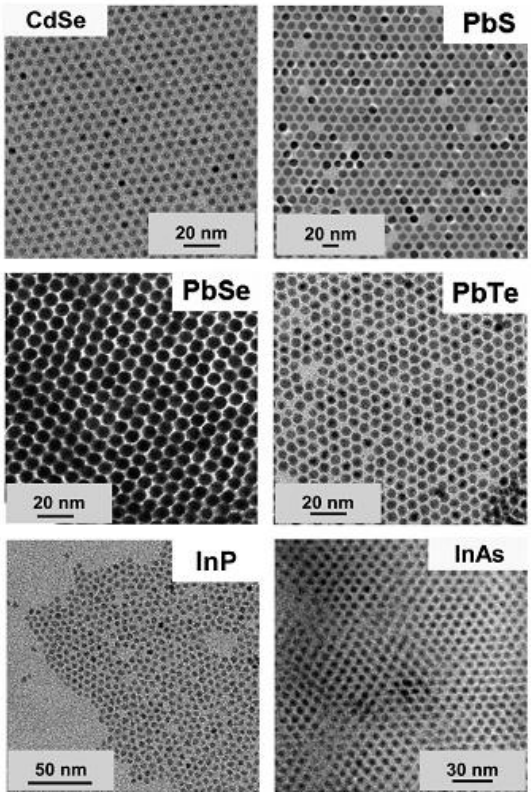

Figure 6.2 Examples of colloidal semiconductor nanocrystals of different materials. Reproduced from ref[19]

One of the most important manifestations of quantum confinement in semiconductors is the relationship between the electronic structure and particle size.[12] Figure 6.3 shows that the emission color for colloidal solutions of CdSe/ZnS core-shell NCs can be tuned by varying particle size[20].

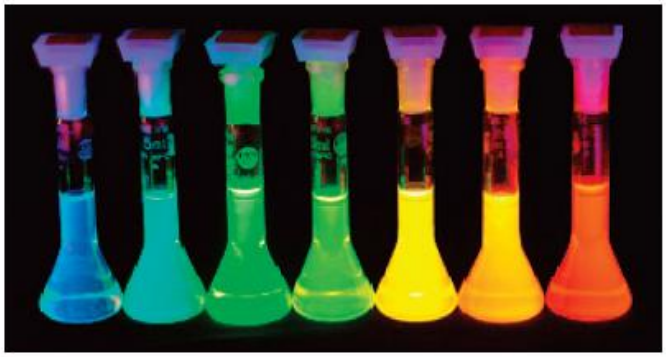

Figure 6.3 Size-dependent change of the emission color for colloidal solutions of CdSe/ZnS core shell nanocrystals. The particles with the smallest (~1.7nm) CdSe core emit blue; the particles with the largest (~5nm) core emit red. Reproduced from ref 20.

In addition, some high quality QDs can also be synthesized in aqueous medium. For example, CdTe QDs can be prepared by reacting a cadmium salt with freshly prepared NaHTe solution in an aqueous medium containing thiol molecules with polar groups. It is generally accepted that the thiol group binds to the QDs surface and the deprotonated carboxylic acid group provides colloidal stability due to electrostatic repulsion of the charged QDs.[21]

6.1.2 Photovoltaics Terminology[19,22]

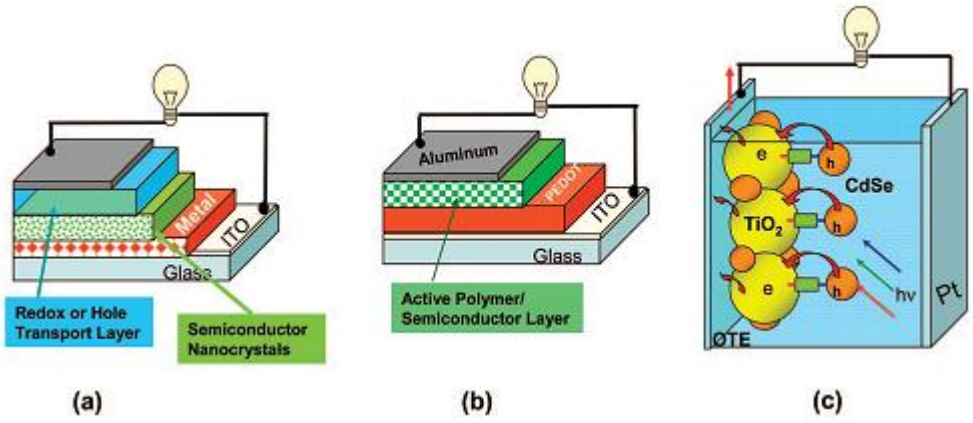

Figure 6.4 Schematic diagram showing the strategies to develop quantum dot (semiconductor nanocrystal) based solar cells: (a) metal-semiconductor junction, (b) polymer-semiconductor, and (c) semiconductor-semiconductor systems; adapted from ref 23.

There are three different types of solar cells that capitalize on salient properties of semiconductor NCs: (a) metal-semiconductor or Schottky junction photovoltaic cell, (b) semiconductor nanostructure-polymer solar cell, and (c) semiconductor quantum dot sensitized

solar cell (QDSSC).[23] Figure 6.4 illustrates each of these three different motifs. The device performance of photovoltaic cell can be characterized by the light-to-energy conversion efficiency, η, which is defined by Equation 1,

$$\eta = \frac{V_{OC} I_{SC} FF}{P_{in}} \qquad (1)$$

where *V*oc is the open-circuit voltage, *I*sc is the short-circuit current, FF is the fill factor, and P_{in} is the incident light power. For solar cell testing, workers typically use an AM 1.5 light source, which is standardized at ~1000 Wm^{-2} with a spectral intensity distribution matching that of the sun of the earth's surface at an incident angle of 45 °. Equation 1 reveals that higher values of parameters such as, I_{SC}, V_{OC} and FF yield larger light to electricity power conversion efficiency. In Figure 6.5, a representative *I-V* curve is shown in which V_{OC}, I_{SC}, V_m, and I_m for a photovoltaic device are marked. The subscript m denotes the maximum power values. In detail, *V*oc is the electrical potential difference between two terminals of a device when the circuit is open or broken; that is, under this condition, no electric current flows through the external circuit. *V*oc is the maximum possible voltage that can be generated by the device. In bulk heterojunction solar cells (e.g. organic P3HT/PCBM solar cells), the maximum V_{OC} obtained by a device is limited to the energy level difference between the HOMO of the donor and the LUMO of the acceptor.[24] Different relaxation and dissipative phenomena cause the *V*oc to be less than this ideal limit in bulk heterojunction cells. The short-circuit current is defined as the current that reaches the two terminals without an applied field; that is, under this condition, V=0. *I*sc is the maximum number of the photogenerated carriers that can be obtained from the solar cell. It is determined by the product of the charge carrier density *n* under illumination, the carrier mobility μ, and the electrical field *E* acting on the carriers,

$$I_{SC} = en\mu E \tag{2}$$

The fill factor (FF) is the ratio between the maximum power generated ($I_m V_m$) and the product of I_{SC} and V_{OC}, namely

$$FF = \frac{I_m V_m}{I_{SC} V_{OC}} \tag{3}$$

The fill factor determines the quality of the voltage-current characteristics. Another important measure of a solar cells performance, is the external quantum efficiency (IPCE), which is defined as equation (4),

$$IPCE\ (\lambda) = \frac{1240\ I_{SC}}{\lambda P_{in}} \tag{4}$$

IPCE values up to 76% have been reported for bulk heterojunction solar cells at the absorption maximum[25] and 100% for DSSCs. The IPCE depends on the light-harvesting efficiency (η_{lh}), charge injection efficiency (η_{inj}), and charge collection efficiency (η_{cc}) by

$$IPCE = \eta_{lh} * \eta_{inj} * \eta_{cc} \tag{5}$$

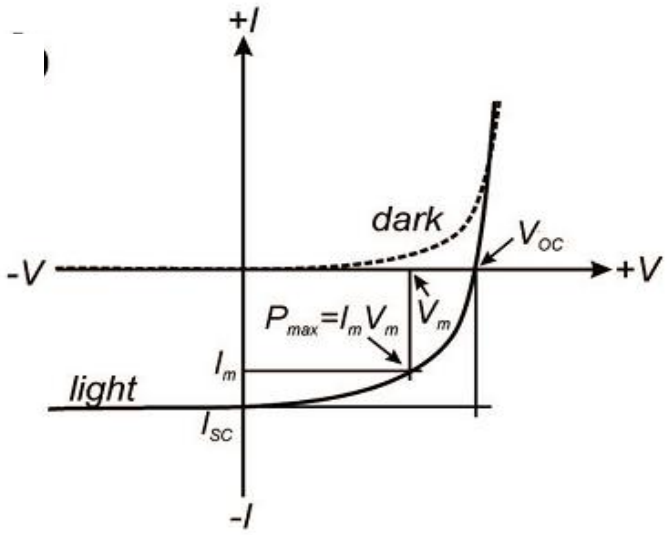

Figure 6.5 I-V *curve for a photovoltaic cell is shown; adapted from ref 19.*

The light-harvesting efficiency, $\eta_{lh,}$ is defined by the ratio of the amount of absorbed photons to that of incoming photons. Hence, in a DSSC, for example, an increase of the absorption coefficient, the density, or the thickness of adsorbed sensitizer can improve η_{lh}. The charge injection efficiency, $\eta_{inj,}$ is determined by factors such as the potential difference between the LUMO of the adsorbed sensitizer and the conduction band edge of the TiO_2, the acceptor density in TiO_2, and the distance between the surface of TiO_2 and the dye. To achieve a high η_{cc}, the electrons must diffuse and reach the electrode before recombination processes occur. The diffusion length of electrons can be expressed by $L = (D\tau)^{1/2}$, where D is the electron diffusion coefficient and τ is electron lifetime in nanoporous TiO_2. A high η_{cc} can be realized by a thinner film, a higher diffusion coefficient, and a longer lifetime for the free electrons.

6.2 IMPROVING THE HYBRID POLYMER-SEMICONDUCTOR SOLAR CELLS EFFICIENCY

Most of the reports to date that use QDs in photovoltaic devices are hybrid polymer-semiconductor designs. These materials possess some of the desirable properties of bulk inorganic semiconductors, but are more easily produced; both polymers and semiconductor QDs have excellent solution processing ability. Nonetheless, conventional inorganic solar cells typically exhibit solar power conversion efficiencies of 10%, and can reach up to 30% efficiency for the most advanced models.[26] For organic solar cells, on the other hand, the power conversion efficiency has only reached up to 2-6%.[27] The main reason for the superior

efficiency of inorganic devices over organic ones lies in the high intrinsic carrier mobilities in inorganic

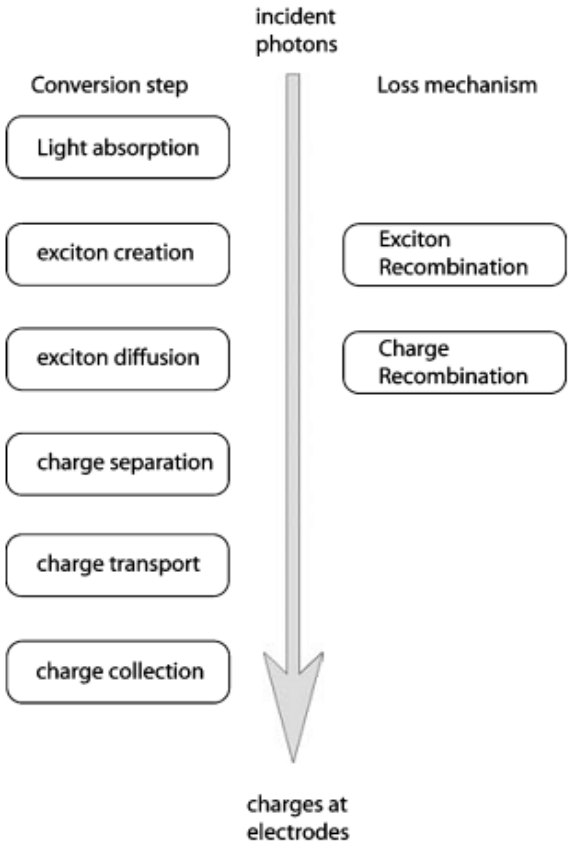

Figure 6.6 Schematic flow chart showing the important processes in molecular and nanocrystalline solar cells. recombination of excitons can be both radiative and nonradiative; adapted from ref 41.

semiconductors. In most conjugated polymers, electron mobilities are typically below 10^{-4} $cm^2V^{-1}s^{-1}$, which leads to more recombination loss for the charge carriers. In addition, the binding energy of an exciton in a bulk inorganic semiconductors is close to kT (~ 25 meV), and the absorption of light leads to essentially separated, free charge carriers. However, the exciton binding energy is substantial in molecular systems such as conjugated polymers or nanocrystals.[28] So the creation of carriers after light absorption is divided into three steps:

exciton creation, exciton dissociation, and charge transport.[41] (Figure 6.6) Thus, the introduction of another material into a polymer photovoltaic that enhances the charge exciton dissociation and charge transport would be beneficial for the overall efficiency. Inorganic semiconductor QDs are a promising way to enhance the efficiency of polymer based photovoltaics. Numerous reports have been focused on hybrid polymer-nanocrystal solar cells based on CdSe,[29,30] CdTe,[31] PbS,[32] PbSe, [33]ZnO, [34]TiO_2[35] and polymers, such as P3HT, MEH-PPV and their derivatives. To achieve high performance of hybrid polymer-semiconductor solar cells, some important factors have been investigated.

(i) Capping ligands on nanocrystals In 1996 Greenham et al[36]. first incorporated CdSe NCs into MEH-PPV and they found that the capping ligands, e.g. the surface of the NCs play an important role in determining the charge transport rate from polymers to NCs, hence the overall conversion efficiency. It was observed that after removing the original capping ligands tri-n-octylphosphineoxide (TOPO) or other conventional ligands with short pyridines, the NCs and the polymers can be brought closer and the charge transfer process facilitated.

(ii) Shape directionality of NCs Success in the synthesis of NCs with shape anisotropy has been achieved by Peng et al. to yield NCs with rod like morphologies.[37] It was observed that the shape directionality of the NCs plays an important role in charge transport to the cathode in photovoltaic devices; in particular, it was shown that using higher aspect ratios of CdSe nanorods enhanced the External Quantum Efficiency (EQE) and power conversion efficiency.[30](See Figure 6.7)

a

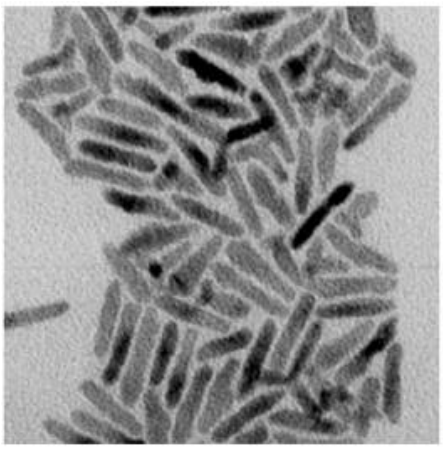

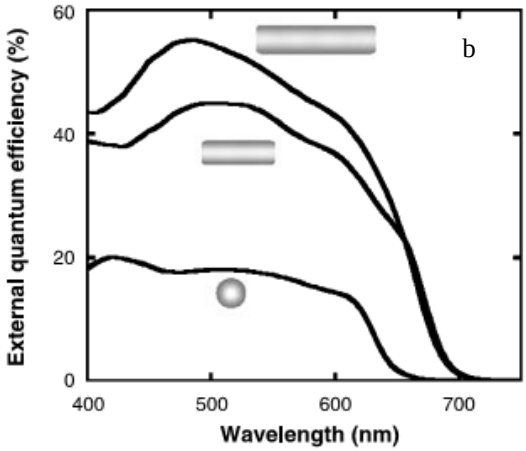

Figure 6.7(a) TEM image of nanorod shaped CdSe nanocrystals. (b) EQEs of 7nm diameter nanorods with lengths 7,30,and 60nm.The intensity of irradiation was0 .084mWcm^{-2}; adapted from ref 30.

(iii) Surface roughness of films A series of experiments done by Huynh et al. indicated that smoother films of CdSe-nanorod-P3HT composites resulted in higher EQEs.[38] They observed that the surface roughness, obtained by tapping mode Atomic Force Microscopy (AFM-TM) images, relates to the phase separation, and this roughness can be modified by pyridine concentration. For low pyridine concentrations, the topography of these images reveals a very rough surface, while higher, i.e. ~8 vol.% pyridine, yields smoother films.

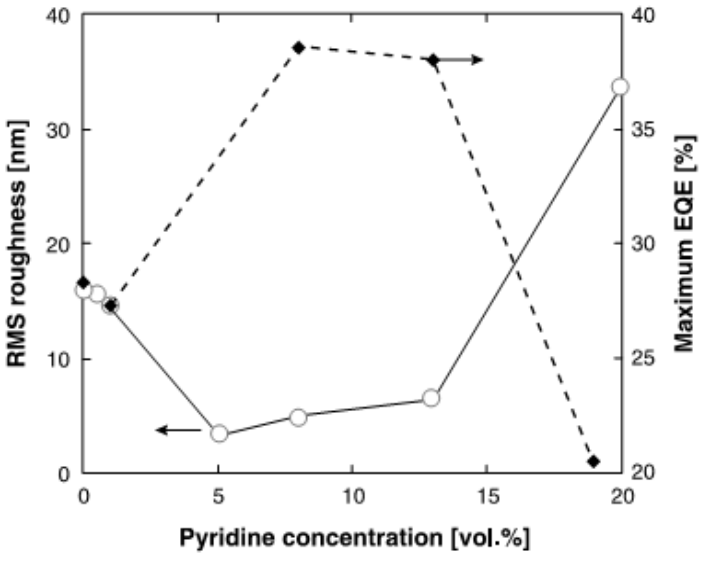

Figure 6.8 Surface roughness (open circles) of films containing 90 wt.% of 8 nm by 13 nm CdSe NCs dispersed in P3HT, spin cast from various concentrations of pyridine in chloroform. The maximum EQE (solid diamonds) is shown of devices made from these films, adapted from ref 38.

(iv) Using NCs that absorb in the red spectral region. Most of the organic semiconductor and CdSe NCs absorb light in the visible range, whereas solar irradiation at the Earth's surface ranges from 300 to 2100 nm, approximately. It is desirable that NCs absorb as much as possible in the red region of solar spectrum. Bulk materials of CdTe absorb around 820 nm, where the solar radiation is centered, thus it is expected to be superior in light harvesting, as compared to CdSe based solar cells. Similarly, the bulk material band gaps of PbS and PbSe are 0.37 and 0.26 eV, respectively, indicating that these materials can collect near-IR solar radiation. However, the overall conversion efficiency of the solar cell based on these materials is typically low.[31,39] Largely, because the open circuit voltage decreases, caused by the lowering of LUMO of the electron acceptor, faster than the increase in the short circuit current, which results from the increased light absorption.[40] Some other factors, like

inefficiencies in the percolation network and large phase separation in composite films may also play a role.

In summary, because of the salient features of QDs, nanocrystal semiconductor based solar cells promise to provide a new generation of photovotaics that have higher efficiency and lower costs. Among them, the performance of hybrid polymer-nanocrystal solar cells is determined by an interplay and compromise between surface capping of NCs, roughness/morphology of the interface between two components, the shape directionality, and chemical composition of the NCs. To further improve the performance of these solar cells one needs to optimize the above mentioned parameters.

6.3 REFERENCES

(1) Talapin, D. V.; Murray, C. B. *Science* **2005**, *310*, 86.

(2) Maheshwari, V.; Saraf, R. F. *Science* **2006**, *312*, 1501.

(3) Sapsford, K. E.; Medintz, I. L.; Golden, J. P.; Deschamps, J. R.; Uyeda, H. T.; Mattoussi, H. *Langmuir* **2004**, *20*, 7720.

(4) Bruchez, M., Jr.; Moronne, M.; Gin, P.; Weiss, S.; Alivisatos, P. A. *Science* **1998**, *281*, 2013.

(5) Chan, W. C. W.; Nie, S. *Science* **1998**, *281*, 2016.

(6) Michalet, X.; Pinaud, F. F.; Bentolila, L. A.; Tsay, J. M.; Doose, S.; Li, J. J.; Sundaresan, G. W., A. M.; Gambhir, S. S.; Weiss, S. *Science* **2005**, *307*, 538.

(7) Jin, W. J.; Fernandez-Arguelles, M. T.; Costa-Fernandez, J. M.; Pereiro, R. S.-M., A. *Chem.Commun.* **2005**, 883.

(8) Sundar, V. C.; Lee, J.; Heine, J. R.; Bawendi, M. G.; Jensen, K. F. *Adv. Mater.* **2000**, *12*, 1102.

(9) Artemyev, M.; Woggon, U.; Wannemacher, R.; Jaschinski, H.; Langbein, W. *Nano Lett.* **2001** *1*, 309.

(10) Klimov, V. I.; Mikhailovsky, A. A.; Xu, S.; Malko, A.; Hollingsworth, J. A.; Leatherdale, C. A.; Eisler, H. J.; Bawendi, M. G. *Science* **2000**, *290*, 314.

(11) Alivisatos, A. P. *Science* **1996**, *271*, 933.

(12) Brus, L. E. *J. Chem. Phys.* **1986**, *90*, 2555.

(13) Ellingson, R. J.; Beard, M. C.; Johnson, J. C.; Yu, P.; Micic, O. I.; Nozik, A. J.; Shabaev, A.; Efros, A. L. *Nano Lett.* **2005**, *5*, 865.

(14) Schaller, R. D.; Sykora, M.; Pietryga, J. M.; Klimov, V. I. *Nano Lett.* **2006**, *6*, 424.

(15) Murray, C. B.; Kagan, C. R.; Bawendi, M. G. *Annu. Rev. Mater. Sci.* **2000**, *30*, 545.

(16) DeSmet, Y.; Deriemaeker, L.; Finsy, R. *Langmuir* **1997**, *13*, 6884.

(17) Murray, C. B.; Norris, D. J.; Bawendi, M. G. *J.Am.Chem.Soc.* **1993**, *115*, 8706.

(18) Micic, O. I.; Curtis, C. J.; Jones, K. M.; Sprague, J. R.; Nozik, A. J. *J.Phys.Chem.* **1994**, *98*, 4966.

(19) Talapin, D. V.; Lee, J. S.; Kovalenko, M. V.; Shevchenko, E. V. *Chem. Rev.* **2010**, *110*, 389.

(20) Rogach, A. L.; Talapin, D. V.; Shevchenko, E. V.; Kornowski, A.; Haase, M.; Weller, H. *Ad .Funct.Mater.* **2002**, *12*, 653.

(21) Gaponik, N.; Talapin, D. V.; Rogach, A. L.; Hoppe, K.; Shevchenko, E. V.; Kornowski, A.; Eychmu ¨ller, A.; Weller, H. *J.Phys.Chem.B* **2002**, *106*, 7177.

(22) Ma, W.; Yang, C.; Gong, X.; Lee, K.; Heeger, A. J. *Adv. Funct. Mater.* **2005**, *15*, 1617-1622.

(23) Kamat, P. V. *J. Phys. Chem. C* **2008**, *112*, 18737.

(24) Brabec, C. J.; Cravino, A.; Meissner, D.; Sariciftci, N. S.; Rispens, M. T.; Sanchez, L.; Hummelen, J. C.; Fromherz, T. *Thin Solid Films* **2002**, 368.

(25) Padinger, F.; Rittberger, R.; Sariciftci, N. S. *Adv. Funct. Mater.* **2003**, *13*, 85.

(26) Green, M. A.; Emery, K.; King, D. L.; Lgari, S.; Warta, W. *Prog. Photovoltaics* **2001**, *9*, 287.

(27) Shaheen, S. E. e. a. *Appl. Phys. Lett.* **2001**, *78*, 841.

(28) Scholes, G. D.; Rumbles, G. *Nature. Mater.* **2006**, *5*, 683.

(29) Sun, B.; Marx, E.; Greenham, N. C. *Nano Lett.* **2003**, *3*, 961.

(30) Huynh, W. U.; Dittmer, J. J.; Alivisatos, A. P. *Science* **2002**, *295*, 2425.

(31) Kumar, S.; Nann, T. *J. Mater. Res.* **2004**, *19*, 1990.

(32) McDonald, S.; Konstantatos, G.; Zhang, S.; Cyr, P. W.; Kleme, J. D.; Levina, L.; Sargent, E. H. *Nature. Mater.* **2005**, *4*, 138.

(33) Qi, D.; Fischbein, M.; Drndic, M.; Selmic, S. *Appl. Phys. Lett.* **2005**, *86*, 093103.

(34) Beek, W. J. E.; Wienk, M. M.; Janssen, R. A. J. *Ad .Funct.Mater.* **2006**, *16*, 1112.

(35) Ravirajan, P.; Haque, S. A.; Durrant, J. R.; Bradley, D. D. C.; Nelson, J. *Adv. Funct. Mater.* **2005**, *15*, 609.

(36) Greenham, N. C.; Peng, X.; Alivisatos, A. P. *Phys. Rev. B.* **1996**, *54*, 17628.

(37) Peng, X.; Manna, L.; Yang, W.; Wickham, J.; Scher, E.; Kadavanich, A.; Alivisatos, A. P. *Nature* **2000**, *404*, 59.

(38) Huynh, W. U.; Dittmer, J. J.; Libby, W. C.; Whitting, G. L.; Alivisatos, A. P. *Adv. Funct. Mater.* **2003**, *13*, 73.

(39) Chaudhari, K. R.; Sahoo, Y.; Ohulchansky, T. Y.; Prasad, P. N. *Appl. Phys. Lett.* **2005**, *87*, 073110.

(40) Shockley, W.; Queisser, H. J. *J. Appl. Phys.* **1961**, *32*, 510.

(41) Kumar, S.; Scholes, G. D. Microchim Acta. **2008**, 160, 315

7.0 CHARGE TRANSFER AND FLUORESCENCE QUENCHING OF NANOCYRSTAL ASSEMBLIES

This work has been published as Mingyan Wu, Prasun Mukherjee, Daniel N. Lamont and David H. Waldeck, J. Phys. Chem. C.; (2010); 114, 13, 5751-5759. Thesis author synthesized the NPs and performed all the spectroscopic measurements.

Abstract

Electron transfer (ET) in aggregates of cadmium selenide, CdSe, and cadmium telluride, CdTe, nanoparticles (NPs) was studied in aqueous solution by fluorescence quenching. Both steady state and time-resolved fluorescence measurements were used to quantify how the ET depends on the nature of the NP assemblies. The aggregation of CdSe and CdTe NPs was controlled by the electrostatic attraction of the charged functionalities placed on the NP surface coating. Electron transfer quenching was found to depend on three factors: the interparticle distance, the energetic alignment of the NP bands (hence the size of the NPs), and the direction of the electric field between the NPs, created by their surface charges.

7.1 INTRODUCTION

Motivated by the increasing worldwide demand for clean energy resources, an effort is being made to develop relatively cheap and highly efficient solar cells. [1,2] Bulk heterojunction (BHJ) solar cells, which are formed by the nanoscale phase separation of organic materials, are one promising new photovoltaic (PV) technology due to their potential as a low cost photovoltaic technology.[3-5] However, the power conversion efficiency of BHJ solar cells is low compared to silicon-based p-n junction solar cells. The highest certified efficiency for BHJ solar cells now is in the range of 6 to 7% and the suggested maximum efficiency is in the range of 10-12%.[6,7] To achieve the highest power conversion efficiency, some prerequisites need be satisfied: optimized energy levels of donor and acceptor materials, efficient charge transport in the donor-acceptor blend, efficient charge generation and limited recombination losses.[7] The formation of composites of organic conductors with inorganic nanoparticles (NPs) is one possible solution to this challenge. Because of their size dependent electronic and optical properties,[8,9] inorganic semiconductor nanoparticles (NPs) have shown great promise for many applications such as photovoltaic cells,[10-13] bioimaging,[14-17]sensing/detection, [18,19] light-emitting diodes (LEDs), [20,21] lasers,[22,23] etc. The worldwide scientific research in this area has grown exponentially because the chemical synthesis of nanometer-sized crystals with controlled size and shape is relatively simple and inexpensive,[24-26] and the NPs are amenable to further synthetic modification. Thus they can serve as building blocks to prepare larger and more complex architectures, *e.g.* NP molecules, two-dimensional arrays, and three-dimensional assemblies. The properties of these

nanoscale, and larger assemblies depend on the properties of the individual NPs, and on the chemical, electronic, and magnetic coupling between them. [27-31]

Controlling the charge-transfer between semiconductor NPs in assemblies[32,33] is essential for improving the performance of photovoltaic cells[34] and LEDs.[35] For example, CdS,[36] CdSe,[37] and PbS[38] NPs, among others, have been used as light absorbing sensitizers for large band gap metal oxide materials (TiO_2, SnO_2). These semiconductor NPs have been shown to enhance the metal oxide's photoelectrochemical and photocatalytic activities by absorbing visible photons and injecting electrons (or holes) into the metal oxide. Recent reports of multiple exciton generation (MEG) by one absorbed photon, in some NPs, is one exciting new phenomenon that is unique to these nanomaterials and offers a mechanism for dramatically improve the efficiency of NP-based solar cells.[39,40] Efficient charge transfer requires strong electronic coupling between the semiconductor NPs and the metal oxide, and efficient charge separation requires favourable energetics (band alignment) to inhibit back electron transfer.[41-45] Generally, closely packed assemblies of NPs may be obtained in different ways, covalently or noncovalently, including drop-casting,[28,46] Langmuir methods,[47] cross-linking precipitation,[48,49] and stepwise self-assembly.[50,51] The exploitation of electrostatic interactions has proved to be a simple, effective approach for generating organized assemblies of charged NPs[52,53]and this latter approach is used here.

Interfacial photoinduced charge transfer to metal NPs[54,55] or dye/chromophore molecules to semiconductor NPs have been extensively investigated.[33,56,57] Except for the previously mentioned sensitization of TiO_2 by NPs,[36-38] core-shell[58] and nanorod heterostructure materials, [59,60] the charge transfer between semiconductor NPs has drawn little attention, especially CdSe and CdTe which are otherwise extensively studied. Recently, Gross et al. studied the charge

separation between thioglycolic (TGA) capped CdTe and CdSe NP aggregates, achieved by the incorporation of divalent Ca^{2+} ions between them.[53] Like that work, this study investigates charge transfer between CdSe and CdTe NPs that have a type II band alignment. Instead of inducing association of similarly charged NPs with divalent Ca^{2+} ions, the charge transfer assembly is formed by the spontaneous self-assembly of the two oppositely charged NPs and can be manipulated by variation of their surface charge. The NP compositions and sizes are chosen so that energy transfer quenching is minimized and the charge transfer can be followed by the photoluminescence (PL) quenching and lifetime shortening of the CdTe NPs by the CdSe NPs. The magnitude of the PL quenching and lifetime shortening was found to depend on the interparticle distance, relative NP sizes, and the direction of the electric field created by the surface charges.

7.2 EXPERIMENTAL DETAILS

7.2.1 Material and Methods:

Selenium powder (99.999%), tellurium powder (99.999%), sodium borohydride (NaBH4 98%), hexadecylamine (HDA, 99%), trioctylphosphine (TOP, 97%), trioctylphosphine oxide (TOPO, 90%), cadmium oxide (CdO 99.999%), cadmium chloride (CdCl2 99%), 3-mercaptopropionic acid (MPA, 97%), N,N-dimethyl-2-aminoethanethiol hydrochloride (DEA, 95%), N,N,N-trimethyl-1-trimethyldodecylammonium chloride (TDA, 99%), N,N,N-trimethyl-2-aminoethanechloride chloride (CEA, 99%) were purchased from Aldrich. N,N,N-trimethyl(11-mercaptoundecyl)ammonium chloride (TMA, 98%) were purchased from

ProChimia Surfaces (www.prochimia.com). All reagents and solvents were used as received. Water used in all experiments was purified by a Barnstead-Nanopure system and its resistance was 18.2 MΩ-cm at 25 °C.

MPA: 3-mercaptopropionic acid 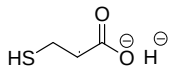

TOPO: trioctylphosphine oxide 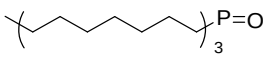

TMA: *N*,*N*,*N*-trimethyl(11-mercaptoundecyl)ammonium chloride 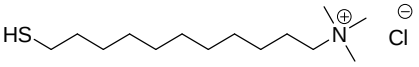

DEA: *N*,*N*-dimethyl-2-aminoethanethiol hydrochloride 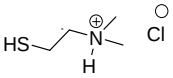

TDA: *N*,*N*,*N*-trimethyl-1-dodecylammonium chloride 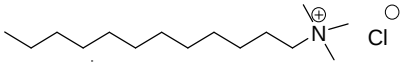

CEA: *N*,*N*,*N*-trimethyl-2-aminoethanechloride chloride 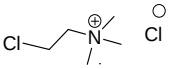

Scheme 7.1 Abbreviations, Definitions and Structures.

published procedure.[24,61] For a typical synthesis of CdSe nanoparticles, 0.0514 g (0.40 mmol) of CdO, 0.1929 g (0.80 mmol) of HDA and 3.8668 g (10.0 mmol) of TOPO were loaded into a 25 mL three-neck round-bottom flask. The mixture was heated to 300 °C under Ar flow until CdO was dissolved. A selenium stock solution (0.0787 g/1.0mmol of selenium powder dissolved in 4 ml of TOP) was then swiftly injected into the reaction flask. After the injection, nanocrystals were allowed to grow at 280 °C until they reached the desired size. Highly luminescent TOPO-capped CdSe NPs in a nonaqueous medium can be readily transferred to water by the following procedure.[62,63] About 20 mg of freshly prepared CdSe nanocrystals were precipitated from toluene solution by adding methanol and then were isolated by centrifugation. The collected NPs were re-dissolved in chloroform. For preparing TMA-CdSe NPs, 2 mg TMA was dissolved in 3 mL of chloroform, then added to the TOPO-CdSe solution and stirred at room temperature in the

dark for 1 hr. The TMA-CdSe NPs were gradually precipitated out of solution and then re-dispersed in water, providing a clear homogeneous dispersion of NPs. The dispersion was purified by using three cycles of concentration/dilution with an Ultra-free centrifugal filtration device (Millipore, MWCO 10,000 Da). These procedures should eliminate soluble organics and excess free ligands from the solution and provided homogeneous aggregate-free NP dispersions that were ready for further use. To obtain DEA-CdSe NPs, 50 mg of DEA was dissolved in 50 μL water, added into the TOPO-CdSe chloroform solution, and stirred at room temperature in the dark for 1 hr. The surface modified CdSe NPs were transferred into water and subsequently purified in a manner similar to that used for the TMA-CdSe NPs. For preparing MPA-CdSe NPs, 20 mg TOPO-CdSe NPs, 100 μL MPA was added into 3 mL DMF. The mixture was heated to ~60 ℃ in oil bath for 2 h under inert atmosphere to get a clear solution. Potassium t-butoxide (~2% Wt) in DMF was added into the mixture to precipitate MPA-CdSe NPs. The obtained CdSe NPs was collected by centrifugation and purified by ultrafiltration.

7.2.2 CdTe NPs Synthesis

CdTe NPs were synthesized in aqueous solution, as described in a previously published procedure.[26,64] The surface charges were controlled to be either negative, by using 3-mercaptopropionic acid (MPA) as capping ligands, or positive, by using N,N-dimethyl 2-aminoethanethiol hydrochloride (DEA) as capping ligands. For example, MPA-CdTe NPs, typically, were prepared as follows: firstly, 50.8 mg (0.4 mmol) of tellurium powder, 37.8 mg (1 mmol) of $NaBH_4$, were loaded in a 25 mL two-necked flask and connected to a Schlenk line. Air was pumped off and replaced with Ar. 10 ml of distilled water was added through a syringe and

the reaction mixture was heated at 80 ℃ for 30 min to get a deep red clear NaHTe solution. Then an aqueous solution containing 0.2 mmol of $CdCl_2$ and 0.34 mmol of MPA was adjusted to pH 11.9 by adding 0.1 M NaOH solution dropwise. This solution was put into a three-neck flask with a condenser attached and connected to the Schlenk line. Air was pumped off and replaced with Ar, and freshly prepared NaHTe solution (0.01 mmol) was injected through a syringe at room temperature. The reaction mixture was heated to reflux (100 ℃), and the timing started when the temperature reached 100 ℃. Both types of modified NPs were purified by ultrafiltration in a manner similar to that used for the CdSe NPs.

The spectroscopic information for the CdTe and CdSe NPs used in this study are summarized in Table 1.

Table 7.1. Spectroscopic information of nanoparticles used in this study[a]

Sample	First excitonic peak in UV-vis (nm)	PL peak (nm)
MPA-CdTe-1	579	638
DEA-CdSe-1	519	quenched
TMA-CdSe	524	quenched
MPA-CdTe-2	660	732
DEA-CdSe-2	456	quenched
DEA-CdTe	575	610
MPA-CdSe	520	quenched

a: . The numbers 1 and 2 are used to distinguish NPs of the same composition but different sizes.

7.2.3 Steady state spectroscopy

Steady-state absorption spectra were measured on an Agilent 8453 spectrometer and the steady-state emission spectra were measured on a Horiba J-Y Fluoromax 3 fluorescence spectrophotometer, respectively.

7.2.4 Time dependent fluorescence spectroscopy

The time-resolved fluorescence data were collected using the time-correlated single photon counting (TCSPC) method. [65] The instrument response function was measured using a sample of colloidal $BaSO_4$. The samples were excited at 440 nm using a diode laser (PIL043, A.L.S. GmbH) and/or a 585 nm synchronously pumped dye laser at 1MHz repetition rate and 6000 counts in the peak channel were collected for each sample. Experiments were also performed with a 300 kHz repetition rate. Lifetime values were found to be nearly identical as to those collected at a 1MHz repetition rate in all the systems studied. The fluorescence decay curves were fit to a sum of exponentials by a convolution and compare method using IBH-DAS6 analysis software. [66]

7.2.5 Dynamic Light Scattering (DLS) and ζ-Potential Measurements

DLS measurements were performed at room temperature in a 90^o geometry and analyzed by using particle sizing software with a 532 nm laser (Brookhaven Instrument Co.). The electrophoretic mobility measurements were performed on the same instrument at room

temperature with an electrical field strength of 10 V/cm by using a Zeta Plus ζ-potential analyzer.

7.3 RESULTS AND DISCUSSION

7.3.1 Formation of Aggregates through Electrostatic Interaction

As shown in Fig. 7.1 MPA-capped CdTe NPs in water show a first excitonic peak at 579 nm (implying a size of about 3.5 nm in diameter[48]) and the corresponding photoluminescence (PL) peak occurs at 638 nm (excitation wavelength at 400 nm). TOPO-capped CdSe NPs, which do not dissolve in water, show a first excitonic peak at 518 nm in toluene (implying a size of about 2.5 nm in diameter) and a corresponding photoluminescence peak at 531 nm.[48] After ligand exchange with TMA or DEA, the CdSe NPs can be completely transferred into water and the absorbance maximum shifts from 518 nm to 524 nm for TMA and from 518 nm to 519 nm for DEA. Other than this shift, the spectra do not change significantly. The photoluminescence of the TMA-CdSe and the DEA-CdSe NPs in water is strongly quenched, as compared to that for the TOPO capped NPs in toluene. The quenching is attributed to trapping states created during the ligand exchange process of CdSe NPs with thiol molecules, as has been reported previously.[67] The absorption spectrum of CdSe shows a very small overlap with the photoluminescence spectrum of the CdTe, so that electronic energy transfer from the CdTe NPs to the CdSe NPs is negligible (see Supporting Information).

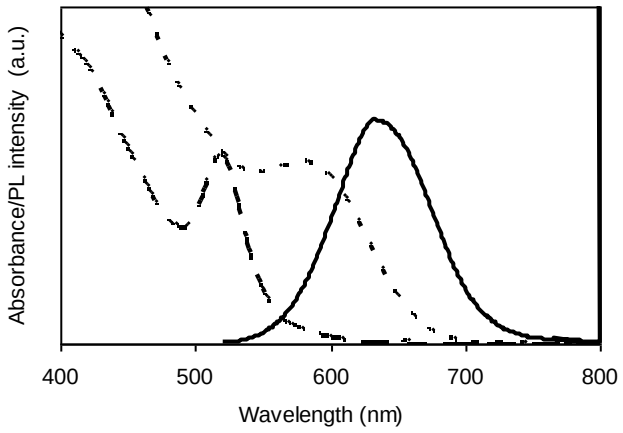

Figure 7.1.Representative absorption and PL spectra of MPA-capped CdTe and TMA-capped CdSe NPs used in this work. From left to right: CdSe absorbance in water after ligand exchange with TMA (— —), CdTe absorption in water (---).CdTe fluorescence in water (—). The quenched CdSe PL is not shown.

Because of mutual electrostatic attraction, the negatively charged MPA-CdTe NPs and positively charged TMA-CdSe NPs are expected to form aggregates under the appropriate electrolyte solution conditions. The pKa value of DEA is about 10.5, so that the DEA-capped CdSe is expected to be positively charged in aerated water (pH=6.6), and it can electrostatically interact with the negatively charged MPA-CdTe. The aggregation was quantified by titrating the positively charged TMA or DEA-capped CdSe NPs into aqueous solutions of negatively charged MPA-capped CdTe NPs, for which the CdTe final concentration was fixed at 0.9×10^{-6} M. Absorption spectra of these solutions show excitonic peaks of both CdSe and CdTe NPs and are a superposition of the individual nanoparticle spectra, indicating that the electronic transitions of the NPs remain isolated on the individual particles after mixing. DLS (dynamic light scattering) experiments confirmed the presence of aggregates upon addition of TMA-CdSe (or DEA-CdSe) NPs to the CdTe NP solutions. With increasing concentration of CdSe, the average diameters of

the aggregates grew from below 10 nm to the order of 100 nm and reached a size on the order of 1-2 μm as the molar ratio of CdSe/CdTe approached 0.5 for the larger TMA-CdSe NPs and 1 for the smaller DEA-CdSe NPs. With further increase in the concentration of positively charged CdSe NPs, the aggregate size decreases to about 100 nm. See the supplemental information for these data in tabular form.

ζ-potential measurements (Fig. 7.2) corroborate the DLS results. The initial zeta potential for a solution of negatively charged MPA-CdTe NPs was about −21 mV. As the concentration of TMA-CdSe NPs increased the zeta potential increased to about +1.1 mV at a CdSe/CdTe molar ratio of 0.5, and then to about +28 mV at a molar ratio of 3. The addition of DEA-CdSe NPs to CdTe NPs solutions causes a similar trend but has a less sharp transition and asymptotes toward a smaller positive potential.

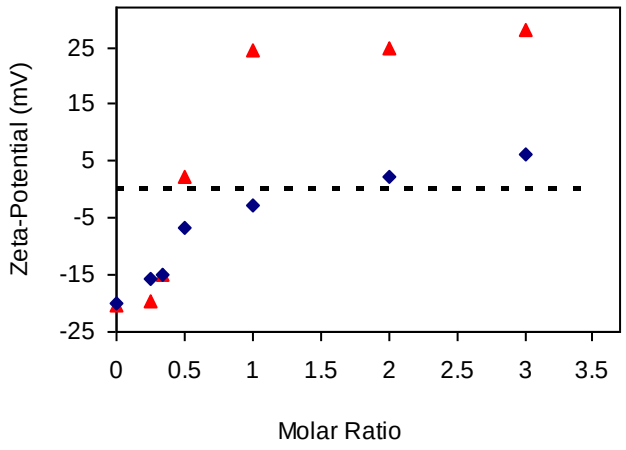

Figure 7.2 ζ-potential measurements of assemblies of CdSe/CdTe with increasing concentration of positively charged TMA-CdSe: ▲ or DEA-CdSe: ♦. The dotted line indicates 0 mV. The concentration of the MPA-CdTe NP is fixed at 0.9 μM.

These data indicate that as the proportion of positively charged TMA-CdSe NPs to negatively charged MPA-CdTe NPs increases, aggregates form in the solution and the zeta-potential approaches zero. The concentration at which the aggregates are close to being neutral, corresponds to the concentration at which DLS gave the largest sizes. As the CdSe NP concentration increases beyond this 'isoelectric' point, the size decreases again because the aggregates again have a net charge (albeit of opposite sign) that acts to inhibit the stability of large aggregates. At a molar ratio of three, the DLS results give an effective diameter of ~ 130 nm for the TMA-CdSe aggregates and ~ 80 nm for the DEA-CdSe aggregates. The sharper zeta-potential change that is observed for the TMA-CdSe may occur because more TMA ligands can be loaded onto the CdSe NP surface as compared to DEA (because the longer TMA ligands reduce electrostatic repulsion between neighboring ligands). This explanation can be rationalized from the ζ-potential values of pure TMA-CdSe NP solutions, + 27 mV, and pure DEA-CdSe NP solutions, ~+ 13 mV.

7.3.2 Aggregation induced self-quenching due to interparticle interaction

Although the poor spectral overlap inhibits energy transfer quenching of CdTe NPs by CdSe NPs, self-quenching of CdTe NPs can occur. Self-quenching is well-known for NP systems where assembly in solution or the formation of a solid NP film from solution takes place and it can be attributed to electronic energy transfer from the smaller NPs to the larger NPs in the NP size distribution.[68-71] For a self-quenching NP solution, a red-shift and quenching of the photoluminescence can be observed as the NPs aggregate. To test for the importance of self-quenching, the surfactant TDA, which has a positive head group and a length similar to the TMA coating on the CdSe NPs, was titrated with a solution of the negatively charged MPA-CdTe NPs.

A 0.9×10^{-6} M solution of MPA-CdTe NPs in water exhibits a strong photoluminescence peak around 638 nm; as TDA surfactant is added to the solution, the emission peak red shifts to 672 nm. Furthermore, the photoluminescence intensity quenches by a factor of two as the TDA/CdTe molar ratio increases from zero to about one (assuming there are about 350 MPA ligands per CdTe NPs) and is saturated at this value for higher molar ratio (see Figure 3b).[72] See supplemental information for PL spectra. A similar phenomenon is observed if the CdTe NP solution is titrated with TMA-capped CdSe NPs; the emission's peak wavelength red shifts and saturates at a value of 665 nm at high molar ratios (see Figure 7.3a). We note that the red shift first appears to reach 671 nm at an intermediate mole ratio (1:3 and 1:2 of CdSe/CdTe) and then blue shifts back to 665 nm for a CdSe/CdTe molar ratio of three. Figure 3b shows that the final photoluminescence intensity quenches by a factor of about two. The similarity of the red-shift and PL quenching of the CdTe emission by the TMA-CdSe NPs and TDA molecules indicates that the changes observed in the emission spectra arise from the same self-quenching mechanism and is caused by interparticle interactions between CdTe NPs.[68-71] Other than driving the aggregation of CdTe NPs, the presence of TMA-CdSe NPs does not provide a significant new nonradiative pathway for quenching.

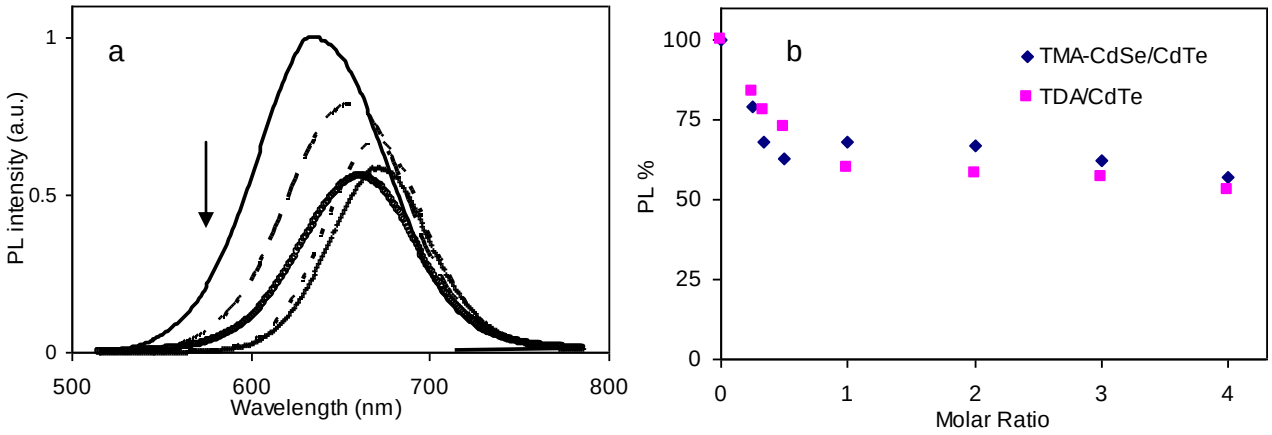

Figure 7.3. Panel a) PL spectra of assemblies of MPA-CdTe in water with increasing concentration of TMA-CdSe, as compared to the pure MPA-CdTe NP concentration (0.9×10^{-6}M). The traces are pure MPA-CdTe NP solution (—), and TMA-CdSe/MPA-CdTe molar ratios at 1: 4 (— —),1:3 (---),1:2(+++),3:1 (◦◦◦). The cases of 1:1 and 2:1 are not shown for clarity. Panel b) shows plots of the relative photoluminescence intensity of MPA-CdTe NP aggregates as a function of increasing molar ratio of TMA-CdSe/MPA-CdTe and TDA/MPA-CdTe. Error bars are small and not shown.

7.3.3 Charge transfer process from CdTe to CdSe NPs

As shown above, the TMA-CdSe NPs, with their eleven methylene thick surface coating, behaves as a surfactant that induces aggregation and self-quenching (a factor of two) of the MPA-CdTe NPs. Here we explore how the photoluminescence quenching of the MPA-CdTe NPs depends on the thickness of the organic surface coating of the CdSe NPs, the relative energetics of the NPs, and the direction of the interparticle electric field.

Interparticle distance dependence: In contrast to the weak (< 50%) photoluminescence quenching of the MPA-CdTe NPs by TMA-CdSe NPs, aggregates of MPA-CdTe NPs with DEA-CdSe NPs (containing only two methylenes) give rise to a very significant (>98%) quenching (see Figure 7.4). For a molar ratio of DEA-CdSe to MPA-CdTe that is less than one, the PL intensity is quenched by about 30%-40% and the peak position is only slightly red shifted. As the molar ratio increases to two, the PL intensity is quenched by more than 75% and the peak red shifts to 665 nm; and when the molar ratio increases to three or larger, the PL intensity is quenched by more than 90% and the peak emission wavelength has shifted back to 656 nm.

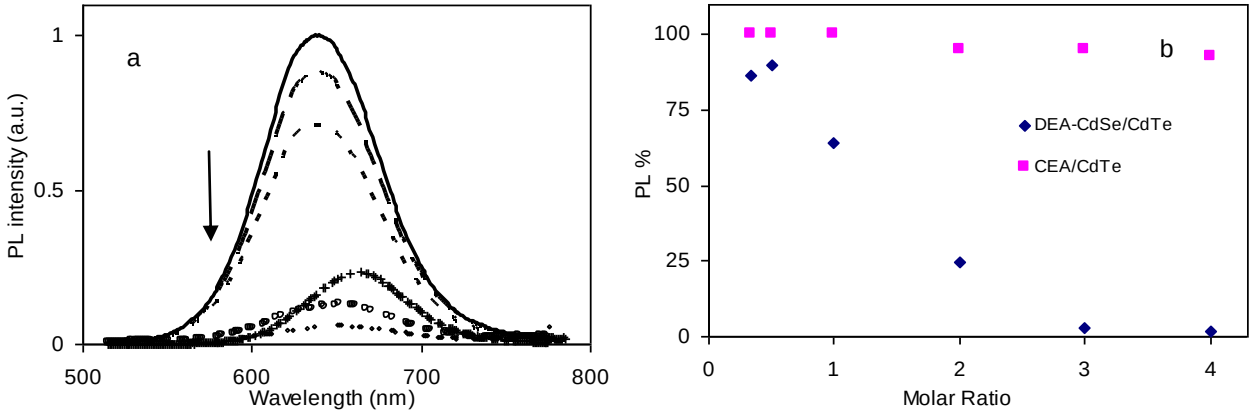

Figure 7.4. Panel a shows photoluminescence spectra of MPA-CdTe NPs in water with increasing DEA-CdSe/MPA-CdTe ratio, compared to the pure MPA-CdTe NP solutions (0.9×10^{-6}M). From top to bottom, the traces are pure MPA-CdTe NP solution (—), and DEA-CdSe/MPA-CdTe molar ratios of 1:2 (— —), 1:1 (---), 2:1 (+++), 3:1 (◦◦◦). 4:1 (◊◊◊). The intensity of 3:1 and 4:1 spectra has been magnified by 5 and 4 times, respectively, for clarity. Panel b shows a plot of the relative photoluminescence intensity of MPA-CdTe NPs with increasing molar ratio of DEA-CdSe/MPA-CdTe and CEA/MPA-CdTe. Error bars are small and not shown.

The quenching of MPA-CdTe NPs photoluminescence by DEA-CdSe NPs was found to be reversible. If 0.5 M NaCl was added to a solution of MPA-CdTe NPs, the PL peak remained in the same spectral position as the original peak and a small amount of quenching (~30%) was observed (Fig. 7.5a). Subsequent addition of DEA-CdSe NPs, to create a molar ratio of 4:1 with MPA-CdTe, did not induce more significant changes. Similarly if a high concentration of NaCl is added into a solution of DEA-CdSe/MPA-CdTe, the emission's peak wavelength blue-shifts back to the original CdTe peak position and the PL intensity recovers to the value found for a NaCl containing solution of MPA-CdTe. These results imply that the NPs do not degrade upon DEA-CdSe addition, nor do they cluster nonspecifically as a result of a high ionic strength of the

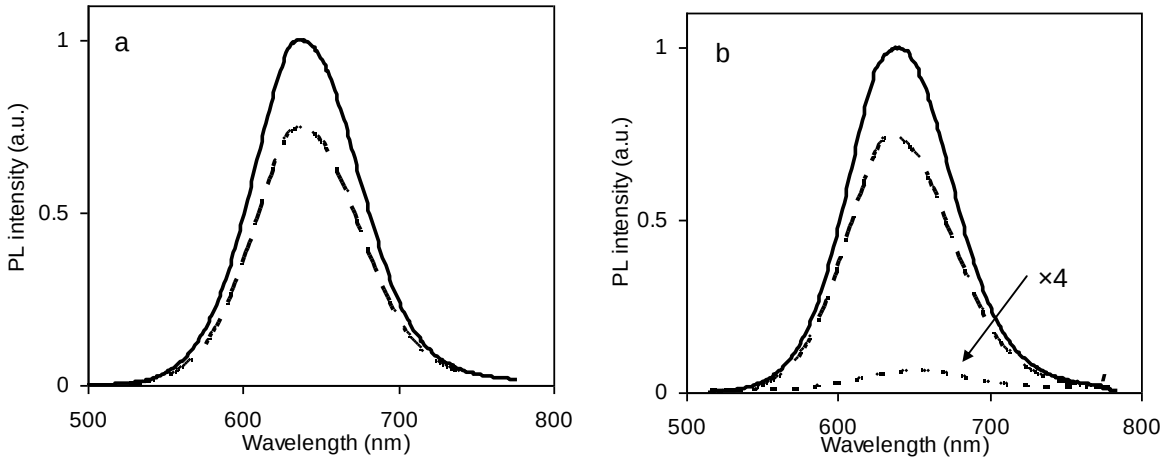

Figure 7.5. Panel a shows plots of photoluminescence spectra for a pure MPA-CdTe NP solution (0.9×10^{-6}M) (—) and a MPA-CdTe NPs in 0.5 M NaCl solution (— —). Panel b shows plots of photoluminescence spectra of pure MPA-CdTe NP solution (0.9×10^{-6}M) (—), of DEA-CdSe/MPA-CdTe at a molar ratio of 4:1 in 0.5M NaCl solution (— —) and of DEA-CdSe/MPA-

CdTe aggregates at a molar ratio 4:1 in water(---). The intensity of CdSe/CdTe at molar ratio 4:1 is magnified by 4 times for clarity.

solution. In addition, this experiment confirms that the close proximity of DEA-CdSe is driven by electrostatic attraction and is required for efficient photoluminescence quenching.

As a control experiment MPA-CdTe NPs were titrated by CEA, which has a similar chain length and positive head group like that of DEA. This experiment showed that the photoluminescence spectra of CEA/MPA-CdTe do not change significantly (see Supporting Information). A plot of the relative PL intensities of DEA-CdSe/MPA-CdTe NPs and CEA/MPA-CdTe NPs (see Fig 7.4b) reveals the dramatic difference in quenching efficiencies. The extent of aggregation and ζ-potential changes in CEA/MPA-CdTe NP solutions are very small. Clearly, the DEA-CdSe NPs are necessary to observe significant PL quenching, and CEA molecules do not play a role in either inducing the aggregates or PL quenching.

In another control experiment the dendrimer PAMAM 2G (Dendritech, Inc.), which has no visible chromophore, was used to induce aggregates of MPA-CdTe NPs. PAMAM 2G is 2.9 nm in diameter and has 16 NH_2 surface group which should be protonated in water at pH 6.6. For a molar ratio of 3:1 (PAMAM 2G:MPA-CdTe) aggregates of several hundreds of nanometers diameter were formed, the accompanying ζ-potential changed from −21 mV to +36 mV. The PL peak red shifts to ~670 nm and the intensity quenches by 30-40%. (see Supporting Information of UV-vis and PL spectra).

These experiments indicate that the DEA-CdSe NPs both enhance aggregate formation, as evidenced by a more significant red shift in PL than the case of CEA ligands only, and cause much stronger quenching, as compared to the PAMAM-2G dendrimer systems, which induces aggregates of a size similar to those found for DEA-CdSe. The red-shift for the DEA-

CdSe/MPA-CdTe NP solution is less than that observed for the TMA-CdSe/MPA-CdTe NP solution (the TMA-CdSe/MPA-CdTe red-shifted from 638 nm to 665 nm and the DEA-CdSe/MPA-CdTe red-shifted from 638 nm to 656 nm), which indicates less self-quenching of the MPA-CdTe even though they may be closer together, on average. Thus, the enhanced quenching of the MPA-CdTe NP photoluminescence and its weaker spectral shift indicates that a new nonradiative pathway is created by the proximity of DEA-CdSe NPs and that this nonradiative pathway is more rapid than the self-quenching of the MPA-CdTe NPs.

We postulate that electron transfer from the MPA-CdTe to the DEA-CdSe NPs is the new nonradiative relaxation pathway, i.e., quenching mechanism. This mechanism is postulated because of the staggered type II band gap alignment of the CdTe and CdSe NPs, in which both the conduction band and the valence band of CdTe NPs are energetically higher than the corresponding band positions of the CdSe NPs (Scheme 7.2a). In the DEA-CdSe/MPA-CdTe NP assemblies, a lower bound on the interparticle distance is determined by the length of the capping ligand molecules and is close to 1 nm, so that the excited electrons from the conduction band of CdTe can tunnel through the organic ligand barrier to the conduction band of the CdSe. In

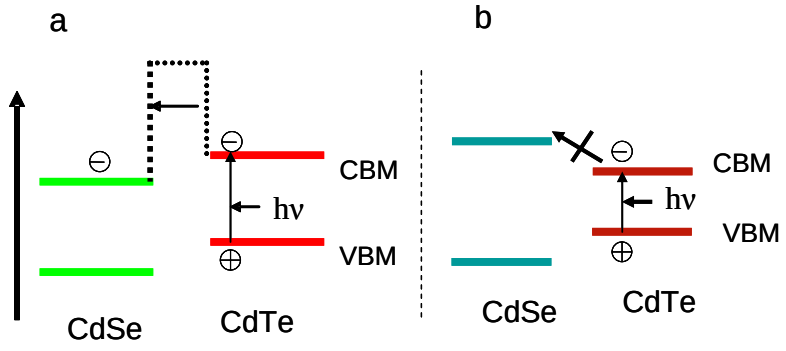

Scheme 7.2. Schematic drawing of type II staggered band gap alignment of appropriate sized CdTe and CdSe NPs (a), and type I band gap alignment of larger size of CdTe and smaller size of CdSe NPs (b).

agreement with the data, this mechanism predicts a much weaker quenching for the TMA-CdSe/MPA-CdTe aggregates than that of DEA-CdSe/MPA-CdTe because of the longer distance (circa 2 nm) between the NPs in the aggregates. (Compare Fig. 7.3 and 7.4).

Nanoparticle size dependence: To test the hypothesis that the enhanced quenching arises from electron transfer, the relative energetics of the NPs was changed by changing their relative sizes. By making the CdSe small and the CdTe large enough, the NPs energy band arrangement can be changed to create a type I band alignment (Scheme 7.2b), which should inhibit charge transfer.[73] The different sizes used were MPA-CdTe NPs of about 4.6 nm in diameter (an excitonic peak near 660 nm and emission maximum near 732 nm) and DEA-CdSe NPs of about 1.9 nm in diameter (an excitonic peak around 456 nm). For a 3:1 molar ratio of DEA-CdSe/MPA-CdTe the DLS measurements gave aggregate sizes of several tens of nanometers; the absorption spectra are shown in Fig. 7.6. Under these conditions, no significant quenching and no apparent red shift of the MPA-CdTe photoluminescence was observed as compared to the pure MPA-CdTe NP solution, supporting the hypothesis that no electron transfer between CdTe and CdSe NPs should occur for this NP combination. The small amount of self-quenching in these aggregates is notable and might be caused by smaller aggregate sizes created in the system and a more monodisperse NP size distribution, so that spectral diffusion is less apparent.[70]

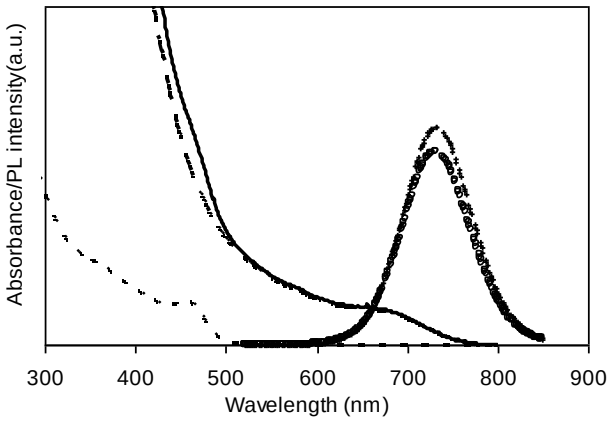

Figure 7.6. From left to right, representative absorption spectra of CdSe in water after ligand exchange with DEA (---), MPA-CdTe in water (— —), DEA-CdSe/MPA-CdTe assemblies at molar ratio 3:1 (—), and relative fluorescence spectra of MPA-CdTe in water(+++) and DEA-CdSe/MPA-CdTe assemblies at molar ratio 3:1(◦◦◦).

Surface charge dependence: The type II band alignment in Scheme 2a implies that the electron transfer mechanism places an extra negative charge on the CdSe NP and a consequent extra positive charge on the CdTe NP. Given that the CdSe NP surface is positively charged and the CdTe NP surface is negatively charged, the net charge separation between the two types of NPs is decreased by the electron transfer. In contrast, one might expect that the transfer of an electron to a negatively charged CdSe NP from a positively charged CdTe NP might be less facile because of the increase in electrostatic energy; i.e., more net charge separation. This aspect of the electron transfer quenching mechanism was explored by switching the capping ligands and thereby changing the sign of the NPs surface charges. DEA-CdTe NPs were synthesized by using a protocol similar to that for the MPA-CdTe NPs preparation and the size was controlled in a similar manner.[64,74] The first excitonic peak of the DEA-CdTe NPs occurs near 575 nm and the photoluminescence peak occurs near 610 nm. The MPA-CdSe NPs were prepared from the same

TOPO-CdSe NPs that have their first excitonic peak at 518 nm; upon ligand exchange with MPA it shifted to 520 nm (see Fig. 7.7).

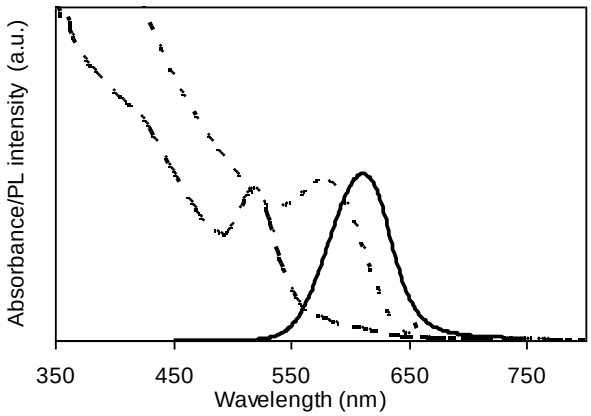

Figure 7.7. Representative absorption and photoluminescence spectra of DEA-CdTe and MPA-CdSe NPs used in surface charge dependence experiments. From left to right, MPA- CdSe NP absorbance in water (— —), DEA-CdTe NP absorbance in water (---), DEA-CdTe fluorescence in water (—).

A solution of MPA-CdSe and DEA-CdTe at a molar ratio of 3:1 showed both excitonic peaks of CdTe and CdSe NPs in absorption spectra but did not show a significant quenching effect, as compared to a solution of DEA-CdTe (PL spectrum of assembly is similar and not shown). DLS experiments gave the aggregate sizes of several tens of nanometer, and Zeta-potential measurements showed that the potential changed from about +14 mV for the original DEA-CdTe to about −8 mV for MPA-CdSe/DEA-CdTe at a molar ratio of 3:1. Thus the aggregation properties are similar to that for the other aggregate type (negatively charged CdTe and positively charged CdSe). The inefficient self-quenching of DEA-CdTe compared to the MPA-CdTe systems may reflect the narrower size distribution of interaction energies (FWHM = 1652 $cm^{-1}$for DEA-CdTe as opposed to 2038 cm^{-1} for MPA-CdTe, see Supporting Information)

as well as the shortening of the average fluorescence lifetime (14.1 ns for DEA-CdSe as compared to 39.1 ns for MPA-CdTe). These findings show that the direction of the interparticle electric field changes the photoluminescence quenching efficiency; a finding that is consistent with charge transfer but not with energy transfer.

Kinetic measurements: Time-resolved photoluminescence measurements, using the time-correlated-single-photon-counting (TCSPC) method, were performed in order to validate the steady-state measurements and quantify the relevant timescales for the quenching. A diode laser at 440 nm and a dye laser at 585 nm were used as excitation sources, and the emission was collected at the PL peak wavelength. None of the samples showed an excitation wavelength dependence, therefore only lifetime parameters from the 585 nm excitation are presented here (Table 7.2 and Fig.7. 8). Studies were performed for samples with molar ratios at which the most pronounced difference in steady-state photoluminescence measurements were observed. Table 7.2 summarizes the findings by presenting the parameters for a best fit of the data to a sum of exponentials; the quantity $\langle\tau\rangle$ is the average lifetime.

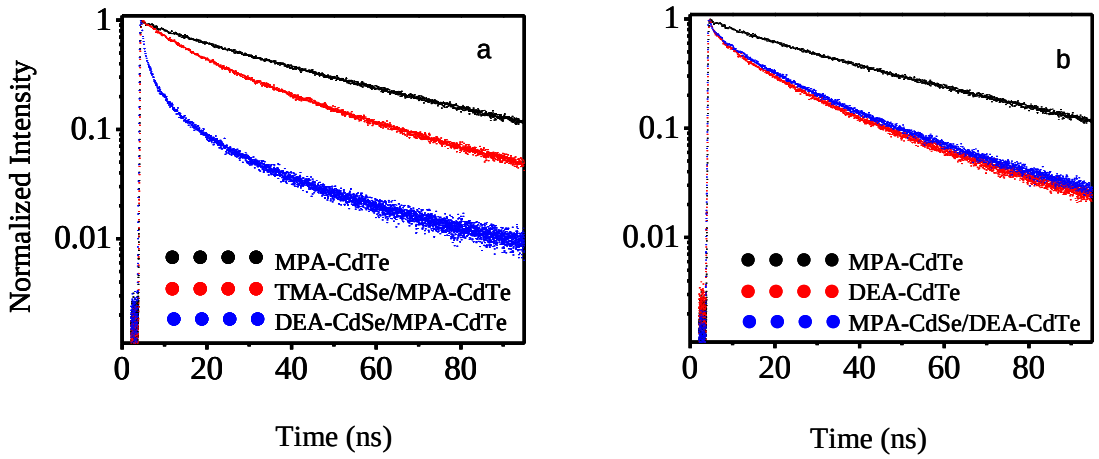

Figure 7.8. (a) Representative time-resolved PL decays of MPA-CdTe, TMA-CdSe/MPA-CdTe at 3:1 molar ratio, DEA-CdSe/MPA-CdTe at 3:1 molar ratio in water. (b) Representative

time-resolved PL decays of MPA-CdTe, DEA-CdTe, MPA-CdSe/DEA-CdTe at 3:1 molar ratio in water. The MPA-CdTe data was included in both panels for better comparison.

Table 7.2 Fluorescence lifetime parameters for different systems studied[a]

System	a_1	τ_1 (ns)	a_2	τ_2 (ns)	a_3	τ_3 (ns)	$<\tau>^{b,c}$ (ns)
MPA-CdTe	0.21	11.4	0.79	46.3	----	----	39.0
TDA/MPA-CdTe	0.56	10.0	0.44	38.4	----	----	22.5
CEA/MPA-CdTe	0.21	12.1	0.79	47.4	----	----	40.0
TMA-CdSe/MPA-CdTe	0.52	10.4	0.48	38.0	----	----	23.6
DEA-CdSe/MPA-CdTe	0.65	0.66	0.24	4.2	0.11	21.8	3.8
DEA-CdTe	0.32	1.23	0.41	11.0	0.27	33.5	13.9
MPA-CdSe/DEA-CdTe	0.35	0.56	0.36	10.3	0.29	33.0	13.5

[a] λ_{ex} = 585 nm, $\lambda_{em} \approx$ Peak maximum. [b] $<\tau>=\sum_i a_i \tau_i$. [c] $\chi^2 < 1.4$

The lifetime data corroborate the steady-state emission data. The photoluminescence decay of the pure MPA-CdTe NPs solution could be fit by a biexponential decay law with decay times that are tens of nanoseconds, giving an average lifetime of 39.1 ns. This value is consistent with typical thiol-capped CdTe NP emission lifetimes reported in the literature.[25,26,75] Typically, the shorter lifetime is attributed to the intrinsic recombination of initially populated core states, and the longer lifetime is attributed to radiative recombination involving surface states.[76-81] The amplitude a_2 of the longer lifetime component accounts for nearly 80% of the total PL decay and indicates good surface reconstruction with few recombination centers created during the sample growth process.[75,78] The TDA/MPA-CdTe and TMA-CdSe/MPA-CdTe NP solutions showed very similar PL decay characteristics with an average lifetime of 22-23 ns. As discussed above these solutions show steady state emission quenching of about a factor of two, and it is attributed to aggregation induced self-quenching of the CdTe NPs; the ratio of average lifetimes is

consistent with the steady-state PL measurement. The decay parameters show that both time constants decrease but only by 10% to 20%. In contrast, the DEA-CdSe/MPA-CdTe solution showed a dramatic lifetime shortening for both components with an average lifetime of 3.8 ns. This observation is consistent with the steady-state studies and strongly suggests that interparticle separation in the aggregates changes the relative importance of non-radiative decay pathways. Lastly, a solution of MPA-CdSe/DEA-CdTe which inverts the NP surface charges, hence the sign of the interparticle electric field, has an average lifetime similar to that of the pure solution of DEA-CdTe. These data corroborate the steady state measurements and their interpretation.

7.4 SUMMARY AND CONCLUSIONS

An electron transfer quenching mechanism provides a consistent understanding of the photoluminescence quenching of the CdSe/CdTe NP aggregates studied here. When TMA-CdSe NPs are mixed with MPA-CdTe NPs, the interparticle distance in the aggregates is about 2 nm (determined by the length of the capping ligands; see Scheme 7.3), and this inhibits electron transfer because the electron tunneling probability through methylene films decays exponentially with distance, with a typical decay length of 10 per nm. Although energy transfer of the CdTe is weak, some self-quenching can be observed in the aggregates.

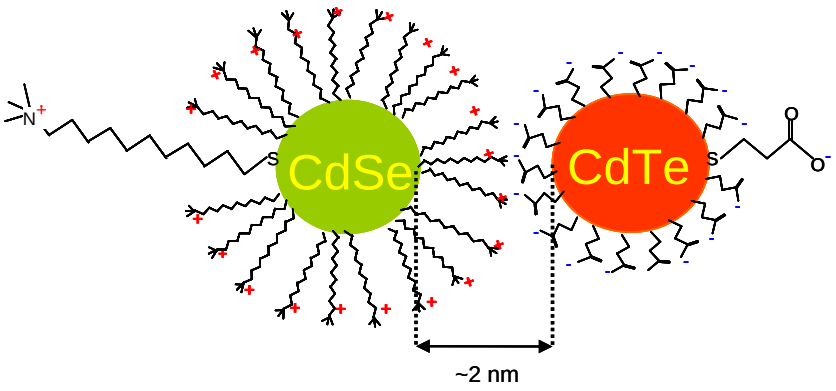

Scheme 7.3. Schematic drawing of assemblies formed between TMA-CdSe/MPA- CdTe.

When DEA-CdSe NPs are mixed with MPA-CdTe NPs, the interparticle distance in aggregates is only about 1 nm, which is about half that of the TMA-CdSe/MPA-CdTe/ aggregates. If the tunneling probability through a methylene chain is taken to be proportional to exp(-*d*), (*d* in Å), then the shorter distance means that the electron tunneling probability is about 20,000 times more probable, making electron transfer a more facile nonradiative decay pathway. Thus the quenching and lifetime shortening observed in these assemblies is attributed to electron transfer from CdTe to CdSe through the interparticle barrier (see Scheme 7.4).

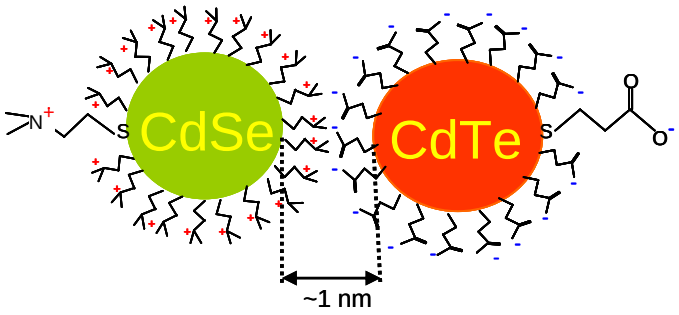

Scheme 7.4. Schematic drawing of assemblies formed between DEA-CdSe/MPA- CdTe.

The assignment of the quenching mechanism to electron transfer was supported by studies that inverted the surface charge on the NPs in the aggregates; in particular, the CdTe was capped with positively charged DEA and the CdSe was capped with negatively charged MPA. Thus the direction of the electric field between the two types of NPs was inverted (see Scheme

7.5). Although the optical properties and the aggregation properties of the NPs did not change significantly with this change in surface ligand, the photoluminescence quenching of their aggregates changed dramatically. Whether the change in rate with the field direction is caused by a change in the tunneling probability and/or the relative energetics of the donor and accepting states of the NPs is not yet known.

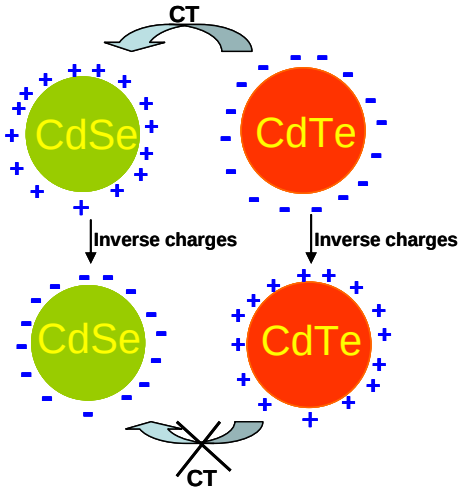

Scheme 7.5. Schematic drawing of assemblies formed between MPA-CdSe/DEA- CdTe after inverse charges.

In conclusion, this study demonstrates that electron transfer and photoluminescence quenching in CdSe/CdTe NP assemblies can be controlled through interparticle distance, energetics, and electric field created by the surface capping group and particle size. Time-resolved studies indicate that the electron transfer process may involve surface localized states. The inhibition of electron transfer by the interparticle electric field is significant and may provide an avenue for inhibiting back electron transfer. These findings should be useful for understanding and controlling charge transfer in nanocrystal-based solar cells.

7.5 ACKNOWLEDGEMENT

This work was supported by the US-DOE (Grant # ER46430). M. Wu acknowledges financial support from a Mellon Fellowship. M.Wu also thankfully acknowledge Dr. Krzysztof Z. Ziach for synthesizing N,N,N-trimethylmercaptoethane chloride used in the preliminary studies.

7.6 REFERENCES

(1) Kamat, P. V. *J. Phys. Chem. C* **2007**, *111*, 2834.

(2) Barnham, K. W. J.; Mazzer, M.; Clive, B. *Nat. Mater.* **2006**, *5*, 161.

(3) Yu, G.; Gao, J.; Hemmelen, J. C.; Wudl, F.; Heeger, A. J. *Science* **1995**, *270*, 1789.

(4) Huynh, W. U.; Dittmer, J. K.; Alivisatos, A. P. *Science* **2002**, *295*, 2425.

(5) Park, S. H.; Roy, A.; Beaupré, S.; Cho, S.; Coates, N.; Moon, J. S.; Moses, D.; Leclerc, M.; Lee, K.; Heeger, A. J. *Nature Photon.* **2009**, *3*, 297.

(6) Green, M. A.; Emery, K.; King, D. L.; Igari, S.; Warta, W. *Prog. Photovoltaics* **2001**, *9*, 287.

(7) Scharber, M. C.; Muhlbacher, D.; Koppe, M.; Denk, P.; Waldauf, C.; Heeger, A. J.; Brabec, C. J. *Adv. Mater.* **2006**, *18*, 789.

(8) Alivisatos, A. P. *Science* **1996**, *271*, 933.

(9) Brus, L. E. *J. Chem. Phys.* **1986**, *90*, 2555.

(10) Talapin, D. V.; Murray, C. B. *Science* **2005**, *310*, 86.

(11) Maheshwari, V.; Saraf, R. F. *Science* **2006**, *312*, 1501.

(12) Mahawela, P.; Jeedigunta, S.; Vakkalanka, S.; Ferekides, C. S.; Morel, D. L. *Thin Solid Films* **2005**, *466*, 480.

(13) Sapsford, K. E.; Medintz, I. L.; Golden, J. P.; Deschamps, J. R.; Uyeda, H. T.; Mattoussi, H. *Langmuir* **2004**, *20*, 7720.

(14) Bruchez, M., Jr.; Moronne, M.; Gin, P.; Weiss, S.; Alivisatos, P. A. *Science* **1998**, *281*, 2013.

(15) Chan, W. C. W.; Nie, S. *Science* **1998**, *281*, 2016.

(16) Michalet, X.; Pinaud, F. F.; Bentolila, L. A.; Tsay, J. M.; Doose, S.; Li, J. J.; Sundaresan, G. W., A. M.; Gambhir, S. S.; Weiss, S. *Science* **2005**, *307*, 538.

(17) Akerman, M. E.; Chan, W. C. W.; Laakkonen, P.; Bhatia, S. N.; Ruoslahti, E. *Proc. Natl. Acad. Sci. U.S.A.* **2002**, *99*, 12617.

(18) Goldman, E. R.; Clapp, A. R.; Anderson, G. P.; Uyeda, H. T.; Mauro, J. M.; Medintz, I. L.; Mattoussi, H. *Anal. Chem.* **2004**, *76*, 684.

(19) Jin, W. J.; Fernandez-Arguelles, M. T.; Costa-Fernandez, J. M.; Pereiro, R. S.-M., A. *Chem.Commun.* **2005**, 883.

(20) Sundar, V. C.; Lee, J.; Heine, J. R.; Bawendi, M. G.; Jensen, K. F. *Adv. Mater.* **2000**, *12*, 1102.

(21) Schlamp, M. C.; Peng, X. G.; Alivisatos, A. P. *J. Appl. Phys.* **1997**, *82*, 5837.

(22) Artemyev, M.; Woggon, U.; Wannemacher, R.; Jaschinski, H.; Langbein, W. *Nano Lett.* **2001** *1*, 309.

(23) Klimov, V. I.; Mikhailovsky, A. A.; Xu, S.; Malko, A.; Hollingsworth, J. A.; Leatherdale, C. A.; Eisler, H. J.; Bawendi, M. G. *Science* **2000**, *290*, 314.

(24) Peng, Z. A.; Peng, X. *J. Am. Chem. Soc.* **2001**, *123*, 183.

(25) Wuister, S. F.; Swart, I.; Van Driel, F.; Hickey, S. G.; De Mello Donega, C. *Nano Lett.* **2003**, *3*, 503.

(26) Rogach, A. L.; Franzl, T.; Klar, T. A.; Feldmann, J.; Gaponik, N.; Lesnyak, V.; Shavel, A.; Eychmuller, A.; Rakovich, Y. P.; Donegan, J. F. *J. Phys. Chem. C* **2007**, *111*, 14628.

(27) Skolnick, M. S.; Mowbray, D. J. *Annu. Rev. Mater. Res.* **2004**, *34*, 181.

(28) Murray, C. B.; Kagan, C. R.; Bawendi, M. G. *Annu. Rev. Mater. Sci.* **2000**, *30*, 545.

(29) Zabet-Khosousi, A.; Dhirani, A.-A. *Chem. Rev.* **2008**, *108*, 4072.

(30) Vanmaekelbergh, D. l.; Liljeroth, P. *Chem. Soc. Rev.* **2005**, *34*, 299.

(31) Wang, L.; Rastelli, A.; Kiravittaya, S.; Benyoucef, M.; Schmidt, O. G. *Adv. Mater.* **2009**, *21*, 2601.

(32) Dimitrijevic, N. M.; Saponjic, Z. V.; Rabatic, B. M.; Rajh, T. *J. Am. Chem. Soc.* **2005**, *127*, 1344.

(33) Issac, A.; Jin, S.; Lian, T. *J. Am. Chem. Soc.* **2008**, *130*, 11280.

(34) McFarland, E. W.; Tang, J. *Nature* **2003**, *421*, 616.

(35) Huang, J.-W.; Bai, S. J. *Nanotechnology* **2005**, *16*, 1406.

(36) Kohtani, S.; Kudo, A.; Sakata, T. *Chem. Phys. Lett.* **1993**, *206*, 166.

(37) Robel, I.; Subramanian, V.; Kuno, M.; Kamat, P. V. *J. Am. Chem. Soc.* **2006**, *128*, 2385.

(38) Plass, R.; Pelet, S.; Krueger, J.; Gratzel, M.; Bach, U. *J. Phys. Chem. B* **2002**, *106*, 7578.

(39) Ellingson, R. J.; Beard, M. C.; Johnson, J. C.; Yu, P.; Micic, O. I.; Nozik, A. J.; Shabaev, A.; Efros, A. L. *Nano Lett.* **2005**, *5*, 865.

(40) Schaller, R. D.; Sykora, M.; Pietryga, J. M.; Klimov, V. I. *Nano Lett.* **2006**, *6*, 424.

(41) Gopidas, K. R.; Bohorquez, M.; Kamat, P. V. *J. Phys. Chem.* **1990**, *94*, 6435.

(42) Nasr, C.; Hotchandani, S.; Kim, W. Y.; Schmehl, R. H.; Kamat, P. V. *J. Phys. Chem. B* **1997**, *101*, 7480.

(43) Vinodgopal, K.; Bedja, I.; Kamat, P. V. *Chem. Mater.* **1996**, *8*, 2180.

(44) Mews, A.; Kadavanich, A. V.; Banin, U.; Alivisatos, A. P. *Phys. Rev. B.* **1996**, *53*, 13242.

(45) Willner, I.; Eichen, Y. *J. Am. Chem. Soc.* **1987**, *109*, 6862.

(46) Andres, R. P.; Bielefeld, J. D.; Henderson, J. I.; Janes, D. B.; Kolagunta, V. R.; Kubiak, C. P.; Mahoney, W. J.; Osifchin, R. G. *Science* **1996**, *273*, 1690.

(47) Heath, J. R.; Knobler, C. M.; Leff, D. V. *J. Phys. Chem. B* **1997**, *101*, 189.

(48) Brust, M.; Schiffrin, D. J.; Bethell, D.; Kiely, C. J. *Adv. Mater.* **1995**, *7*, 795.

(49) Leibowitz, F. L.; Zheng, W.; Maye, M. M.; Zhong, C. J. *Anal. Chem.* **1999**, *71*, 5076.

(50) Bethell, D. B., M.; Schiffrin, D. J.; Kiely, C. *J. Electroanal. Chem.* **1996**, *409*, 137.

(51) Liu, Y.; Wang, Y.; Claus, R. O. *Chem. Phys. Lett.* **1998**, *298*, 315.

(52) Kalsin, A. M.; Fialkowski, M.; Paszewski, M.; Smoukov, S. K.; Bishop, K. J. M.; Grzybowski, B. A. *Science* **2006**, *312*, 420.

(53) Gross, D.; Susha, A. S.; Klar, T. A.; Como, E. D.; Rogach, A. L.; Feldmann, J. *Nano Lett.* **2008**, *8*, 1482.

(54) Kamat, P. V. *J. Phys. Chem. B* **2002**, *106*, 7729.

(55) Zhou, Q.; Li, X.; Fan, Q.; Zhang, X.; Zheng, J. *Angew. Chem. Int. Ed.* **2006**, *45*, 3970.

(56) Sudeep, P. K.; Takechi, K.; Kama, P. V. *J. Phys. Chem. C* **2007**, *111*, 488.

(57) Cui, S.-C.; Tachikawa, T.; Fujitsuka, M.; Majima, T. *J. Phys. Chem. C* **2008**, *112*, 19625.

(58) Kim, S.; Fisher, B.; Eisler, H.-J.; Bawendi, M. J. *J. Am. Chem. Soc.* **2003**, *125*, 11466.

(59) Lo, S. S.; Khan, Y.; Jones, M.; Scholes, G. D. *J. Chem. Phys.* **2009**, *131*, 084714.

(60) Dooley, C. J.; Dimitrov, S. D.; Fiebig, T. *J. Phys. Chem. C* **2008**, *112*, 12074.

(61) Qu, L.; Peng, Z. A.; Peng, X. *Nano Lett.* **2001**, *1*, 333.

(62) Uyeda, H. T.; Medintz, I. L.; Jaiswal, J. K.; Simon, S. M.; Mattoussi, H. *J. Am. Chem. Soc.* **2005**, *127*, 3870.

(63) Pathak, S.; Choi, S. K.; Arnheim, N.; Thompson, M. E. *J. Am. Chem. Soc.* **2001**, *123*, 4103.

(64) Zou, L.; Gu, Z.; Zhang, N.; Zhang, Y.; Fang, Z.; Zhu, W.; Zhong, X. *J. Mater. Chem.* **2008**, *18*, 2807.

(65) Liu, M.; Kaur, P.; Waldeck, D. H.; Xue, C.; Liu, H. *Langmuir* **2005**, *21*, 1687.

(66) Liu, M.; Waldeck, D. H.; Oliver, A. M.; Head, N. J.; Paddon-Row, M. N. *J. Am. Chem. Soc.* **2004**, *126*, 10778.

(67) Aldana, J.; Wang, Y. A.; Peng, X. *J. Am. Chem. Soc.* **2001**, *123*, 8844.

(68) Kagan, C. R.; Murray, C. B.; Nirmal, M.; Bawendi, M. G. *Phys. Rev. Lett.* **1996**, *76*, 1517.

(69) Tang, Z.; Zhang, Z.; Wang, Y.; Glotzer, S. C.; Kotov, N. A. *Science* **2006**, *314*, 274.

(70) Koole, R.; Liljeroth, P.; De Mello Donega, C.; Vanmaekelbergh, D.; Meijerink, A. *J. Am. Chem. Soc.* **2006**, *128*, 10436.

(71) Crooker, S. A.; Hollingsworth, J. A.; Tretiak, S.; Klimov, V. I. *Phys. Rev. Lett.* **2002**, *89*, 186802/1.

(72) Mayilo, S.; Hilhorst, J.; Susha, A. S.; Hohl, C.; Franzl, T.; Klar, T. A.; Rogach, A. L.; Feldmann, J. *J. Phys. Chem. C* **2008**, *112*, 14589.

(73) Sant, P. A.; Kamat, P. V. *Phys. Chem. Chem. Phys.* **2002**, *4*, 198.

(74) Gaponik, N.; Talapin, D. V.; Rogach, A. L.; Hoppe, K.; Shevchenko, E. V.; Kornowski, A.; Eychmu1ller, A.; Weller, H. *J. Phys. Chem. B* **2002**, *106*, 7177.

(75) Zhao, K.; Li, J.; Wang, H.; Zhuang, J.; Yang, W. *J. Phys. Chem. C* **2007**, *111*, 5618.

(76) Bawendi, M. G.; Carroll, P. J.; Wilson, W. L.; Brus, L. E. *J. Chem. Phys.* **1992**, *96*, 946.

(77) Alivisatos, A. P.; Harris, A. L.; Levinos, N. J.; Steigerwald, M. L.; Brus, L. E. *J. Chem. Phys.* **1988**, *89*, 4001.

(78) Wang, X.; Qu, L.; Zhang, J.; Peng, X.; Xiao, M. *Nano Lett.* **2003**, *3*, 1103.

(79) Wehrenberg, B. L.; Wang, C.; Guyot-Sionnest, P. J. *J. Phys. Chem. B* **2002**, *106*, 10634.

(80) Byrne, S. J.; Corr, S. A.; Rakovich, T. Y.; Gun'ko, Y. K.; Rakovich, Y. P.; Donegan, J. F.; Mitchell, S.; Volkov, Y. *J. Mater. Chem.* **2006**, *16*, 2896.

(81) Jones, M.; Lo, S. S.; Scholes, G. D. *Proc. Natl. Acad. Sci. U.S.A* **2009**, *106*, 3011.

7.7 SUPPORTING INFORMATION

1. The importance of energy transfer from CdTe to CdSe NPs in aggregates formed in water can be estimated by using the simple Förster model; the Foerster distance R_0 can be expressed by[1,2]:

$$R_0 = (8.8 \times 10^{-25} \kappa^2 \eta^{-4} Q_D J(\tilde{\nu}))^{\frac{1}{6}}$$

where $\kappa^2 = 2/3$, $\eta = 2.87$, $Q_D = 0.20$, $J(\tilde{\nu}) = 4.72 \times 10^{-14}$ in M^{-1} cm^3. $J(\tilde{\nu})$ is the overlap integral between the emission spectrum of the donor, MPA-CdTe NPs (0.9 μM), and the absorption spectrum of the acceptor, TMA-CdSe NPs or DEA-CdSe NPs (0.9 μM), in wavenumbers , and it is calculated as follows:

$$J(\tilde{\nu}) = \frac{\int_0^\infty \frac{F_D(\tilde{\nu})\varepsilon_A(\tilde{\nu})}{\tilde{\nu}^4} d\tilde{\nu}}{\int_0^\infty F_D(\tilde{\nu}) d\tilde{\nu}}$$

For the CdTe to CdSe NPs aggregates, we find a Förster distance of

$R_0 = 20.8$ Å $= 2.08$ **nm**

Given this value, we can estimate the extent of the quenching from

$$E = \frac{1}{1 + \left(\frac{r}{R_0}\right)^6}$$

For DEA-CdSe/MPA-CdTe with a center-to-center distance of about 4.0 nm, we find that $\mathbf{E = 1.9\%}$, and for TMA-CdSe/MPA-CdTe with a center-to-center distance of about 5.0 nm, we find that $\mathbf{E = 0.52\%}$. Thus we conclude that the electronic energy transfer pathway is minor. This estimate from the Förster theory is corroborated by the control experiments using the PAMAM 2G dendrimer and the TDA surfactant (see text).

2. Table of DLS data for MPA-CdTe solutions upon adding TMA-CdSe or DEA-CdSe NPs in water

Table 7.3 DLS data for MPA-CdTe solutions upon adding TMA-CdSe or DEA-CdSe NPs in water

System	Diameters at different molar ratio of CdSe/CdTe (nm)					
	0	1:3	1:2	1:1	2:1	3:1
TMA-CdSe+ MPA-CdTe	<10	243±8	2209±216	241±25	180±32	137±5
DEA-CdSe+ MPA-CdTe	<10	109±17	158±40	1302±125	314±51	85±15

3. The figure shows how the PL spectra of MPA-CdTe change upon adding TDA, in water.

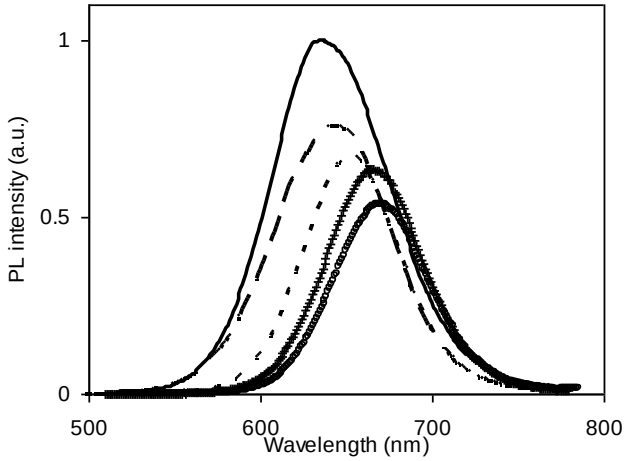

Figure 7.9 PL spectra of CdTe NPs (0.9×10^{-6}M) in water with increasing concentration of TDA, compared to the pure CdTe NPs solution (—). The TDA concentrations are 1.58×10^{-4}M (— —), 6.30×10^{-4}M (---).9.45×10^{-4}M (++), and 1.26×10^{-3}M (∘∘).

4. The figure shows how the PL spectra of MPA-CdTe change upon adding CEA surfactant, in water.

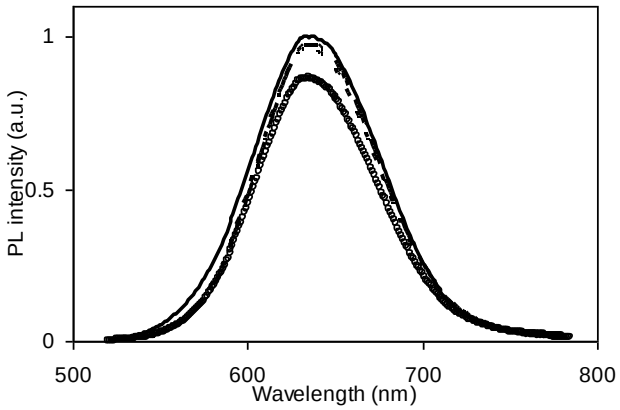

Figure 7.10 PL spectra of CdTe in water with increasing CEA concentration compared to the pure CdTe NPs solution (0.9×10^{-6}M; —). The CEA concentrations are 1.58×10^{-4}M (— —), 3.16×10^{-4}M (---), and 9.45×10^{-4}M (◦◦). Other concentrations are not shown for clarity.

5. Absorbance and photoluminescence (PL) spectra of MPA-CdTe changes upon adding PAMAM 2G in water

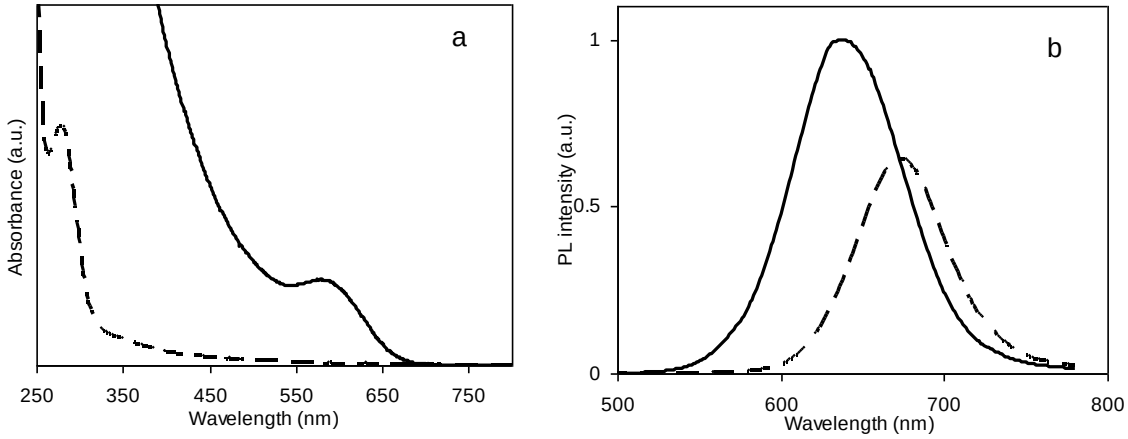

Figure 7.11 Panel a shows representative absorption spectra for MPA-capped CdTe (—) and PAMAM 2G (— —) solutions in water. Panel b shows PL spectra for solutions of MPA-capped CdTe (—), and PAMAM 2G/MPA-CdTe at charge molar ratio 3:1 (— —), in water.

6. The figure compares the PL spectra of MPA-CdTe and DEA-CdTe NPs in water.

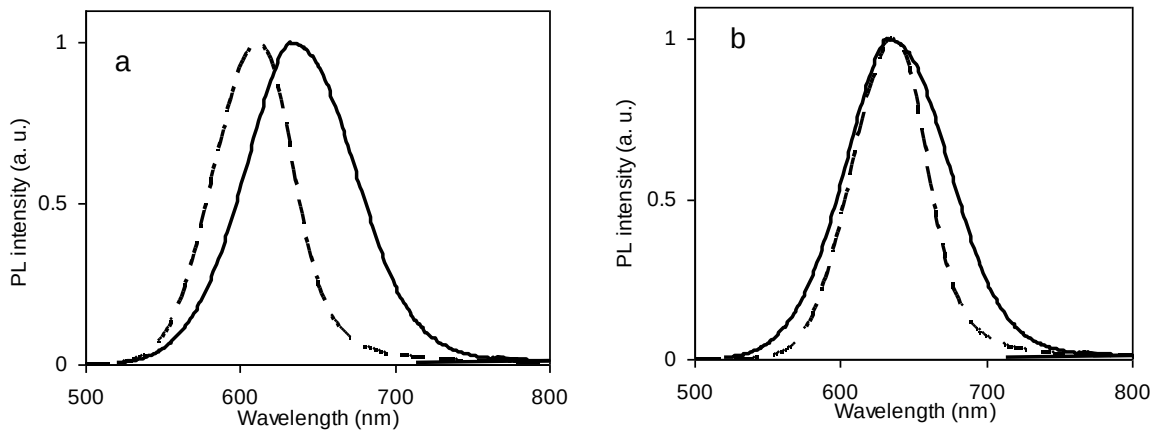

Figure 7.12 Panel a shows normalized PL spectra of MPA-CdTe (—) and DEA-CdTe (— —) NPs aqueous solutions. Panel b shows a PL spectrum of DEA-CdTe (— —) that is manually shifted along the wavelength axis so that the peak position coincides with that of MPA-CdTe NPs(—). This plot makes the difference in peak widths more apparent

References:

(1) Lakowicz, J. R. *Principles of Fluorescence Spectroscopy*, *3rd ed. Springer: New york. 2006*.

(2) Osovsky, R.; Shavel, A.; Gaponik, N.; Amirav, L.; Eychmller, A.; Weller, H.; Lifshitz, E. *J. Phys. Chem. B* **2005**, *109*, 20244.

8.0 THE ELECTRONIC STRUCTURE OF CDSE NANOPARTICLES ADSORBED ON AU ELECTRODES BY AN ORGANIC LINKER: FERMI LEVEL PINNING OF THE HOMO

This work has been published as T. Z. Markus, M. Wu, L. Wang, D. H. Waldeck, D. Oron, R. Naaman in J. Phys.Chem. C; (2009); 113, 14200-14206. Thesis author synthesized NPs for voltammetry studies.

Assemblies of CdSe nanoparticles (NPs) on a dithiol coated Au electrode were created and their electronic energetics were quantified. This report describes the energy level alignment of the filled and unfilled electronic states of CdSe nanoparticles with respect to the Au Fermi level. Using cyclic voltammetry it was possible to measure the energy of the filled states of the CdSe NPs with respect to the Au substrate relative to a $Ag/AgNO_3$ electrode, and by using photoemission spectroscopy it was possible to independently measure both the filled state energies (via single photon photoemission) and those of the unfilled states (via two photon photoemission) with respect to the vacuum level. Comparison of these two different measures shows good agreement with the IUPAC accepted value of the absolute electrode potential. In contrast to the common model of energy level alignment, the experimental findings show that the CdSe filled states become 'pinned' to the Fermi level of the Au electrode, even for moderately small NP sizes.

8.1 INTRODUCTION

Semiconductor nanoparticles (NPs) are envisioned as materials for light harvesting and photovoltaic applications. This desire has sparked intensive research into the nature of light induced charge transfer between NPs and between NPs and various substrates.[1,2,3,4,5,6] One may envision that a device based on NPs will contain NPs of various band gaps, so as to cover the entire solar spectrum, and that one could engineer the device so that the NPs self-assemble into a robust superstructure. To design such structures efficiently, one would like to know the position of the electronic states, both occupied and unoccupied, so that efficient charge separation can be made possible. This work describes a set of studies that measures this energetics for CdSe NPs on gold electrodes.

In this study, the NPs are adsorbed onto a solid substrate that serves as an electrode. For any photoelectronic application, the energy of the HOMO (valence band) and LUMO (conduction band) of the NPs relative to the Fermi level of the electrode is of major importance. When NPs are adsorbed on electrodes the electrochemical potential of the solid and the NP layer come into equilibrium. Hence it is expected that the relative positions of the bulk electrode's Fermi level and the HOMO and LUMO of the NPs will adjust, and the adjustment will depend on the properties of the interface and the properties of the NPs, *e.g.,* their size. In a simple model, the effective mass approximation, it is assumed that the HOMO-LUMO gap varies with size, so that the shift is inversely proportional to the effective mass of the relevant charge carrier, i.e., the hole and electron.[7,8,9,10]

This work addresses the questions, 'How do the HOMO and LUMO vary as a result of attaching the NPs to a metal electrode and how does its variation depend on the size of the NPs?'. We use two independent methods for determining the energy alignment between a gold substrate and the HOMO and LUMO of CdSe NPs as a function of size; the NPs are linked to the gold through a self-assembled monolayer of dithiols. In the first method we combine single photon photoelectron spectroscopy with two photon photoelectron spectroscopy[11] to provide a direct measure of the position of the electronic states, both HOMO and LUMO, with respect to the vacuum level. In the second method, we apply cyclic voltammetry to measure the position of the HOMO and LUMO with respect to a Ag/AgCl reference potential. In both cases we compare the energy gaps with the peak fluorescence emission wavelength of the nanoparticles and find good agreement. Comparison of these results (photoemission, voltammetry, and fluorescence) provides a consistent view of the electronic state energies and how they evolve with the nanoparticle size.

A few studies have investigated the position of the electronic states of NPs relative to the Fermi level of the substrate on which they are adsorbed. These studies include tunneling spectroscopy,[12,13] cyclic voltammetry, [14,15,16,17] and photoemission.[18]

The voltammetry studies relate most directly to the work reported here. Previous work has assigned a strong oxidation peak between 1 and 1.5 V versus $Ag/AgNO_3$ to the injection of a hole into the HOMO of the CdSe nanoparticle. In most studies a corresponding reduction wave, albeit weaker, is also observed. The voltammetry studies reported here provide reasonable agreement with earlier studies. A new feature of this study is the comparison of the voltammetry measurements of the band position with electron photoemission measurements of the band positions under UHV conditions. This comparison provides an important test of the voltammetry

assignment and an assessment of the accuracy in assigning an absolute electrochemical potential for the NPs.

8.2 EXPERIMENTAL SECTION

8.2.1 Synthesis of NPs

The CdSe nanoparticles were synthesized, purified, and characterized using standard protocols and details of these procedures are provided in the Supplementary Material.

8.2.2 Absorption and Fluorescence Emission Spectra

The absorption and emission spectra for five of the NPs in solution are presented in Figure 8.1A, and the emission from three of the NPs monolayer assemblies (NPs attached to Au electrodes via a dithiol linker) are shown in Figure 8.1B.

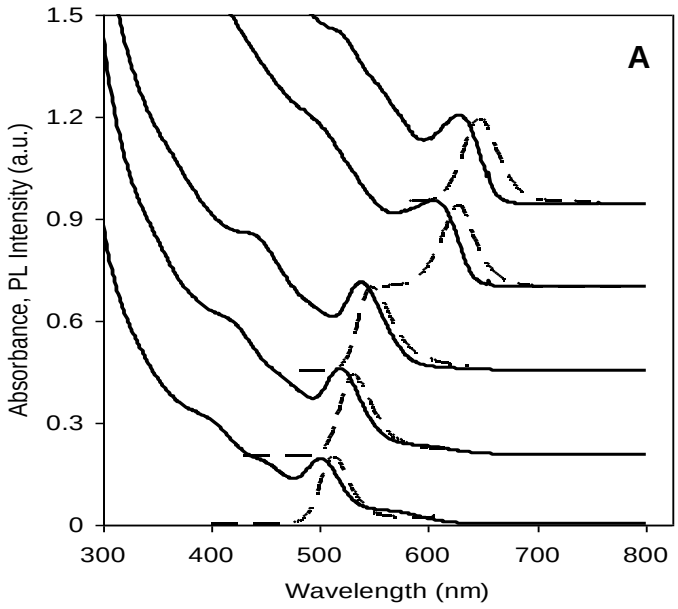

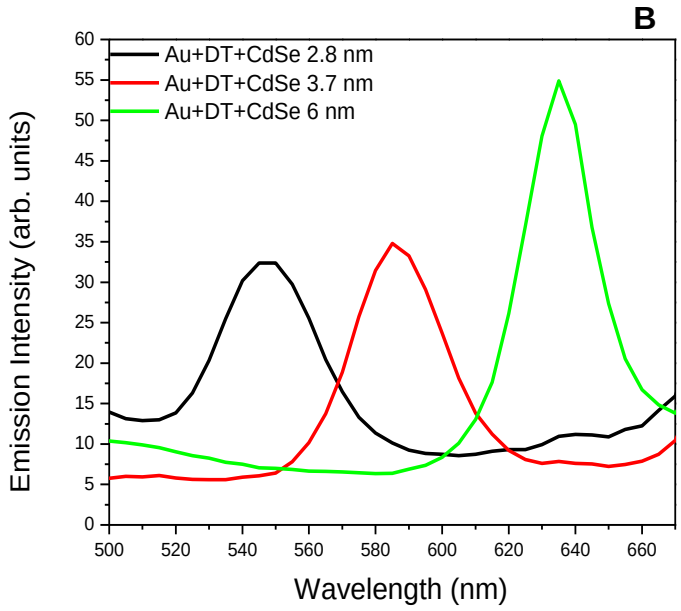

Figure 8.1 Panel A shows normalized absorbance spectra (solid lines) and photoluminescence spectra (dashed lines, λ_{ex} = 400 nm) of five different sizes of CdSe nanocrystal samples in toluene; the curves for different NPs are shifted vertically for clarity. Panel B shows the photoluminescence signal (λ_{ex} = 350 nm) obtained for three sizes of CdSe NPs when adsorbed to the gold substrate through the organic linker.

The UV-vis absorption spectra in panel A were measured at room temperature with an Agilent 8453 spectrometer. Photoluminescence (PL) spectra in panel A were measured at room temperature with a Horiba J-Y Fluoromax 3 Fluorescence Spectrophotometer, using an excitation wavelength of 400 nm. The photoluminescence (PL) spectra in panel B were collected in a Fluorolog-3 Spectrofluorometer (Horiba Jobin Yvon, France) at room temperature using an excitation wavelength of 350nm. The sample was placed at an angle of 30º to the incident light and the emitted PL was collected (Front Face PL measurement) through a monochromator. In

general, only a small shift of about 2 nm was observed in the spectra of the adsorbed NPs, as compared to those taken in solution.

The position of the first absorption peak was used to define the NP size, by using the empirical formula

$$d = (1.6122 \cdot 10^{-9})\lambda^4 - (2.6575 \cdot 10^{-6})\lambda^3 + (1.6242 \cdot 10^{-3})\lambda^2 - (0.4277)\lambda + 41.57 \quad \textbf{(1)}$$

where d and λ are in nm.[19]

8.2.3 Voltammetry Studies

Gold ball electrodes. A Au wire (0.5 mm diameter, 99.99% purity) was cleaned by reflux in concentrated nitric acid (68-70%) at 130° C overnight and then was washed with deionized water. The tip of the gold wire was heated to form a ball of ~0.06-0.15 cm^2 surface area. The gold ball was reheated in the flame until glowing and then quenched in deionized water. This annealing process was performed more than 15 times to make a smooth gold ball. The exposed Au wire was sealed in a glass capillary tube, and the Au ball tip was annealed and cooled in a high-purity stream of Ar gas.

Immobilization of CdSe nanoparticles (NPs). Chemically modified electrodes were prepared by placing the gold ball electrodes into the 5 mM 1,10-decanedithiol SAM solution for overnight (> 12 hours). After that, the electrodes were taken out from the solution, rinsed with absolute ethanol, and dried under a nitrogen stream. The CdSe NP layers were prepared by immersing the Au-dithiol sample into a CdSe NP dispersion for 6 hours, rinsed with toluene, dried and immediately used in voltammetry studies.

Electrochemical Measurements. A computer-controlled CHI 618B electrochemical workstation (CH Instruments, Austin, TX) and a Faraday cage was used for all electrochemical measurements. The three-electrode cell was composed of a platinum counter electrode, a Ag|0.01 M $AgNO_3$, 0.1 M $TBAPF_6$ as reference electrode, and the SAM-coated Au as a working electrode. The voltammetry measurements were performed in 100 mM solution of $TBAPF_6$ in acetonitrile to inhibit corrosion. The $Ag/AgNO_3$ has a potential at 0.54 V versus NHE.[20]

8.2.4 Photoemission studies

Sample preparation and characterization:

The NP/electrode assemblies consisted of CdSe NPs linked to a gold film by a monolayer of 1,9-nonanedithiol (DT). First a DT monolayer on Au was prepared according to the procedures described in ref 1 by immersing a clean gold substrate[22] in a methanol solution of 1 mM DT. Adsorption was carried out overnight in N_2-filled vials that were placed in a desiccator. After adsorption, the samples were rinsed with ethanol and then dried with N_2. In order to attach the CdSe NPs, the DT-SAM coated gold substrates were immersed in 0.5-10 μM solutions of CdSe NPs in anhydrous toluene (99.8%, Aldrich). Four different CdSe NPs were used, large with an average diameter of 6 nm (maximum emission at 635 nm), medium-large with average diameter of 3.7 nm (maximum emission at 590 nm), medium-small with average diameter of 2.8 nm (maximum emission at 550 nm), and small with an average diameter of 2.3 nm (maximum emission at 500 nm). The samples were than rinsed and sonicated in toluene to remove excess NPs that were not covalently attached. The samples were dried under an N_2 gas flow.

SEM Characterization: High-resolution scanning electron microscope (HRSEM) inlense-detector imaging was carried out with a LEO-Supra 55 VP HRSEM. Figure 2 shows a clean Au

substrate (A) and a monolayer of CdSe NPs 6 nm in diameter on the Au-DT substrate (B). A uniform high coverage was observed for all three larger sizes of NPs.

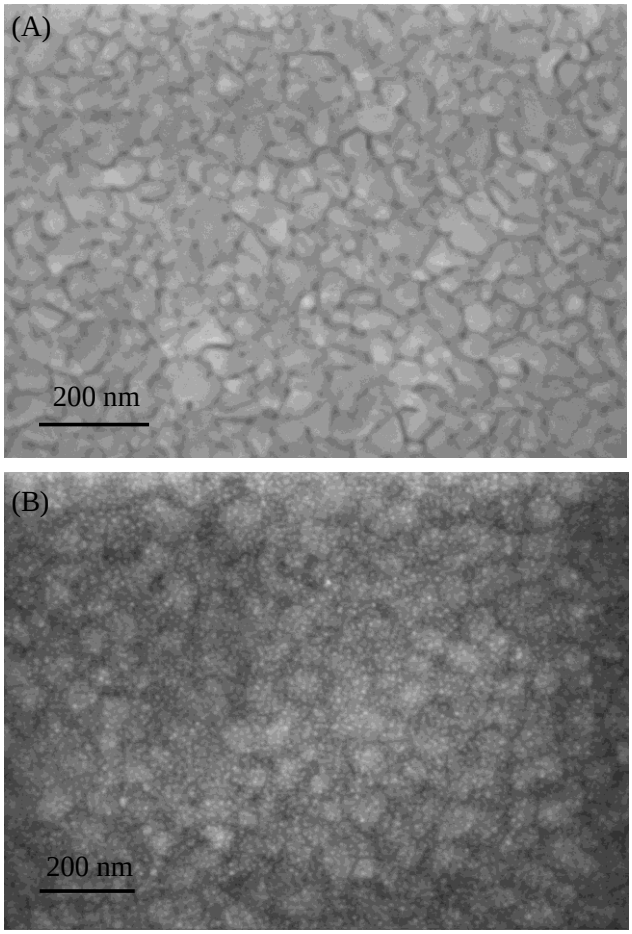

Figure 8.2 SEM Image: (A) Au reference (B) Au covered with a DT monolayer and CdSe NPs. Contrast the small bright spots in panel B with the reference image in panel A.

Photoemission Measurement:

The photoemission experiments were based on ejection of photoelectrons from the NP-coated-Au assemblies. The experimental setup is similar to that described in reference 23. The experiments were performed in an ultrahigh vacuum chamber ($<10^{-8}$ Torr). The photoelectrons are emitted from the sample to the vacuum, where their energy is measured by a time-of-flight spectrometer. Because of the short lifetime of the electrons that are captured by the NPs and

monolayer and because of the low laser intensity and repetition rate, the monolayer and the NPs are not charged by electrons between laser pulses. This was verified by observing a stable electron energy spectrum which does not vary with time.

In the Low Energy Photoelectron Transmission (LEPET) method, electrons are ejected by photons with energy higher than the work function of the sample. The photoelectrons are emitted from states below the Fermi level to above the vacuum level, from which they escape the sample and are transmitted to the detector. These studies provide information about the density of states below the Fermi level, hence the position of the HOMO.

In two-photon photoelectron (TPPE) spectroscopy, photons with energy lower than the work function of the sample are used. The "pump" photons interact with electrons that reside in states below the Fermi level and excite them to states above the Fermi level but below the vacuum level of the sample. If the laser pulses used are not very intense and are relatively long, the electrons excited by these first photons can relax either back to states below the Fermi level or to originally unoccupied states in the monolayer, an 'intermediate' state. The second laser pulse, the "probe", also has photons with energies below the work function of the sample; nevertheless they are able to photoeject electrons from occupied 'intermediate' states to an energy above the vacuum level, from which they can escape the sample and be detected. The measured kinetic energy of these photoelectrons provides information on the binding energy of the electron in the intermediate state, the LUMO of the NPs.

In this experiment we used two photons from the same laser pulse to induce the two-photon-photoemission of electrons. Because of the relatively long laser pulse (laser pulse length of ~10 nsec) and the low intensities, no significant contribution to the signal from a two-photon coherent process was observed. In the coherent process the kinetic energy of electrons would be

$2h\nu - (\Phi + E_b)$ because of energy conservation; Φ is the substrate workfunction and E_b is the electron binding energy. Thus when varying the energy of the photons the change in the kinetic energy difference between photoelectrons should increase as twice the photon energy. In contrast, the observed photoelectron energy increases as one times. This observation indicates that the observed photoelectrons from the TPPE process arise from long lived intermediate states; the first photon excites an electron that relaxes to some long-lived intermediate state, and only then can the electron be photoejected from this intermediate state by the second photon. In order for these intermediate states to be long-lived, they must be localized on the NPs. Hence, the kinetic energy of the electrons reflects their binding energy in the monolayer so that

$$E_b = \Phi - (h\nu - E_k) \quad \textbf{(2)}$$

In all of these studies, the sample was biased by -1 V versus the detector.

8.3 RESULTS

8.3.1 Photoemission

Figure 8.3 shows photoelectron energy distributions for photoelectrons that are ejected by 6.42 eV photons impinging on NP/gold assemblies (LEPET spectra). The high energy cutoff in the spectra results from electrons near the Fermi level that are the most easily ejected to above the vacuum level. Their kinetic energy is taken to be $h\nu - \Phi$, where Φ is the substrate work function. The work function is calculated from the total width of the signal which is ~1.8 eV for Au-DT and ~2.1 eV for the Au-DT-NP; so that Φ = ~4.6 eV for Au-DT and ~4.3eV for the monolayers containing NPs (depending on the coverage). The photoemission spectrum taken for

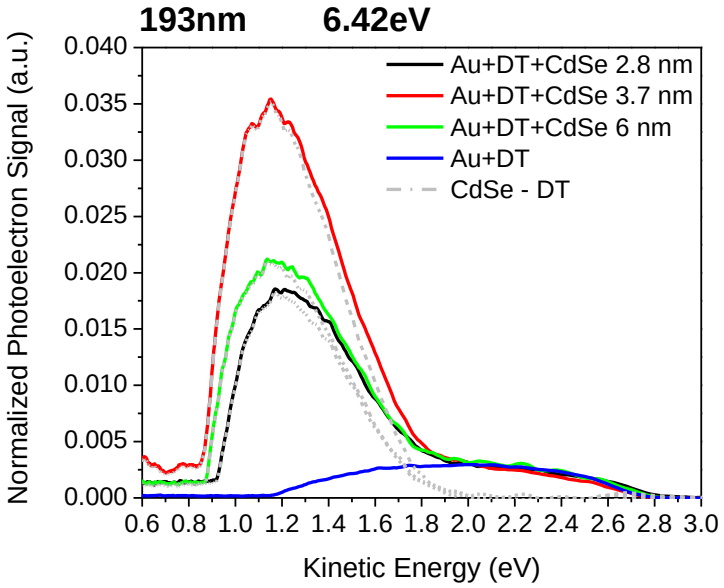

Figure 8.3 LEPET spectra are shown for the four NPs monolayers studied. The dashed gray curves show difference spectra that are obtained by subtracting the spectrum of the Au-DT; note the similar peak for the NP's in this case.

a Au substrate that is covered only by the organic monolayer (DT) is weak, broad, and peaks at a kinetic energy of about 2 eV (Figure 8.3). The spectra for the monolayers containing NPs are much more intense and they can be qualitatively described as having two characteristic peaks: one with a maximum kinetic energy of ~1.15 eV and a second with a maximum kinetic energy of ~2 eV. While the peak at 2 eV is also observed for the Au-DT sample, the peak at 1.15 eV is a unique feature of the monolayers containing NPs. In addition, if one subtracts the spectrum obtained for the Au-DT sample from that obtained for the Au-DT-NP assemblies, then the resulting difference peak rises similarly for all three assemblies of the larger NPs. These difference spectra are shown in Figure 8.3 by the dashed gray curves. Although the intensity of the subtracted spectra varies with the NP size, the difference spectra shown here occur at the

same energy. Because of the likely variation of the NP absorption cross section with size and the variability in the surface coverage of NPs, no effort was made to interpret the variation in signal intensity between samples. Because the LEPET spectra reflect the energy dependence of the density of states below the Fermi level, these data show that all three sizes of NPs have the HOMO located at nearly the same energy of 1.25±0.05 eV below the Fermi level. In the case of the smallest NPs with an average diameter of 2.3 nm, the LEPET shows no variations as compared to the LEPET of Au-DT (Data not shown). Hence, no direct evidence for its position can be obtained. It is important to appreciate that for the same samples the fluorescence spectra indicate the existence of a monolayer of 2.3 nm diameter NPs.

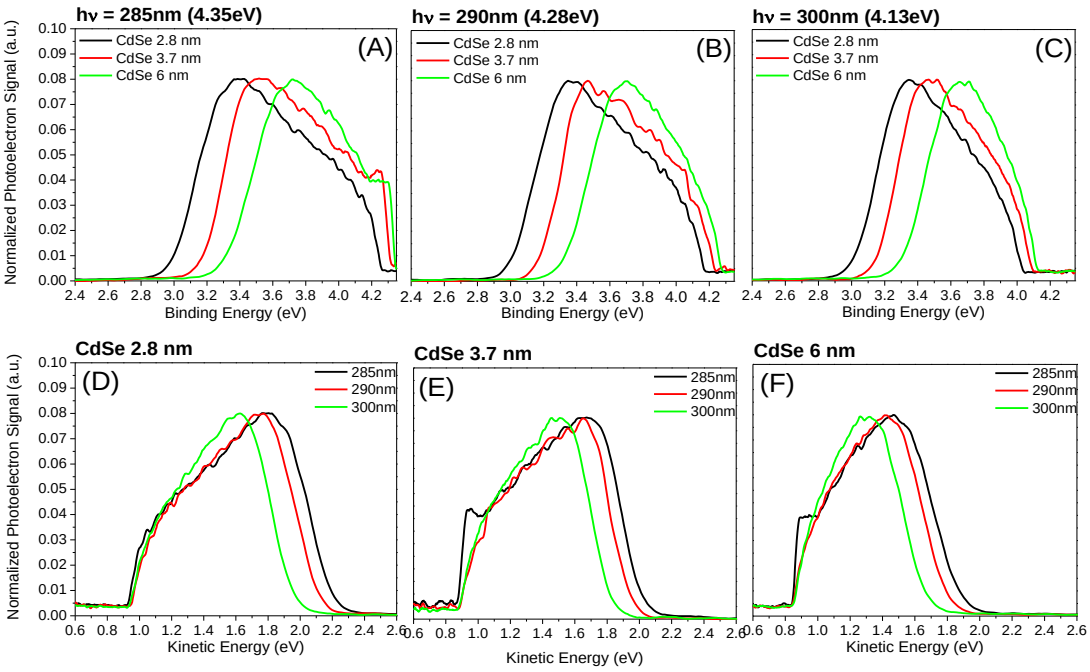

Figure 8.4 TPPE spectra for the systems containing the three different NPs and represented by the electrons binding energy relative to the Fermi level (A-C). The TPPE spectra for each of the NPs size obtained with different laser wavelength (D-F).

Figure 8.4 presents the TPPE spectra for three sizes of NPs, presented either as a function of the binding energy (top) or kinetic energy (bottom) of the electrons. The spectra were taken at three different wavelengths. As a control experiment, photoelectron spectra of a Au-DT sample (no NPs) were collected at the same laser intensities used to obtain the spectra in Figure 4. In these control experiments, no significant photoelectron current was observed, indicating that the photoelectron signals shown in Figure 4 originate from the NPs. In the top row, the spectra for a given laser wavelength are shown for all three sizes. The peak at high binding energy for the 285 nm wavelength laser pulse (see panel A) results from a contribution by a single photon process**.** The sharp cutoff at the high energy edge reflects the density of states in the NPs. In addition, the LUMO seems to be broadened but not symmetrically, perhaps because of a higher density of states in the gold at lower energies. The clear shift in the peak positions for the different NP's spectra, indicates that the state, from which electrons are ejected by the second photon, changes with the NPs size; its energy shifts relative to the Fermi level, indicating a shift in the LUMO position with the size of the NPs. Panels D through F show the spectra for each of the NP sizes at the three wavelengths used. These data clearly demonstrate that the high kinetic energy edge of the spectrum shifts as ($\Delta h\nu$) rather than as $2x(\Delta h\nu)$. This variation indicates that the TPPE process is not a coherent one; namely after absorption of the first photon the electron relaxes to an intermediate state and then absorbs the second photon. Based on Figure 8. 4 we can conclude that the LUMO varies with the NP's size. The shifts observed correspond to an energy of ~0.15 eV between the NPs, which is the optical energy gap difference between the different NPs. By assigning the peak to the LUMO state we get the values of 0.95 eV, 0.8 eV, and 0.65 eV above the Fermi level for the medium-small, medium-large, and large NPs respectively.

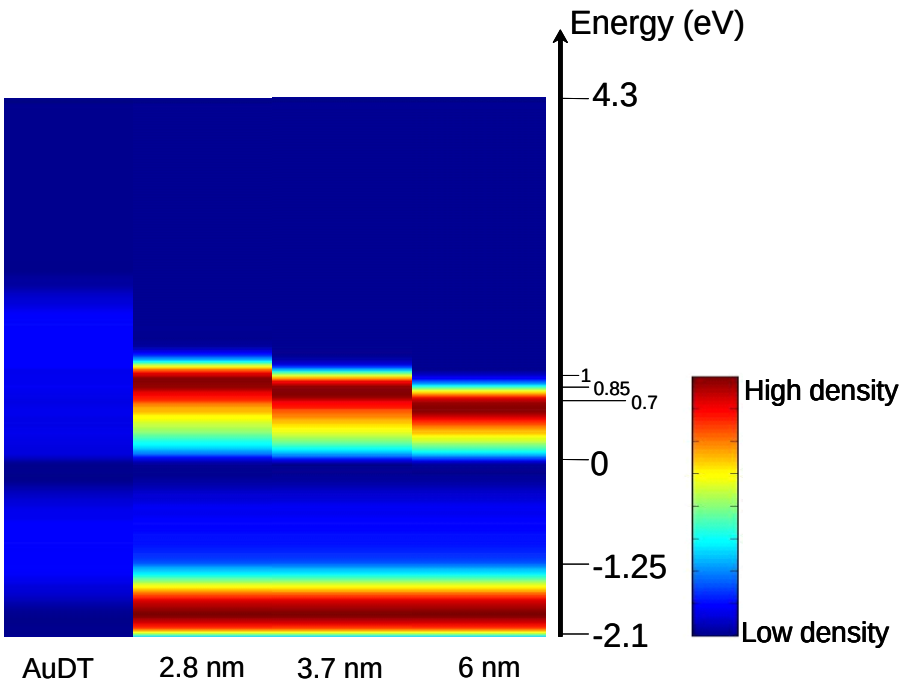

Figure 8.5 Inferred density of states for the four monolayers studied. The results are in good agreement with the optical energy gap observed for the three sizes of NPs (2.8, 3.7 and 6 nm) when positioning the HOMO at the deviation from the Au-DT spectra (1.25eV below the Fermi).

Figure 8. 5 presents the inferred density of states above and below the Fermi level for the systems containing the three sizes of nanoparticles and for the gold covered with DT only. The peaks from the TPPE and the LEPET were normalized for this analysis. While, as mentioned above, the HOMO seems to have the same energy for all sizes, the LUMO position varies. The energy gap between the HOMO and LUMO positions found from the photoemission data are in excellent agreement with the band gap energy obtained from the fluorescence emission data. Figure 8. 5 clearly shows that the HOMO position of the larger NPs is pinned to the same energy level while the LUMO of the system shifts in a way that is expected from the fluorescence data and the changing size of the NPs.

8.3.2 Voltammetry

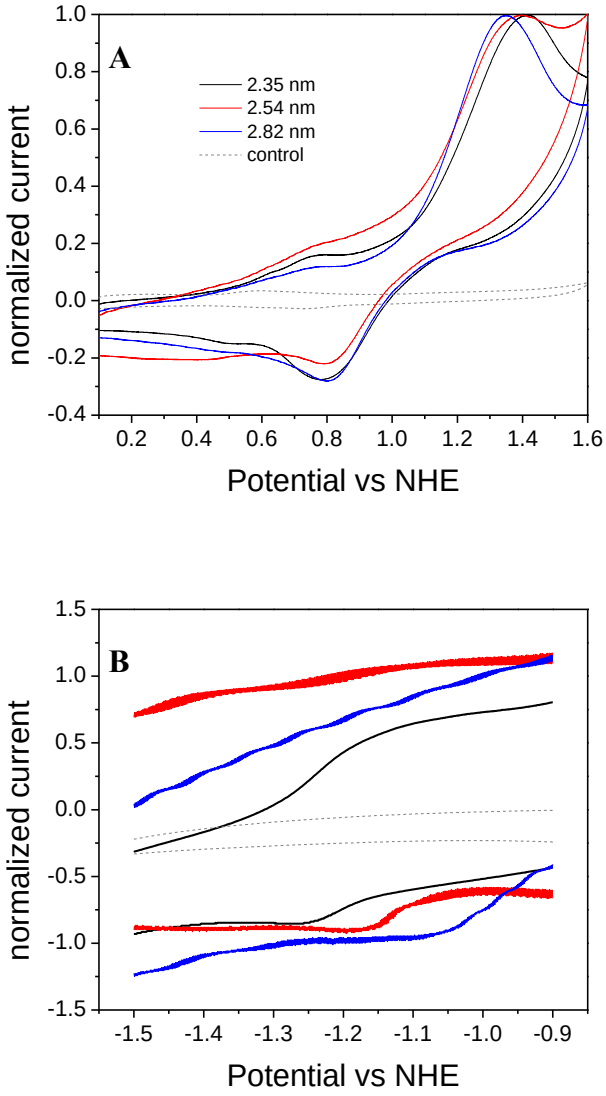

Figure 8.6 Oxidation (A) and reduction (B) voltammograms for different sizes of CdSe NPs immobilized onto a C10 dithiol SAM in acetonitrile solution (the black trace is 2.35 nm NPs, the red trace is 2.54 nm NPs, the blue trace is 2.82 nm NPs and the grey dashed trace is dithiol SAM with no NPs). The scan rate is 100 mV/s. The traces shown in panel B are an expanded region of a broader scan voltammogram.

Figure 8.6 shows cyclic voltammograms for three differently sized CdSe NPs adsorbed on a dithiol SAM on a gold electrode in acetonitrile solution. The voltammograms in Figure 8.6A show strong oxidation waves in the range of 1.22 V to 1.44 V versus NHE that depend on the different particle sizes. The oxidation and corresponding reduction peaks do not appear to change significantly with the potential scan rate. These voltammograms are in good agreement with those reported by others; e.g., see Ref.16 The weak peak near 0.7 V is not assigned, however such a peak could arise from filled interband (i.e., between the HOMO and LUMO) trap states in the particle. The position of this peak is similar to that reported by Inamdar et al.[15] In contrast to Inamdar, the fluorescence spectra (see Figure 8. 1) do not reveal the presence of such trap states; however the peak observed in the voltammograms is much weaker than that reported by Inamdar; these differences may reflect a difference in the number density of such defect states between the two studies. Following these earlier results, the peak of the oxidation wave is assigned to the oxidation potential of the NP. Eventually, with subsequent potential scans the oxidation peaks disappear, suggesting that the oxidation/corrosion products may form[i] and the process is not totally reversible. Assuming that the particle charging energy can be neglected, the oxidation potential corresponds to the HOMO energy. Using the IUPAC value for the absolute electrode potential, 4.44 V, these voltammograms indicate energies of 5.66 V to 5.88 V on the vacuum scale. These values are shifted by about 100 mV from those observed in the photoemission experiments.

The LUMO energies of the CdSe NPs could be determined from the reduction waves and were found to lie between -0.89 V and -1.25 V versus NHE, depending on the particle size. Figure 8.6B shows some example voltammograms. In this case the assignment of the peak was less clear. In part, the smaller signal levels reflect the irreversibility observed in the oxidation

peaks. Nevertheless, an excellent agreement between the values assigned in this manner and those calculated by adding the bandgap energy of the NP to the observed HOMO energy was found.

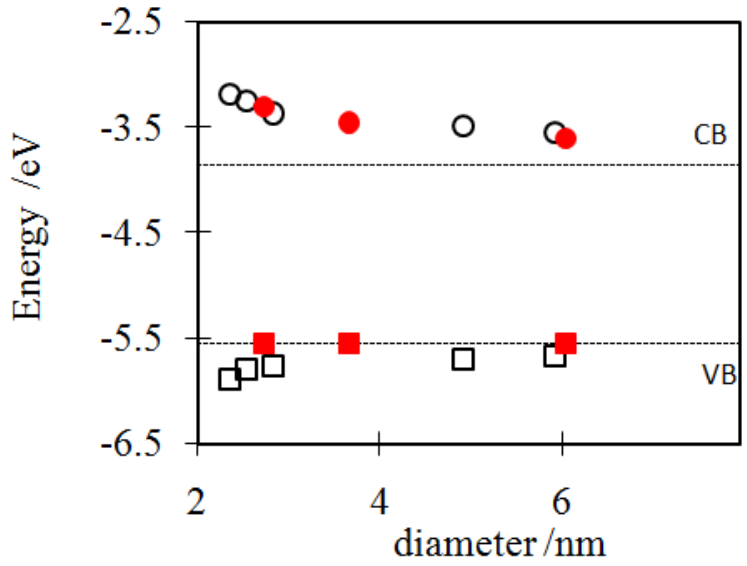

Figure 8.7 The graph plots the HOMO energies (open squares from electrochemistry and filled squares from photoemission measurements) and LUMO energies (open circles from electrochemistry and filled circles from photoemission measurements) of the different CdSe NPs as a function of their diameter. The dashed lines mark the bulk CdSe band positions, assuming that its valence band is pinned at 1.25 eV below the Fermi level of Au. The error bars are smaller than the size of the symbols.

Figure 8.7 shows a plot of the HOMO and LUMO energy positions for the differently sized NPs; both those obtained from the voltammetry and those obtained from the photoemission experiments. The NP size assignments are made based upon the position of the first absorption peaks that were observed in solution for the NPs. The HOMO positions in this graph include those taken from the oxidation potential of the NPs and those obtained from the single photon

photoemission studies. In both cases, the data for the HOMO energy display a relatively flat size dependence for NPs larger than 2.8 nm. The voltammetry experiments reveal a negative energy shift with decreasing size for sizes below 2.8 nm. The positions obtained from the electrochemistry measurements are shifted systematically by about 100 mV more negative than those found from the photoemission measurement. This difference may be the result of the way the energy of the HOMO was defined in the photoemission spectra, but could also result from uncertainties in the accepted value of the absolute electrode potential.[25] The valence band edge position for bulk CdSe is reported to lie near -6.0 eV on the vacuum scale,[26] however this would place it below the HOMO of the NPs. The diagram in Figure 8.7 assumes that the valence band of the bulk CdSe is pinned to a value of 1.25 eV below the Au Fermi level, as is the HOMO of the NPs. The figure also shows the change in LUMO energy with NP size. The LUMO energy appears to shift systematically over the entire range of NP sizes and is converging on the value of -3.85 eV corresponding to the valence band edge of bulk CdSe.

8.4 DISCUSSION

Figure 8.8 plots the shift in the LUMO energy position, as obtained from the experiments reported here (open circles are voltammetry and filled circles are photoemission). In addition, this plot includes a comparison to literature data (x's) for the change in the NP energy gap with size. This comparison was performed by pinning the HOMO energy at the value measured in this work and adding to it the literature value of the energy gap in order to predict a LUMO energy position. This comparison demonstrates the agreement/consistency between the energy level assignments reported here and the bandgap energy, which is well known.

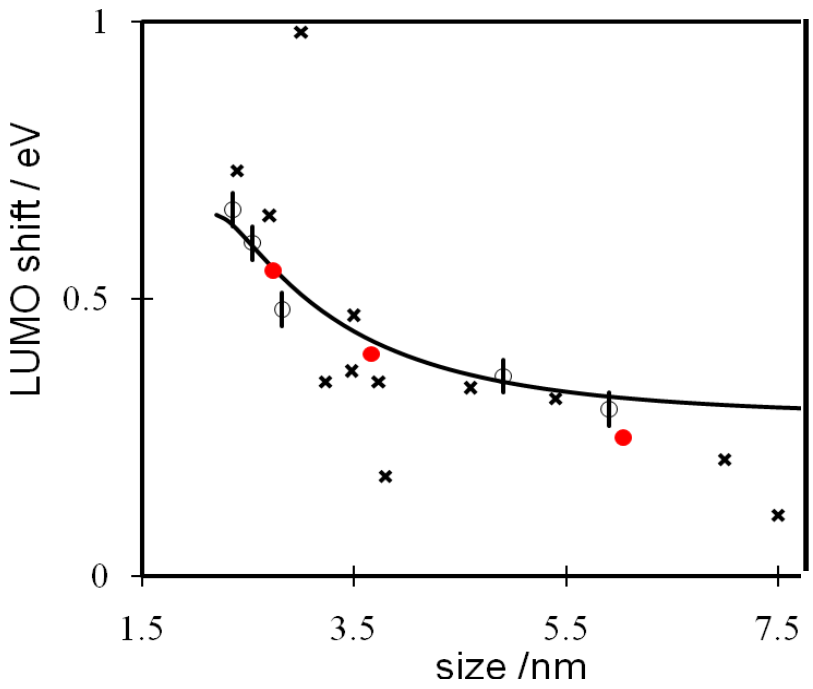

Figure 8.8 The shift of the lowest excited electronic state energy (LUMO) from the bulk value is plotted as a function of particle diameter. The open circles are data obtained from electrochemistry data; the filled circles are data obtained from the photoemission; and the x's are values reported in the literature.[14,16,17] *The solid curve represents the theoretical prediction from Brus.*[7] *The error bars for the photoemission results are smaller than the size of the symbols.*

Brus has proposed a model for the shift in the energy gap of NPs with particle diameter.[7] In this model, the bandgap change ΔE is expressed as a perturbation to the bulk energy gap; Brus finds that

$$\Delta E = \frac{h^2}{2d^2}\left[\frac{1}{m_e} + \frac{1}{m_h}\right] - \frac{3.6\,e^2}{\varepsilon_2 d} + \frac{2e^2}{d}\overline{\sum_{n=1}^{\infty} \alpha_n \left(\frac{2S}{d}\right)^{2n}} \qquad \textbf{(3)}$$

where m_e and m_h are the effective electron and hole masses ($m_e = 0.13m_0$, $m_h = 0.44m_0$ for bulk CdSe, m_0 as electron rest mass), ε_2 is the dielectric coefficient of the particle (4.86 for CdSe), and *S* is the position where a real positive charge exists in the sphere with the radius *d/2*. The first term is the quantum energy of localization, the second term is the coulomb attraction, and the third term is the solvation energy loss. The curve through the data set corresponds to the prediction of this model for the LUMO energy position, obtained by assuming that the HOMO energy is pinned. Because the HOMO energy is pinned, the LUMO energy should shift in the same manner as the energy gap. The solid curve is a best fit of the experimental LUMO energies by equation 1, with the parameters given above.

The most interesting and surprising finding of the present studies is the fact that the HOMO of the NPs, when attached to the surface, is pinned and its position does not vary with the particle size. A similar effect has been observed for pentacene adsorbed on conducting polymers.[27] In that case it has been rationalized by charge transfer that causes the pinning of the HOMO. This explanation cannot be valid in our case, since contact potential difference studies show that the charge transfer between the NPs and the substrate does not depend on the size of the NPs. Hence, the HOMO pinning must be explained by interactions between the HOMO of the NPs and the states of the substrate coated with the DT. Indeed, it has been found and verified that the thiol coated gold has a high density of states at energies of about 1.2 eV to 1.6 eV below the Fermi level.[28] These interfacial states (thiol:Au states) may act to couple strongly with the NP. Hence, the coupling of the HOMO of the NPs to the high density of states of the gold is through these states that, at least partially, are located on the DT. As a result one expects that the effective mass of the hole in the NPs will increase. Apparently, the LUMO couples more weakly to the substrate and therefore is more localized on the NPs. Hence, the effective mass of the electron is small and

when level adjustment occurs, the LUMO's energy varies more than expected based on the effective masses of the hole and the electron in the unbound nanoparticle. This weak coupling of the LUMO with the substrate also explains the relatively efficient photoemission observed from the adsorbed NPs.

8.5 ACKNOWLEDGEMENTS

This work was partially supported by the US-DOE (Grant # ER46430), by the Israel Ministry of Science, and by the Grand Center for Sensors and Security at the Weizmann Institute. The electron microscopy studies were conducted at the Irving and Cherna Moskowitz Center for Nano and Bio-Nano Imaging at the Weizmann Institute of Science.

8.6 REFERENCES

(1). Zhang J. Z. *J. Phys. Chem. B* **2000**, *104*, 7239**.**

(2). Guldi, D. M.; Zilbermann, I.; Anderson, G.; Kotov, N. A.; Tagmatarchis, N.; Prato, M. *J. Mat. Chem.* **2005,** *15***,** 114.

(3). S. Kang, M.; Yasuda, H.; Miyasaka, H.; Hayashi, M.; Kawasaki, T.; Umeyama, Y.; Matano, K.; Yoshida, S.; Isoda, H. I. *Chem. Sus. Chem* **2008,** *1*, 254.

(4). Robel, I .; Subramanian, V.; Kuno, M .; Kamat, P. V. *J. Am. Chem.Soc.* **2006,** *128*, 2385.

(5). Kongkanand, A.; Tvrdy, K.; Takechi, K.; Kuno, M.; Kamat, P. V. *J. Am. Chem. Soc.* **2008**, *130*, 4007.

(6). Jiang, X.; Schaller, R. D.; Lee, S. B.; Pietryga, J. M.; Klimov, V. I .; Zakhidov, A. A. *J. Mat. Res.* **2007**, *22***,** 2204.

(7). L. E. Brus, *J. Chem. Phys.* **1983**, *79*, 5566.

(8). H. Weller *et al.*, *Chem. Phys. Lett*. **1986**, *124,* 557.

(9). Y. Kayanuma, *Phys. Rev. B*, **1988**, *38*, 9797.

(10). Y. Kayanuma and H. Momiji, *Phys. Rev. B*, **1990**, *41*, 10261; D. B. Tran Thoai, Y. Z. Hu, and S. W. Koch, *Phys. Rev.***1990**, *B*, *42*, 11261; Y. Nosaka, *J. Phys. Chem.* **1991**, *95*, 5054; J. L. Marı´n, R. Riera, and S. A. Cruz, *J. Phys.: Condens. Matter* **1998**, *10*, 1349; S. V. Nair, S. Sinha, and K. C. Rustagi, *Phys. Rev. B*, **1987**, *35*, 4098; J. M. Ferreyra and C. R. Proetto, *Phys. Rev. B*, 1999, *60*, 10672; S. Horiguchi, *Physica B* **1996**, *227*, 336; G. W. Bryant, *Phys. Rev. B* ,**1995**, *52*, R16997; K. K. Nanda, F. E. Kruis, H. Fissan, *Nano Lett.* **2001**, *1*, 605.

(11). T. Z. Markus, S. S. Daube, R. Naaman, A. M. Fleming, J. G. Muller, C. J. Burrows, *J. Am. Chem. Soc.* **2009***, 131*, 89–95.

(12). P. Liljeroth, L. Jdira, K. Overgaag, B. Grandidier, S. Speller, D. Vanmaekelbergh, *Phys. Chem. Chem. Phys.* **2006**, *8*, 3845–3850.

(13). D. Steiner, D. Dorfs, U. Banin, F. D. Sala, L. Manna, O. Millo, *Nano Lett.*, **2008**, *8* (9), 2954-2958.

(14). Wang, C.; Shim, M.; Guyot-Sionnest, P.; Franck, J. *Science* **2001**, *291*, 2390.

(15). S. N. Inamdar, P. P. Ingole, . S. K. Haram, *ChemPhysChem*. **2008**, *9*, 2574; E. Kucur, W. Bucking, R. Giernoth, T. Nann, *J. Phys. Chem. B*, **2005**, *109*, 20355; E. Kucur, W. Bucking, S. Arenz, R. Giernoth, T. Nann, *ChemPhysChem*. **2006**, *7*, 77–81.

(16). E. Kucur, J. Riegler, G. A. Urban, and T. Nann *J. Chem. Phys.* **2003**, *119*, 2333-2337.

(17). I. Robel, M. Kuno, and P. V. Kamat, *J. Am. Chem. Soc*. **2007**, *129*, 4136-4137.

(18). Meulenberg, R. W., Lee, J. R.I., Wolcott, A., Zhang, J. Z., Terminello, L. J., and van Buuren T. *ACS Nano* **2009**, *3*, 325-330.

(19). W. W. Yu, L. Qu, W. Guo, and X. Peng *Chem Mater* **2003**, *15*, 2854-2860..

(20). *Electroanalytical Methods: Guide to Experiments and Applications*, Edited by Fritz Scholz. Springer. Verlag, Heidelberg , **2002**, p298

(21). T. Aqua, H. Cohen, A. Vilan, R. Naaman *J. Phys. Chem. C*, **2007**, *111* (44), pp 16313–16318

(22). Ron, H.; Matlis, S.; Rubinstein, I. *Langmuir* **1998**, *14*, 1116-1121.

(23). Ray, S. G.; Daube, S. S.; Cohen, H.; Naaman, R. *Isr. J. Chem* **2007**, *47*, 149.

(24). S. K. Poznyak, N. P. Osipovich, A. Shavel, D. V. Talapin, M. Gao, A. Eychmueller, and N. Gaponik *J. Phys. Chem. B* **2005**, *109*, 1094-1100.

(25). a) Gomer, R.; Tryson. G.. *J. Chem. Phys*. **1977**, *66*, 4413; b) Trasatti, S. *Pure and Appl. Chem*. **1986**, *58*, 955.

(26). J. Jasieniak, J. Pacifico, R. Signorini, A. Chiasera, M. Ferrari, A. Martucci, and P. Mulvaney *Adv. Func. Mat.* **2007**, *17*, 1654-1662

(27). N. Koch, A. Elschner, J.P. Rabe, R.L. Johnson, *Adv. Mat*. **2005**, *17*,330; N. Koch, A. Vollmer, *App. Phys. Lett*. **2006**, *89*, 162107.

(28). A. L. Graham,. R. Colorado, Jr., V. H. Wysocki, T. R. Lee, P. A. Lee, N. R. Armstrong, *J. Phys. Chem. B* **2003**, *107,* 11690-11699.

8.7 SUPPLEMENTAL INFORMATION

Chemicals

All aqueous solutions were prepared with 18.3 MΩ cm^{-1} deionized water (Nanopure, Barnstead, Dubuque, IA). 1,10-decanedithiol ($HSC_{10}H_{20}SH$) was purchased from Alfa Aesar, and tetrabutylammoniumhexafluorophosphate ($TBAPF_6$) was purchased from Sigma. Electrodes used in all experiments were gold ball electrodes made from gold wire (0.5 mm diameter, 99.99%, Alfa Aesar). Selenium powder (99.999%), hexadecylamine (HDA, 99%), trioctylphosphine (TOP, 97%), trioctylphosphine oxide (TOPO, 90%), oleylamine (97%), oleic acid (90%), 1-octadecene (ODE, 90%), CdO (99.999%) were purchased from Aldrich and used as received. All reagents and solvents were obtained from commercial sources and used as received.

CdSe NP synthesis and purification

Spherical CdSe nanoparticles were prepared in a manner similar to a previously published procedure.[1] All synthetic routes were carried out under argon gas using Schlenk techniques. For a typical synthesis of 2-4 nm CdSe nanoparticles, 0.0514 g of CdO, 0.2919 g of HDA and 3.8768 g of TOPO were loaded into a 25 mL three-neck round-bottom flask. The mixture was heated to 300℃ under Ar flow, and CdO was dissolved in HDA and TOPO. A selenium stock solution (0.0787 g of selenium powder dissolved in 4 ml of TOP) was injected quickly. After injection, nanocrystals were allowed to grow at 280℃ until they reached the desired size. For 4-6 nm CdSe nanoparticles, typically, 5.0 mL of oleylamine and 0.15 mL of Se stock solution (2.1 M in TOP) were loaded in a 50-mL flask, and the mixture was heated to 90 °C and degassed under a vacuum for 30 min. The reaction vessel was then filled with argon, and the temperature was increased to 300°C under stirring. A 1.0 mL volume of Cd stock solution

(0.3 M in 1:1 v/v oleic acid and ODE) was injected quickly into the reaction flask. The temperature was then set at 280°C for the subsequent growth and annealing of nanocrystals.

For the photoemission measurements, particles were synthesized in a non-coordinating solvent. 0.013 g of CdO and 0.3ml of oleic acid were added to 5ml octadecene. 0.008g of Se in 2ml TOP was injected at 280℃ , and particles were grown at 250℃ . For the largest particles, Cadmium oleate in octadecene and Se in TOP were further injected until the desired size was reached.

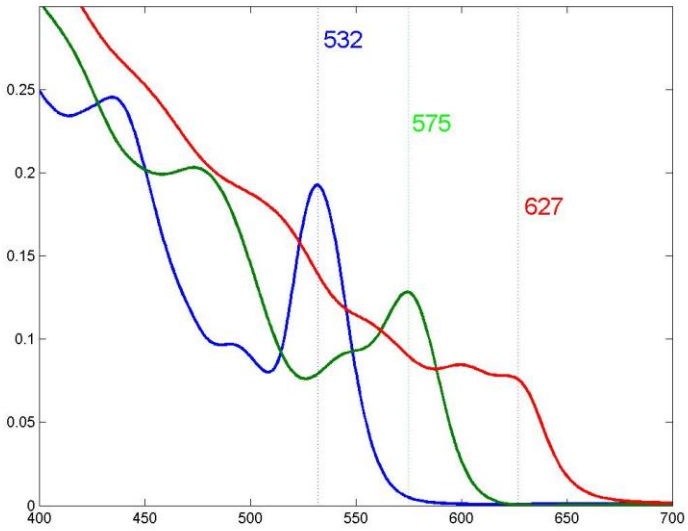

Figure 8.9 The absorption spectra of the nanoparticles taken in solution.

References

(1). a) Peng, Z. A. ; Peng, X. *J. Am. Chem. Soc.* **2001,** *123,* 183-184; b) Zhong, X; Feng, Y.; Zhang ,Y. *J. Phys. Chem. C* **2007,** *111,* 526-53; c) Talapin, D.V.; Rogach, A.L.; Kornowski, A.; Haase, M., Weller, H. *Nano Letters*, **2001,** *1* (4), 207-211

9.0 LIQUID-LIQUID INTERFACE STUDY

Electrochemistry at the interface between two immiscible electrolyte solutions (ITIES) is of great fundamental importance because of its relevance to a wide range of applications that involve charge transport across phases. Photoelectrochemical studies at the liquid-liquid interface provide a good model system for understanding photoinduced charge transfer processes that are relevant to our long range goal of understanding charge transfer in bulk heterojunction solar cells, which are composed of bicontinous conducting polymer films doped by dyads. This chapter describes our preliminary studies on investigating the organization and reactivity of CdTe nanoparticles at the water/dichloromethane interface in the presence of the Galvani potential bias.

9.1 INTRODUCTION

An interface between two immiscible electrolyte solutions (ITIES), or a liquid|liquid interface, can be formed between two liquid solvents of low mutual miscibility, each containing an electrolyte. Typically, one of these solvents is water, and the other one is a polar organic solvent of a moderate or high dielectric permittivity, such as nitrobenzene, 1,2-dichloroethane, or 1,1-dicholormethane, which allows for at least partial dissociation of dissolved electrolytes into ions.[1] The study of electrochemical processes at the liquid|liquid interface dates back to at least

the beginning of the last century and such studies are highly relevant to a wide range of systems in chemistry and biology[2].

Toward the goal of creating efficient solar cells, tremendous effort has been concentrated in optimizing solid-state and solid/liquid junctions. However, interfaces involving solid-state components are subject to structural defects which can act as traps and recombination centers for charge carriers. Liquid-liquid interfaces can be used to explore how phase boundaries might be exploited to enhance photoinduced charge transfer for systems in which the decay of the excited state and the geminate recombination (back electron transfer) are important competing processes.[3,4] The liquid|liquid interface can be a simple and unique approach to separate photogenerated reactants and products (to block back electron transfer) physically and provide an intimate defect-free junction (see equation 1).[5-7]

$$D(org) + A(aq) \xrightarrow{h\nu} D(org) + A^*(aq) \rightarrow D^+(org) + A^-(aq) \qquad (1)$$

At polarized ITIES, two types of processes can lead to photocurrent signals involving electron transfer steps; one is photoinduced electron transfer followed by ion transfer (PE-IT), and the other is interfacial photoinduced electron transfer (IPET).[4] The photocurrents correspond to the products generated in a homogeneous photoreaction transferring across the liquid/liquid interface. For example, in the PE-IT process reported by Kotov and Kuzmin[8-10] the photoresponses originated from the protoporphyrins/quinines and the quinines/tetraphenylborate systems at the water/1,2-dichloroethane (DCE) interface. The photocurrent responses associated with IPET reactions are more complicated because of interferences arising from the transfer of either ionic reactants or products.[7] Girault et al [11,12]studied the photoinduced electron transfer between $Ru(bpy)^{2+}$ in water and the quenchers $C7V^{2+}$ and TCNQ in DCE. In both cases, the fact that neither reactants nor products transfer across the interface indicates that the photocurrent

responses are associated with electron transfer across the liquid-liquid interface. They also investigated the dependence of the photocurrent on the applied potential, porphyrin concentration (ZnTPPC), and light intensity.[4] If the photoresponses are interpreted in terms of efficiencies as in solar energy conversion they are on the order of 0.05%. [13] Despite the low efficiency obtained, the simplicity of this approach provides numerous possibilities for optimization of the cell output power.

In addition to the detailed studies on photocurrent responses originating from the heterogeneous quenching of photoexcited water-soluble dyes, including porphyrins, chlorines and phthalocyanines by hydrophobic redox species,[14-17] recent studies have demonstrated that titanium dioxide (TiO_2) nanoparticles (NPs) can be electrostactially assembled at the polarised interface between water and DCE electrolyte solutions.[18,19] Assembling TiO_2 NPs at the interface effectively increases the interface excess charge, which is dependent on the Galvani potential difference across the water/DCE interface. Band-gap illumination of the interface led to interfacial transfer of holes or electrons to redox species located in the organic phase. Due to the unique electronic and optical properties of semiconductor quantum dots (QDs), Su et al extended the photoelectrochemical study to CdSe QDs.[20] They observed that mercaptosuccinic acid (MSA)-capped CdSe could be adsorbed at the water/DCE interface as the Galvani potential difference was tuned negative with respect to the potential in the organic phase.[20] Heterogeneous photocurrent responses arising from the adsorbed CdSe NPs were recorded upon illumination of the interfacial region in the presence of redox species in the organic phase. The photocurrent efficiency strongly depends on the applied Galvani potential difference and the formal redox potential of the electron acceptor.

As a model of nanocrystal-dyads based bulk heterojunction solar cells, we have created bilayers of NPs at liquid/liquid interfaces in the presence of potential bias, and we observed the heterogeneous electron transfer from NPs on one side of the interface to those on the other side. Toward this goal, this chapter briefly describes the preliminary studies done on organization and reactivity of NPs (CdTe) at the water/DCM interface observed by four-electrode cyclic voltammetry.

9.2 EXPERIMENTAL SECTION

The supporting electrolyte in the organic phase was bis(triphenylphosphoranylidene) ammonium tetrakis(penta-nuorophenyl)borate (BTPPATPFB). This salt was prepared by metathesis of bis(triphenylphosphoranylidene)ammonium chloride (BTPPACl) and lithium tetrakis(pentafluorophenyl) borate diethyl etherate LiTPFB in 2 : 1 mixtures of methanol and water. Aqueous solutions were prepared with water purified by a Barnstead Nanopure system, and its resistance was 18.2 MΩ. All other reagents and solvents were analytical grade reagents and were used as received.

The blank electrochemical cell is schematically displayed in Figure 9.1.

Figure 9.1 Representation of the blank electrochemical cell employed in all measurements

A computer-controlled CHI 700C four-electrode electrochemical workstation (CH Instruments, Austin, TX) and a Faraday cage were used for all electrochemical measurements. The water/DCM junction was controlled via a custom-built four-electrode all-glass cell that

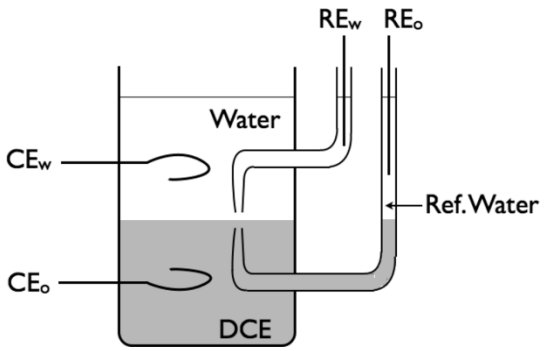

Figure 9.2 Schematic representation of the four-electrode glass cell. REw and REo are two reference electrodes, and CEw and CEo are two counter electrodes in water and DCM phase, respectively, adapted from Ref 20.

contains two lateral compartments for the reference electrodes, which were approached to the interface by Luggin capillaries. (Figure 9.2). The interface between the upper aqueous phase and the bottom organic phase is formed between the two Luggin capillaries with geometric area of 1.53 cm^2. (See Appendix for details)

In each phase, a platinum gauze counter electrode is positioned, which allows the passage of the current. The interface is polarized by means of the two reference electrodes RE1 and RE2, which are usually silver|silver chloride (Ag|AgCl). It should be mentioned that RE2 functions as the reference electrode in the organic phase together with a nonpolarizable water|DCE interface formed in the capillary.

9.3 RESULTS AND DISCUSSION

9.3.1 Blank CV Measurement

Blank cyclic voltammetry measurments were performed using the electrochemical cell configuration shown in Figure 9.1 for a liquid-liquid junction formed between water and dichloromethane (DCM). The obtained cyclic voltammogram is shown in figure 9.3. Note that the potential shown on the x-axis is the total potential between the two reference electrodes, not the Galvani potential applied to the polarizable interface, and the y-axis is the current, not the current density.

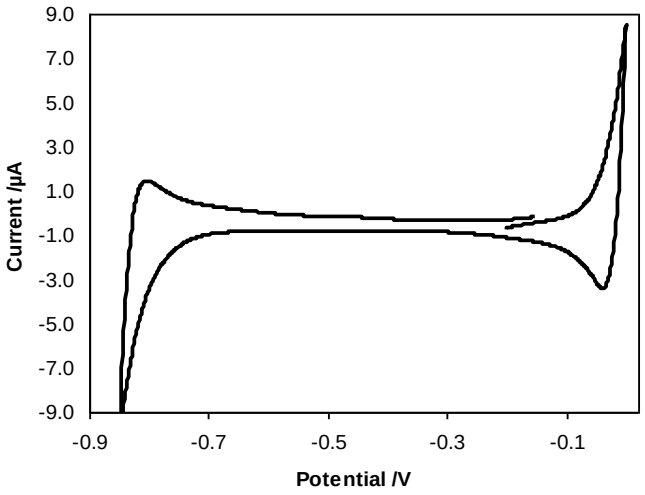

Figure 9.3 Blank CV scanned from -0.88 V to 0 V, Scan rate is 50 mv/s

9.3.2 Ion Transfer of Chemical Standard Across the Interface

To convert the total potential to a Galvani potential, a chemical standard, such as tetramethylammonium chloride (TMA) or tetraethylammonium chloride (TEA), with known interfacial ion transfer potential can be used. The electrochemical cell is schematically displayed in Figure 9.4.

		NaCl	BTPPATPFB	BTPPACl 1 mM			
Ag	AgCl	10 mM	5 mM	LiCl 10 mM		AgCl	Ag
			TMA				
		(aq)	(DCM)	(aq)			

Figure 9.4 Representation of the electrochemical cell employed

Figure 9.5 shows the measured voltammogram of TMA with a formal ion transfer potential for

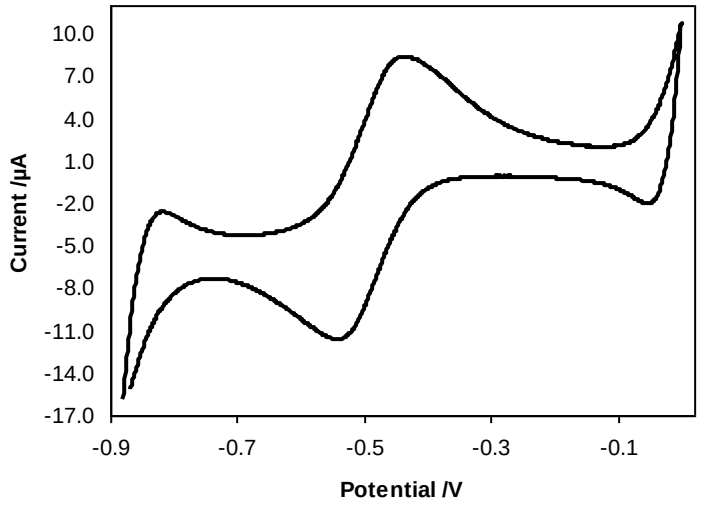

Figure 9.5 Cyclic voltammogram of TMA ion transfer at water/DCM interface

TMA at -0.48 V. Taking the known Galvani ion transfer potential value for TMA to be +0.16 V, we can convert the total potential difference to the Galvani potential at the interface by shifting the whole window positively by 0.64 V. Using this calibration, the potential window for the water/DCM junction ranges from -0.24 V to+ 0.64 V.

9.3.3 Adsorption of CdTe NPs at Interface

To investigate CdTe NPs adsorption behavior at the liquid/liquid interface upon applying potential difference, mercaptoprionic acid (MPA) capped-CdTe NPs were synthesized first and purified. With the concentration of MPA-CdTe in the water phase gradually increased, the cyclic voltammograms were recorded. The electrochemical cell is schematically displayed in Figure 9.6.

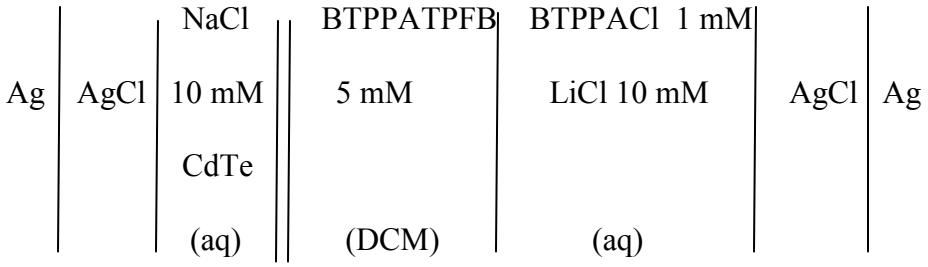

Figure 9.6 Representation of the electrochemical cell employed in adsorption of CdTe NP experiments

Cyclic voltammograms of the water/DCM interface for increasing concentrations of the CdTe NPs in the aqueous phase are illustrated in Figure 9.7. With increasing concentration of MPA-CdTe in the water phase, the currents at the edge of the negative potential window increase and the ones at the edge of the positive potential window remain the same, consistent with the MPA-CdTe NPs being mostly negatively charged in water at neutral pH. However, no bumps or

peaks were observed in the middle of the potential range, as shown in the reference 20 for MSA-CdSe NPs .

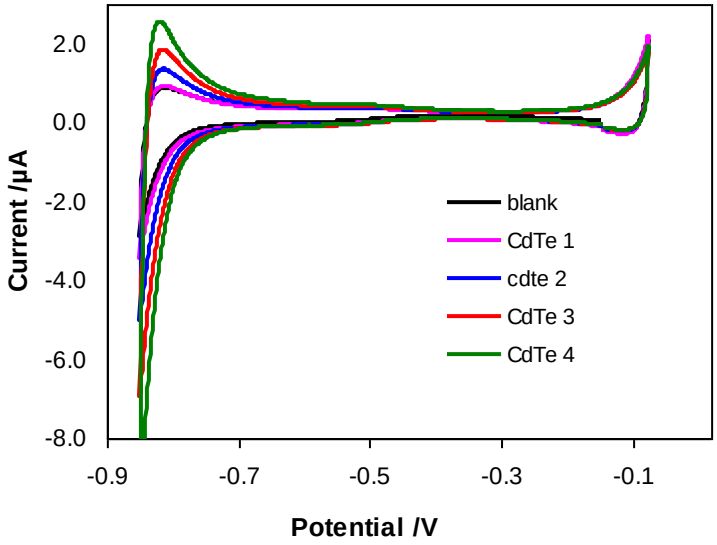

Figure 9.7 Cyclic voltammogram of MPA-CdTe NPs at water/DCM interface, from CdTe 1 to CdTe 4 follows the pattern of increasing concentration of CdTe NPs in aqueous phase

To test how the ligands might contribute to the different adsorption behaviour between MPA-CdTe and MSA-CdSe NPs, MSA-CdTe NPs were also synthesized and tested at water/DCM

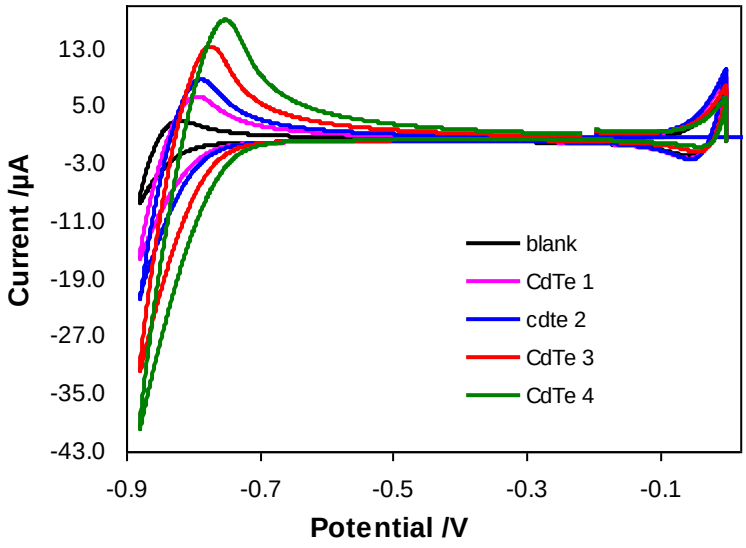

Figure 9.8 Cyclic voltammogram of MSA-CdTe NPs at water/DCM interface, from CdTe 1 to CdTe 4 follows the pattern of increasing concentration of CdTe NPs in aqueous phase

junctions. Two batches of MSA-CdTe were tried and examples of the cyclic voltammograms are shown in figure 9.8. As can be seen, the CVs of MSA-CdTe NPs resemble those of MPA-CdTe, but with a more pronounced increase in the currents at the edge of the negative potential window.

9.3.4 CV Measurements with Redox Species in Bulk DCM

Motivated by previous work on the redox photoreactivity of CdSe NPs at the water/DCE interface in the presence of redox species in bulk DCE, cyclic voltammograms measurements with various redox species in the organic phase DCM were also carried out. The CV of all the redox species used, including 7,7',8,8'-tetracyanoquinodimethane (TCNQ/$TCNQ^-$), 2,3,5,6-tetrachloro-1,4-benzoquinone(TCBQ/$TCBQ^-$), 2,6-dichloro-1,4-benzoquinone (DCBQ/$DCBQ^-$), benzoquinone (BQ/BQ^-), and ferrocene (Fc^+/Fc) in the organic phase without MPA-CdTe

present in the aqueous phase had responses that were similar to the blank (see Figure 9.9 a). For the case where TCNQ is present in the organic phase and MPA-CdTe NPs are present in the water phase, very well defined peaks were observed in the center of the potential window (see Figure 9.9 b). When only MPA-CdTe was present in the aqueous phase or only TCNQ was present in the organic phase, no peak could be observed. Whether CdTe was added to the aqueous phase first or the TCNQ was added to the organic phase first did not have an obvious effect on the electrochemical cell's CV response.

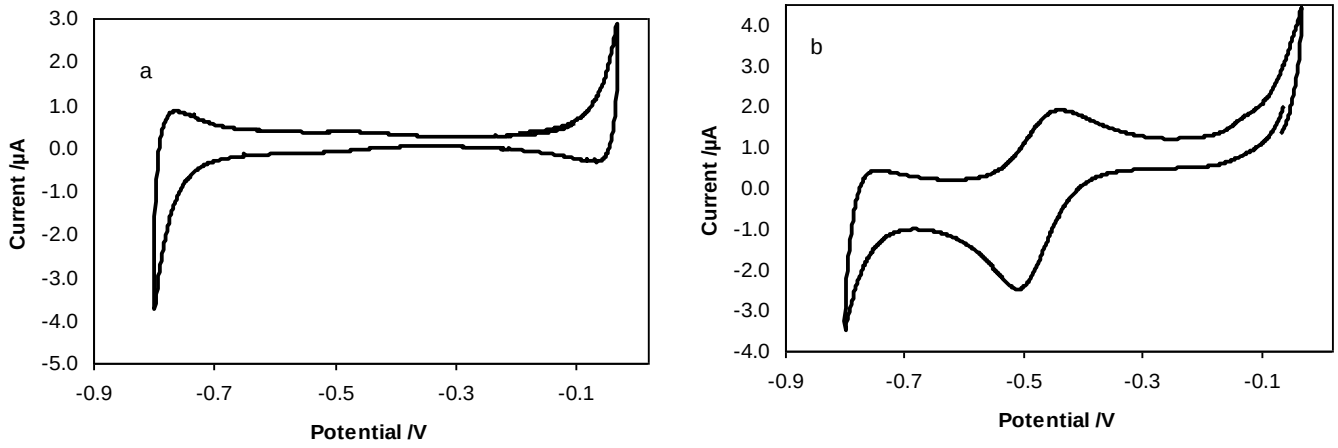

Figure 9.9 a) Cyclic voltammogram of blank, with CdTe in aqueous phase only, or TCNQ in organic phase only; b) Cyclic voltammogram with both CdTe in aqueous phase and TCNQ in organic phase.

All of the other CVs with redox species in the organic phase did not show any peaks or bumps with MPA-CdTe NPs present in the aqueous phase; they remained identical to the blank.

When adding MSA-CdTe NPs into the water phase with TCNQ present in organic phase, similar results were observed, although the shape and current intensity varied. A representative

CV is shown in figure 9.10. The CVs with other redox species in the organic phase remained the same as the blank as well.

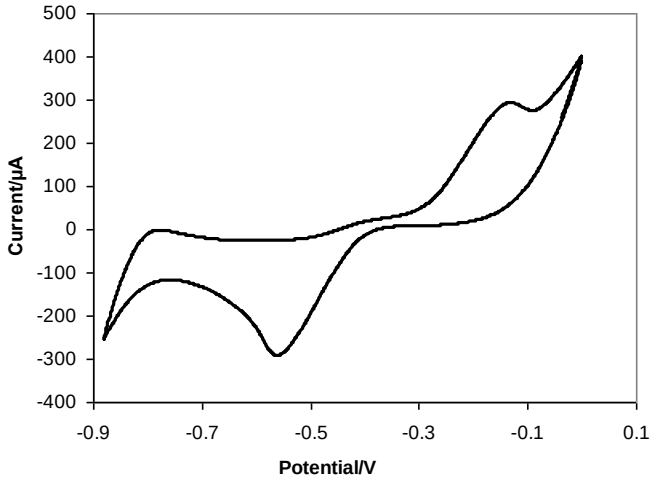

Figure 9.10 Cyclic voltammogram with both MSA-CdTe in aqueous phase and in presence of TCNQ in organic phase

The observed electrochemical signal might arise from heterogeneous electron transfer from the valence band of CdTe NPs adsorbed at the water/DCM interface to TCNQ in bulk DCM. Assuming that the formal redox potentials vs. the standard hydrogen electrode (SHE) of various redox species in bulk DCM remain similar in bulk DCE, i.e, TCNQ is 0.29 V, TCBQ is 0.17 V, DCBQ is − 0.02 V, BQ is − 0.34 V and Fc is 0.64 V,[20] the energy difference between the valence band of CdTe and TCNQ might be the largest, and thus enough to drive the electron transfer at the applied potential window. This may explain why only TCNQ show peaks in CV measurements.

9.4 FUTURE WORK

To further understand and confirm the adsorption and assembly behaviour of CdTe NPs at the interfacial boundary, differential capacitance measurements and a scan rate dependence as mentioned in ref 20 can be carried out. Differential capacitance should increase as a function of the potential difference applied at the interface and the currents at the edge of the negative window should depend linearly on the scan rate. The organic phase solvent DCE, which is commonly used in the literature, should also be tried to see if it makes any difference. The reactivity of CdTe NPs with redox species in the organic phase can be repeated with an appropriate light source illuminating the interfacical region. After the redox characteristics of the adsorbed NPs at the interface is determined by comparison to redox species in the organic phase, an attempt of making dyads at liquid/liquid interface can be tried. This can be done by putting negatively charged CdTe NPs in aqueous phase and using pyridine-capped CdSe, partially ligand exchanged with mercaptodimethylamine (DEA), in the organic phase.

9.5 ACKNOWLEDGEMENT

This work was supported by the US-DOE (Grant # ER46430). M.Wu also thankfully acknowledges Prof. Amemiya and his postdoc, Dr. Ryoichi Ishimatsu, who kindly offered lots of valuable information on liquid-liquid interface studies.

9.6 REFERENCES

(1) Samec, Z. *Pure Appl. Chem.* **2004**, *76*, 2147.

(2) Senda, M.; Kakiuchi, T.; Osakai, T. *Electrochimi. Acta* **1991**, *36*, 253.

(3) Fermin, D. J.; Duong, H.; Ding, Z.; Brevet, P. F.; Girault, H. H. *Chem. Commun.* **1998**, 1125.

(4) Fermin, D. J.; Ding, Z.; Duong, H.; Brevet, P. F.; Girault, H. H. *J. Phys. Chem. B.* **1998**, *102*, 10334.

(5) Marecek, V.; Armond, A. H. D.; Armond, M. K. D. *J . Am. Chem. Soc.* **1989**, *111*, 2561.

(6) Kott, K. L.; Higgins, D. A.; Mcmahon, R. J.; Corn, R. M. *J . Am. Chem. Soc.* **1993**, *115*, 5342.

(7) Marecek, V.; De Armond, A. H.; De Armond, M. K. *J . Am. Chem. Soc.* **1989**, *111*, 2561.

(8) Kotov, N. A.; Kuzmin, M. G. *J . Electroanal. Chem.* **1990**, *285*, 223.

(9) Kotov, N. A.; Kuzmin, M. G. *J. Electroanal. Chem.* **1992**, *341*, 47.

(10) Kotov, N. A.; Kuzmin, M. G. *J. Electroanal. Chem.* **1992**, *338*, 99.

(11) Brown, A. R.; Yellowlees, L. J.; Girault, H. H. *J. Chem. Soc. Faraday Trans.* **1993**, *89*, 207.

(12) Thomson, F. L.; Yellowlees, L. J.; Girault, H. H. *J. Chem. Soc. Chem. Commun.* **1988**, 1547.

(13) Fermin, D. J.; Duong, H.; Ding, Z.; Brevet, P. F.; Girault, H. H. *Electrochem. Commun.* **1999**, *1*, 29.

(14) Fermin, D. J.; Duong, H.; Ding, Z.; Brevet, P. F.; Girault, H. H. *Phys. Chem. Chem. Phys.* **1999**, *1*, 1461.

(15) Fermin, D. J.; Duong, H.; Ding, Z.; Brevet, P. F.; Girault, H. H. *J . Am. Chem. Soc.* **1999**, *121*, 10203.

(16) Jensen, H.; Kakkassery, J. J.; Nagatani, H.; Fermin, D. J.; Girault, H. H. *J . Am. Chem. Soc.* **2000**, *122*, 10943.

(17) Eugster, N.; Fermin, D. J.; Girault, H. H. *J. Phys. Chem. B.* **2002**, *106*, 3428.

(18) Fermin, D. J.; Jensen, H.; Moster, J. E.; Girault, H. H. *Chem. Phys. Chem.* **2003**, *4*, 85.

(19) Jensen, H.; Fermin, D. J.; Moster, J. E.; Girault, H. H. *J. Phys. Chem. B.* **2002**, *106*, 10908.

(20) Su, B.; Fermin, D. J.; Abid, J.; Eugster, N.; Girault, H. H. *J. Electroanal. Chem.* **2005**, *583*, 241.

10.0 CONCLUSION

This thesis consists of two parts. The first part described the work performed on understanding the affect of different solution conditions on the association of organic macromolecules and the role played by the charge density of the backbone on the optical properties of polyphenylethynylene (PPE) based conjugated polyelectrolytes. The second part of the thesis described fundamental studies of the charge transfer and fluorescence quenching of nanocrystal assemblies, the electronic structure of CdSe NPs adsorbed on Au electrode by an organic linker, and preliminary electrochemical studies of NPs adsorbed at the interface between two immiscible electrolyte solutions.

The studies of polyphenylethynylene based anionic polyelectrolytes in dilute solutions in Chapter 2 showed how solvation and aggregation affects the optical properties of PPE based conjugated polyelectrolytes. The studies showed that the photophysical properties of these polyelectrolytes are very sensitive to electrolyte concentration and surfactants. Because of the formation of aggregates, the fluorescence intensity of polylelectrolytes decreased with increasing ionic strength of inorganic and organic salts. If the aggregates and the unaggregated form have different sensitivities for the analyte, then the aggregation will need to be controlled for sensing applications.

Chapter 3 described the fluorescence quenching mechanism for PPE based conjugated polyelectrolytes in the presence of macromolecules, namely cytochrome-*c* and dendrimers

(PAMAM 3G and DAB-4G). These studies showed that the fluorescence quenching of the dendrimer materials does not involve energy transfer or electron transfer, but is correlated to the overall charge on the dendrimer and its size. The quenching is hypothesized to result from conformational changes that occur upon binding the polyelectrolyte to the protein, or dendrimer. This mechanism is qualitatively different from that invoked for small molecule analytes.

In Chapter 4, fluorescence correlation spectroscopy was used to reveal how the hydrodynamic properties of the complexes between PPE-based conjugated polyelectrolytes (PPE-SO_3) and octadecyl trimethylammoniumbromide (OTAB) evolve with surfactant concentration. This study showed that a series of structures of PPE-SO_3^-/OTAB complexes with different size, chemical composition, and conformation exist depending on the comparative concentration of polyelectrolyte and surfactant when the concentration of OTAB is far lower than its CMC and CAC. Fluorescence correlation spectroscopy (FCS) proved to be a powerful tool for studying these complexes. These findings indicate that the rigidity of the polymer backbone plays an important role in determining the conformation between polyions and surfactant, and the ratio C_{OTAB} /$C_{monomer}$ might be a dominant factor for the composition of the complexes. The PPE-SO_3 represents the type of polyelectrolytes with rigid backbone, including ds DNA. The results may have important implications for the field of gene delivery.

Chapter 5 describes the low charge density PPE based conjugated polyelectrolytes (PPE-SO_3Na-L and PPE-CO_2Na-L), which feature sulfonate and carboxylate groups on every other phenyl ring, form aggregates in water, whereas high charge density poly(p-phenylene-ethynylene)s (PPE-SO_3Na-H and PPE-CO_2Na-H), which possess sulfonate or carboxylate groups on every phenyl ring, do not aggregate in water. The formation of aggregates of PPE-SO_3Na-L and PPE-CO_2Na-L is demonstrated by comparing the concentration and temperature dependence

of their steady-state spectra in water to that in DMSO, in which the two polymers do not aggregate. For the weak polyelectrolytes PPE-CO_2Na-H and PPE-CO_2Na-L, the solution pH was changed to vary the charge density. In addition, the cationic surfactant, octadecyltrimethyl ammonium (OTAB) was shown to dissociate the low charge density polymer aggregates and to form supramolecular complexes with each of the different polyelectrolytes. FCS was applied to provide insight into the sizes of aggregates under different solution conditions

In Chapter 7, electron transfer (ET) in aggregates of cadmium selenide, CdSe, and cadmium telluride, CdTe, nanoparticles (NPs) was studied in aqueous solution by fluorescence quenching. Both steady state and time-resolved fluorescence measurements were used to quantify how the ET depends on the nature of the NP assemblies. The aggregation of CdSe and CdTe NPs was controlled by the electrostatic attraction of the charged functionalities placed on the NP surface coating. Electron transfer quenching was found to depend on three factors: the interparticle distance, the energetic alignment of the NP bands (hence the size of the NPs), and the direction of the electric field between the NPs, created by their surface charges.

In chapter 8, assemblies of CdSe nanoparticles (NPs) on a dithiol coated Au electrode were created and their electronic energetics were quantified. We determined the energy level alignment of the filled and unfilled electronic states of CdSe nanoparticles with respect to the Au Fermi level. Using cyclic voltammetry it was possible to measure the energy of the filled states of the CdSe NPs with respect to the Au substrate relative to a $Ag/AgNO_3$ electrode, and by using photoemission spectroscopy it was possible to independently measure both the filled state energies (via single photon photoemission) and those of the unfilled states (via two photon photoemission) with respect to the vacuum level. Comparison of these two different measures shows good agreement with the IUPAC accepted value of the absolute electrode potential. In

contrast to the common model of energy level alignment, the experimental findings show that the CdSe filled states become "pinned" to the Fermi level of the Au electrode, even for moderately small NP sizes.

Chapter 9 describes our preliminary studies done on the organization and reactivity of NPs (CdTe) at the water/DCM interface in the presence of a Galvani potential bias. Photoelectrochemical studies were performed at the interface between two immiscible electrolyte solutions (ITIES). These systems promise to provide a reference systems for testing the ability of NPs to drive charge separation between two phases, and guide the development of bulk heterojunction solar cells composed of bicontinous conducting polymer films doped by dyads.

In summary, the main part of this thesis described the spectroscopic intevestigations on nanoscale aggregates and their electron transfer properties in solution. In part I, the absorption and fluorescence properties of conjugated polyelectrolytes were demonstrated to depend on solution conditions such as concentration, temperature, solvent, surfactant, and the ionic strength change. The equilibrium between unaggregated and aggregated forms of the polymer in aqueous solution was described and quantified. The fluorescence quenching of polymers by positively charged and neutral macromolecules was also investigated and shown that the quenching depends on electrostatic, hydrophobic, and energy transfer interactions with the quencher. Furthermore, it was also found that the optical and aggregation properties of these conjugated polyeletrolytes can be manipulated by changing the charge density along the polymer backbone. By increasing the charge density, it was possible to improve the solvation of these polymers in water enough so that single-strand behavior was observed. In part II, two types of charged nanoparticles (NP) CdSe and CdSe with staggered energy level configuration were brought together to form aggregates electrostatically. Aggregates size and the interparticle distance inside

the aggregates were manipulated by controlling the molar ratio of two NPs and NP surface ligands. Electron transfer in aggregates from CdTe to CdSe NPs was studied in aqueous solution by fluorescence quenching. Both steady state and time-resolved fluorescence measurements indicated that electron transfer quenching depended on three factors: the interparticle distance, the energetic alignment of the NP bands and the direction of the electric field between the NPs, created by their surface charges. In both parts of this thesis, spectroscopy proved to be a powerful tool to investigate the nanoscale aggregates in two different systems. Through spectroscopic measurements of UV-Visible absorbance, steady-state fluorescence, time-resolved fluorescence, and fluorescence correlation spectroscopy (FCS), important information and phenomena were provided and revealed. Electronic state, fluorescence, fluorescence quenching, fluorescence lifetime, electron transfer of/in aggregates can be illustrated. The experimental results may provide useful guidance for the applications of conjugated polyelectrolytes and NPs where aggregates play a significant role.

APPENDIX A

DETAILS OF LIQUID LIQUID CELL

Detailed information about the liquid liquid electrochemical cell used in the experiments described in Chapter 9 is provided in this appendix.

Photograph of empty cell is shown as Figure 10.1

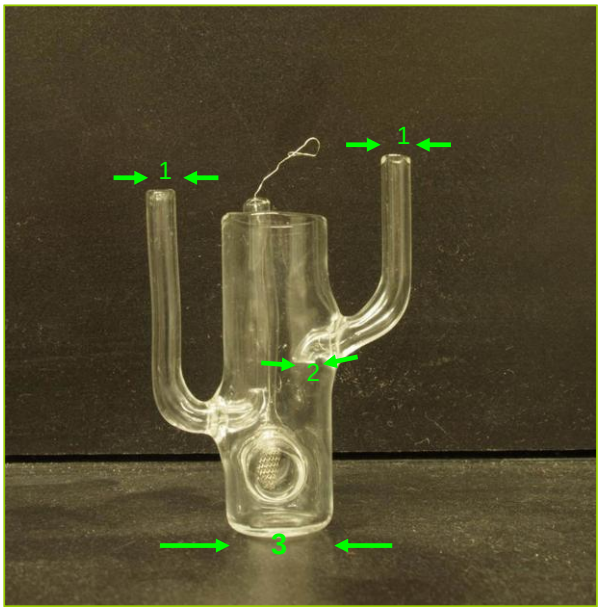

Figure 10.1 Photograph of empty electrochemical cell used in experiments performed in Chapter 9.

The most important parameter of the cell is the interface area. The interface area is ~ 1.53 cm^2 with the inner diameter of the cell (3)~ 1.40 cm as typical value used in literatures. The inner diameter of arms for reference electrodes and counter electrode (1) is ~0.50 cm. The height of the cell is ~5 cm and the tip diameter of Luggin capillaries (2) are less than 2 mm.

In typical experiments, the cell was first filled up with DCM containing supporting electrolyte (such as BTPPATPFB) until the liquid level lies between the two arms through which the Luggin capillaries will be placed, then carefully add BTPPACl and LiCl dissolved in water into arm in lower phase. Caution has to be taken to avoid air bubbles and leaking into interface. Finally water solution containing NaCl and/or CdTe NPs is added into upper phase, electrodes are put into solution and connected to computer-controlled CHI 700C four-electrode electrochemical workstation (CH Instruments, Austin, TX).

Photograph of the cell filled with solutions and connected is shown in Figure A2.

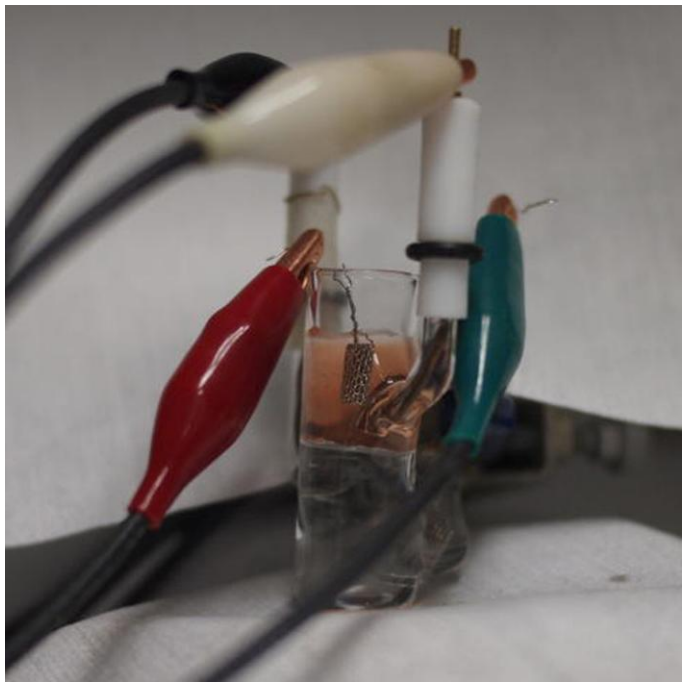

Figure 10.2 Photograph of the cell filled with solutions and connected. Upper phase is MSA-CdTe NPs in water solution (red) and lower phase is DCM with supporting electolyte (transparent).

As shown in Figure 10.2, the reference electrode in the water phase is connected to the white alligator clip, the reference electrode in the DCM phase is connected to the black alligator clip, the counter electrode in the water phase is connected to the red alligator clip, and the counter electrode in the DCM phase is connected to the green alligator clip, respectively.